# Connecting Ocean Circulation with Ocean Heat Storage: Experiments with an Idealised Aquaplanet Model

a thesis submitted in partial fulfilment

of the requirements for the degree of

Doctor of Philosophy

at Imperial College London

by

Peter Shatwell

Supervised by:

Dr Arnaud Czaja (Imperial College London, Physics)

Dr David Ferreira (University of Reading, Meteorology)

Prof. Greg Pavliotis (Imperial College London, Mathematics)

Space and Atmospheric Physics

Department of Physics

Imperial College London

180 Queen's Gate, London, SW7 2AZ

August 2022

I certify that this thesis, and the research to which it refers, are the product of my own work, and that any ideas or quotations from the work of other people, published or otherwise, are fully acknowledged in accordance with the standard referencing practices of the discipline.

Signed: _____

# Copyright

The copyright of this thesis rests with the author and is made available under a Creative Commons Attribution Non-Commercial No Derivatives licence. Researchers are free to copy, distribute or transmit the thesis on the condition that they attribute it, that they do not use it for commercial purposes and that they do not alter, transform or build upon it. For any reuse or redistribution, researchers must make clear to others the licence terms of this work.

# Abstract

Global warming is really 'ocean warming' as ∼93% of the excess heat energy entering the climate system is taken up by the oceans. The heat storage distribution is highly nonuniform in space, affected by a multitude of ocean heat uptake (OHU) processes across many spatial scales. These processes contribute to a substantial spread in climate model projections of future heat storage, sea-level rise, and surface warming. A better understanding of OHU processes is essential in order to reduce our uncertainty in climate projections.

I probe OHU processes using a coupled climate model with idealised geometry ('Double-Drake') under an abrupt $CO_2$-doubling. By projecting the Double-Drake circulation onto depth-temperature coordinates, I find that the ocean circulation response leads to an increase in the downward vertical heat transport of ∼0.2 W $m^{-2}$, enabling more interior heat storage. This supports the idea that changes in ocean circulation may further reinforce the ocean's role as a buffer of surface warming.

I examine in more detail the circulation response of an analogous Atlantic meridional overturning circulation (AMOC) in Double-Drake. Many models project a weakening of the AMOC in the future, where the implications for ocean warming are highly uncertain. I find that the link between the AMOC and heat storage rate is counterintuitive in Double-Drake, and that AMOC weakening may not be as important as traditionally thought.

Finally, I explore the representation of OHU in two-layer energy-balance models (EBMs), and find that increasing/decreasing the sensitivity of OHU to the stratification in the EBM improves/worsens the representation for Double-Drake and a suite of other coupled climate models. This suggests that improving OHU representation might be achieved via a simple change to the two-layer EBM.

The results reaffirm that an understanding of OHU is incomplete without a grasp of the underlying ocean circulation processes.

*"Our mission is to teach the world what man ne'er knew before; all truth, by science is unfurl'd, which nature has in store." — Crew song from the HMS Challenger expedition, 1872–1876*

*"When a problem comes along, you must whip it." — Devo, 1980*

# List of Abbreviations

| Abbreviation | |
|---|---|
| AABW | Antarctic Bottom Water |
| ACC | Antarctic Circumpolar Current |
| AMOC | Atlantic Meridional Overturning Circulation |
| AOGCM | Atmosphere-Ocean General Circulation Model |
| CMIP5 | Coupled Model Intercomparison Project phase 5 |
| DWBC | Deep Western Boundary Current |
| DWF | Deep Water Formation |
| EBM | Energy Balance Model |
| ECCO | Estimating the Circulation and Climate of the Ocean |
| ECS | Equilibrium Climate Sensitivity |
| EEI | Earth's Energy Imbalance |
| GCM | General Circulation Model |
| IPCC | Intergovernmental Panel on Climate Change |
| LB | Large Basin (DDrake region) |
| MHT | Meridional Heat Transport |
| MOC | Meridional Overturning Circulation |
| NADW | North Atlantic Deep Water |
| NOAA | National Oceanic and Atmospheric Administration |
| OHC | Ocean Heat Content |
| OHS | Ocean Heat Storage |
| OHT | Ocean Heat Transport |
| OHU | Ocean Heat Uptake |
| OHUE | Ocean Heat Uptake Efficiency |
| OSNAP | Overturning in the Subpolar North Atlantic Program |
| RAPID | The 'Rapid' climate change monitoring array at 26.5°N |
| RMSE | Root Mean-Square Error |
| SAMBA | South Atlantic MOC Basin-wide Array |
| SAT | Surface Air Temperature |
| SB | Small Basin (DDrake region) |
| SO | Southern Ocean (DDrake region) |
| SST | Sea Surface Temperature |
| TCR | Transient Climate Response |
| TOA | Top Of the Atmosphere |
| VHT | Vertical Heat Transport |
| WBC | Western Boundary Current |
| WMT | Water Mass Transformation |

| Model | |
|---|---|
| ACCESS-OM2 | Australian Community Climate and Earth System Simulator Ocean Model version 2 |
| CANESM2 | Canadian Earth System Model version 2 |
| CCSM4 | Community Climate System Model version 4 |
| CNRM-CM5 | Centre National de Recherches Météorologiques Coupled Model version 5 |
| GFDL-ESM2M | Geophysical Fluid Dynamics Laboratory Earth System Model version '2M' |
| HadCM3 | Hadley Centre Coupled Model version 3 |
| MIROC-ESM | Model for Interdisciplinary Research On Climate Earth System Model |
| MITgcm | Massachusetts Institute of Technology general circulation model |
| MPI-ESM-LR | Max Planck Institute for meteorology Earth System Model (Low Resolution) |
| MRI-CGCM3 | Meteorological Research Institute Coupled Global Climate Model version 3 |
| NASA-GISS-E2-H | National Aeronautics and Space Administration Goddard Institute for Space Studies (United States) model version 'E2-H' |
| NEMO | Nucleus for European Modelling of the Ocean |
| NorESM-1M | Norwegian Earth System Model version '1M' |
| UVic ESM | University of Victoria Earth System Model |

# List of Figures

1.1 The Spilhaus projection or world ocean map in a square, rendered in ArcGIS Pro 2.5 (reproduced from https://arcg.is/1vTXHn, by Bojan Šavrič, David Burrows, and Melita Kennedy) . . . . . 2

1.2 Estimates of zonal-mean meridional ocean heat transports over 1984-2006 based on the COREv2 climatological surface air-sea flux data set. Green shading indicates the interannual variation. The triangles and squares are observational heat transport estimates derived from the basin-wide hydrographic sections compiled by [Bryden and Imawaki, 2001]. Figure reproduced from [Large and Yeager, 2009]. . . 3

1.3 Temperature reconstructions from the Greenland ice core GISP2 (blue, [Grootes et al., 1993]), and ocean sediment proxy data from the subtropical Atlantic (green, [Sachs and Lehman, 1999]). D/O warm events are numbered, and Heinrich events (corresponding to large ice sheet discharges into the North Atlantic) are marked as red squares. The grey vertical lines are spaced 1470 years apart, illustrating the tendency for D/O events to occur with this spacing. Figure reproduced from [Rahmstorf, 2002]. . . . . 5

1.4 Schematic of the main surface ocean currents, highlighting the dominance of the subtropical gyres. The zonally-averaged zonal surface winds are shown in the left-hand panel. Figure taken from [Vallis, 2012], kindly made available on his personal website: http://empslocal.ex.ac.uk/people/staff/gv219/. . . . . 7

1.5 Schematic showing the 'Upper' and 'Lower' cells of the MOC, reproduced from [Marshall and Speer, 2012]. Arrows indicate the direction of the circulation, with colours representing the average density of water masses from lightest (red-yellow) to densest (green-blue). Surface buoyancy fluxes and wind stress directions are also indicated. In the background is the zonally-averaged distribution of dissolved oxygen, and the thin black line roughly indicates the depth of the Mid-Atlantic Ridge. . . . . 8

1.6 Schematic of the global overturning circulation, reproduced from [Talley, 2013]. Arrows indicate the direction of the circulation and colours represent the average density of water masses from lightest (purple-red) to densest (green-blue). A small leakage of less than 1 Sv makes its way from the Pacific to the Atlantic through the Bering Strait. . . 9

1.7 Two-dimensional schematic of the MOC, reproduced from [Ferrari et al., 2017]. Green is NADW, blue is AABW, red is Indian and Pacific deep waters (IDW/PDW), and yellow is intermediate waters. The vertical dashed lines indicate diapycnal mixing transforming AABW into NADW, or AABW into IDW/PDW. The jagged line represents the main bathymetric features in the Indo-Pacific, below which diapycnal mixing is enhanced. . . . . 10
1.8 Schematic of the global annual-mean energy flows through the climate system (in W $m^{-2}$). Earth's energy imbalance, or the net absorbed, is estimated at $0.9 \pm 0.2$ W $m^{-2}$. Figure reproduced from [Trenberth, 2020], based on [Trenberth et al., 2009] and [Wild et al., 2015]. . . . . 14
1.9 Annual global-mean surface temperature anomalies relative to 1961-1990 from three different data sets (HadCRUT4, NASA-GISS, and NCDC-MLOST). Reproduced from [Hartmann et al., 2013]. . . . . 15
1.10 Observational estimates of changes in ocean heat content since 1950 from the IPCC's fifth assessment report [Rhein et al., 2013]. a) Annual global-mean upper-ocean (0-700 m) heat content adapted from [Levitus et al., 2012, Ishii and Kimoto, 2009, Domingues et al., 2008, Palmer et al., 2007, Smith and Murphy, 2007]. b) Five-year running means of global-mean mid-depth (700-2000 m, data from [Levitus et al., 2012]) and deep (2000-6000 m, data from [Purkey and Johnson, 2010]) ocean heat content changes. . . . . 16
1.11 Spatial maps of the annual mean net heat flux divided into components of (a) Latent Heat, (b) Sensible Heat, (c) Longwave Flux, and (d) Shortwave Flux in W $m^{-2}$. Positive values are directed downwards. Panels (a) and (b) use the Objectively Analyzed Air-sea Fluxes (OAFlux) dataset [Yu and Weller, 2007], while panels (c) and (d) use the satellite-only International Satellite Cloud Climatology Project (ISCCP) fields [Zhang et al., 2004]. Figure reproduced from [Josey et al., 2013]. . . . . 18
1.12 Climatological annual-mean net air-sea heat flux from OAFlux [Yu and Weller, 2007] and ISCCP [Zhang et al., 2004], reproduced from [Josey et al., 2013]. . . . . 19
1.13 Linear trends in 0-700 m OHC anomalies (OHCA) over the period 1993-2019 (W $m^{-2}$) from (a) NOAA's Pacific Marine Environmental Laboratory (PMEL) [Lumpkin et al., 2020], (b) Japan Meteorological Agency (JMA) [Ishii et al., 2017], (c) Institute of Atmospheric Physics (IAP) [Cheng et al., 2017], and (d) NOAA's National Center for Environmental Information (NCEI) [Levitus et al., 2012]. Figure reproduced from [Johnson and Lyman, 2020]. . . . . 20
1.14 Schematic of the simple model developed by [Gnanadesikan, 1999]. The effects of Southern Ocean winds and compensating eddies are represented by the volume flux $T_s$, NADW formation is represented by the flux $T_n$, and diapycnal mixing is represented by a low-latitude upwelling flux $T_u$. . . . . 23

2.1 Time-averaged sea surface temperature (in °C) in the control integration, showing the model DDrake geometry from above (left) and below (right). The small basin (SB), large basin (LB), and southern ocean (SO) regions are labelled. . . . . 35

2.2 Meridional ocean heat transports (OHT) and freshwater transports (FWT) for (left) the small and large basins of DDrake and (right) the Atlantic and Indo-Pacific basins. Observations for OHT are taken from [Trenberth and Caron, 2001], while observations of FWT are taken from [Wijffels et al., 1992]. Figure reproduced from [Ferreira et al., 2010]. . . . . 36

2.3 Zonally-averaged atmospheric potential temperature (a) and zonal winds (b) for the DDrake control climate. . . . . 42

2.4 Control climate zonally and sector-averaged potential temperature (top), salinity (middle), and potential density $\sigma_0$ (bottom) distributions for the small basin plus southern ocean (SBSO, left column) and large basin plus southern ocean (LBSO, right column) DDrake regions. Potential temperature and potential density fields are referenced to the surface. . . . . 43

2.5 Spatial maps of the DDrake control climate (a) sea surface temperature (SST, in °C), (b) sea surface salinity (SSS, in psu), and (c) surface density ($\sigma_0$, in kg m$^{-3}$). . . . . 43

2.6 Hydrographic sections of potential temperature (top, in °C) and salinity (bottom, in psu) for the Atlantic (left) and Pacific (right) basins taken during the World Ocean Circulation Experiment (WOCE), from [Schlitzer, 2000]. . . . . 44

2.7 Decadally averaged surface climatological fields over the period 1955-2017 of (a) sea surface temperature (in °C), (b) sea surface salinity (in psu), and (c) surface density ($\sigma_0$, in kg m$^{-3}$), from the World Ocean Atlas 2018 [Boyer et al., 2018]. . . . . 45

2.8 Control climate residual overturning stream functions for the (a) small basin, (b) large basin, and (c) global regions of DDrake (in Sv, 1 Sv $\equiv 10^6$ m$^3$ s$^{-1}$). The southern ocean residual overturning is shown south of 35°S (thick black line) in panels (a) and (b). . . . . 48

2.9 Zonally-averaged potential density referenced to 2100 dbar (top) and meridional overturning circulations (bottom) for the Atlantic (left) and Indo-Pacific (right), calculated from the ECCOv4 ocean reanalysis [Forget et al., 2015]. Panels a and b are reproduced from [Cessi, 2019] while panels c and d are reproduced from [Ferreira et al., 2018a]. 49

3.1 DDrake control climate vertical heat balance for advective (ADV) and diffusive (DIFF) processes, and shortwave (SW) radiation penetration (in W m$^{-2}$). A downward heat flux is positive. The zero line is black dotted. Only the top 1.5 km are shown for clarity. . . . . 59

3.2 Comparison of model-outputted vertical advective heat fluxes (solid lines) with those calculated from the thermal overturning $\Psi_{\theta z}$ (dash-dotted lines), for the DDrake control climate. The zero line is black dotted. Only the top 1.5 km are shown for clarity. . . . . 61

3.3 DDrake control climate zonally-averaged $\Psi_{res}^{ctrl}$ (colour, in Sv) and $\theta$ distributions (black dashed lines, in °C) for the (a) global, (b) southern ocean, (c) small basin, and (d) large basin regions. Contour interval is 5 Sv for panels a, c, and d. For panel b, the interval is 2 Sv; also, note the different colour-bar scale. Red cells circulate clockwise while blue cells circulate anti-clockwise. . . . . 62

3.4 Control climate DDrake global thermal overturning circulations (in Sv). (a) Resolved circulation $\overline{\Psi_{\theta z}}$, (b) eddy-induced circulation $\Psi'_{\theta z}$, and (c) net circulation $\Psi_{\theta z} = \overline{\Psi_{\theta z}} + \Psi'_{\theta z}$. Red cells circulate clockwise while blue cells circulate anti-clockwise. . . . . 64

3.5 DDrake global net control thermal overturning circulation ($\Psi_{\theta z}$, in Sv), decomposed into a warm cell (red solid, for $\theta > 15$°C), a cool cell (blue dashed, for $\theta < 20$°C), and a tropical cell (green dashed, for $\theta > 20$°C). Dashed lines denote negative values and circulate anti-clockwise, while solid lines denote positive values and circulate clockwise. Only the top 2 km are shown. . . . . 65

3.6 DDrake net control thermal overturning circulations ($\Psi_{\theta z}$, in Sv) calculated for the (a) global, (b) southern ocean, (c) small basin, and (d) large basin regions. The large basin dominates the global $\Psi_{\theta z}$ structure. Red cells circulate clockwise while blue cells circulate anti-clockwise. . . . . 67

3.7 Vertical heat transport profiles for the three thermal overturning cells of DDrake in the control climate (in W m$^{-2}$). Here, a positive heat transport is directed downwards. The solid black line is the sum of the red, blue, and green lines. The dash-dotted black line is the total global advective VHT, accounting for cells not included in the $\Psi_{\theta z}$ three cell decomposition. Only the top 2 km are shown. . . . . 72

3.8 DDrake control global net overturning circulation in depth-density coordinates, as a function of potential density $\sigma_0$. (a) The net $\Psi_{\sigma_0 z}$ overturning (in Sv) and (b) its decomposition into a warm cell (red dashed, for $\sigma_0 < 25.2$ kg m$^{-3}$), a cool cell (blue solid, for $\sigma_0 > 24$ kg m$^{-3}$), and a tropical cell (green solid, for $\sigma_0 < 24$ kg m$^{-3}$). In panel a, red cells circulate clockwise and blue cells circulate anti-clockwise. In panel b, solid lines denote positive values and circulate clockwise, while dashed lines denote negative values and circulate anti-clockwise. 76

3.9 (a) DDrake control climate (solid lines) and perturbed climate (dashed lines) vertical heat balance for advective (ADV) processes split into resolved and eddy-induced advection (EIA), diffusive (DIFF) processes and shortwave (SW) radiation penetration (in W $m^{-2}$). (b) Change in vertical heat flux due to the $CO_2$-doubling perturbation (difference between the dashed and solid lines in panel a). A downward heat flux is positive. Only the top 2 km are shown. . . . . 77

3.10 Response of the DDrake global thermal overturning circulation to an abrupt $CO_2$-doubling (in Sv). Top row: (a) control climate thermal overturning $\Psi_{\theta z}^{ctrl}$, (b) perturbed climate thermal overturning $\Psi_{\theta z}^{perturbed}$, (c) their difference $\Delta\Psi_{\theta z} = \Psi_{\theta z}^{perturbed} - \Psi_{\theta z}^{ctrl}$. Red cells circulate clockwise while blue cells circulate anticlockwise. Bottom row: same as the top row but decomposed into the tropical, warm, and cool thermal overturning cells as defined in the text. Here, solid lines circulate clockwise and dashed lines circulate anticlockwise. . . . 79

3.11 Small basin thermal overturning circulation response to an abrupt $CO_2$-doubling. (a) control climate thermal overturning $\Psi_{\theta z}^{ctrl}$, (b) perturbed climate thermal overturning $\Psi_{\theta z}^{perturbed}$, (c) their difference $\Delta\Psi_{\theta z} = \Psi_{\theta z}^{perturbed} - \Psi_{\theta z}^{ctrl}$. Red cells circulate clockwise while blue cells circulate anticlockwise. . . . . 79

3.12 Large basin thermal overturning circulation response to an abrupt $CO_2$-doubling. (a) control climate thermal overturning $\Psi_{\theta z}^{ctrl}$, (b) perturbed climate thermal overturning $\Psi_{\theta z}^{perturbed}$, (c) their difference $\Delta\Psi_{\theta z} = \Psi_{\theta z}^{perturbed} - \Psi_{\theta z}^{ctrl}$. Red cells circulate clockwise while blue cells circulate anticlockwise. . . . . 80

3.13 Southern ocean thermal overturning circulation response to an abrupt $CO_2$-doubling. (a) control climate thermal overturning $\Psi_{\theta z}^{ctrl}$, (b) perturbed climate thermal overturning $\Psi_{\theta z}^{perturbed}$, (c) their difference $\Delta\Psi_{\theta z} = \Psi_{\theta z}^{perturbed} - \Psi_{\theta z}^{ctrl}$. Red cells circulate clockwise while blue cells circulate anticlockwise. . . . . 80

3.14 Zonally-averaged zonal surface wind stress $\tau_x$ (solid lines) and its response to an abrupt $CO_2$-doubling (dashed lines) (in N $m^{-2}$). Solid coloured lines correspond to 50-year time-means throughout the 200 year experiment. Dashed lines are equivalent to the solid coloured lines with the control zonal-average subtracted. . . . . 81

3.15 Zonally-averaged Ekman pumping velocity $W_{Ek}$ (solid lines) and its response to an abrupt $CO_2$-doubling (dashed lines) (in m $yr^{-1}$). Solid coloured lines correspond to 50-year time-means throughout the 200 year experiment. Dashed lines are equivalent to the solid coloured lines with the control zonal-average subtracted. . . . . 83

3.16 Changes in vertical heat transports (VHTs) carried by the tropical, warm, and cool cells of the DDrake thermal overturning circulation. Positive = downward. (a) Control climate (solid lines) and perturbed climate (dashed lines) VHT profiles. (b) VHT responses due to the $CO_2$-doubling. The black dash-dotted line is the net global advective VHT response. The net global response takes into account circulations not included in the three-cell decomposition of the thermal overturning. (c) Comparison of the three-cell sum and net global VHT responses. Their difference (black dashed) is attributed to the deep warm cell. . . . . 86

3.17 Changes in the peak (positive or negative) VHT carried by the tropical, warm, and cool cells of the DDrake thermal overturning, in response to the $CO_2$-doubling. (a) Control and perturbed climate values, and their difference (in W $m^{-2}$), (b) percentage changes. . . . 87

3.18 Changes in the work performed by the tropical, warm, and cool cells of the DDrake thermal overturning, in response to the $CO_2$-doubling (using equation 3.8 with $\Psi_{\sigma_0 z}$). (a) Control and perturbed climate values, and their difference (in GW), (b) percentage changes. . . . . 88

3.19 Changes in the work performed by the global resolved and eddy-induced circulations, and their sum (net circulation), in response to a $CO_2$-doubling (using equation 3.8 with $\Psi_{\sigma_0 z}$). (a) Control and perturbed climate values, and their difference (in GW), (b) percentage changes. . . . . 88

4.1 Control residual overturning stream functions $\Psi_{res}^{ctrl}$ for the (a) small basin, and (b) large basin (in Sv, 1 Sv $\equiv 10^6$ $m^3$ $s^{-1}$). The southern ocean residual overturning is shown south of 35°S (thick black line). . 100

4.2 Time series of annually-averaged (a) SB and LB heat storage rates ($\partial_t(\Delta\text{OHC})$, in W $m^{-2}$); (b) OHC anomalies ($\Delta$OHC, in J $m^{-2}$); (c) the difference in heat storage rates i.e. the heat storage contrast ($\partial_t(\Delta\text{OHC}_{SB} - \Delta\text{OHC}_{LB})$, in W $m^{-2}$); and (d) SBMOC strength ($\max(\Psi_{res}^{pert})$, in Sv) following an abrupt doubling of $CO_2$. Thick lines are decadal running means and horizontal dash-dot lines indicate time-mean values. The time-mean heat storage contrast is 0.6 ± 0.2 W $m^{-2}$ (standard error, assuming 20 degrees of freedom accounting for decadal oscillations). . . . . 102

4.3 (a) Time-series of heat storage responses (in J) for all DDrake basins. (b-d) Comparison of actual versus expected heat storage responses (in J) considering the fractional coverage of the total surface area for (b) the small basin (SB), (c) the large basin (LB), and (d) the southern ocean (SO) of DDrake. For each basin B, the 'expected' curves are (B's surface-area/global surface-area)*(global response) i.e. the surface-area-weighted fraction of the black curve in (a). From this perspective, we see that the SB overperforms (while the LB underperforms) with respect to its size. . . . . 103

4.4 Depth-time plots of the anomalous temperature response (in K) in the (a) small and (b) large basins of DDrake following an abrupt $CO_2$-doubling. The contour interval is 0.1 K, and the 0.1, 0.5, 1.0, and 1.5 K contours are highlighted. The upper ocean responses are similar, but the differences at depth are substantial. . . . . 105

4.5 Vertically-averaged $\Delta\theta$ (in K) after 200 years following an abrupt doubling of atmospheric $CO_2$ in DDrake for the depth intervals (a) 0-1 km and (b) 1-3 km. The temperature anomaly at depth follows a deep western boundary current in the small basin. (c) Zonally-averaged $\Delta\theta$ (colour, in K) in the small basin after 200 years' warming, and streamlines (white dashed contours, in Sv) for the control residual overturning $\overline{\Psi_{res}}$. . . . . 106

4.6 Time series of time-integrated net surface heat flux (OHU) and changes in OHC (OHS), and their difference (OHS−OHU) (in J $m^{-2}$) for the (a) small basin, (b) large basin, and (c) southern ocean regions of DDrake. . . . . 107

4.7 (a) Map of time-mean SST warming trends during the first 30 years (i.e. SBMOC weakening regime) of the $CO_2$-doubling experiment (in K/decade), (b) Zonally-averaged time-mean SST warming trends over the same period. . . . . 108

4.8 Time-mean vertically-averaged convective index for (a) the control climate, (b) the first 50 years following the $CO_2$-doubling, and (c) their difference. The dark blue lines indicate the meridional barriers enclosing the small basin (they don't contribute to the convection). . 109

4.9 Time series of warming responses for the small basin MOC downwelling ($\Delta\theta_{\downarrow}$, red) and upwelling ($\Delta\theta_{\uparrow}$, blue) regions, and their difference ($\Delta(\delta\theta)$, black) (in K). The downwelling region warms at a faster rate than the upwelling region. . . . . 110

4.10 Zonal-mean structures of the SBMOC response. (a) 0-30 years time-mean $\Psi_{res}^{pert}$ (colour), and $\overline{\Psi_{res}}$ (white dashed contours) overturning in the small basin (in Sv) during the weakening regime; (b) 0-30 years time-mean $\Delta\Psi_{res} = \Psi_{res}^{pert} - \overline{\Psi_{res}}$ overturning response (colour and pink dashed contours) in the small basin (in Sv) during the weakening regime; (c-d) same as panels (a) and (b) except time-means are taken over the period 30-200 years during the non-weakening regime. In panels (a) and (c), the contour interval is 5 Sv and the zero contour is highlighted in black. . . . . 111

4.11 (a) Decomposition of the change in SB downward (positive) MOC heat flux ($\Delta(\Psi_{res}\delta\theta)$, magenta) into differential warming ($\overline{\Psi_{res}}\Delta(\delta\theta)$, blue), SBMOC weakening ($\Delta\Psi_{res}\overline{\delta\theta}$, orange), and nonlinear ($\Delta\Psi_{res}\Delta(\delta\theta)$, yellow) terms (annual averages, in W m$^{-2}$). A vertical dotted line is plotted at 30 years to separate the weakening and non-weakening SBMOC regimes. (b) Decadal running means of the SB heat uptake rate ($\Delta\mathcal{F}_s^{SB}$, blue), heat storage rate ($\partial_t(\Delta\text{OHC}_{SB})$, red), SBMOC heat flux ($\Delta\mathcal{H}_{MOC}$, magenta), and leakage rate to the southern ocean ($\Delta\mathcal{H}_{leak} = \partial_t(\Delta OHC_{SB}) - \Delta\mathcal{F}_s^{SB}$, black) (in W m$^{-2}$). Note that the sum of the heat storage rate and SBMOC heat flux (light blue, dashed) almost matches the heat uptake rate. Horizontal dashed lines are centennial time-means. . . . . 112

4.12 (a) Atlantic vs. Pacific top-3 km column-averaged annual OHC anomalies (in J m$^{-2}$) immediately following an abrupt quadrupling of atmospheric $CO_2$ in CMIP5 models (each dot represents one year). Atlantic and Pacific basins defined from 30°S to 65°N. The deviation from the identity line (black dashed) highlights the Atlantic's enhanced warming rate relative to the Pacific in these experiments. (b) Decadal running means of individual model Atlantic–Pacific heat storage contrasts $\partial_t(\Delta\text{OHC}_{Atl} - \Delta\text{OHC}_{Pac})$ (in W m$^{-2}$). . . . . 114

5.1 Diagram of the simple two-layer energy balance model. Arrows represent energy fluxes. $\mathcal{F}$ is the effective forcing at the ocean surface, $\alpha$ is the globally-averaged climate feedback parameter, $\gamma$ is the heat exchange parameter, $T$ and $T_0$ are temperature perturbations, and $C$ and $C_0$ are effective heat capacities. . . . . 122

5.2 Time-series of annually-averaged surface air temperature (SAT, orange line) and sea surface temperature (SST, blue line); and vertically-averaged upper-layer temperature ($T$, yellow line) and lower-layer temperature ($T_0$, purple line) corresponding to the derived layer thicknesses presented in table 5.1 for the (a) global, (b) small basin, (c) large basin, and (d) southern ocean regions of DDrake, relative to the control climate state. The fitted Geoffroy EBM responses for $T$ and $T_0$ are shown as black dashed lines. . . . . 128

5.3 Comparison of fitted EBM responses (black dashed) for the Geoffroy EBM (left column) and quadratic EBM (right column). Presented are time-series of annually-averaged SST responses (magenta), and vertically-averaged upper-layer (red, $T$) and lower-layer (blue, $T_0$) temperature responses corresponding to the layer thicknesses $h$ and $H$ implied by the EBM (see table E.1), for the DDrake $CO_2$-doubling experiment. Panels (a-d) correspond to the different basins of DDrake: (a) Global responses, (b) Small basin responses (blue shading), (c) Large basin responses (red shading), and (d) southern ocean responses (yellow shading). . . . . 133

5.4 Percentage improvement in the RMSE of the fitted DDrake temperature responses after changing from the Geoffroy EBM to the quadratic EBM. The change improves fits for all basins but the southern ocean. A substantial increase ($> 50\%$) is seen for the global lower-layer temperature response. . . . . 134

5.5 Comparison between the annual-average global-mean SST response from CMIP5 model abrupt $4\times CO_2$ experiments, and the upper-layer $T$ responses fitted from the two-layer (a) Geoffroy and (b) quadratic EBMs. Points for the abrupt $CO_2$-doubling experiment in DDrake are also plotted for comparison. . . . . 136

5.6 Comparison between the inferred upper-layer $T$ responses (top row) and lower-layer $T_0$ responses (bottom row) from CMIP5 models with the corresponding fitted responses from both the Geoffroy (left column) and quadratic (right column) two-layer EBMs. Points for the abrupt $CO_2$-doubling experiment in DDrake are also plotted for comparison. . . . . 137

5.7 Comparison between the RMSEs of the fits found from the Geoffroy and quadratic two-layer EBMs for CMIP5 model temperature responses in abrupt $4\times CO_2$ experiments. The (a) total, (b) upper-layer, and (c) lower-layer RMSEs are shown. Points corresponding to the abrupt $CO_2$-doubling experiment in DDrake are also shown as blue diamonds. . . . . 138

5.8 Percentage improvement in the RMSE of the fitted CMIP5 model (and DDrake) temperature responses after changing from the Geoffroy EBM to the quadratic EBM. The change improves fits for the lower-layer response for 4 out of the 5 CMIP5 models analysed. . . . 139

5.9 Comparison of fitted EBM responses (black dashed) for the Geoffroy EBM (left column) and RY EBM (right column). Presented are time-series of annually-averaged SST responses (magenta), and vertically-averaged upper-layer (red, $T$) and lower-layer (blue, $T_0$) temperature responses corresponding to the layer thicknesses $h$ and $H$ implied by the EBM (see table E.3), for the DDrake $CO_2$-doubling experiment. Panels (a-d) correspond to the different basins of DDrake: (a) Global responses, (b) Small basin responses (blue shading), (c) Large basin responses (green shading), and (d) southern ocean responses (yellow shading). . . . . 143

5.10 Percentage improvement in the RMSE of the fitted DDrake temperature responses after changing from the Geoffroy EBM to the RY EBM. The change worsens fits overall, mainly due to the especially poor fit for the SB. . . . . 144

5.11 Percentage improvement in the RMSE of the fitted CMIP5 model (and DDrake) temperature responses after changing from the Geoffroy EBM to the RY EBM. The change leads to poorer fits across the board apart from MRI-CGCM3. . . . . 145

6.1 Census of water masses for the DDrake control climate in temperature-salinity coordinates for (a) global, (b) southern ocean, (c) small basin, and (d) large basin regions (colour, in $\log_{10}\mathrm{m}^3/^\circ\mathrm{C}/\mathrm{psu}$). In white are contours of potential density $\sigma_0$ (kg $\mathrm{m}^{-3}$). . . . . 156
6.2 (a) Global water mass census for the DDrake control climate in temperature-salinity coordinates in $\log_{10}\mathrm{m}^3/^\circ\mathrm{C}/\mathrm{psu}$ (equivalent to panel a from figure 6.1). (b) Average water mass transformation rate between the control climate and year 200 of the $CO_2$-doubling run in 0.1 $\mathrm{Sv}/^\circ\mathrm{C}/\mathrm{psu}$. Black lines are contours of potential density $\sigma_0$ (kg $\mathrm{m}^{-3}$). . . . . 158

D.1 Two-layer EBM reduces to two separate one-layer EBMs in the limit $\gamma << \alpha$. . . . . 222
D.2 Two-layer EBM reduces to a one-layer system with effective heat capacity $C + C_0$ when $\gamma >> \alpha$. . . . . 224

# List of Tables


5.1 Upper-layer heat capacity $C$, lower-layer heat capacity $C_0$, the corresponding upper- and lower-layer thicknesses $h$ and $H$, heat exchange coefficient $\gamma$, and fitted slow and fast timescales $\tau_s$ and $\tau_f$ for each of the DDrake basins, following the fitting procedure in [Geoffroy et al., 2013b]. . . . . 126

5.2 Calculated radiative parameters for each of the DDrake basins using the SAT, following the fitting procedure in [Geoffroy et al., 2013b]: the radiative forcing $\mathcal{F}$, the climate feedback $\alpha$, and the corresponding equilibrium temperature $T_{eq}$. . . . . 126

5.3 Root mean-square errors (RMSEs) for the EBM fits for the upper- and lower-layer temperature responses $T$ and $T_0$ for each basin of DDrake. The RMSE for the upper-layer EBM fit is also evaluated against the SAT response, shown in the left-most column for comparison. . . . . 129

5.4 Root mean-square errors (RMSEs) for the (Geoffroy; quadratic) EBM fits for the upper- and lower-layer temperature responses $T$ and $T_0$ for each basin of DDrake. The RMSE for the upper-layer EBM fit evaluated against the SST response is also shown in the left-most column for comparison. . . . . 132

5.5 Root mean-square errors (RMSEs) for the (Geoffroy; quadratic) EBM fits for the upper- and lower-layer temperature responses $T$ and $T_0$ from CMIP5 abrupt $4\times CO_2$ experiments. The RMSE for the upper-layer EBM fit evaluated against the SST response is also shown in the left-most column for comparison. Equivalent RMSEs for DDrake (same as the 'Global' row in table 5.4) are shown in the bottom row for reference. Note that the ensemble means and standard deviations don't include the DDrake values. . . . . 138

5.6 Root mean-square errors (RMSEs) for the (Geoffroy; RY) EBM fits for the upper- and lower-layer temperature responses $T$ and $T_0$ for each basin of DDrake. The RMSE for the upper-layer EBM fit evaluated against the SST response is also shown in the left-most column for comparison. . . . . 142

5.7 Root mean-square errors (RMSEs) for the (Geoffroy; RY) EBM fits for the upper- and lower-layer temperature responses $T$ and $T_0$ from CMIP5 abrupt $4\times CO_2$ experiments. The RMSE for the upper-layer EBM fit evaluated against the SST response is also shown in the left-most column for comparison. Equivalent RMSEs for DDrake (same as the 'Global' row in table 5.4) are shown in the bottom row for reference. Note that the ensemble means and standard deviations don't include the DDrake values. . . . . 145

E.1 Fitted physical parameters for both the (Geoffroy; quadratic) EBMs using an interior point algorithm: the radiative forcing $\mathcal{F}$, radiative feedback $\alpha$, upper-layer heat capacity $C$, lower-layer heat capacity $C_0$, the corresponding upper-layer and lower-layer thicknesses $h$ and $H$, and the heat exchange coefficient $\gamma$ (or $\gamma^*$) for each of the DDrake basins. . . . . 226
E.2 Fitted physical parameters for both the (Geoffroy; quadratic) EBMs using an interior point algorithm. The effective radiative forcing $\mathcal{F}$ and climate feedback $\alpha$ values for CMIP5 models are taken from [Kostov et al., 2014]. Upper-layer heat capacity $C$, lower-layer heat capacity $C_0$, the corresponding upper-layer and lower-layer thicknesses $h$ and $H$, and the heat exchange coefficient $\gamma$ (or $\gamma^*$) estimates for the five CMIP5 models used. The equivalent parameters found for DDrake (same as the 'Global' row in table E.1) are shown in the bottom row for comparison. Ensemble means and standard deviations don't include the values from DDrake. . . . . 227
E.3 Fitted physical parameters for both the (Geoffroy; RY) EBMs using an interior point algorithm: the radiative forcing $\mathcal{F}$, radiative feedback $\alpha$, upper-layer heat capacity $C$, lower-layer heat capacity $C_0$, the corresponding upper-layer and lower-layer thicknesses $h$ and $H$, and the heat exchange coefficient $\gamma$ (or $\gamma^*$) for each of the DDrake basins. . . . . 228
E.4 Fitted physical parameters for both the (Geoffroy; RY) EBMs using an interior point algorithm. The effective radiative forcing $\mathcal{F}$ and climate feedback $\alpha$ values for CMIP5 models are taken from [Kostov et al., 2014]. Upper-layer heat capacity $C$, lower-layer heat capacity $C_0$, the corresponding upper-layer and lower-layer thicknesses $h$ and $H$, and the heat exchange coefficient $\gamma$ (or $\gamma^*$) estimates for the five CMIP5 models used. The equivalent parameters found for DDrake (same as the 'Global' row in table E.3) are shown in the bottom row for comparison. Ensemble means and standard deviations don't include the values from DDrake. . . . . 229

# Contents


1 Introduction **1**
- 1.1 Setting the stage . . . 1
- 1.2 The ocean's role in climate . . . 2
- 1.3 A brief overview of large-scale ocean circulation . . . 6
- 1.4 The ocean's response to warming . . . 13
  - 1.4.1 Ocean Heat Storage Patterns . . . 17
  - 1.4.2 Ocean Heat Uptake Processes . . . 21
- 1.5 A roadmap for this thesis . . . 28
  - 1.5.1 First results chapter . . . 28
  - 1.5.2 Second results chapter . . . 28
  - 1.5.3 Third results chapter . . . 29

2 Experiment Design **31**
- 2.1 Modelling philosophy . . . 32
- 2.2 The MITgcm . . . 33
- 2.3 The DDrake configuration . . . 35
  - 2.3.1 Technical description . . . 37
  - 2.3.2 Control Climatology . . . 41
- 2.4 Forcing experiment: an abrupt $CO_2$-doubling . . . 50

3 Changes in vertical heat transports by ocean circulation under global warming **53**
- 3.1 Introduction . . . 54
- 3.2 Stream functions in other coordinates . . . 56
- 3.3 Control climate vertical heat balance . . . 58
  - 3.3.1 The DDrake thermal overturning circulation . . . 61
  - 3.3.2 Vertical heat transports . . . 72
  - 3.3.3 Thermally or mechanically driven? . . . 73
- 3.4 Perturbed climate vertical heat balance . . . 77
  - 3.4.1 Changes in ocean circulations and the associated vertical heat transports . . . 78
  - 3.4.2 Changes in energetics . . . 87
- 3.5 Conclusion . . . 90
  - 3.5.1 Summary . . . 90
  - 3.5.2 Discussion and Conclusions . . . 91
  - 3.5.3 Key points . . . 94

4 Ocean heat storage response to an AMOC slowdown **95**
- 4.1 Introduction . . . 96

4.2 Control climate overturning circulations . . . 99
4.3 Results . . . 101
4.3.1 Small and Large Basin Heat Storage Rates . . . 101
4.3.2 Role of the Small Basin MOC . . . 104
4.3.3 Role of the southern ocean region . . . 107
4.3.4 Heat storage response to SBMOC Weakening . . . 108
4.3.5 Parallels with CMIP5 Models . . . 113
4.4 Discussion and Conclusions . . . 114
4.4.1 Key points . . . 117

5 Representation of OHU in Two-Layer EBMs **119**
5.1 Introduction . . . 120
5.2 The traditional EBM framework . . . 123
5.2.1 Fitting procedure . . . 123
5.2.2 Results with traditional EBM: DDrake fitted responses . . . 125
5.3 A new EBM framework . . . 129
5.3.1 New fitting procedure . . . 130
5.3.2 Increasing the sensitivity ($\zeta = 2$) . . . 131
5.3.3 Decreasing the sensitivity ($\zeta = 2/3$) . . . 140
5.4 Conclusions . . . 146
5.4.1 Key points . . . 148

6 Conclusion **149**
6.1 Summary . . . 149
6.2 Conclusions and Outlook . . . 153

Bibliography **163**

Appendix A Eddy parameterisation in MITgcm **207**

Appendix B Derivation of the change in SBMOC heat flux **211**

Appendix C Analytical solution of the Geoffroy EBM under a step-forcing **213**
C.1 Particular solution . . . 214
C.2 Solution to the homogeneous equation . . . 214
C.2.1 Eigenvalues of $\mathbb{A}$ . . . 215
C.2.2 Eigenvectors of $\mathbb{A}$ . . . 215
C.2.3 Solution . . . 217
C.3 General solution . . . 217

Appendix D Non-dimensionalisation of the Geoffroy EBM and Limiting Cases **219**
D.1 Limiting cases . . . 221
D.1.1 Radiative feedbacks dominate, $\gamma/\alpha << 1$ . . . 221
D.1.2 Heat exchange dominates, $\gamma/\alpha >> 1$ . . . 222

Appendix E Fitted parameter values for two-layer EBMs **225**

Appendix F Vertical buoyancy transport within a wind-driven gyre **231**

*Ocean, n. : A body of water occupying about two-thirds of a world made for man — who has no gills.*

Ambrose Bierce, 1911

# 1 Introduction

## 1.1 Setting the stage

The global ocean covers about 71% of the Earth's surface, and contains more than 99% of Earth's habitable space. There is the oceanographer's quip that if extraterrestrials came to visit our planet, they would have good reason to call it 'Water' rather than 'Earth'. Carl Sagan's coinage of Voyager 1's famous photograph was the pale *blue* dot, after all, and not the pale green dot.

According to the United Nations (UN) Convention on the Law of the Sea, any waters beyond 370 km from a nation's coastline are the *common heritage of humankind*. The oceans thus act as a bridge connecting all nations, and they should be protected for the benefit of future generations. This call has come to great prominence recently, with 2021-2030 being declared the UN Decade of Ocean Science for Sustainable Development (https://www.oceandecade.org). The protection of the oceans is also enshrined in the UN sustainable development goals 'Climate Action' and 'Life below Water' for their 2030 Agenda (https://sdgs.un.org/goals).

Perhaps a visual will help further cement the fundamental importance of the world's oceans. In 1942, the oceanographer Athelstan Spilhaus presented two world ocean

maps [Spilhaus, 1942], and discussed a cut on the surface of the globe that would intersect the oceans as little as possible. He later collaborated with geodesists Robert Hanson and Erwin Schmid to create a new conformal map projection in 1983 that placed the oceans front and centre, now often dubbed the 'Spilhaus projection' [Spilhaus, 1983]. This is shown in figure 1.1.

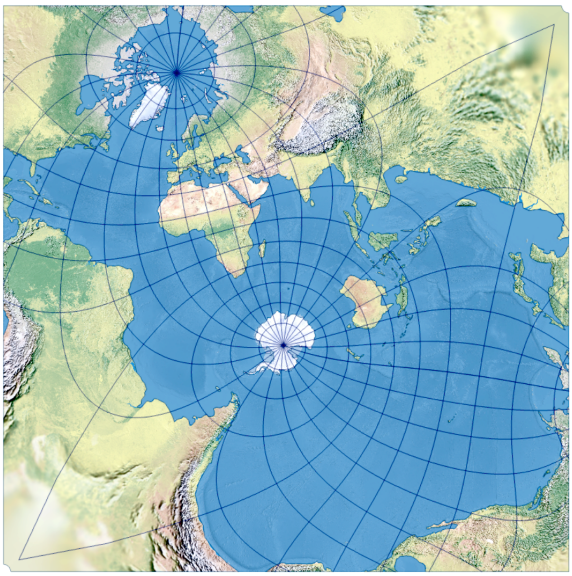


**Figure 1.1:** The Spilhaus projection or world ocean map in a square, rendered in ArcGIS Pro 2.5 (reproduced from `https://arcg.is/1vTXHn`, by Bojan Šavrič, David Burrows, and Melita Kennedy)

It is quite a remarkable picture, showing the seas as an almost uninterrupted whole. As a change in perspective often does, it belies our previous biases; in this case, our bias towards the land. One could imagine that on a different evolutionary timeline, intelligent aquatic life would come up with this projection as the default picture of the world. We do not live on that timeline, but this change in perspective is useful. It sets the stage for the rest of this thesis, the main focus of which is the oceans.

## 1.2 The ocean's role in climate

The ocean is a major component of the Earth's climate system. Two of the main ways it affects global climate include: 1. moderating/damping the atmospheric temperature fluctuations above it, and 2. transporting/redistributing heat around the globe via its circulation.

The first effect is due to the ocean's heat capacity being, overall, about 2000 times

that of the atmosphere. In fact, the top ∼3 m of an ocean column can store the same amount of heat as the corresponding atmosphere above it. The ocean also has a typically lower albedo than that of land. These facts help explain why coastal regions have considerably attenuated seasonal cycles compared to land-locked regions. The ocean's thermal inertia is also the principal reason why the coldest and warmest days of the year do *not* fall on the winter or summer solstices, but are in fact delayed to a few weeks later. And in the context of long-term global warming, it is because of the ocean that our warmest days are yet to come.

The second effect is a result of large-scale ocean circulation, which we discuss in section 1.3. The ocean (like the atmosphere) transports heat away from tropical regions and towards higher latitudes. Estimates of the climatological-mean meridional heat transports are shown in figure 1.2. One noteworthy aspect is that the poleward transport is significantly larger in the Northern Hemisphere than in the Southern Hemisphere; the heat transport in the Atlantic ocean is directed northward *at all latitudes*. This is a result of the pole-to-pole overturning circulation that is unique to the Atlantic basin, and leads to a global, positive cross-equatorial heat transport of ∼0.5 PW. This likely contributes to the Northern Hemisphere being ∼2°C warmer than the Southern Hemisphere [Marshall et al., 2014b].

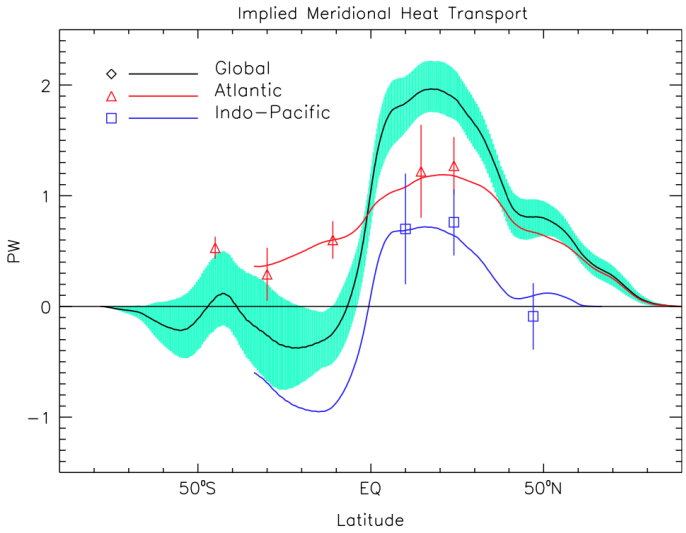



**Figure 1.2:** Estimates of zonal-mean meridional ocean heat transports over 1984-2006 based on the COREv2 climatological surface air-sea flux data set. Green shading indicates the interannual variation. The triangles and squares are observational heat transport estimates derived from the basin-wide hydrographic sections compiled by [Bryden and Imawaki, 2001]. Figure reproduced from [Large and Yeager, 2009].

Without this ocean heat transport (OHT), Earth would probably develop large ice sheets in the mid and high latitudes, making the climate much colder than it is at present. In model experiments by [Winton, 2003], the ocean was replaced by a mixed-layer, removing the effect of ocean currents and thus ocean heat transports. Despite the continuing presence of atmospheric meridional heat transports, the lack of ocean heat transports allowed sea ice to grow, which was then further enhanced by a positive sea ice-albedo feedback. In two coupled climate models, each with two different sea ice components, all simulations without ocean heat transport developed large sea ice extents. Furthermore, in fixed-current runs where the circulation was systematically increased and decreased by 50%, sea ice extent retreated and grew commensurately, with the slow current experiments having the most sea ice and the fast current experiments the least [Winton, 2003].

Earth has existed through many different climate states in the past, ranging from a possible completely ice-covered state ('snowball Earth') during the Cryogenian period (∼700 million years ago, e.g. [Hoffman et al., 1998]), to an ice-free state in the Cretaceous (∼100 million years ago, e.g. [Hay, 2008]). In the more recent past, throughout the Late Quaternary (from ∼1 million years ago to the present), Earth has cycled through glacial and interglacial periods on a cycle of approximately 100,000 years, characterised by the growth and decay of continental ice sheets (e.g. [Imbrie et al., 1993]). Within these glacial/interglacial periods are shorter stadials (cold states, lasting up to ∼1000 years) and interstadials (warm states, lasting 1-10 thousand years). Measurements from Greenland ice cores reveal large and abrupt climate changes (at least in the North Atlantic) during the last glacial period (last 120,000 years) [Dansgaard et al., 1993]. These abrupt changes ('Dansgaard-Oeschger' or D/O events) have a characteristic 'sawtooth' pattern with rapid warming (a few decades) into an interstadial, followed by a slow cooling into a stadial over several centuries (figure 1.3). They tend to occur around every 1500 years [Alley et al., 2001].

It is believed that changes in insolation due to the Milankovitch cycles cause the glacial/interglacial cycles [Imbrie et al., 1993]. However, changes in ocean circulation, particularly the overturning in the Atlantic, have been invoked to explain the D/O events (e.g. [Rahmstorf, 2002]). This is inspired by Stommel's original work

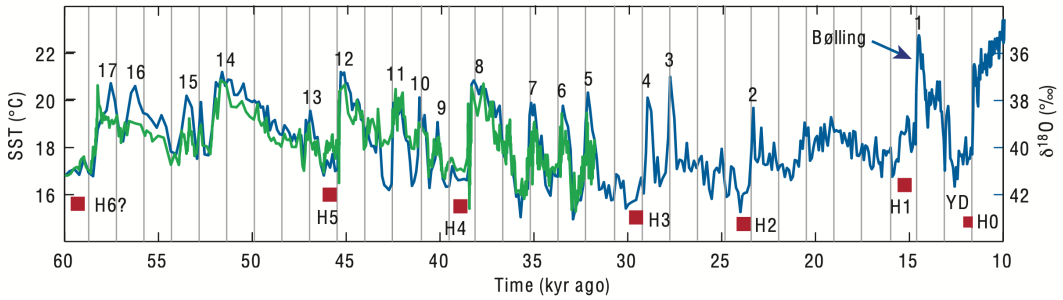



**Figure 1.3:** Temperature reconstructions from the Greenland ice core GISP2 (blue, [Grootes et al., 1993]), and ocean sediment proxy data from the subtropical Atlantic (green, [Sachs and Lehman, 1999]). D/O warm events are numbered, and Heinrich events (corresponding to large ice sheet discharges into the North Atlantic) are marked as red squares. The grey vertical lines are spaced 1470 years apart, illustrating the tendency for D/O events to occur with this spacing. Figure reproduced from [Rahmstorf, 2002].

using an idealised two-box model of the overturning circulation, which under certain conditions exhibited two stable states: a strong mode and a weak mode [Stommel, 1961]. Carbon isotopic ratios in sediments suggest that the Atlantic has occupied three distinct circulation modes in its past: a strong 'warm' mode (current conditions), a weak 'cool' mode, and an 'off' state [Sarnthein et al., 1994]. The idea is that some outside trigger causes transitions between these stable circulation states, leading to abrupt changes in climate. What this outside trigger is remains unknown.

Man-made $CO_2$ emissions have been put forward as a novel trigger candidate [Broecker, 1997], causing significant worry about the Atlantic overturning being forced into an 'off' state. This could bring with it stark Northern Hemisphere cooling and extensive Arctic sea ice (e.g. [Vellinga and Wood, 2008]), similar to the results from [Winton, 2003] (imagine subtracting the Atlantic OHT contribution from figure 1.2). Such severe consequences have prompted international observational monitoring of the Atlantic circulation (`https://www.rapid.ac.uk`), as well as scientifically-inaccurate Hollywood disaster movies (*The Day After Tomorrow*).

Significant attention has thus been directed to studying changes in ocean circulation affecting OHT. The moniker 'ocean heat transport' has come to be synonymous with *meridional* ocean heat transport (e.g. [Herweijer et al., 2005, Ferrari and Ferreira, 2011, Macdonald and Baringer, 2013, Forget and Ferreira, 2019]). But the ocean also transports and redistributes heat in the *vertical*, which has received less attention. This is perhaps surprising as, in the context of transient climate change, the surface

warming response is greatly dependent on the rate of heat sequestration in the ocean interior, which is communicated via changes in vertical heat transports (e.g. [Gregory, 2000, Exarchou et al., 2015]).

This thesis concerns the role of ocean circulation in transient climate change, and how vertical heat transports are effected by circulation. We will examine the outputs of a coarse-resolution, coupled general circulation model with idealised geometry under an abrupt doubling of atmospheric $CO_2$. This $CO_2$-doubling simulation is run for 200 years, so we are primarily concerned with the top 2 km of the model ocean responding on multi-decadal to centennial timescales. The model (described in Chapter 2) has a flat-bottomed ocean with a constant depth of 3 km. This precludes a realistic abyssal branch of the ocean circulation, so our neglect of millennial timescale responses is appropriate.

Before considering how the ocean is responding to climate change, and how it may respond in the future, we first take a look at our current understanding of the present Earth's large-scale ocean circulation.

## 1.3 A brief overview of large-scale ocean circulation

At the most basic level, Earth's ocean circulation can be split into two distinct components: a quasi-horizontal circulation that is primarily wind-driven, giving rise to great circulating *gyres*, and a vertical meridional overturning circulation (MOC) that is driven by winds, tidal forces, and surface buoyancy fluxes.

There exist subtropical gyres in the North and South Atlantic and Pacific oceans, and in the Indian ocean, from about 15° to 45° (figure 1.4). The flow is westward on their equatorial branches and eastward in the midlatitudes. These directions correspond to the surface easterly winds in equatorial regions, and westerly winds in midlatitudes in the atmosphere. In the Northern Hemisphere, there also exist subpolar gyres that circulate in an opposite sense. For each subtropical gyre, there is an associated intense western boundary current, formed via recirculation of equatorward Sverdrup interior flow due to the variation of the Coriolis parameter with latitude (or 'beta effect') [Sverdrup, 1947, Stommel, 1948].

Although the gyres appear isolated to their respective basins in figure 1.4, the subtropical gyres in the Southern Hemisphere are also connected via the Tasman and Agulhas leakages in a 'supergyre' circulation, with the main gyre circulations nested within (e.g. [Roemmich, 2007, Ridgway and Dunn, 2007, Qu et al., 2019]).

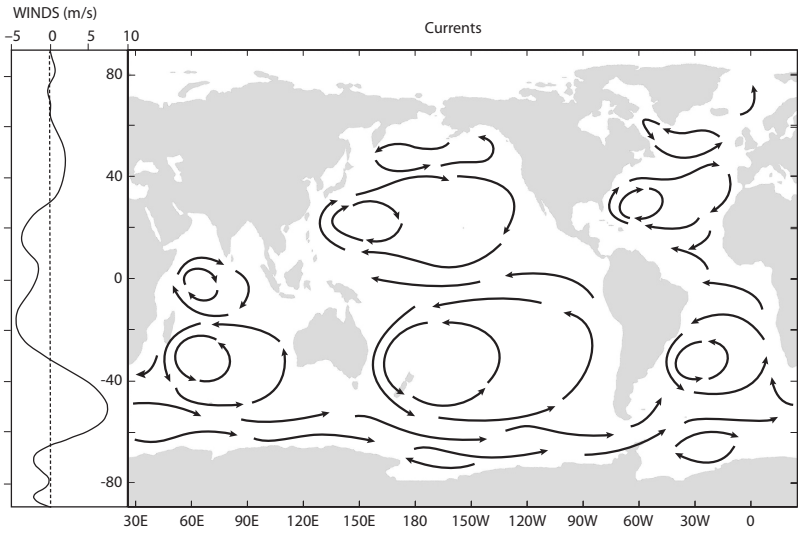



**Figure 1.4:** Schematic of the main surface ocean currents, highlighting the dominance of the subtropical gyres. The zonally-averaged zonal surface winds are shown in the left-hand panel. Figure taken from [Vallis, 2012], kindly made available on his personal website: `http://empslocal.ex.ac.uk/people/staff/gv219/`.

Gyres are traditionally considered wind-driven, but it has been shown that gyre-like circulations can be driven by surface buoyancy fluxes alone in an eddy-permitting ocean model [Hogg and Gayen, 2020]. So, the plain language of "wind-driven gyres" is potentially misleading. In reality, both surface winds and surface buoyancy fluxes likely play a role.

The MOC is characterised by cold, dense water sinking at high-latitudes and subsequently upwelling at lower latitudes. The classic schematic of the MOC is a zonally-averaged view of two global-scale 'Upper' and 'Lower' overturning cells stacked on top of each other (e.g. [Lumpkin and Speer, 2007, Marshall and Speer, 2012]). See, for example, figure 1.5. The Upper and Lower cells are also known as the 'mid-depth' and 'abyssal' cells in other literature (e.g. [Nikurashin and Vallis, 2012, Cessi, 2019]).

The Upper Cell of the MOC is associated with deep water forming at convective sites in the Nordic and Labrador seas in the North Atlantic, while the Lower Cell involves sites in the Weddell and Ross seas in the Southern Ocean. At these sites,

the stratification is sufficiently weak, and both heat fluxes to the atmosphere and brine rejection from sea ice formation cause large buoyancy losses. Once the surface water becomes denser than water at depth, it becomes convectively unstable and sinks in localised plumes on the order of 1 km in horizontal scale [Marshall and Schott, 1999].

As sinking within the Upper Cell is confined to the Atlantic basin, the basic structure of the Upper Cell is dominated by the Atlantic overturning (e.g. [Lumpkin and Speer, 2007]). Because of this, the Upper Cell is often used synonymously with the Atlantic MOC, or AMOC (e.g. [Buckley and Marshall, 2016, Cessi, 2019, Johnson et al., 2019]), and it is the AMOC that has received extensive study due to its climatic importance (e.g. [Kuhlbrodt et al., 2007, Weaver et al., 2012, Wunsch and Heimbach, 2013, Kostov et al., 2014, Chen and Tung, 2018]). Although the 2d-schematic in figure 1.5 is a useful mnemonic, with sinking in the North Atlantic and upwelling in the Southern Ocean, it necessarily ignores zonal transports and interbasin exchanges. The idea of two distinct, separated cells is an artefact of taking a zonal average.

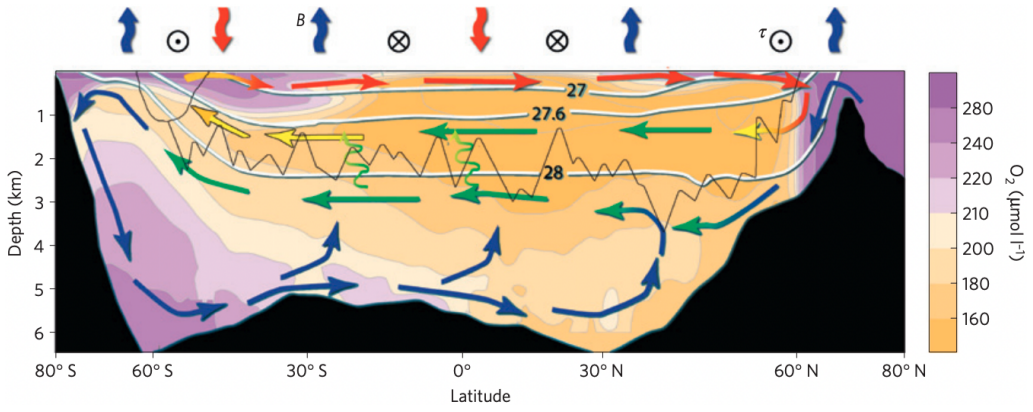



**Figure 1.5:** Schematic showing the 'Upper' and 'Lower' cells of the MOC, reproduced from [Marshall and Speer, 2012]. Arrows indicate the direction of the circulation, with colours representing the average density of water masses from lightest (red-yellow) to densest (green-blue). Surface buoyancy fluxes and wind stress directions are also indicated. In the background is the zonally-averaged distribution of dissolved oxygen, and the thin black line roughly indicates the depth of the Mid-Atlantic Ridge.

According to [Talley, 2013], once water sourced from the North Atlantic (North Atlantic Deep Water/NADW) upwells in the Southern Ocean, only a small fraction immediately returns northwards to complete the circuit. The majority of NADW that surfaces in the Southern Ocean is first transformed into denser Antarctic Bot-

tom Water (AABW). Once converted into AABW, it then flows northwards into the Indian and Pacific basins where it is transformed into lighter waters via turbulent diapycnal mixing. These lighter waters then resurface around Antarctica, and only then are they transformed into intermediate waters to return to the North Atlantic. The true structure of the MOC is thus a complex, three-dimensional network of intertwining pathways, with interbasin transports mediated by the Southern Ocean. A summary schematic is shown in figure 1.6.

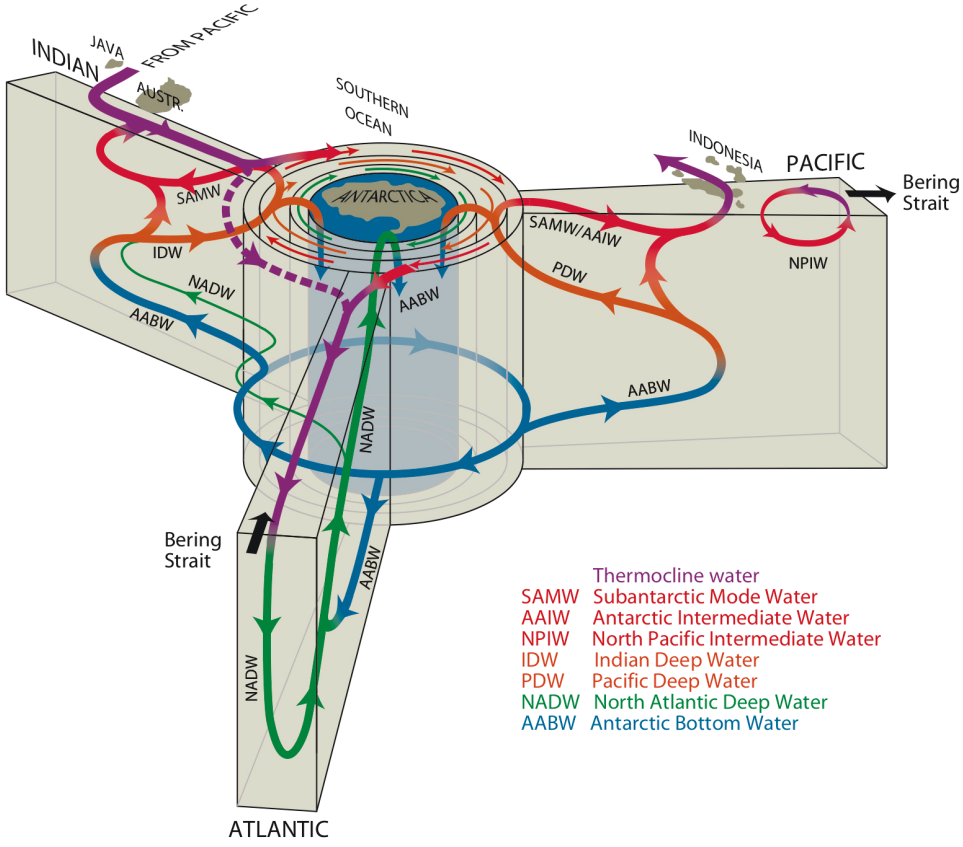



**Figure 1.6:** Schematic of the global overturning circulation, reproduced from [Talley, 2013]. Arrows indicate the direction of the circulation and colours represent the average density of water masses from lightest (purple-red) to densest (green-blue). A small leakage of less than 1 Sv makes its way from the Pacific to the Atlantic through the Bering Strait.

If we wish to retain the two-dimensional view, a more accurate picture of the MOC is given by [Ferrari et al., 2017], reproduced in figure 1.7. Here, the Upper and Lower cells are connected by vertical dashed lines, indicating diapycnal mixing-driven upwelling between the different water masses. In this simpler picture, the MOC is best described as a 'figure eight' circulation that spans the Atlantic and Indo-Pacific basins, consistent with the more complicated picture put forward by

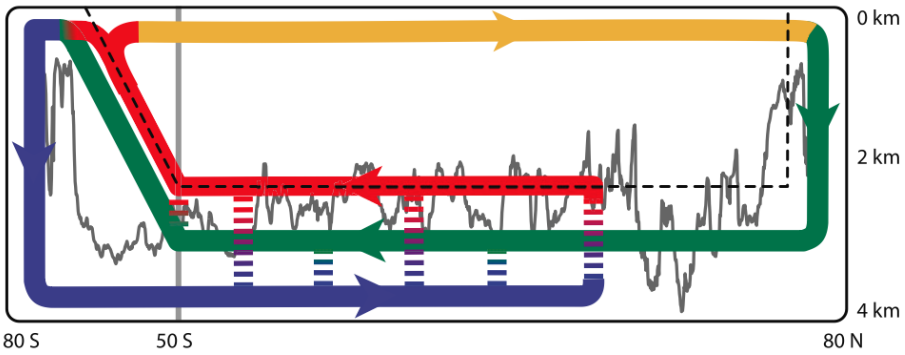



**Figure 1.7:** Two-dimensional schematic of the MOC, reproduced from [Ferrari et al., 2017]. Green is NADW, blue is AABW, red is Indian and Pacific deep waters (IDW/PDW), and yellow is intermediate waters. The vertical dashed lines indicate diapycnal mixing transforming AABW into NADW, or AABW into IDW/PDW. The jagged line represents the main bathymetric features in the Indo-Pacific, below which diapycnal mixing is enhanced.

[Talley, 2013] in figure 1.6.

Now, the upwelling of deep waters involves a vast range of processes across a range of spatial scales (e.g. [Huang, 2010]), but figure 1.7 provides a useful overview. The surfacing of the green and red ribbons from depth indicates one type of upwelling, and the vertical dashed lines between the blue and green/red ribbons indicate another type of upwelling.

The first type of upwelling is a wind-driven pathway, where waters are drawn up adiabatically along density surfaces by Ekman suction, caused by strong surface westerly winds over the Southern Ocean (e.g. [Toggweiler and Samuels, 1998, Gnanadesikan, 1999, Webb and Suginohara, 2001, Wolfe and Cessi, 2011]). The second type of upwelling involves diapycnal mixing — that is, the mixing of water masses across density surfaces. Both the surface winds and diapycnal mixing thus exert primary controls on the strength of the MOC (e.g. [Nikurashin and Vallis, 2011, Nikurashin and Vallis, 2012]).

Since isopycnals in the ocean are approximately horizontal across large areas of the ocean, diapycnal mixing is also often referred to as vertical mixing. It is typically modelled as a diffusive process, with a canonical diapycnal (vertical) diffusivity of $10^{-4}$ m$^2$ s$^{-1}$ over the entire abyssal ocean, first put forward by [Munk, 1966] (note that molecular diffusivities of heat and salt are on the order of $10^{-7}$ and $10^{-9}$ m$^2$ s$^{-1}$, respectively [Gill, 1982]).

Now, diapycnal mixing implies a mass flux across density surfaces and, in a stably stratified fluid, pushes light water down and heavy water up. This raises the potential energy of the system, so requires an external source of mechanical energy to maintain it. Munk originally suggested that this diapycnal mixing could be facilitated by breaking internal waves in the ocean interior [Munk, 1966]. These internal waves are generated via a variety of processes such as internal tides, wind-driven near-inertial waves, and lee waves from abyssal flows impinging on topography (e.g. [Whalen et al., 2020]). In a follow-up paper, [Munk and Wunsch, 1998] estimated that about 2 TW of power would be needed to mix bottom waters up to the surface via breaking internal waves. About 1 TW is supplied by tidal forces [Ferrari and Wunsch, 2009], and perhaps ∼0.2-0.8 TW is supplied by surface winds [Zhai et al., 2012]. This is not enough to bring abyssal waters to the surface.

However, in-situ observations show that internal waves tend to break close to bottom topography, thus confining mixing to close to the ocean bottom (e.g. [Waterhouse et al., 2014]). The emerging view is that diapycnal mixing need only bring waters from the ocean bottom to a depth of ∼2 km, the characteristic height of the most prominent oceanic topographic features (indicated by the jagged line in figure 1.7). Once waters reach this depth, a 'hand-off' occurs whereby they are then brought up adiabatically to the surface via the westerly winds over the Southern Ocean [Ferrari, 2014]. This is what is suggested in figure 1.7. As mixing only brings dense waters to ∼2 km depth, the power needed is about half that estimated by [Munk and Wunsch, 1998].

In addition to breaking internal waves, diapycnal mixing can be facilitated by other processes such as geothermal heating (e.g. [Mashayek et al., 2013, De Lavergne et al., 2016b]), dissipation from mesoscale eddies (e.g. [Eden and Greatbatch, 2008, Yang et al., 2019]) and shear-induced turbulence from entrainment in localised overflows (e.g. [Legg et al., 2009, Salehipour et al., 2015, De Lavergne et al., 2016a]).

Until quite recently, the consensus was that abyssal diapycnal mixing would drive upwelling of waters in the ocean interior. But, as pointed out by [Ferrari et al., 2016], bottom-enhanced mixing should drive *sinking* and not rising of waters through density surfaces. They conclude that water parcels only rise along the sloping oceanic

boundaries, highlighting the crucial role of bottom topography. So, the net upwelling of abyssal waters is really a residual between downwelling of waters in the ocean interior and upwelling in bottom boundary layers along topography.

This is at odds with numerical models, where mixing is often represented with a constant vertical diffusivity i.e. with no bottom-enhancement. Because of this, waters are expected to rise rather than sink in a model's abyssal ocean interior. This is true for the idealised model used in this thesis, and the implications of this will be discussed further in Chapter 2. Suffice it to say here, our idealised model has no bottom topography, and precludes a realistic abyssal branch of the ocean circulation, so we are primarily concerned with the Upper Cell and not the Lower Cell of the MOC.

Finally, the structure of the MOC highlights a key difference between the Atlantic and Pacific basins. Deep water formation is confined to the northern high latitudes of the Atlantic basin, resulting in a pole-to-pole overturning circulation. No such deep water formation exists in the northern high latitudes of the Pacific (e.g. [Warren, 1983]), nor a pole-to-pole overturning (figure 1.6). This is a fundamental global asymmetry in overturning and has persisted for perhaps 2-3 million years (e.g. [Raymo et al., 2004]). There is still no clear, settled explanation for this overturning asymmetry.

The asymmetry is fundamentally linked to the salinity contrast between the two basins [Ferreira et al., 2018a]. Salty water is heavier than fresh water at the same temperature, such that adding salt can have a similar effect to that of cooling the surface. The North Atlantic is more saline than the North Pacific, so it can more easily maintain an overturning circulation. This salinity contrast could be set by differences in net precipitation over the basins (e.g. [Craig et al., 2017, Wills and Schneider, 2015]), or by differences in salt transport resulting from ocean circulation (e.g. [Nilsson et al., 2013, Cessi and Jones, 2017]). However, the relative contributions of these atmospheric and oceanic processes in setting the salinity contrast between the two basins remain to be found [Ferreira et al., 2018a].

## 1.4 The ocean's response to warming

Earth's surface is warmed by solar radiation and emits infrared (longwave) radiation upward in response. Greenhouse gases in the atmosphere (mainly $CO_2$ and water vapour) absorb this longwave radiation, thus reducing the proportion that escapes to space. This absorption by greenhouse gases warms the atmosphere, which in turn re-emits infrared radiation. Some of this radiation is then absorbed at Earth's surface ('Downwelling Radiation' in figure 1.8). This is the greenhouse effect, the main mechanism for global warming.

There is now greater absorbed solar radiation than outgoing long-wave radiation over the surface of the Earth, leading to an imbalance, designated Earth's energy imbalance (EEI) (e.g. [Hansen et al., 2011, Trenberth et al., 2014, Von Schuckmann et al., 2016, Von Schuckmann et al., 2020]). More precisely, this imbalance is the result of the difference between the incoming solar radiation and the reflected solar radiation plus outgoing longwave radiation (OLR) (figure 1.8). The difference is largely due to humans changing the composition of the atmosphere by increasing the concentration of greenhouse gases by burning fossil fuels (e.g. [Trenberth, 2018, Masson-Delmotte et al., 2021]).

It is now undeniable that global-mean surface temperatures are rising, and that we are the cause [Masson-Delmotte et al., 2021]. Figure 1.9 shows a time series of the annual global-mean surface temperature since 1850, relative to a 1961-1990 mean. The upward warming trend is unmistakable.

Instead of greenhouse gas emissions, another possible candidate to explain the observed warming is that of natural variability; specifically, there being a variation in the ocean such that it releases heat to the atmosphere. If the ocean were to have given up heat to the atmosphere, it would have become cooler over the last few decades. In fact, the heat content of the ocean has *increased* over the last few decades (figure 1.10). This implies that the ocean is warming *because of* the surface temperature increase, and is not the cause.

The EEI estimated from [Trenberth, 2020] is $0.9 \pm 0.2$ W m$^{-2}$ (figure 1.8). The vast majority ($\sim$93%) of the excess energy resulting from this imbalance goes into

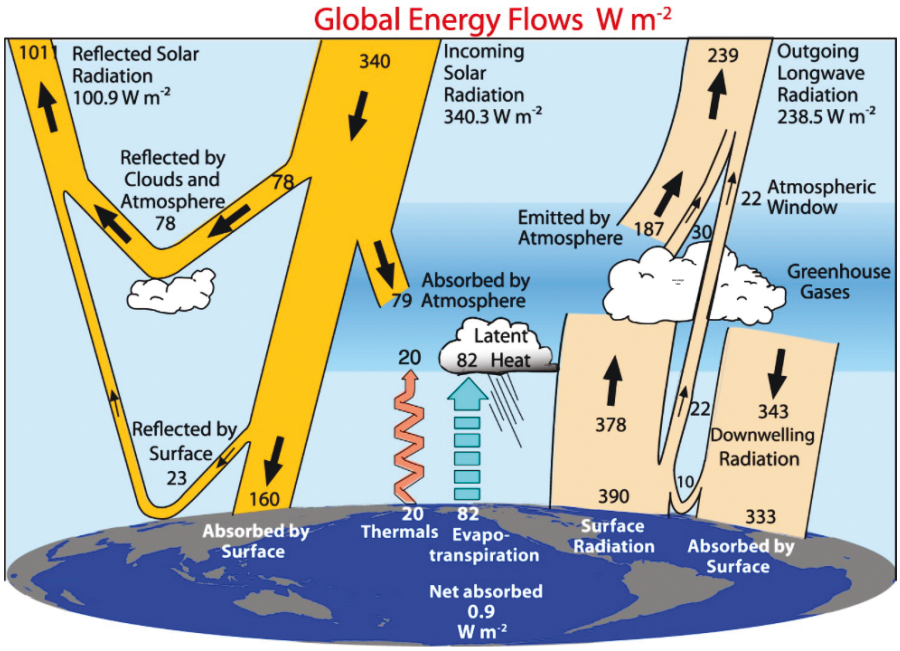



**Figure 1.8:** Schematic of the global annual-mean energy flows through the climate system (in W $m^{-2}$). Earth's energy imbalance, or the net absorbed, is estimated at $0.9 \pm 0.2$ W $m^{-2}$. Figure reproduced from [Trenberth, 2020], based on [Trenberth et al., 2009] and [Wild et al., 2015].

the ocean, leading to an increase in ocean heat content (OHC) (figure 1.10). Only ~4% has contributed to warming the atmosphere and the continents [Rhein et al., 2013]. This increase in OHC is also tightly linked to rising sea-levels (e.g. [Church et al., 2013]), with about 40% of the global-mean increase in sea-level since 1957 accounted for by thermal expansion [Frederikse et al., 2020].

Over an ocean column, a change in OHC is due to an anomalous net air-sea heat flux $\mathcal{F}_s$ (W $m^{-2}$) as well as the heat transport into or out of the column:

$$\partial_t \int_{-H}^{0} \rho_0 c_p \theta \, dz = \mathcal{F}_s - \rho_0 c_p \int_{-H}^{0} \nabla \cdot (\mathbf{v}\theta) \, dz \tag{1.1}$$

where $\theta$ is the oceanic potential temperature, $\rho_0$ the seawater density, and $c_p$ the specific heat capacity of seawater. Ocean heat uptake (OHU) is synonymous with $\mathcal{F}_s$ (i.e. energy transfer from the atmosphere to the ocean surface), while ocean heat storage (OHS) refers to an increase in OHC (l.h.s. of equation 1.1). Thus, OHU and OHS are equivalent globally, but can be very different regionally due to the ocean heat transport divergence $\nabla \cdot (\mathbf{v}\theta)$. (Note that the terms OHU and OHS are sometimes used interchangeably in the literature, and 'OHU' is often used as a

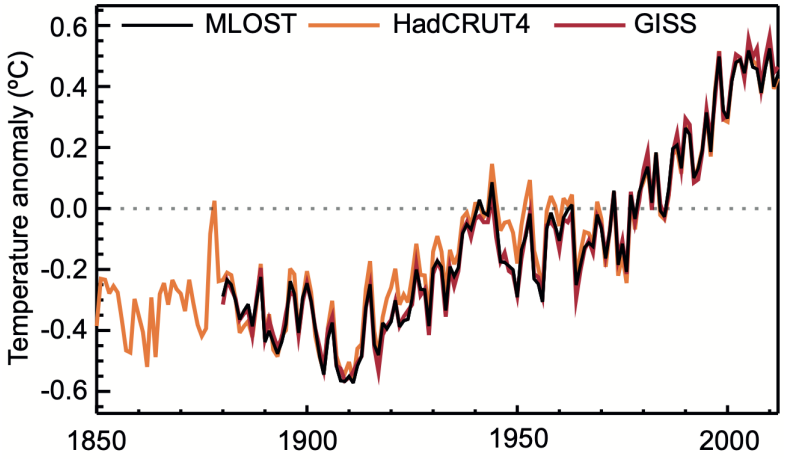



**Figure 1.9:** Annual global-mean surface temperature anomalies relative to 1961-1990 from three different data sets (HadCRUT4, NASA-GISS, and NCDC-MLOST). Reproduced from [Hartmann et al., 2013].

shorthand for 'OHU processes', which are processes that lead to a change in OHC, as discussed in section 1.4.2.)

Ocean heat uptake and subsequent storage redirects heat that would otherwise have warmed the surface. OHU thus plays a critical role in slowing the pace of global warming (e.g. [Gregory, 2000, Held et al., 2010, Kostov et al., 2014]). For example, the so-called 'surface warming hiatus' during the beginning of the 21st century (figure 1.9) has been linked to enhanced OHU (e.g. [Meehl et al., 2011, Watanabe et al., 2013, Drijfhout et al., 2014]).

Globally, over the period 2005-2017, CMIP5 models estimate an OHS rate of 0.68 $\pm$ 0.02 W m$^{-2}$ over the top 2 km [Cheng et al., 2019], while observations give rates of 0.64 $\pm$ 0.02 W m$^{-2}$ [Domingues et al., 2008] and 0.54 $\pm$ 0.02 W m$^{-2}$ [Cheng et al., 2017]. Over the period 2000-2010, a full depth estimate of the OHS rate from CMIP5 models is 0.73 $\pm$ 0.21 W m$^{-2}$ [Smith et al., 2015]. And a full-depth estimate from observations over the period 1993-2017 is 0.66 $\pm$ 0.22 W m$^{-2}$ (from [Meyssignac et al., 2019], combining contributions from [Blunden et al., 2018] and [Purkey and Johnson, 2010]). Other observational full-depth estimates vary from $\sim$0.5-0.8 W m$^{-2}$ depending on the time period and dataset used (see [Meyssignac et al., 2019]).

About two thirds of the global OHS is accounted for by the upper 0-700 m of the ocean (figure 1.10). This change in upper-ocean heat content only corresponds to

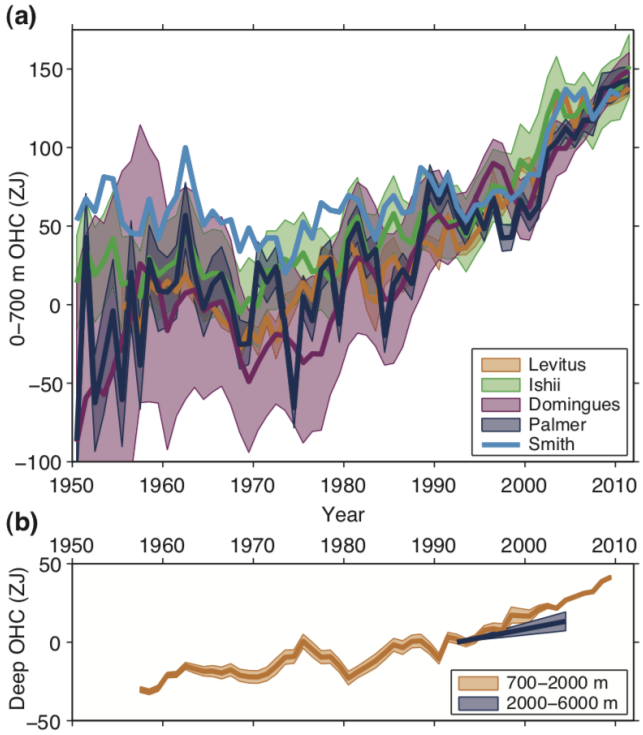



**Figure 1.10:** Observational estimates of changes in ocean heat content since 1950 from the IPCC's fifth assessment report [Rhein et al., 2013]. a) Annual global-mean upper-ocean (0-700 m) heat content adapted from [Levitus et al., 2012, Ishii and Kimoto, 2009, Domingues et al., 2008, Palmer et al., 2007, Smith and Murphy, 2007]. b) Five-year running means of global-mean mid-depth (700-2000 m, data from [Levitus et al., 2012]) and deep (2000-6000 m, data from [Purkey and Johnson, 2010]) ocean heat content changes.

a mean temperature increase of about 0.15°C, whereas the corresponding mean surface temperature increase is about 0.6°C (figure 1.9). This discrepancy means that the ocean still has a long way to go in terms of warming, as we assume that at equilibrium the deep ocean temperature increase will be similar to that at the surface.

The ocean is the pacemaker of global climate change due to its slow circulation and large thermal inertia. In response to greenhouse gas forcing, the climate system adjusts towards a new equilibrium on multiple timescales. The stratosphere and troposphere respond on timescales of days to weeks [Gregory and Webb, 2008, Andrews et al., 2012], and the land-surface and oceanic mixed-layer on timescales of months to years (e.g. [Hansen et al., 1985, Wallace et al., 1990, Vallis, 2012]). But the deeper ocean responds on timescales of centuries to millennia (e.g. [Stouffer, 2004, Yang and Zhu, 2011, Li et al., 2013]). So, even if we stopped emitting green-

house gases, it would take the full-depth ocean several millennia to fully equilibrate, during which time the Earth's surface temperature would nevertheless continue to increase [Held et al., 2010].

To properly quantify the response timescale of the full-depth ocean, we rely on multi-millennial integrations of atmosphere-ocean general circulation models (AOGCMs), run to equilibrium. But this is rarely done due to its enormous computational expense [Li et al., 2013]. Instead, the focus of climate prediction has shifted towards the time-development of climate change, or 'transient' climate change, rather than the eventual equilibrated state. This is more practical, as our immediate interest lies in what the climate might be in the next several decades. To that end, this thesis is primarily concerned with the oceanic response above 2 km depth on multidecadal to centennial timescales, so we will not be concerned with timescales longer than this.

### 1.4.1 Ocean Heat Storage Patterns

Figure 1.8 shows the annual-mean energy fluxes absorbed by Earth's surface in the global average, but doesn't show how these fluxes vary spatially. Air-sea flux datasets that combine in-situ observations, satellite observations and atmospheric reanalyses can provide us with this spatial information. However, these datasets usually have a global mean net surface heat flux from the atmosphere to the ocean in the range of 10-30 W $m^{-2}$ [Josey et al., 2013]. This is much higher than the global OHS rate estimates of 0.5-0.8 W $m^{-2}$ [Meyssignac et al., 2019], indicating that there are still major unresolved biases in these air-sea flux datasets, with the discrepancy having been termed the 'ocean heat budget closure problem'. Model biases in air-sea fluxes are also one of the key sources of uncertainty in climate projections [Huber and Zanna, 2017]. The qualitative spatial pattern these air-sea flux datasets afford is still valuable, but the quantitative values are nevertheless secondary.

Climatological annual-means of surface heat flux components are shown in figure 1.11. As expected from the global-mean values in figure 1.8, latent, sensible, and longwave fluxes are all directed upward, while the shortwave flux is directed downward. The shortwave flux decreases towards the poles as expected, with the exception of a band of reduced solar radiation near the equator that marks cloud

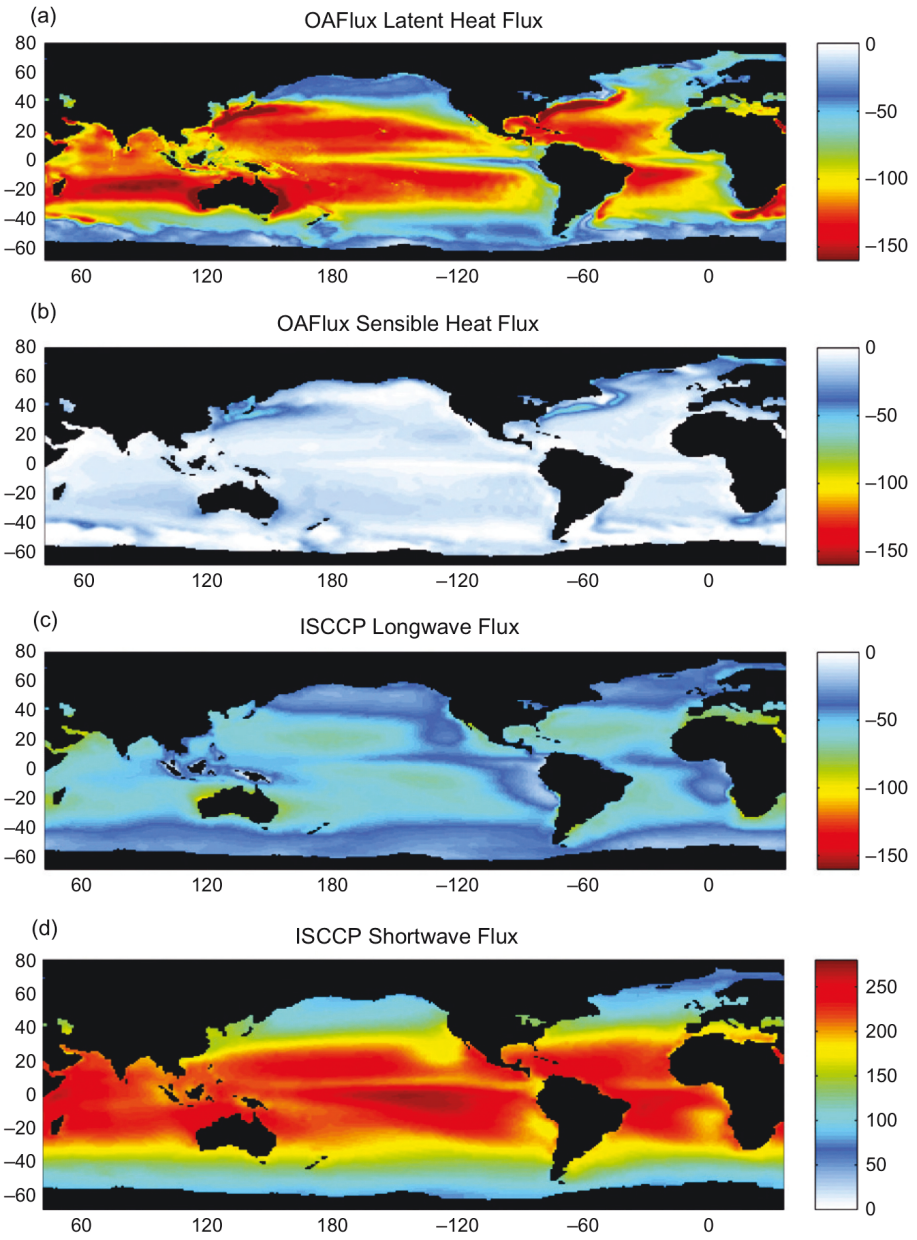



**Figure 1.11:** Spatial maps of the annual mean net heat flux divided into components of (a) Latent Heat, (b) Sensible Heat, (c) Longwave Flux, and (d) Shortwave Flux in W $m^{-2}$. Positive values are directed downwards. Panels (a) and (b) use the Objectively Analyzed Air-sea Fluxes (OAFlux) dataset [Yu and Weller, 2007], while panels (c) and (d) use the satellite-only International Satellite Cloud Climatology Project (ISCCP) fields [Zhang et al., 2004]. Figure reproduced from [Josey et al., 2013].

cover over the intertropical convergence zone (ITCZ) (figure 1.11d). In contrast, the longwave flux is a much more homogeneous field with a range of about 40 W $m^{-2}$ (figure 1.11c). Major latent and sensible heat losses are associated with the western boundary currents (figure 1.11a, b), although globally the sensible heat flux tends to be an order of magnitude smaller than the latent heat flux.

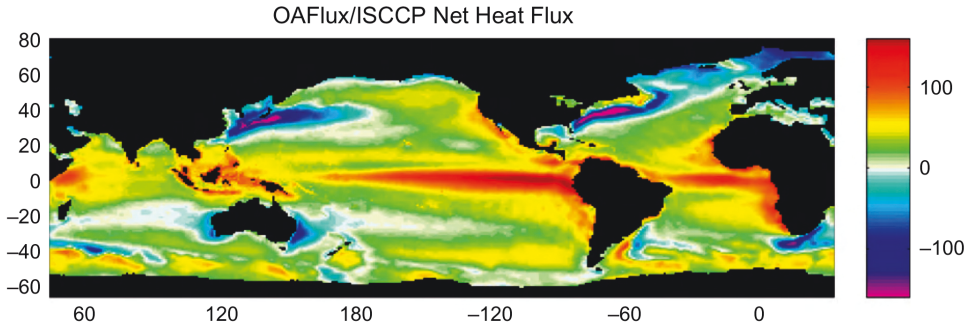



**Figure 1.12:** Climatological annual-mean net air-sea heat flux from OAFlux [Yu and Weller, 2007] and ISCCP [Zhang et al., 2004], reproduced from [Josey et al., 2013].

By summing panels a-d from figure 1.11, we can get an estimate for the net air-sea heat flux, shown in figure 1.12. The spatial pattern for the net heat flux primarily comes from the balance between the latent heat and shortwave flux components. Heat is mainly taken up in the tropics (particularly the tropical Eastern Pacific), and lost over the western boundary currents and at high northern latitudes. The global-mean net heat flux from this OAFlux/ISCCP combination is 29 W $m^{-2}$, however, when it should be close to zero. So, it cannot be used to infer OHS. To do that, we'd need to be able to detect a *change* in the global-mean net heat flux of ∼0.5-0.8 W $m^{-2}$ on multidecadal timescales in accord with the OHS rate [Meyssignac et al., 2019], which is not possible with the heat flux datasets we have currently.

Estimates of OHS can be made using in-situ observations of oceanic temperature and satellite altimeter observations of sea-level anomalies associated with thermal expansion. A study from [Johnson and Lyman, 2020] examined gridded ocean heat content maps from four research groups, three based on ocean temperature alone and one combining ocean temperature with satellite altimeter data. Their analysis revealed that, over the period 1993-2019, about 60% of the global ocean area had a significant positive trend in 0-700 m OHC anomalies, while only about 7% had a

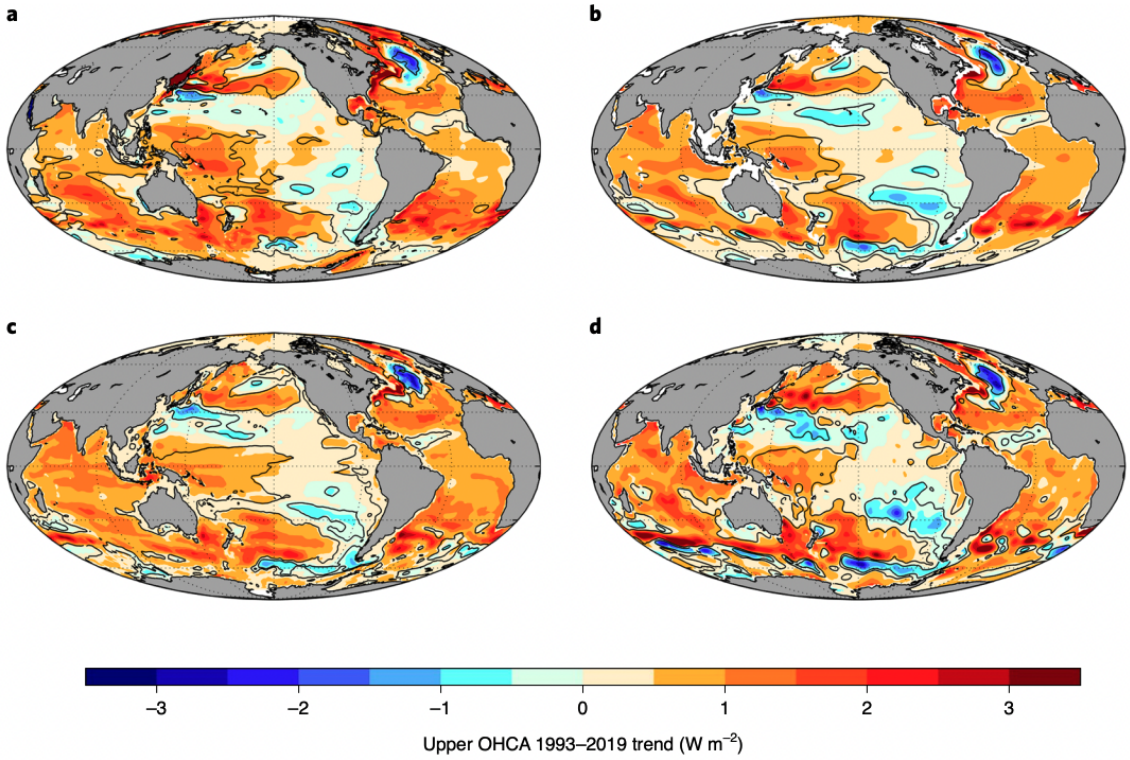



**Figure 1.13:** Linear trends in 0-700 m OHC anomalies (OHCA) over the period 1993-2019 (W m$^{-2}$) from (a) NOAA's Pacific Marine Environmental Laboratory (PMEL) [Lumpkin et al., 2020], (b) Japan Meteorological Agency (JMA) [Ishii et al., 2017], (c) Institute of Atmospheric Physics (IAP) [Cheng et al., 2017], and (d) NOAA's National Center for Environmental Information (NCEI) [Levitus et al., 2012]. Figure reproduced from [Johnson and Lyman, 2020].

significant negative trend (their Table 1).

The large-scale patterns of OHS from the four maps are all very consistent (figure 1.13). There is a clear asymmetry in OHS between the Atlantic and Pacific basins, with the Atlantic taking up more heat per unit area than the Pacific. This is a fact we'll explore further in Chapter 4, but it is possibly due to the presence of the AMOC [Shatwell et al., 2020].

The patterns of OHS reveal pronounced warming over the western boundary currents (WBCs), which is consistent with enhanced sea surface temperature (SST) trends over these regions [Wu et al., 2012]. The authors in [Wu et al., 2012] suggested that a poleward shift and/or intensification of the ocean gyres were associated with these SST trends. Further work has provided more evidence from observations and models for both these effects (e.g. [Yang et al., 2016, Yang et al., 2020]), perhaps driven by changes in surface westerly winds (e.g. [Yin, 2005, Chen et al., 2008, Swart and

Fyfe, 2012]).

Another consistent pattern in OHS from figure 1.13 is the dominance of the Southern Hemisphere (particularly the Southern Ocean), which has been seen in previous studies (e.g. [Roemmich et al., 2015, Wijffels et al., 2016, Durack et al., 2018]). A mechanism put forward to explain this is the wind-driven upwelling of cold deep waters around Antarctica, and their subsequent warming, northward transport, and subduction into the ocean interior (e.g. [Marshall et al., 2014a, Marshall et al., 2015, Armour et al., 2016]).

The other conspicuous feature across the four panels in figure 1.13 is the blue region of cooling in the subpolar North Atlantic. This is highly reminiscent of the so-called 'warming hole', a region of *surface* cooling in the same area, which has been linked to a weakening AMOC (e.g. [Drijfhout et al., 2012, Rahmstorf et al., 2015, Caesar et al., 2018]). The given explanation is that a weakening of the AMOC leads to a weakening meridional heat transport into the warming hole region. However, an increase in northward heat transport *out of* the warming hole region and a shortwave cloud feedback have also been implicated in driving the warming hole [Keil et al., 2020].

Patterns of OHS in models are similar, with CMIP5 model simulations over the 1861-2005 historical period also revealing an Atlantic/Pacific asymmetry, an enhancement over western boundary currents, a dominance of the Southern Ocean, and a region of cooling in the subpolar North Atlantic [Frölicher et al., 2015]. But how does heat get stored in the ocean in the first place?

### 1.4.2 Ocean Heat Uptake Processes

We noted previously that around 93% of the excess energy from EEI ends up in the ocean [Rhein et al., 2013]. This value (93%) is significantly larger than the surface area covered by the oceans (71%). This is due to a number of reasons, such as the ocean typically having a lower albedo than land, and the ability of sunlight to penetrate the upper ocean to ∼200 m depth. But most importantly, it is because the ocean is in constant *motion*, carrying heat downwards from the surface to the interior via small-scale mixing processes and large-scale circulation.

The mechanisms by which heat is taken from the ocean surface into the interior are normally denoted 'OHU processes' (e.g. [Exarchou et al., 2015, Kuhlbrodt et al., 2015]). This is confusing language, as OHU commonly refers to the net air-sea heat flux (e.g. [Raper et al., 2002, Gregory et al., 2004, Gregory and Forster, 2008]), which suggests that OHU processes only pertain to the atmosphere-ocean boundary layer. This is not the case, as OHU processes can involve circulations that span the full-depth ocean column (e.g. [Newsom et al., 2016]). So, in a broader sense, 'OHU' can refer to the energy transfer from the atmosphere to the ocean surface, as well as its subsequent transfer into the ocean interior via a suite of mechanisms i.e. processes that lead to a change in OHC. A reduction in energy *lost* from the ocean to the atmosphere is also classed as OHU.

### Stratification and the Pycnocline

On timescales longer than a day, the ocean is in most places stably stratified, with lighter water sitting atop heavier water (e.g. [Talley, 2011]). A decrease in OHC near the surface destabilises the stratification, resulting in overturning and mixing of the water column to remove the instability. Whereas, an increase in OHC near the ocean surface increases the stability of the stratification, further isolating surface waters from deep waters. This difference means that warm anomalies penetrate the ocean interior significantly slower than cool anomalies (e.g. [Stouffer, 2004]). The ocean's stable stratification thus acts as a barrier to heat uptake.

This is supported by evidence from climate models, where it's been found that the vertical temperature gradient (a proxy for the stratification) negatively correlates with the ocean heat uptake efficiency (OHUE, defined as the net heat flux into the climate system divided by the global surface air temperature change [Gregory and Mitchell, 1997, Raper et al., 2002]) in CMIP3 and CMIP5 models [Kuhlbrodt and Gregory, 2012]. This is because a weaker temperature gradient implies a weaker stratification, thus enabling more heat to be taken up. In addition, [Kuhlbrodt and Gregory, 2012] suggest that models may overestimate OHU and thus underestimate surface warming as most models' stratification is too weak compared to observations.

Related to the stratification is the pycnocline, the region in the upper ocean where

density increases rapidly with depth, typically several hundred metres in extent. A useful framing of OHU processes is to consider the processes that maintain the pycnocline, which in turn effectively control the rate of OHU. A simple conceptual model was put forward by [Gnanadesikan, 1999], consisting of two homogeneous layers with the top layer representing the pycnocline and bottom layer representing the deeper ocean below. The pycnocline layer thickness (or 'pycnocline depth') is controlled by volume transports between the two layers, caused by four key processes: Southern Ocean Ekman transport, Southern Ocean eddies, NADW formation, and diapycnal mixing (see figure 1.14).

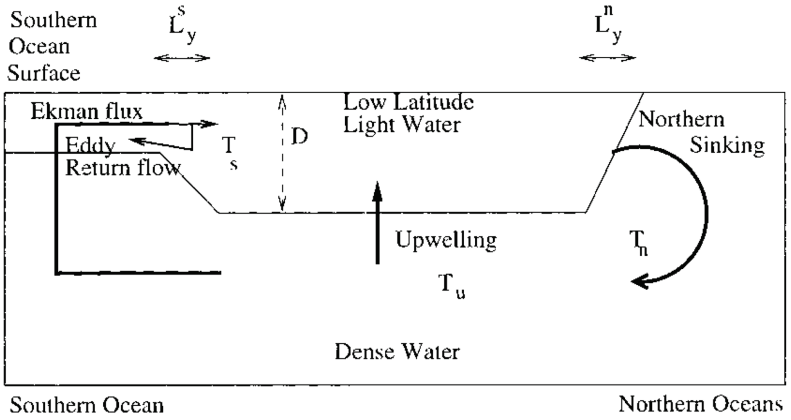



**Figure 1.14:** Schematic of the simple model developed by [Gnanadesikan, 1999]. The effects of Southern Ocean winds and compensating eddies are represented by the volume flux $T_s$, NADW formation is represented by the flux $T_n$, and diapycnal mixing is represented by a low-latitude upwelling flux $T_u$.

Over the Southern Ocean, strong surface westerlies drive an equatorward Ekman transport that acts to steepen isopycnals (weakening stratification). At the same time, mesoscale eddies within the Antarctic Circumpolar Current (ACC), formed via baroclinic instability, extract available potential energy from the flow which acts to flatten isopycnals (strengthening stratification). The collective action of the eddies results in a poleward return flow that compensates the wind-driven equatorward Ekman transport above the depth of the Drake Passage (e.g. [Marshall and Radko, 2003, Hallberg and Gnanadesikan, 2006]). In Gnanadesikan's model [Gnanadesikan, 1999], the pycnocline is deepened by the Ekman transport and shallowed by the eddies ($T_s$). The other processes are diapycnal mixing (leading to a net upwelling of abyssal waters as discussed in section 1.3), which serves to deepen the model pycnocline ($T_u$), and NADW formation, which shallows it ($T_n$).

This simple model was extended by [Marshall and Zanna, 2014], where they developed a multilayer generalisation in order to probe OHU processes. In their model, a deepening/shallowing of the pycnocline is related to an increase/decrease in OHU. In a pure surface warming scenario, they found that the dominant process governing OHU was due to the Southern Ocean Ekman transport, corresponding to Ekman pumping of the surface heat anomaly into the ocean interior. Southern Ocean eddies oppose this Ekman heat uptake, controlling the long-term adjustment over many centuries, with a lower eddy diffusivity leading to a longer adjustment period. The importance of Southern Ocean processes in OHU has been highlighted in many other studies (e.g. [Gregory, 2000, Xie and Vallis, 2012, Marshall et al., 2014a, Frölicher et al., 2015, Armour et al., 2016]).

Winds over the Southern Ocean have shifted poleward and increased in strength by about 20% over the last few decades (e.g. [Thompson and Solomon, 2002, Swart and Fyfe, 2012]). From modelling studies, it's expected that this trend will lead to a strengthening of the overturning in the Southern Ocean (e.g. [Abernathey et al., 2011, Gent, 2016]), although the effects of eddy compensation may mean that the net increase in overturning strength is greatly reduced (e.g. [Downes and Hogg, 2013, Munday et al., 2013]). Nevertheless, the response of the Southern Ocean overturning will have knock-on effects on Southern Ocean heat uptake and surface warming (e.g. [Fyfe et al., 2007, Morrison et al., 2013, Gao et al., 2018, Doddridge et al., 2019]). The effect of Southern Ocean winds on OHU is captured by the simple model of [Marshall and Zanna, 2014], where an increase in the wind stress of 10% (in conjunction with surface warming) leads to an increase in the peak OHU rate by about 50%. The impact of the winds on OHU more generally will be explored further in Chapter 3.

Finally, coupled climate models project a decline in the AMOC strength over the 21st century (e.g. [Gregory et al., 2005, Cheng et al., 2013, Weijer et al., 2020]), with CMIP6 models suggesting a decline of 34-45% by 2100 [Weijer et al., 2020], although the strength of the future decline is highly uncertain (e.g. [Reintges et al., 2017]). In-situ observations don't preclude the possibility of a weakening AMOC, but large interannual and decadal variability make the detection of long-term trends difficult [Frajka-Williams et al., 2019, Jackson et al., 2022], especially as continuous

direct observations from RAPID only go as far back as 2004 [McCarthy et al., 2015]. Indirect evidence from proxy observations, however, supports the hypothesis that the AMOC is weakening (e.g. [Rahmstorf et al., 2015, Caesar et al., 2018, Zhu and Liu, 2020]).

A weakening of the AMOC is expected as a result of positive buoyancy forcing in the northern high latitudes from heat fluxes due to Arctic amplification (e.g. [Serreze and Barry, 2011, Dai, 2022]) and freshwater fluxes from increased high-latitude precipitation and river runoff (e.g. [Stouffer et al., 2006]), melting of the Greenland Ice Sheet (e.g. [Lenaerts et al., 2015, Van den Broeke et al., 2016]) and Arctic sea ice (e.g. [Jahn and Holland, 2013, Sévellec et al., 2017]). This positive buoyancy forcing both suppresses deep convection at the sites of NADW formation, leading to a commensurate reduction in the AMOC strength (e.g. [Thornalley et al., 2018]), and reduces the meridional density gradient, which is thought to scale with the AMOC strength (e.g. [Stommel, 1961, Griesel and Maqueda, 2006, Gregory and Tailleux, 2011, Ragen et al., 2022]).

It is thought that a reduction in AMOC strength will lead to an increase in OHU, owing to a reduction in heat lost from the ocean to the atmosphere over the sites of NADW formation (e.g. [Winton et al., 2013, Drijfhout et al., 2014, Garuba and Klinger, 2016]), which we will discuss further in Chapter 4. An increase in OHU with a reduction in NADW formation is still captured by the simple model of [Marshall and Zanna, 2014], as this deepens the pycnocline, weakening the stratification, thus leading to more heat uptake. Their model thus highlights the importance of high-latitude dynamical processes in the North Atlantic and Southern Ocean on OHU, while the role of diapycnal mixing is secondary.

### Partitioning in GCMs

Another framing of OHU processes is through the treatment and partitioning of different processes in ocean models. Early ocean models represented OHU as a diffusive (e.g. [Hansen et al., 1985]) or upwelling-diffusive process (e.g. [Hoffert et al., 1980, Wigley and Raper, 1987]) based on the classic upwelling-diffusion balance put forward by [Munk, 1966]. Modern general circulation models (GCMs) or coupled

atmosphere-ocean GCMs (AOGCMs) reveal a variety of other OHU processes such as advection by the mean circulation or isopycnal diffusion (e.g. [Gregory, 2000]).

Recent model intercomparisons (e.g. [Exarchou et al., 2015, Kuhlbrodt et al., 2015]) divide OHU processes according to how they are treated in a model's temperature ($T$) tracer equation. The convergence of heat is determined by advective processes (of the form $\nabla \cdot (\mathbf{v}T)$) and diffusive processes (of the form $\nabla \cdot (\underline{\underline{\mathbf{K}}}\nabla T)$), as well as surface fluxes and parameterisations of subgrid-scale processes such as convection and near-surface mixing.

According to the study of [Exarchou et al., 2015], the most important OHU processes found across three global climate models in $CO_2$-quadrupling experiments were: convection, near-surface mixing, and resolved advection. In their study, convection and near-surface mixing are lumped together as 'vertical mixing' (not to be confused with diapycnal mixing in the ocean interior). They find that 'vertical mixing' and resolved advection contribute more than 80% to the OHUE (defined with respect to SST rather than surface air temperature), with each process contributing approximately 40%. The remaining 20% is due to the remaining processes of diapycnal mixing, isopycnal diffusion, and eddy-induced advection.

In another $CO_2$-quadrupling experiment, with an eddy-permitting model (1/3° resolution), [Kuhlbrodt et al., 2015] find that warming below 1 km is mainly caused by advection, while warming in the top 1 km is dominated by vertical mixing (as defined in the previous paragraph). Both [Exarchou et al., 2015] and [Kuhlbrodt et al., 2015] (as well as previous work from [Gregory, 2000]) also reveal that OHU is dominated by advection at low latitudes, and by vertical mixing at high latitudes, where there is weak stratification.

Recent work from [Saenko et al., 2021] analysed a suite of 11 AOGCMs under 1% $yr^{-1}$ $CO_2$-increase experiments (all with an ocean resolution ~1°), and broadly confirmed this latitudinal dependence of OHU processes. In the control simulations, they find a leading-order global heat balance between resolved advection warming the subsurface ocean, and eddy-induced advection/diffusion cooling it, a finding echoed by several previous studies (e.g. [Gregory, 2000, Hieronymus and Nycander, 2013, Griffies et al., 2015]). And in the warming simulations, they find that below

400 m the OHU is dominated by the sum of these processes (dubbed the 'super-residual transport' (SRT) [Kuhlbrodt et al., 2015, Dias et al., 2020a]).

However, [Saenko et al., 2021] also perform a heat budget analysis in a density framework, revealing that most of the interior OHU processes are isopycnal, contrary to older upwelling-diffusion models where it is assumed that diapycnal diffusion is the main OHU process (e.g. [Raper et al., 2001, Meinshausen et al., 2011]). This result suggests that it is the *advective* component of the SRT that accounts for most of the OHU.

#### Connection with circulation

A common thread throughout all of section 1.4.2 above is that an understanding of OHU is incomplete without an understanding of ocean circulation processes, particularly advective transports (e.g. [Gregory, 2000, Xie and Vallis, 2012, Marshall and Zanna, 2014, Exarchou et al., 2015, Kuhlbrodt et al., 2015, Zika et al., 2015, Dias et al., 2020b, Saenko et al., 2021]). Far from being an inert diffusive heat reservoir, a myriad of intricate and intertwined OHU processes affect the vertical and lateral distributions of OHS making it highly nonuniform in space (e.g. [Zanna et al., 2019, Johnson and Lyman, 2020], and see figure 1.13).

Such intricacies means that there is a substantial spread in the contributions to OHS from different OHU processes across models (e.g. [Exarchou et al., 2015, Saenko et al., 2021]), which could, in part, explain the spread in OHUE across CMIP3 and CMIP5 models [Kuhlbrodt and Gregory, 2012]. This spread in OHUE also accounts for about half the intermodel spread in thermal expansion, which is the largest contributor to sea-level rise (e.g. [Church et al., 2013, Frederikse et al., 2020]). As a result, spread in OHU processes significantly contributes to the uncertainty in climate projections of OHS and sea-level rise, which in turn leads to uncertainty in projections of transient surface warming.

The lack of process-based observations with a global coverage (e.g. [Gould et al., 2013]) means that models are valuable for analysing these OHU processes. Yet, only a handful of model-based OHU process studies have been performed in the past (e.g. [Gregory, 2000, Huang et al., 2003, Exarchou et al., 2015, Kuhlbrodt

et al., 2015, Saenko et al., 2021]). In order to reduce our uncertainty in future climate projections, a better understanding of OHU processes and their connection to circulation processes is essential. That is the aim of this thesis.

## 1.5 A roadmap for this thesis

This thesis concerns the role of ocean circulation in transient climate change, which we will probe using an idealised aquaplanet model, the 'Double-Drake' configuration (described in Chapter 2), and its response to an abrupt $CO_2$-doubling. The main body of this thesis consists of the results Chapters 3, 4, and 5, with a concluding Chapter 6.

### 1.5.1 First results chapter

How do particular ocean circulation components transport heat vertically? And how will these components respond to global warming? In Chapter 3, we take ideas from [Zika et al., 2013] and project the Double-Drake ocean circulation onto depth-temperature coordinates, revealing 'thermal overturning cells'. In response to an abrupt $CO_2$-doubling, we find that changes in these thermal cells lead to an increase in the downward vertical heat transport of $\sim$0.2 W m$^{-2}$ in the top 2 km. Rather than 'resisting' the warming, the circulation response enables more warming of the ocean interior. Our results suggest that changes in ocean circulation will further reinforce the ocean's role as a buffer of global surface warming, complementing findings from [Winton et al., 2013].

### 1.5.2 Second results chapter

What is the link between the AMOC and ocean heat storage? And what will happen if this circulation weakens in the future? In Chapter 4, we focus on the weakening of the deep meridional overturning circulation in the small basin of Double-Drake. We look in detail at the transient warming response in Double-Drake following a weakening (slowdown) of the overturning circulation, and explain why this weakening is surprisingly unimportant for changes in the small basin's heat storage rate. This

challenges previously established links between the AMOC and ocean heat storage (e.g. [Kostov et al., 2014, Chen and Tung, 2018]).

### 1.5.3 Third results chapter

Can we emulate OHU in the Double-Drake model using a simple two-layer energy-balance model (EBM) [Geoffroy et al., 2013b]? And can we improve the emulation by increasing/decreasing the sensitivity of OHU to the stratification in the EBM? We find that increasing the sensitivity improves the emulation for Double-Drake and four other CMIP5 models, while decreasing the sensitivity worsens the emulation across all models analysed. The improvement following an increase in the sensitivity might highlight the importance of the stratification for OHU, and it suggests that a simple change to the two-layer EBM could lead to better representation of OHU.

We conclude in Chapter 6, where we summarise the main findings of the three results chapters and assess their relevance for the real world and the field of climate modelling. We address the limitations of the work presented and establish directions for possible future work.

*"What is the Earth but a lump of clay surrounded by water?"*
*From Vairāgyaśataka*

Bhartṛhari, c. 625 CE

# 2

# Experiment Design

This chapter details the model used for the thesis results presented in Chapters 3, 4, and 5. We use a coupled atmosphere-ocean model of intermediate complexity (Double-Drake, or 'DDrake'), underpinned by the MITgcm. A strong radiative forcing mimicking an abrupt $CO_2$-doubling has not been implemented before in this model. We study the model's response to such a radiative forcing on multidecadal to centennial timescales (primarily the top 2 km of the model ocean) to aid our understanding of OHU processes, particularly those related to ocean circulation. We give an overview of the MITgcm in section 2.2, and in section 2.3, we introduce the DDrake configuration and provide a description of the model set-up. A few key diagnostics from the control climate of DDrake are presented in section 2.3.2. We conclude with a brief history of the $CO_2$-doubling thought-experiment in section 2.4, and how this is implemented in DDrake. Our results and discussion throughout the rest of the thesis will centre around differences between the control and $CO_2$-perturbed climates of DDrake.

## 2.1 Modelling philosophy

According to [Katzav and Parker, 2015], there are currently three approaches to the development of climate modelling: the unified approach, the pluralist approach, and the hierarchy approach. The unified approach seeks to pool international resources to create a small number of multinational climate modelling centres, aiming to develop very high resolution models with an eye towards more accurate predictions. The pluralist approach calls for substantially increasing the diversity of models used in climate research, aiming to more widely sample the range of model structural uncertainties. This will allow a better quantification of uncertainties in predictions. The hierarchy approach is the one exhorted by [Held, 2005], which aims to establish a hierarchy of models of increasing complexity, ultimately leading to improvements in understanding the climate system.

There has arguably been a lot more focus on the unified and pluralist approaches in the modern development of climate science. This has led to large collaborations of scientists, software engineers, and other staff developing sophisticated general circulation models (GCMs) and Earth system models (ESMs). These models have grown enormously in complexity over the last few decades, and are so resource intensive that only a few dozen of them can be developed and maintained at any one time. The results from these models are compared periodically in global 'coupled model intercomparison projects' or CMIPs (e.g. [Meehl et al., 2007, Taylor et al., 2012, Eyring et al., 2016]).

Rather than follow the unified or pluralist approaches, the work in this thesis presents a contribution to the hierarchy approach. Due to the overwhelming collaborative nature of the current climate modelling enterprise, and the resulting complexity of the models developed, no single person can wholly understand what one of these models is doing. According to [Held, 2005], there is a gap between comprehensive climate models (GCMs, ESMs) and simple idealised models (e.g. energy-balance models, layered models) that has not been successfully closed. This thesis analyses the outputs of a coarse-resolution, coupled atmosphere-ocean GCM with highly-idealised geometrical constraints on ocean circulation. This model ('Double-Drake', [Ferreira et al., 2010]) is put forward to fill this gap and thus occupy an intermediate

position in the model hierarchy.

We will analyse the output of an abrupt $CO_2$-doubling experiment using the Double-Drake model. Such a scenario is an established test case in aiding understanding of the climate response to $CO_2$ increase in the atmosphere (e.g. [Manabe and Wetherald, 1975, Washington and Meehl, 1984, Schlesinger and Mitchell, 1987]). Understanding gained from this idealised forcing experiment is then extrapolated to other forcing scenarios. The Double-Drake model is not the real world, but, in a similar way, it is hoped that improvements in understanding this model will extrapolate to features of the real world. Such an understanding then feeds back onto the development of the state-of-the-art GCMs and ESMs that inform the IPCC in assessment reports (e.g. [Solomon et al., 2007, Stocker et al., 2013, Masson-Delmotte et al., 2021]), aiding improvements in the accuracy and uncertainty quantification of climate projections.

## 2.2 The MITgcm

The MITgcm (or Massachusetts Institute of Technology General Circulation Model) is a numerical computer model that solves the equations of motion governing the Earth's atmosphere or ocean [Marshall et al., 1997a, Marshall et al., 1997b]. It is able to model processes on a wide range of scales from tens of metres to thousands of kilometres. The MITgcm is used widely by the atmosphere, ocean, and climate modelling communities, with over 100 research articles using the MITgcm published in 2021 alone (`https://mitgcm.org/2022/01/06/2021-research-roundup/`).

The model code exploits an isomorphism between equation sets for the atmosphere and ocean so that the same dynamical kernel can be used to drive either fluid [Marshall et al., 2004]. The equations are written in a generic vertical coordinate $r$, and this is interpreted as pressure if modelling the atmosphere, and as height if modelling the ocean. The standard equations of motion used for the ocean are the 'semi-compressible' Boussinesq equations:

$$\frac{D\mathbf{u}}{Dt} + f\mathbf{k} \times \mathbf{u} + \frac{1}{\rho_0}\nabla_z p' = \mathcal{F} \tag{2.1}$$

$$\epsilon_{nh}\frac{Dw}{Dt} + g\frac{\rho'}{\rho_0} + \frac{1}{\rho_0}\frac{\partial p'}{\partial z} = \epsilon_{nh}\mathcal{F}_w \tag{2.2}$$

$$\nabla_z \cdot \mathbf{u} + \frac{\partial w}{\partial z} = 0 \tag{2.3}$$

Here, $D/Dt$ is the total derivative, $\mathbf{u}$ is the horizontal velocity and $w$ the vertical velocity, $f$ is the Coriolis parameter, and $\nabla_z$ is the gradient operator at constant $z$. The dashed quantities $p'$ and $\rho'$ are deviations away from some reference state. For the pressure, $p'$ is a deviation from a reference profile $p_0(z)$ such that $p(x, y, z, t) = p_0(z) + p'(x, y, z, t)$. For the density, $\rho'$ is a deviation from a constant reference density: $\rho' = \rho(\theta, S, p_0(z)) - \rho_0$. The $\mathcal{F}$ terms are forcings provided by different forcing packages, and the $\epsilon_{nh}$ parameter encapsulates the non-hydrostatic terms. The 'hydrostatic primitive equations' are recovered if $\epsilon_{nh} = 0$. The hydrostatic primitive equations are the model equations solved for the DDrake configuration used for the results in this thesis (the DDrake configuration is described in the following section).

Equations 2.1 and 2.2 are the horizontal and vertical momentum equations, respectively, while equation 2.3 ensures continuity. Together with an appropriate equation of state for $\rho$, and tracer equations for the potential temperature $\theta$ and salinity $S$:

$$\frac{D\theta}{Dt} = \mathcal{Q}_\theta \tag{2.4}$$

$$\frac{DS}{Dt} = \mathcal{Q}_S \tag{2.5}$$

where the $\mathcal{Q}$ terms are forcing and dissipation of each tracer, equations 2.1 to 2.5 form a complete set describing the hydrodynamics and thermodynamics of the model ocean.

These equations are then discretised in space onto a model grid and solved using finite volume methods. The grid can be initialised using Cartesian, spherical-polar, or general orthogonal curvilinear coordinate systems. The grid used for the DDrake configuration is the conformally expanded spherical cube [Rančić et al., 1996, Ad-

croft et al., 2004a]. This grid avoids the problem of converging meridians in traditional latitude-longitude model grids where the smallest grid-element length scales as $\Delta x_{min} \sim N^{-2}$, where $N$ is the number of points around the equator. For the latitude-longitude grids, doubling the number of points thus halves the resolution at the equator but quarters the resolution near the poles. The cube-sphere grid provides a more uniform coverage of the sphere and has a much better scaling of $\Delta x_{min} \sim N^{-4/3}$. This means it can be taken to a much higher resolution before becoming computationally unmanageable [Adcroft et al., 2004b].

## 2.3 The DDrake configuration

Our model set-up is the 'Double-Drake' or 'DDrake' configuration, first introduced in [Ferreira et al., 2010]. In this geometry, two sea-floor to sea-surface barriers are set 90° apart and joined at the North Pole. This separates the ocean into a large basin (LB) and a small basin (SB), with both of them connected by a 'southern ocean' region (SO) south of 35°S. The small and large basins in the DDrake configuration exhibit distinctive Atlantic-like and Pacific-like characteristics, respectively, with the small basin being warmer and saltier, and exhibiting a deep interhemispheric overturning circulation (see section 2.3.2). The configuration captures two important asymmetries relevant to the Earth's climate: a zonal asymmetry splitting the ocean into small and large basins, and a meridional asymmetry allowing for circumpolar flow in the Southern Hemisphere, but not in the Northern Hemisphere.

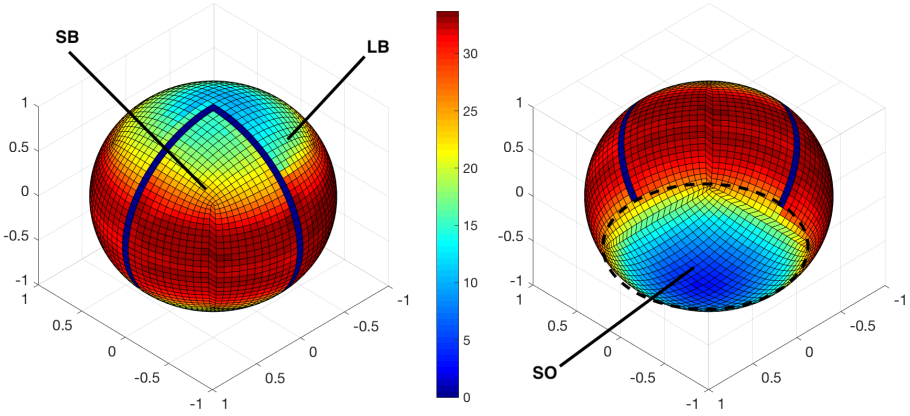



**Figure 2.1:** Time-averaged sea surface temperature (in °C) in the control integration, showing the model DDrake geometry from above (left) and below (right). The small basin (SB), large basin (LB), and southern ocean (SO) regions are labelled.

In [Ferreira et al., 2010], the DDrake configuration was used to help explain the localisation of deep water formation to the Atlantic basin in the real-world present climate. A deep overturning circulation is seen in the Atlantic basin (AMOC) but not in the Pacific. Similarly, a deep overturning circulation is seen in the small basin of DDrake, but not in the large basin. This is because of the difference in the zonal widths of the two basins, which results in a net atmospheric freshwater transport out of the small basin and into the large basin. The freshwater transport sets up a salinity contrast between the two basins, which localises the sinking to the small basin. Note this is only one suggested mechanism to explain the real-world Atlantic/Pacific salinity contrast, and it is not yet known what the true mechanism is (e.g. [Craig et al., 2017, Cessi and Jones, 2017, Ferreira et al., 2018a]).

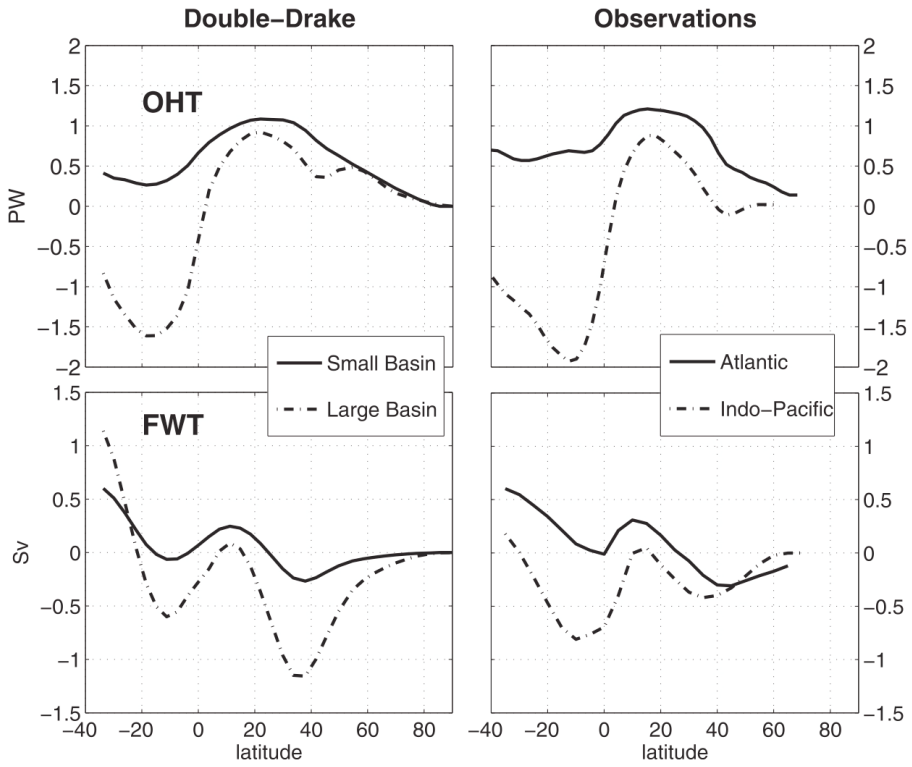



**Figure 2.2:** Meridional ocean heat transports (OHT) and freshwater transports (FWT) for (left) the small and large basins of DDrake and (right) the Atlantic and Indo-Pacific basins. Observations for OHT are taken from [Trenberth and Caron, 2001], while observations of FWT are taken from [Wijffels et al., 1992]. Figure reproduced from [Ferreira et al., 2010].

The meridional barriers in DDrake act as geometrical constraints on the large-scale ocean circulation, having a profound effect on the climate of the coupled system. The constraints are sufficient in reproducing fundamental properties of the present

Earth's climate. For example, figure 2.2 shows the meridional ocean heat transports and freshwater transports for the small and large basins of DDrake in comparison with estimates from observations. The transports are strikingly similar to those of the Atlantic and Indo-Pacific basins, despite DDrake's highly idealised geometry.

### 2.3.1 Technical description

The DDrake configuration uses the MITgcm code to drive the dynamics [Marshall et al., 1997a, Marshall et al., 1997b]. An isomorphism between the atmospheric and oceanic dynamics is exploited so that either fluid can be driven by the same dynamical core [Marshall et al., 2004]. The isomorphic vertical coordinates used are: a rescaled pressure coordinate $p^*$ for the compressible atmosphere, and a rescaled height coordinate $z^*$ for the Boussinesq ocean (as described in [Adcroft and Campin, 2004]). The use of the $z^*$ coordinate allows for perfect (machine accuracy) conservation of freshwater, heat, and salt during extended integration, as discussed in [Campin et al., 2008].

Both the atmosphere and ocean component models use the same horizontal cubed-sphere grid [Adcroft et al., 2004a] at a coarse C24 resolution (24x24 points per face, giving a resolution of 3.75°, or approximately 400 km, at the equator). Fluxes of momentum, heat, and freshwater are exchanged between the atmosphere and ocean every hour (constrained by the ocean model time step). The seasonal cycle of insolation is represented, but there is no diurnal cycle.

The atmosphere has a low vertical resolution of five levels, and its physics is based on the 'simplified parameterisations primitive-equation dynamics' (SPEEDY) scheme [Molteni, 2003]. The lowest vertical level represents the planetary boundary layer, the middle three levels are placed in the troposphere, and the top vertical level crudely represents the stratosphere. The physics package comprises a four-band radiation scheme, a boundary layer scheme, resolved baroclinic eddies, and parameterisations of moist convection, large-scale condensation, and cloud cover.

The ocean is flat-bottomed with a constant depth of 3 km, and is split into 15 levels with increasing vertical resolution from 30 m at the surface to 400 m at depth. A depth of 3 km is chosen so that the resulting heat capacity of the global ocean is

comparable to that of Earth's. The absence of land in the configuration means we must compensate by having this shallower depth (the average depth of the present Earth's oceans is about 3.7 km). A big caveat is that the flat-bottom topography means that topographic form drag plays no role in balancing momentum input from the surface winds. Hence, an enhanced linear bottom friction is employed and tuned to damp abyssal currents towards zero at the ocean floor. The seawater equation of state is the nonlinear international equation of state for seawater [Millero and Poisson, 1981], modified in terms of potential rather than in-situ temperature [Jackett and Mcdougall, 1995].

Oceanic mesoscale eddies are parameterised as an advective process ('GM') [Gent and Mcwilliams, 1990] and an isopycnal diffusion [Redi, 1982], both with a transfer coefficient of 1200 $m^2\ s^{-1}$ (both transfer coefficients can be interpreted as 'eddy diffusivities'; see Appendix A for a full description). Although it is numerically convenient to set both coefficients to the same value, this is a simplification, as the isopycnal diffusivity is generally larger than the GM diffusivity (e.g. [Smith and Marshall, 2009, Vollmer and Eden, 2013]).

Values of $\mathcal{O}(10^3)$ $m^2\ s^{-1}$ are standard in representing mesoscale eddy processes in coarse-resolution ocean models (e.g. [Griffies, 2018]). This is consistent with estimates of lateral eddy diffusivities that use direct observations from tracer release experiments (e.g. [Ledwell et al., 1998]), dispersion of subsurface floats (e.g. [LaCasce et al., 2014]), and satellite altimetry (e.g. [Abernathey and Marshall, 2013]).

However, these studies and others (e.g. [Groeskamp et al., 2017, Groeskamp et al., 2020]) reveal that eddy diffusivities vary widely with location (from $\sim$0 to $\mathcal{O}(10^4)$ $m^2\ s^{-1}$), with enhanced mixing in western boundary currents and a general decay with depth. So, a constant background value for the eddy diffusivity in DDrake is a large simplification, but one that has been used in more sophisticated coupled climate models with realistic geometries (e.g. [Salas-Mélia et al., 2005, Watanabe et al., 2010, Kuhlbrodt and Gregory, 2012]).

Additionally, it's been shown that models are quite sensitive to the value of the isopycnal diffusion ('$\kappa_\rho$') and the GM diffusivity ('$\kappa_{GM}$'). The isopycnal diffusion affects the uptake of anthropogenic carbon [Gnanadesikan et al., 2015], deep ventilation

[Jones and Abernathey, 2019], and global surface climate [Pradal and Gnanadesikan, 2014]. As argued in [Pradal and Gnanadesikan, 2014], an increase in isopycnal diffusion results in increasing high-latitude surface salinity, which decreases the stratification and enhances convection. This mechanism could explain why isopycnal diffusion also affects deep ventilation and carbon uptake, and possibly OHU as well (e.g. [Gregory, 2000]).

The GM diffusivity negatively correlates with the ACC transport in coupled climate models [Kuhlbrodt et al., 2012], and negatively correlates with the ocean heat uptake efficiency (OHUE) in CMIP3 models [Kuhlbrodt and Gregory, 2012]. A possible explanation linking these two results is that an increased ACC transport leads to steepened isopycnals in the Southern Ocean, resulting in a weakened stratification and hence greater OHU (e.g. [Gnanadesikan, 1999, Marshall and Zanna, 2014]). Another mechanism involves the AMOC, where it's been found that $\kappa_{GM}$ negatively correlates with the AMOC strength [Marshall et al., 2017], and that the AMOC strength positively correlates with OHUE [Kostov et al., 2014]. Taking both these relationships together suggests that $\kappa_{GM}$ controls OHU indirectly by controlling the strength of the AMOC [Saenko et al., 2018].

In addition to mesoscale eddies, the other key ocean processes that are parameterised in DDrake are convection, which is represented by an enhanced vertical mixing of temperature and salinity [Klinger et al., 1996], and diapycnal mixing, which is represented with a uniform background vertical diffusivity set to $3 \times 10^{-5}$ m$^2$ s$^{-1}$. This is broadly in accord with observational estimates of diapycnal mixing in the ocean interior from tracer release experiments (e.g. [Ledwell et al., 1993, Ledwell et al., 2011, Watson et al., 2013]) and microstructure profiles (e.g. [Gregg et al., 2003, Klymak et al., 2006]).

Like eddy diffusivities, diapycnal mixing also varies widely with depth and location (e.g. [Whalen et al., 2012, Waterhouse et al., 2014]), and it is particularly enhanced over rough bottom topography (e.g. [Polzin et al., 1997, Ledwell et al., 2000]). The global survey of diapycnal mixing measurements from [Waterhouse et al., 2014] reveals that diapycnal diffusivities above 1 km depth are $\mathcal{O}(10^{-5})$ m$^2$ s$^{-1}$ while those below 1 km depth are $\mathcal{O}(10^{-4})$ m$^2$ s$^{-1}$ (although values can reach $\mathcal{O}(10^{-3})$ m$^2$ s$^{-1}$ in

specific locations). A choice of $\kappa_v = 3 \times 10^{-5}$ m$^2$ s$^{-1}$ for DDrake lies between these two regimes.

As discussed in Chapter 1, the magnitude of diapycnal mixing plays a primary role in maintaining the MOC, particularly the Lower Cell. In idealised model studies, it's been found that the strength and structure of the Lower Cell is influenced by the magnitude of diapycnal mixing [Ito and Marshall, 2008, Nikurashin and Vallis, 2011] as well as the vertical profile of diapycnal mixing [Saenko and Merryfield, 2005, Mashayek et al., 2015].

A constant background value for diapycnal mixing in DDrake is an oversimplification, and this partly explains why there is no realistic Lower Cell circulation in DDrake (seen later in figure 2.8). Additionally, the lack of bottom topography means that diapycnal upwelling in the DDrake ocean interior is unrealistic, as, in the real world, bottom-enhanced diapycnal mixing drives *downwelling* in the ocean interior, while upwelling takes place in bottom boundary layers along sloping topography [Ferrari et al., 2016].

The lack of a realistic Lower Cell circulation in DDrake (and the relatively shallow ocean depth of 3 km) means that we should limit our discussion of results to the top ∼2 km of the ocean, so we are primarily concerned with the Upper Cell of the MOC (AMOC). Although $\kappa_v$ does affect the strength of the AMOC (classical scaling arguments suggest that AMOC strength $\propto \kappa_v^{2/3}$ (e.g. [Bryan and Cox, 1967, Park and Bryan, 2000])), the study of [Saenko and Merryfield, 2005] found that bottom-enhancement of $\kappa_v$ had very little effect on the AMOC and the corresponding OHT, so, a constant $\kappa_v$ profile for DDrake is not inappropriate for studying this circulation.

However, the magnitude of $\kappa_v$ does raise questions surrounding spurious diapycnal mixing in DDrake. The model vertical coordinate is height (rescaled $z^*$), and it was pointed out in [Griffies et al., 2000] that, in z-coordinate ocean models, truncation errors in numerical advection schemes can cause isopycnal processes to become erroneously projected onto the cross-isopycnal direction, leading to spurious diapycnal mixing. This spurious mixing could become non-negligible in particular regions, reaching values of $\mathcal{O}(10^{-4}$ m$^2$ s$^{-1})$, thus swamping the prescribed vertical diffusivity.

It is likely that there is some spurious diapycnal mixing in DDrake, but its magnitude

is not known. However, experiments with a similar aquaplanet configuration* have shown that the model is sensitive to the magnitude of $\kappa_v$, which suggests that the spurious mixing does not dominate over the prescribed vertical mixing.

Unlike the set-up in [Ferreira et al., 2010], we now include a frictional heating term in the atmospheric temperature equation that allows a conversion from mechanical dissipation to thermal energy. This captures the effects of friction, mainly in the planetary boundary layer, which generates turbulent eddies in the atmospheric flow field, after which internal viscous forces eventually dissipate kinetic energy into heat. Without such a term, the net energy imbalance at the top of the atmosphere (TOA) in the control climate is on the order of 1 W $m^{-2}$ downward, a feature of many contemporary climate models [Lucarini and Ragone, 2011]. This is because energy dissipated through friction is simply lost from the system, and needs to be continually replaced to close the energy cycle.

Including frictional heating reduces the energy bias at the TOA to $\sim$0.1 W $m^{-2}$, which greatly aids interpretation of the net energy imbalance in a $CO_2$-doubling experiment, which we describe in section 2.4. The model is spun up for 6000 years until a statistically steady state is reached. The time-mean of the last 50-year integration is used as the equilibrated control climate state.

The simplifications and caveats detailed above mean we must not confuse DDrake with the real-world ocean, and we should be careful about what conclusions we draw from the model. Throughout this thesis, we thus value qualitative over quantitative results. However, as mentioned in section 2.1, even if some conclusions only apply to DDrake, this is still useful as a contribution to the hierarchy approach of climate model development [Held, 2005].

### 2.3.2 Control Climatology

A discussion of the control climate of DDrake, particularly in comparison to the Drake configuration, is given in [Ferreira et al., 2010]. We recapitulate some of that discussion here, but with a greater emphasis on the model ocean. (Note that the climate state is slightly different owing to the addition of frictional heating in the

*Rheinlænder et al. 2022 (in prep.)

atmosphere.) Recall that the distribution of the continents is shown in figure 2.1 and the meridional ocean heat transports and freshwater transports in figure 2.2. All remaining diagnostics shown in this section are time-averages of the last 50 years of the 6000-year-long model spin-up.

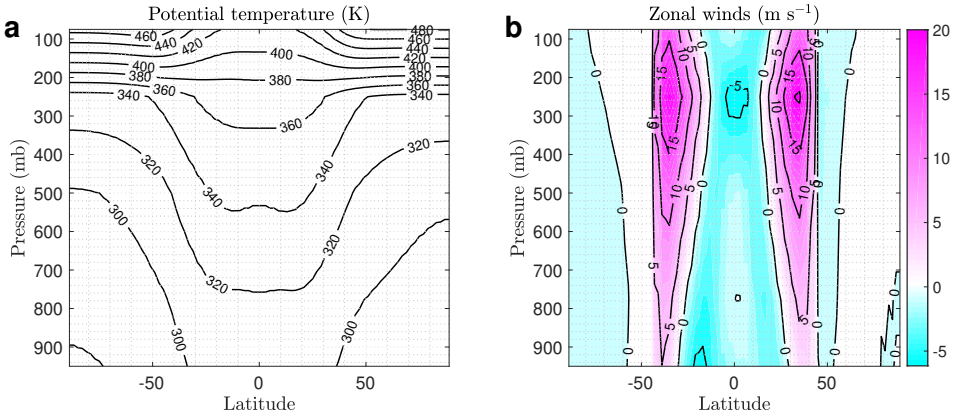



**Figure 2.3:** Zonally-averaged atmospheric potential temperature (a) and zonal winds (b) for the DDrake control climate.

Figure 2.3 shows the zonal mean distributions of the atmospheric potential temperature (panel a) and zonal winds (panel b). There's a good level of structural detail despite there being only 5 vertical levels in the atmospheric model. Westerly jet streams are seen in both hemispheres around 40° (collocated with the strong meridional temperature gradients), reaching near 20 m s$^{-1}$ at 250 mb. These jets are surrounded by much weaker trade winds and polar easterlies.

The southern hemisphere is slightly cooler than the northern hemisphere, due to two principal reasons: 1. an absence of meridional barriers south of 35°S permits circumpolar flow in the ocean, acting as a barrier to southward heat transport; and 2. the deep overturning circulation of the small basin permits a northward cross-equatorial heat transport, warming the northern hemisphere while cooling the southern hemisphere. Both these oceanic effects then imprint on the overlying atmospheric temperature distribution.

In figure 2.4 we plot the zonally-averaged temperature, salinity, and density distributions for the small and large basins of DDrake. The surface distributions for these fields are also plotted in figure 2.5. For comparison, north-south hydrographic sections of temperature and salinity across the Atlantic and Pacific basins from the

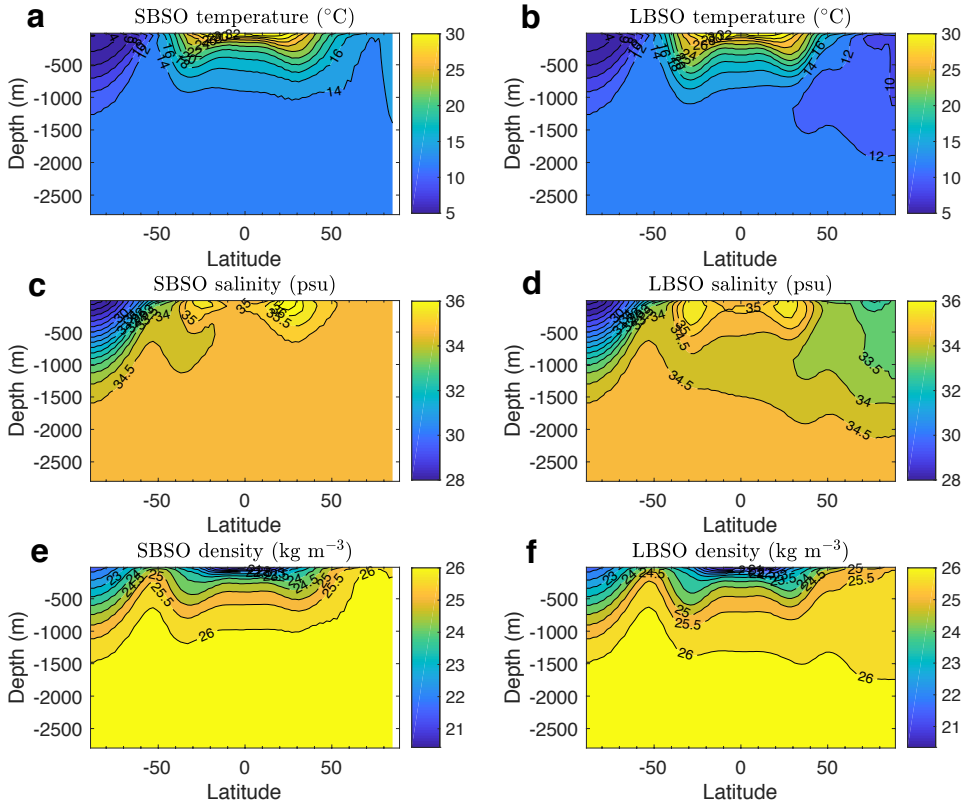



**Figure 2.4:** Control climate zonally and sector-averaged potential temperature (top), salinity (middle), and potential density $\sigma_0$ (bottom) distributions for the small basin plus southern ocean (SBSO, left column) and large basin plus southern ocean (LBSO, right column) DDrake regions. Potential temperature and potential density fields are referenced to the surface.

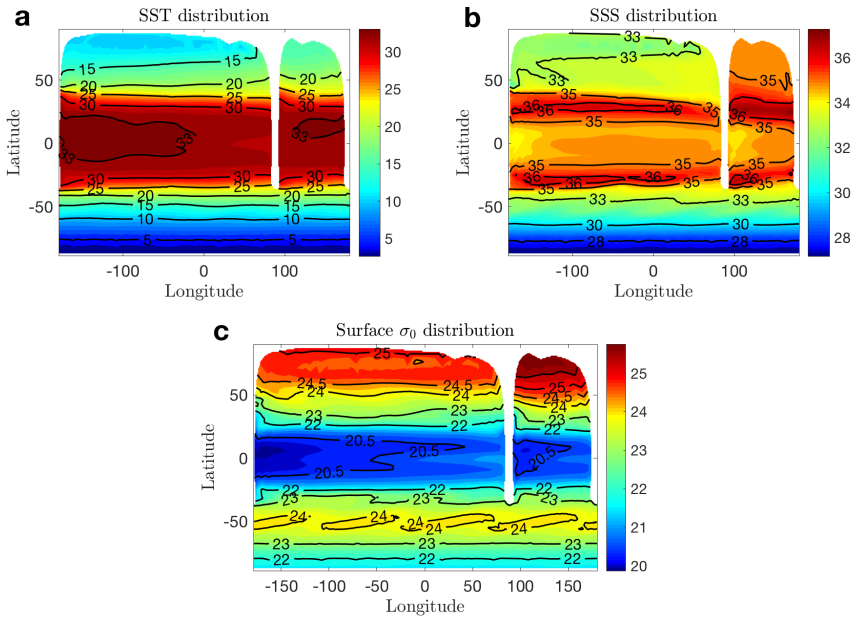



**Figure 2.5:** Spatial maps of the DDrake control climate (a) sea surface temperature (SST, in °C), (b) sea surface salinity (SSS, in psu), and (c) surface density ($\sigma_0$, in kg m$^{-3}$).

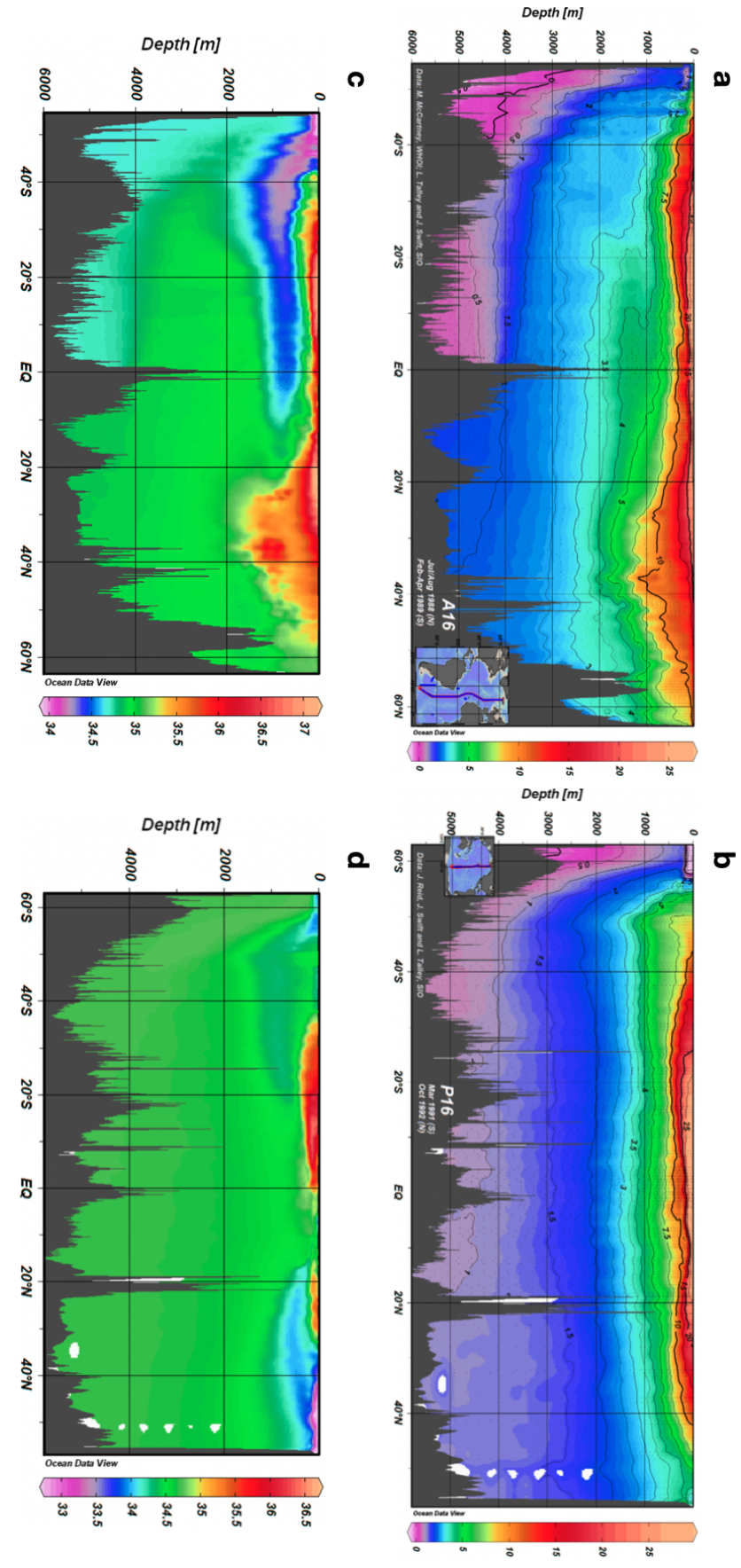



**Figure 2.6:** Hydrographic sections of potential temperature (top, in °C) and salinity (bottom, in psu) for the Atlantic (left) and Pacific (right) basins taken during the World Ocean Circulation Experiment (WOCE), from [Schlitzer, 2000].

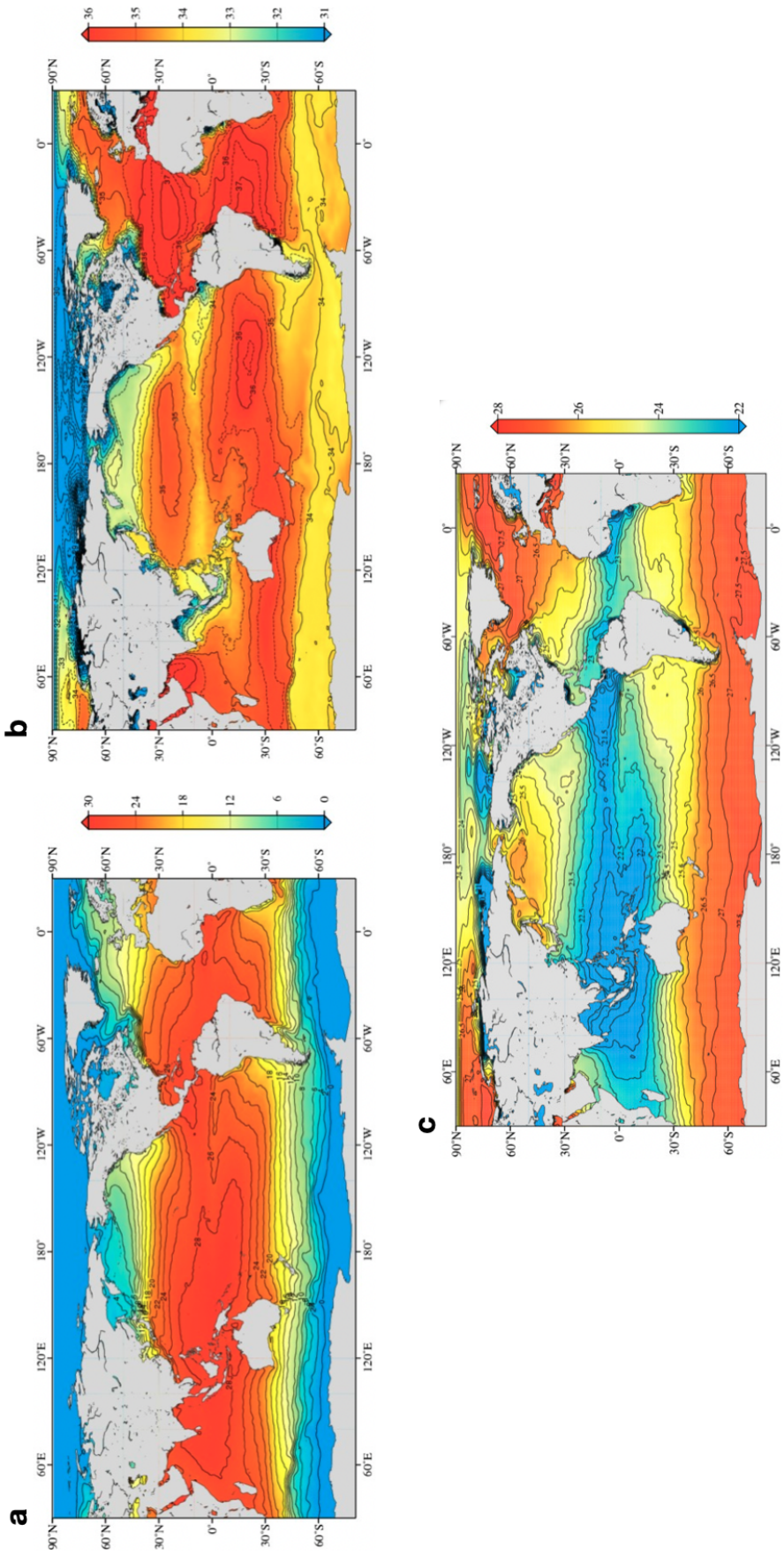



**Figure 2.7:** Decadally averaged surface climatological fields over the period 1955-2017 of (a) sea surface temperature (in °C), (b) sea surface salinity (in psu), and (c) surface density ($\sigma_0$, in kg m$^{-3}$), from the World Ocean Atlas 2018 [Boyer et al., 2018].

World Ocean Circulation Experiment (WOCE) are shown in figure 2.6, and climatologies of surface temperature, salinity, and density from the World Ocean Atlas (WOA) are shown in figure 2.7.

The zonal-average structures of temperature and salinity for the small and large basins are broadly in accord with those seen in observations (figures 2.4 and 2.6). The comparison is more favourable if we restrict our view to the top 3 km of the hydrographic sections from WOCE. The small basin (SB) is both warmer and saltier than the large basin (LB), just as the Atlantic is warmer and saltier than the Pacific. There is a tongue of fresher water protruding under the subtropical salinity maxima in the SB (figure 2.4c) reminiscent of Antarctic Intermediate Water (AAIW) in the Atlantic basin (figure 2.6c). Similarly, the tongue of cooler, fresher water in the northern high latitudes of the LB is reminiscent of North Pacific Intermediate Water (NPIW) (figures 2.4d and 2.6d).

However, there are clearly major differences. The biggest one perhaps is the lack of any analogous Antarctic Bottom Water (AABW) mass (purple in figure 2.6a, b) in DDrake. This means that the global water mass properties of DDrake are biased towards 'SB deep water', which results in the DDrake ocean being almost 10°C warmer on average than the Earth's. The absence of an Antarctic land mass in DDrake also means there's a deep bowl of cool, fresh water over the South Pole that's not seen in the present Earth's Southern Ocean (figure 2.4). Here, there is a temperature inversion, and the stable stratification is controlled by salinity (e.g. compare panels a and c with panel e in figure 2.4).

Turning to the surface distributions, we see that DDrake reproduces reasonable meridional gradients for the surface temperature, salinity, and density fields (figures 2.5 and 2.7). Surface salinity maxima are created near 30° in both hemispheres of DDrake due to large evaporation under the descending branches of analogous 'Hadley cells', in a similar mechanism to the present climate (figures 2.5b and 2.7b).

The contrast between the small and large basins of DDrake is similar to the contrast between the Atlantic and Pacific basins. Again, the SB is warmer and saltier than the LB, particularly in the northern high latitudes (figure 2.5a, b). Although the SST contrast between the small and large basins is large at these latitudes, the

surface waters in the SB are still denser than those in the LB (figure 2.5c), just as the North Atlantic is denser than the North Pacific (figure 2.7c). This is due to the nonlinear equation of state for seawater [Millero and Poisson, 1981], as the salinity exerts a greater control on the density at lower temperatures (e.g. [Nycander et al., 2015]).

Unlike in the LB, the absence of relatively fresher water in the SB northern high latitudes leads to a very weak stratification with many outcropping density surfaces (figure 2.4e, f). This difference in stratification is also readily apparent between the Atlantic and Indo-Pacific basins (panels a and b in figure 2.9).

Figures 2.4 and 2.5 reveal a controlling influence of the northern high latitudes on the key differences between the two basins of DDrake. Indeed, these differences lead to profoundly different ocean circulations in both basins, with deep convection being localised solely to the small basin. As noted in section 2.3, this is due to the salinity contrast between the two basins (figures 2.4c, d and 2.5b). This contrast exists due to the narrowness of the SB relative to the LB, and is brought about by a net atmospheric freshwater transport out of the SB into the LB, as explained in [Ferreira et al., 2010].

As could be expected from figure 2.4e, the weak stratification in the SB northern high latitudes leads to deep convection, which feeds the downwelling branch of a deep overturning circulation. The control climate overturning circulations are shown in figure 2.8, revealing the radically different circulations of the SB and LB. The SB circulation is dominated by a deep clockwise overturning cell (SBMOC) spanning the entire length of the basin (35°S to 90°N). The two shallow, subtropical Ekman cells about the equator are dwarfed by the convectively-driven overturning cell. In the LB, however, the shallow Ekman cells are of primary importance, and there is a northward intrusion of bottom water from the southern ocean, about half of which upwells at the equator. There is no circulation associated with deep convection in the LB.

If we compare with the overturning circulations in the Atlantic and Indo-Pacific basins, we find that the circulation structures are remarkably similar (figures 2.8a, b and 2.9c, d). Both the SB and the Atlantic are dominated by a deep clockwise

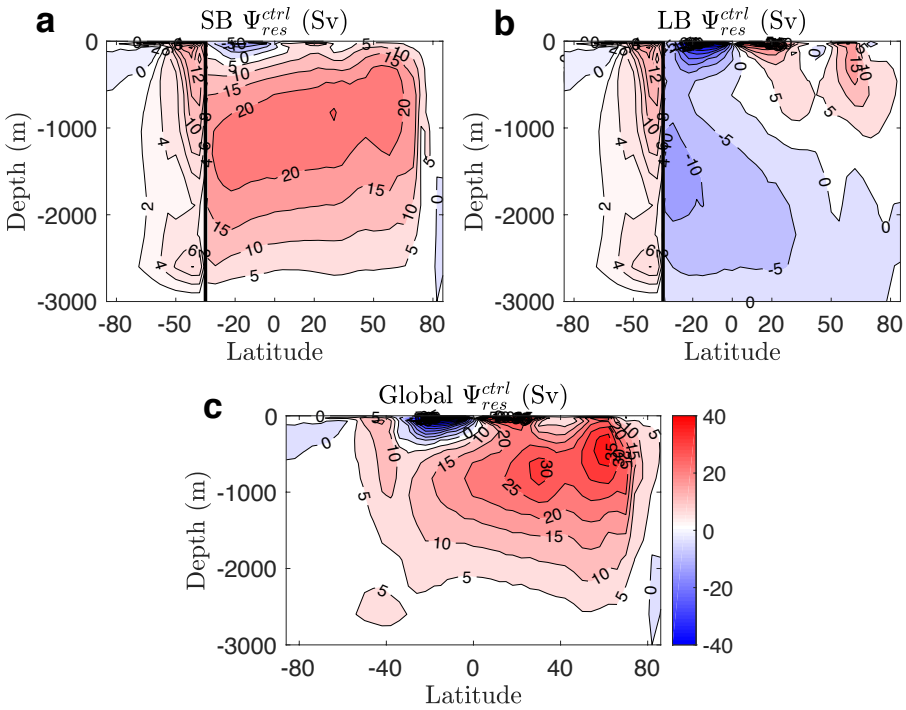



**Figure 2.8:** Control climate residual overturning stream functions for the (a) small basin, (b) large basin, and (c) global regions of DDrake (in Sv, 1 Sv $\equiv 10^6$ m$^3$ s$^{-1}$). The southern ocean residual overturning is shown south of 35°S (thick black line) in panels (a) and (b).

overturning (Upper Cell), while the LB and Indo-Pacific have shallow Ekman cells and an anticlockwise overturning (Lower Cell). However, there is an unrealistic cancellation of the 'Upper' and 'Lower' Cells in the global-average in DDrake (figure 2.8c), so the global MOC is dominated by the SBMOC (compare with figure 1.5 from the Introduction).

This lack of an abyssal Lower Cell is one of the major shortcomings of the DDrake model in its applicability to study OHU below 2 km. The warming of the ocean below 2 km is primarily driven by the warming of AABW [Purkey and Johnson, 2010, Purkey and Johnson, 2013], and this is not captured in DDrake. However, the contribution below 2 km to global OHU is likely less than 10% (e.g. [Desbruyères et al., 2016, Meyssignac et al., 2019]).

Another unrealistic aspect of the DDrake circulation is that the SBMOC strength (stream function maximum) is 26 Sv, which is approximately 40% stronger than the real-world AMOC (e.g. measurements from RAPID are ∼18 Sv [Frajka-Williams et al., 2019, Danabasoglu et al., 2021]), although this is still within the CMIP6 model

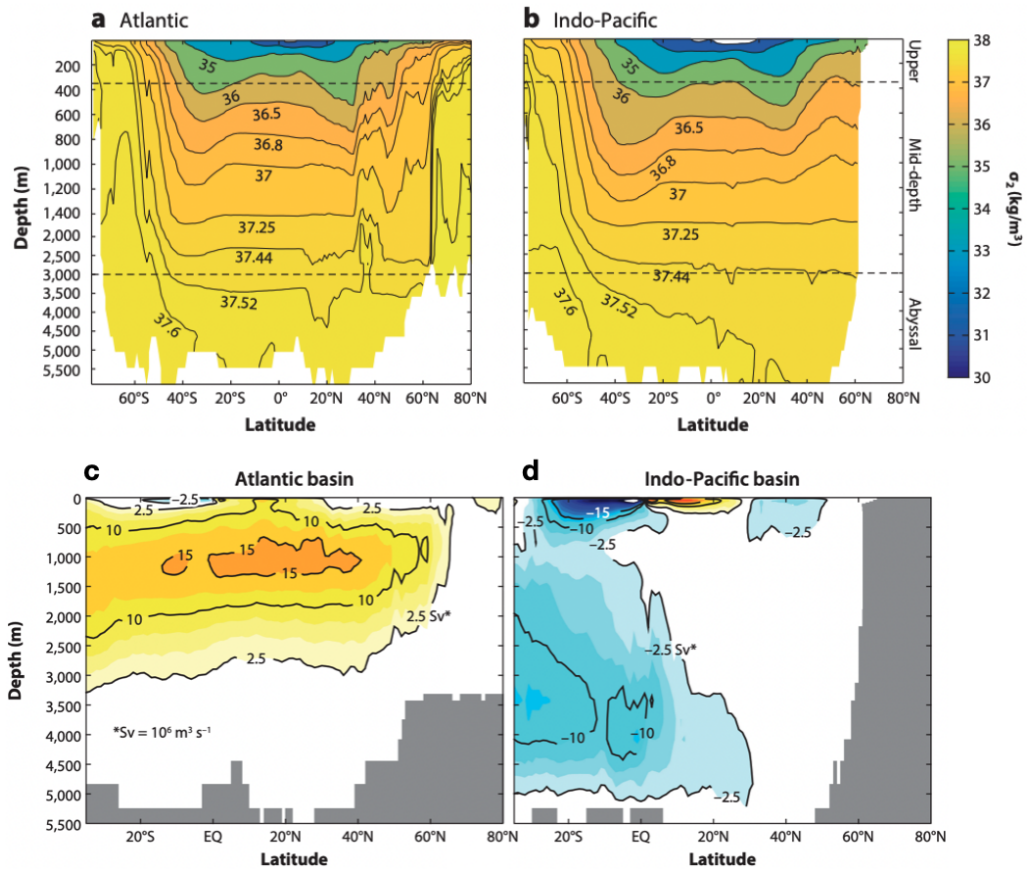



**Figure 2.9:** Zonally-averaged potential density referenced to 2100 dbar (top) and meridional overturning circulations (bottom) for the Atlantic (left) and Indo-Pacific (right), calculated from the ECCOv4 ocean reanalysis [Forget et al., 2015]. Panels a and b are reproduced from [Cessi, 2019] while panels c and d are reproduced from [Ferreira et al., 2018a].

range [Weijer et al., 2020]. Additionally, there is an unusual clockwise overturning cell in the LB northern high latitudes between ∼50 and 80°N (figure 2.8b) that's not seen in the Indo-Pacific (figure 2.9d) due to interruption from topography. In Chapter 3, we associate this cell with polar easterlies encircling the DDrake North Pole.

The clockwise overturning cell in the DDrake southern ocean (south of 35°S) is also unrealistically deep, spanning the full ocean depth (compared with the Deacon Cell in the Southern Ocean, which reaches approximately mid-depth (e.g. [Döös et al., 2008])). The lack of topography in DDrake means that waters must plunge to the ocean bottom, as only the linear bottom friction can provide the zonal pressure gradient needed to balance the Coriolis force for the southward geostrophic flow.

Finally, the real-world MOC is inherently interbasin in nature (e.g. [Talley, 2013])

and the DDrake circulation likely is as well (e.g. [Nilsson et al., 2013]), so the SB and LB overturning circulations cannot be cleanly separated. The three-dimensional pathways of the DDrake circulation may thus be more similar to the real-world than figure 2.8c would suggest, but this is obscured in the zonal average. A proper assessment of the three-dimensional pathways would require Lagrangian trajectory studies (e.g. [Van Sebille et al., 2018, Rousselet et al., 2021]) but this isn't explored in this thesis.

## 2.4 Forcing experiment: an abrupt $CO_2$-doubling

Whether the global ocean circulation will even strengthen or weaken in the future is not settled (e.g. [Toggweiler and Russell, 2008, Hu et al., 2020, Wunsch, 2020]). What this means for future ocean heat storage is even less clear, and this is tied to uncertainties regarding the future trajectory of global surface warming. A better understanding of ocean circulation and heat storage is a worthy goal in itself (even one specific to DDrake), but it also leads to concomitant advances in climate model formulation, projection accuracy, and eventual policy recommendations.

As a starting point, we go back to the canonical climate thought-experiment: a doubling of atmospheric $CO_2$. This idea arguably came to prominence with the 'Charney Report' in 1979, the first comprehensive assessment of $CO_2$-induced climate change [Charney et al., 1979]. The warming effects of increasing $CO_2$ in the atmosphere, however, were first articulated by Eunice Newton Foote over a hundred years prior in 1856 [Foote, 1856]! And the effects of a doubling of $CO_2$ on global climate have been thought about as early as 1896 by Arrhenius [Arrhenius, 1896], and later revived by Callendar in 1938 [Callendar, 1938]. The notion of a $CO_2$-doubling in climate science has endured to this day (to this thesis!), providing an easy thought-experiment to hone our understanding of the essentials of global climate.

A $CO_2$-doubling now underpins our concept of equilibrium climate sensitivity (ECS), defined as the expected increase in global mean surface temperature to occur once a steady state has been reached after a $CO_2$-doubling. Arrhenius estimated an ECS of 5-6°C [Arrhenius, 1896], while Callendar's estimate was around 2°C [Callendar,

1938]. In the Charney Report, the authors state: "We estimate the most probable global warming for a doubling of $CO_2$ to be near 3°C with a probable error of ±1.5°C" [Charney et al., 1979]. This estimate has been lauded as remarkably prescient as, 34 years later, the fifth IPCC assessment report (AR5) states: "there is high confidence that ECS is extremely unlikely to be less than 1°C and medium confidence that the ECS is likely between 1.5°C and 4.5°C and very unlikely greater than 6°C" [Stocker et al., 2013]. The ECS for DDrake is likely close to 3°C, so well within the range for Earth (see Chapter 5).

A $CO_2$-doubling has framed our way of thinking about climate change for a very long time, with many norms and concepts growing out of this initial thought-experiment. It is thus a natural experimental choice for the DDrake configuration, and this thesis presents the first results arising from that scenario for DDrake. Such an idealised step-forcing experiment is achieved in DDrake by abruptly changing the longwave absorption in the $CO_2$-band in the model atmosphere. This causes an initial top-of-atmosphere forcing of approximately 4.4 W $m^{-2}$ (see Chapter 5), thus mimicking a doubling of atmospheric $CO_2$ (e.g. [Myhre et al., 1998, Byrne and Goldblatt, 2014]). We then run the model from this state for 200 years. The imposed radiative forcing results in a warming of the climate system as it attempts to reach a new equilibrium. We diagnose the ensuing climate responses relative to the control climate.

The rest of this thesis explores how the DDrake model ocean responds to such an abrupt radiative forcing, and what this might say about other climate models, both simpler and more complex, as well as the future state of Earth's oceans.

*"In the heat of the sun, the ocean is the boiler and condenser of a gigantic steam engine, a weather engine that governs crops, floods, droughts, frosts, hurricanes, at times as serene as motherhood or as frightening as God's wrath."*

Jacques-Yves Cousteau, 1981

# 3

# Changes in vertical heat transports by ocean circulation under global warming

The rate of surface warming depends on the rate of OHU, which, in turn, depends on vertical advective heat transports by ocean circulation. In this chapter, we project the DDrake global ocean circulation onto depth-temperature coordinates and decompose it into three circulation cells: a thermally indirect 'warm cell', a thermally direct 'cool cell', and a thermally direct, shallow, 'tropical cell'. We identify each of these cells with distinct locations and physical processes, and diagnose their vertical heat transport (VHT) profiles. We then analyse the circulation responses of each of these cells to an abrupt $CO_2$-doubling, and the resultant changes in their advective VHTs. We find that the warm cell strengthens and the cool cell weakens (the tropical cell response is negligible). Both these responses lead to an increase in the downward VHT of $\sim$0.2 W m$^{-2}$ in the top 2 km, enabling greater warming of the ocean interior. This suggests that changes in ocean circulation will further reinforce the ocean's role as a buffer of global surface warming.

## 3.1 Introduction

Vertical advective heat transport by ocean circulation is a key OHU process (e.g. [Gregory, 2000, Exarchou et al., 2015, Kuhlbrodt et al., 2015, Saenko et al., 2021]). In this chapter, we seek a description of OHU due to changes in ocean circulation directly. One approach to this problem is the use of novel overturning stream functions in thermodynamic coordinates.

Overturning stream functions have previously been calculated in density-latitude coordinates. Doing so reduces potential overestimates of spuriously strong diabatic circulations such as the Deacon cell in the Southern Ocean (e.g. [Gregory, 2000, Döös and Webb, 1994, Nurser and Lee, 2004]). For example, a horizontal circulation along an isopycnal surface can show up as a meridional cell when projected into depth-latitude coordinates, if there happens to be a zonal variation in the depth of the isopycnal surface for the northward and southward flow. Such a meridional cell would vanish in density-latitude coordinates.

Another choice is to calculate the overturning in depth-density coordinates. The projection into depth-density coordinates allows one to determine whether an overturning cell is driven by mechanical or thermal means, as work needs to be done on a fluid to lift dense water upwards (e.g. [Nycander et al., 2007]). Stream functions have also been calculated in depth-temperature and depth-salinity coordinates enabling analysis of vertical transports [Zika et al., 2013], and even purely thermohaline coordinates to analyse global water mass transformations [Zika et al., 2012, Döös et al., 2012].

As our focus is on vertical heat transports by ocean circulation, the most pertinent tool for our needs is the overturning stream function in depth-temperature coordinates and its changes under global warming. Such a study was performed by [Zika et al., 2015] using the Community Climate System Model 4 (CCSM4) [Gent et al., 2011]. In the depth-temperature diagram, they identify a 'warm' cell that fluxes heat downwards, coincident with the AMOC, and a compensating 'cold' cell that fluxes heat upwards, coincident with Antarctic Bottom Water (AABW) formation (as was found previously in [Zika et al., 2013] for the University of Victoria Earth

System Climate Model (UVic ESM)). Under anthropogenic forcing, they find that the cool cell collapses while the warm cell continues fluxing heat downwards at an increasing rate, leading to net ocean heat uptake.

In this chapter, we perform a similar study using the MITgcm DDrake configuration under an abrupt $CO_2$-doubling, focussing on the top 2 km of the model ocean. Although the deep ocean below 2 km contributes ∼10% to global OHU (e.g. [Desbruyères et al., 2016]), we neglect the ocean below 2 km for three principal reasons:

1. Warming below 2 km is primarily driven by warming of AABW (e.g. [Purkey and Johnson, 2013]) — DDrake lacks a realistic Lower Cell of the MOC, so this process is not captured.

2. The ocean below 2 km responds on a multi-centennial to millennial timescale (e.g. [Stouffer, 2004, Yang and Zhu, 2011, Li et al., 2013]) — we are interested in the transient response of the ocean circulation after 200 years following the $CO_2$-doubling, so the slow response below 2 km is not relevant for our purposes.

3. Bottom topography is increasingly being shown to have a controlling influence on the abyssal overturning (e.g. [Ferrari et al., 2016, Holmes et al., 2018]) — DDrake has no bottom topography, and so cannot accurately capture circulation processes below 2 km.

We find similar results to [Zika et al., 2015] whereby a warm cell strengthens and a cool cell weakens, both contributing to an increase in the downward vertical heat transport, enabling greater ocean heat uptake. In section 3.2 we introduce the concept of stream functions in thermodynamical coordinates and formally define the thermal overturning circulation. In section 3.3, we examine the DDrake vertical heat balance in the control climate, and decompose the global thermal overturning circulation into specific circulation features, identifying them with physical circulations in geographical coordinates. In section 3.4, we analyse the thermal overturning response to an abrupt $CO_2$-doubling and the resultant changes in vertical heat transport. We conclude in section 3.5.

## 3.2 Stream functions in other coordinates

An overturning stream function is normally defined as the zonally-integrated meridional volume transport (e.g. [Buckley and Marshall, 2016]):

$$\Psi(y,z) = \frac{1}{\Delta t}\int_t^{t+\Delta t}\int_z^{\eta}\int_{x_W}^{x_E} v\; dx\; dz\; dt \tag{3.1}$$

where $v$ is the meridional velocity averaged over some period of time $\Delta t$, $\eta$ is the free-surface height, and $x_W$ and $x_E$ define the longitudinal positions of the meridional boundaries enclosing the basin. Here, a positive stream function circulates clockwise, with northward flow at the surface and southward flow at depth. The key conceptual leap to find $\Psi$ in other coordinates is that the averaging in equation 3.1 need not simply take place at constant *position* (latitude), it could take place over *any* scalar variable identifiable with a water parcel.

We choose to take a statistical approach to describing the circulation, following [Pauluis et al., 2011] and [Zika et al., 2013]. Generalising the presentation in [Zika et al., 2013], for some tracer $C(x,y,z,t)$, one can calculate a distribution function $M_C^{\mathbf{r}}$ for the transport at concentration $C^*$ in a particular direction $\mathbf{r}$ using:

$$M_C^{\mathbf{r}}(C^*,\mathbf{r}) = \frac{1}{\Delta t}\int_t^{t+\Delta t}\int_A \delta(C^*-C)\;\mathbf{v}\cdot\frac{\mathbf{r}}{|\mathbf{r}|}\;dA\;dt \tag{3.2}$$

where $\delta$ is the Dirac delta function, $\mathbf{v}$ is the velocity field, $t$ is time, and $A$ is a two-dimensional surface with normal parallel to $\mathbf{r}$ through which we wish to calculate the tracer transport. In equation 3.2, the averaging takes place at constant $C$, in contrast to equation 3.1 where it takes place at constant $y$. A volumetric stream function can then be calculated by cumulatively integrating the transport up to a particular value of $C$:

$$\Psi_{C\mathbf{r}}(C,\mathbf{r}) = \int_{-\infty}^{C} M_C^{\mathbf{r}}(C^*,\mathbf{r})\;dC^* \tag{3.3}$$

$M_C^{\mathbf{r}}$ is the volume transport per unit tracer, so the actual tracer transport (in $C$-units $\mathrm{m}^3$) is then related to $M_C^{\mathbf{r}}$ and $\Psi_{C\mathbf{r}}$ via:

$$T_C^{\mathbf{r}}(\mathbf{r}) = \int_{-\infty}^{+\infty} M_C^{\mathbf{r}}(C^*, \mathbf{r}) C \, dC = \int_{-\infty}^{+\infty} \Psi_{C\mathbf{r}}(C, \mathbf{r}) \, dC \tag{3.4}$$

For vertical heat transport, the scalar tracer is the potential temperature $\theta$ and direction the local vertical $\mathbf{k}$, so that $\mathbf{v} \cdot \mathbf{k} = w$, the vertical velocity. In the model configuration used, there is both a resolved velocity $w$ and an eddy-induced velocity $w_b$ due to the Gent-McWilliams parameterisation [Gent and Mcwilliams, 1990]. Both of these are thus incorporated in the distribution function using a residual vertical velocity $w_{res} = w + w_b$. Equation 3.2 then becomes:

$$M_\theta^z(\theta^*, z) = \frac{1}{\Delta t} \int_t^{t+\Delta t} \int_{y_S}^{y_N} \int_{x_W}^{x_E} \delta(\theta^* - \theta) w_{res} \, dx \, dy \, dt \tag{3.5}$$

where $x_W, x_E, y_S$, and $y_N$ define the boundaries of the horizontal region we wish to consider. At some depth $z$, $M_\theta^z$ is the area integral of the vertical velocity where $\theta = \theta^*$. Using equation 3.3, a thermal overturning stream function can then be determined from $M_\theta^z$ by:

$$\Psi_{\theta z}(\theta, z) = \int_{-\infty}^{\theta} M_\theta^z(\theta^*, z) \, d\theta^* \tag{3.6}$$

This framework can be extended to two (or even $n$) scalar variables to calculate joint distributions. For example, this was done for dry entropy and moist entropy in the atmosphere by [Pauluis et al., 2008], who used it to help determine a new picture of the global atmospheric circulation.

In practice, we don't use $w_{res}$ in equation 3.5 but rather $w_{res} - \langle w_{res} \rangle$, where $\langle w_{res} \rangle$ is the time and spatially averaged residual vertical velocity over a model vertical layer (non-zero due to small numerical truncation errors in the calculation). This enforces mass conservation at each model vertical level, which ensures that the thermal overturning stream function contains closed streamlines. The global residual volume flux resulting from $\langle w_{res} \rangle$ is $\sim$0.01 Sv, so is very small compared to the strength of the circulations considered here.

In order to build up distribution functions $M_C^z$ for the control and perturbed climates of DDrake, we perform two five-year integrations with data outputted every

five days: one starting from the end of the control integration, and one starting from year 200 following the abrupt $CO_2$-doubling. The overturning stream functions we calculate for the control and perturbed climates are thus five-year time-means. We choose a sampling frequency of five days to ensure a high degree of temporal correlation between the sampled fields. We note that [Zika et al., 2013] use monthly-averaged fields, finding a negligible difference between monthly- and five-day-average derived vertical heat transport. Thus, a five day sampling frequency may be unnecessarily high, but we have chosen to err on the side of caution here. We have not checked whether using monthly-averaged fields instead modifies our results.

We calculate $M_\theta^z$ globally and regionally for both the DDrake control and perturbed climates and use it to diagnose thermal overturning cells. Taking ideas from [Ferrari and Ferreira, 2011], we decompose the global thermal overturning into specific ocean circulation features and examine their responses to the $CO_2$ perturbation, linking them to physical processes. By integrating over the thermal overturning cells, we examine the vertical heat transport responses due to these circulation features and determine which features dominate the global response.

## 3.3 Control climate vertical heat balance

Before looking at the thermal overturning and diving into specific circulation features, we first consider how the advective transport in DDrake fits into the global vertical heat balance. We plot the total vertical advective (ADV) and diffusive (DIFF) heat fluxes outputted from the model in figure 3.1. The advective heat flux is further decomposed into contributions from resolved and eddy-induced circulations (due to the GM eddy parameterisation [Gent and Mcwilliams, 1990]).

The diffusive flux outputs include contributions from the background uniform vertical diffusion ($k_v = 3 \times 10^{-5}$ m$^2$ s$^{-1}$), the Redi isopycnal mixing scheme [Redi, 1982], and the strong vertical mixing due to convective adjustment [Klinger et al., 1996]. We take the convention that a downward heat flux is positive.

As noted in Chapter 2, there will be a small amount of spurious vertical diffusion due to truncation errors in the advection scheme (e.g. [Griffies et al., 2000]), and

its magnitude is not known. However, this doesn't overwhelm the prescribed background vertical diffusion, as we do not need to factor it into the vertical heat balance in order to balance the other processes in the DDrake control climate (black line in figure 3.1).

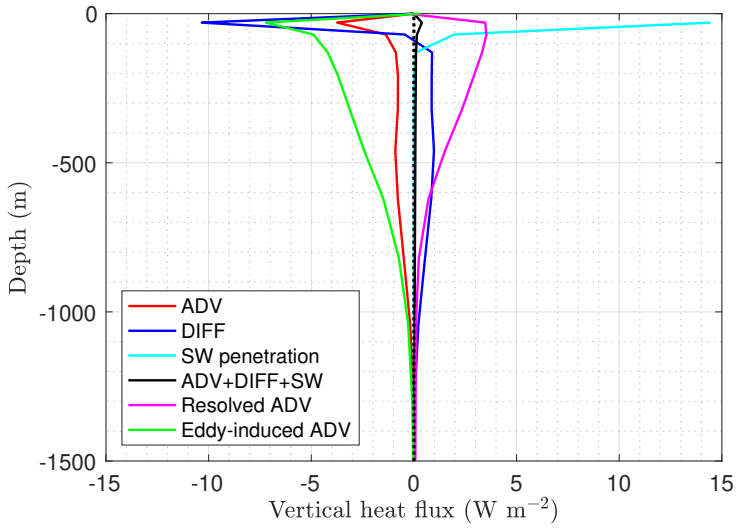



**Figure 3.1:** DDrake control climate vertical heat balance for advective (ADV) and diffusive (DIFF) processes, and shortwave (SW) radiation penetration (in W m$^{-2}$). A downward heat flux is positive. The zero line is black dotted. Only the top 1.5 km are shown for clarity.

In figure 3.1, we see that below ∼150 m, the advective and diffusive fluxes balance each other closely (red and blue curves). This supports the classic vertical 'upwelling-diffusion' balance first popularised by [Munk, 1966], where a cooling effect from the upwelling of abyssal waters is balanced by a downward diffusion of heat (although, here, the upward advective flux is due to the sum of the resolved and eddy-induced circulations i.e. the residual circulation).

In the top 150 m, the advective and diffusive processes sum to produce an upward heat flux. The upward diffusive flux is most likely due to the convective mixing (e.g. [Gnanadesikan et al., 2005]). These upward fluxes are balanced by shortwave radiation penetrating below the surface (cyan curve). This penetration is an exponential decay, based on a two-band solar absorption model from [Paulson and Simpson, 1977].

Notably, advection by the resolved circulation is associated with a *downward* heat flux (magenta curve), confirming the findings of more modern modelling studies

such as [Gregory, 2000, Zika et al., 2013, Exarchou et al., 2015, Saenko et al., 2018]. However, the (parameterised) eddy-induced circulation (green curve) more than compensates this downward heat flux, leading to a net *upward* advective heat flux (red curve). This is similar to the vertical heat balance seen in other models, where the main process transporting heat downwards is the resolved advection, while the bulk of the upward heat transport is due to parameterised eddy advection (e.g. [Gnanadesikan et al., 2005, Hieronymus and Nycander, 2013, Griffies et al., 2015]).

As pointed out by [Hieronymus and Nycander, 2013], isopycnal mixing by eddies could also be interpreted as an advective flux, like the eddy-induced circulation. Thus, it is possible to add its contribution to the residual circulation, resulting in a 'super-residual' transport (SRT), first suggested by [Kuhlbrodt et al., 2015]. The SRT framework was used by [Dias et al., 2020a], who found that the SRT heat balance has two depth-dependent regimes. In the upper-ocean (0-700 m), downward SRT heat flux is balanced by convection and near-surface mixing, while below 700 m, upward SRT heat flux is balanced by diapycnal diffusion. We do not consider the effects of the SRT here.

It is the net upward advective heat flux we wish to zoom in on (i.e. that due to the residual circulation, the sum of the resolved and eddy-induced circulations), and subsequently decompose its structure into particular ocean circulation components using $\Psi_{\theta z}$. To check the soundness of this premise, we compare these model-outputted vertical advective fluxes (direct calculation) with those inferred from $\Psi_{\theta z}$ (an indirect diagnostic). Using equation 3.4, the vertical heat transport $\mathcal{H}^z_\theta$ is given by:

$$\mathcal{H}^z_\theta(z) = \rho_0 \, c_p \int_{-\infty}^{+\infty} \Psi_{\theta z}(\theta, z) \, d\theta \tag{3.7}$$

where $\rho_0$ is a reference seawater density, and $c_p$ is the specific heat capacity of seawater at constant pressure. The resolved, eddy-induced, and net $\mathcal{H}^z_\theta$ profiles are plotted in figure 3.2 as dash-dotted lines, alongside the same advective terms from figure 3.1 as solid lines for comparison.

The correspondence between the model-outputted terms and the $\mathcal{H}^z_\theta$ calculations is fairly good. The overall shapes of the profiles are well-captured, with discrepancies

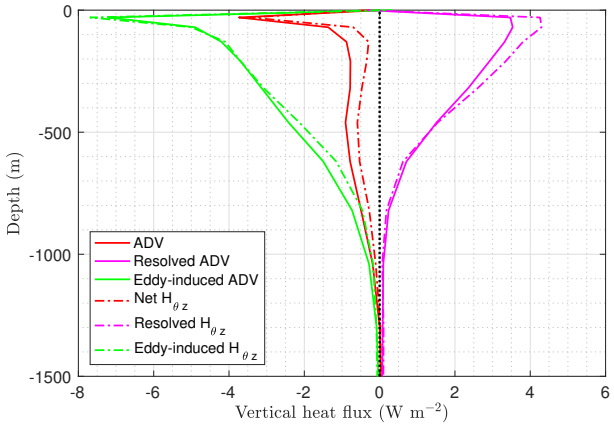



**Figure 3.2:** Comparison of model-outputted vertical advective heat fluxes (solid lines) with those calculated from the thermal overturning $\Psi_{\theta z}$ (dash-dotted lines), for the DDrake control climate. The zero line is black dotted. Only the top 1.5 km are shown for clarity.

within $\sim$0.5 W m$^{-2}$. The $\mathcal{H}_\theta^z$ calculation systematically underestimates the net upward advective heat flux, due to an overestimation of the downward resolved heat flux in the top $\sim$400 m, and an underestimation of the upward eddy-induced heat flux below $\sim$400 m depth. This could be due to the shortness of the $M_\theta^z$ averaging period (five years), or a sensitivity to the $\theta^*$ bin size. Nevertheless, the mismatch between the solid and dash-dotted lines in figure 3.2 is small enough for our purposes.

### 3.3.1 The DDrake thermal overturning circulation

We first look at the control DDrake overturning circulation $\Psi_{res}^{ctrl}$ in geographical $(y, z)$ coordinates. This is the zonally-integrated meridional volume transport as defined in equation 3.1, where for $v$ we use the model $v_{res} = v + v_b$. This is shown in figure 3.3, calculated for the different basins of DDrake in the control climate. The zonally-averaged $\theta$ contours are superimposed as black dashes.

Due to the DDrake ocean being only 3 km deep, the overturning in the small basin (SB) reaches almost the full depth of the basin (figure 3.3c). Although the real-world AMOC also reaches a depth of $\sim$3 km, this is approximately mid-depth in the Atlantic (e.g. [Buckley and Marshall, 2016, Cessi, 2019]). Thus, rather than the Upper and Lower MOC cells stacking on top of each other like in other zonally-averaged views of the overturning circulation (e.g. [Lumpkin and Speer, 2007, Marshall and Speer, 2012]), the SB and LB MOC cells in DDrake overlap and unrealistically can-

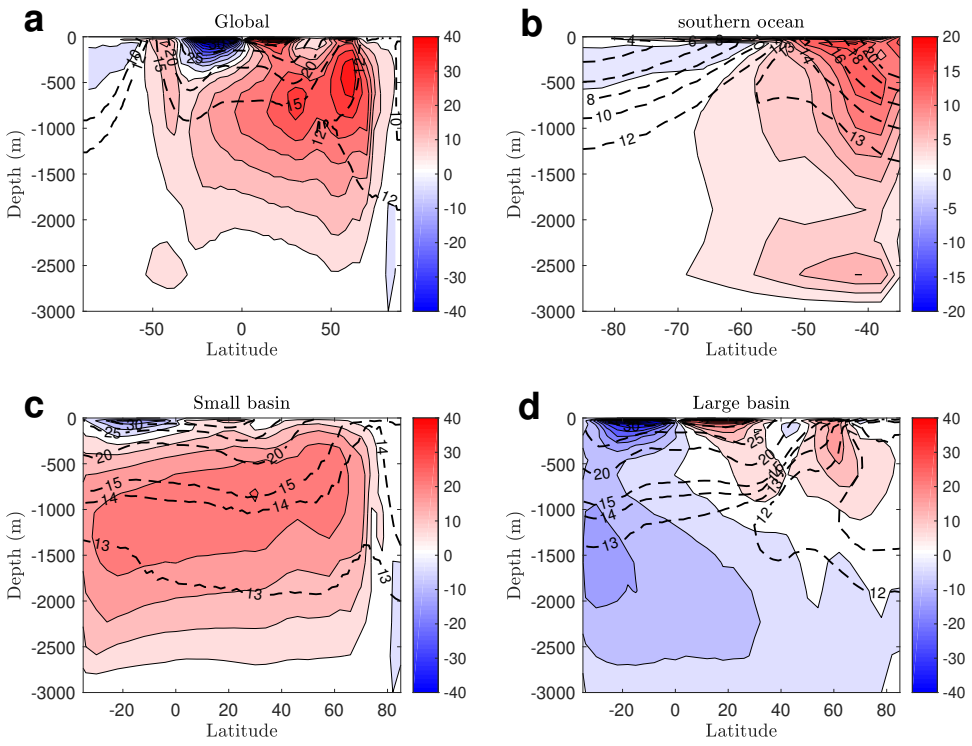



**Figure 3.3:** DDrake control climate zonally-averaged $\Psi_{res}^{ctrl}$ (colour, in Sv) and $\theta$ distributions (black dashed lines, in °C) for the (a) global, (b) southern ocean, (c) small basin, and (d) large basin regions. Contour interval is 5 Sv for panels a, c, and d. For panel b, the interval is 2 Sv; also, note the different colour-bar scale. Red cells circulate clockwise while blue cells circulate anti-clockwise.

cel at depth in the global-average (figure 3.3a). This means that the global picture is dominated by the clockwise overturning in the SB, and there is no realistic Lower Cell of the MOC, as noted in Chapter 2.

In both the small and large basins there are shallow tropical overturning cells with downwelling in the subtropical gyres at ∼30°S and 30°N and upwelling at the equator. In the large basin, these shallow cells are deeper and stronger, and there is also a fairly deep (∼1 km) clockwise cell at ∼60°N associated with the subpolar gyre (figure 3.3d). Such a deep subpolar gyre overturning does not exist in the present-day Indo-Pacific due to interruption from topography (e.g. [Talley, 2013, Newsom and Thompson, 2018, Ferreira et al., 2018a]), so the relevance of this LB cell to the real world is questionable.

In the DDrake southern ocean, the overturning is dominated by a single clockwise cell, mimicking the Deacon cell, with wind-driven upwelling ∼55°S and subsequent downwelling in the convergence to the north (figure 3.3b). As discussed in Chapter 2, this overturning cell is unrealistically deep, as waters must plunge to the ocean bottom where only the linear bottom friction can provide the zonal pressure gradient needed to support the southward geostrophic flow. The lack of any Lower MOC cell is also readily apparent from this panel (figure 3.3b). In the DDrake southern ocean high latitudes, there is a weak anticlockwise circulation due to convergence and downwelling at the South Pole. Of course, such a circulation does not exist in the real world due to the presence of Antarctica.

We will refer back to these circulation features when discussing the thermal overturning in DDrake. But we should keep in mind that, throughout, we are discussing the circulation of the DDrake model, which should not be confused with the real world. The caveats above surrounding $\Psi_{res}^{ctrl}$ will also carry over to the DDrake thermal overturning. There is no bottom topography, no bottom-enhanced mixing, and no realistic Lower MOC Cell, so we restrict our discussion to the top 2 km of the model ocean.

The DDrake control climate global $\Psi_{\theta z}$, calculated from $M_\theta^z$, is shown in figure 3.4. By substituting $w_{res}$ for $w$ or $w_b$ in equation 3.5, we decompose the circulation into resolved (panel a) and eddy-induced (panel b) components, respectively. Here, red

cells circulate clockwise and transport heat downwards, while blue cells circulate anti-clockwise and transport heat upwards. The resolved circulation is dominated by a clockwise cell for water masses between ∼12°C and 30°C (figure 3.4a). The eddy-induced circulation is dominated by an anti-clockwise cell occupying the same temperature range (figure 3.4b). These cells cancel each other out, leaving a weaker, residual net circulation with a different structure (figure 3.4c).

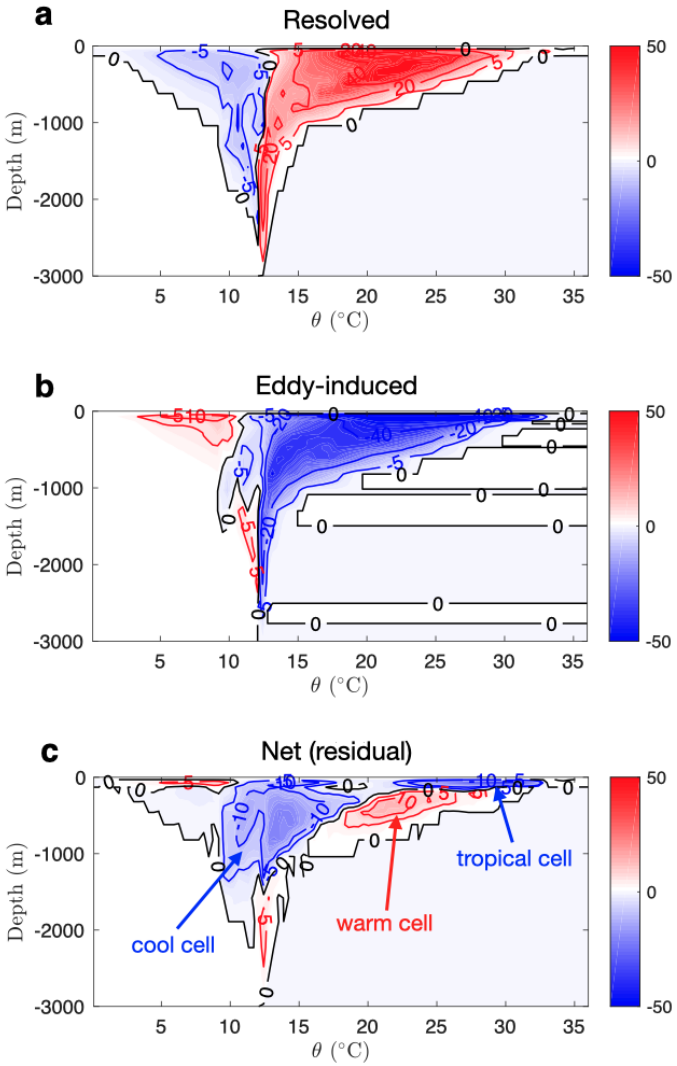



**Figure 3.4:** Control climate DDrake global thermal overturning circulations (in Sv). (a) Resolved circulation $\overline{\Psi_{\theta z}}$, (b) eddy-induced circulation $\Psi'_{\theta z}$, and (c) net circulation $\Psi_{\theta z} = \overline{\Psi_{\theta z}} + \Psi'_{\theta z}$. Red cells circulate clockwise while blue cells circulate anti-clockwise.

In this net circulation, we identify a 'warm' (clockwise) cell at ∼500 m depth, occupying the temperature range 20-30°C fluxing heat downwards ('warm cell' in figure 3.4c). This is compensated by a 'cool' (anti-clockwise) cell in the range 10-20°C

that extends down to ∼1.5 km depth, which fluxes heat upwards ('cool cell' in figure 3.4c). The warmest water masses from ∼25-30°C are associated with a shallow, cool cell confined to the top ∼200 m ('tropical cell' in figure 3.4c). We will refer to this cell as the 'tropical' cell, as only at low 'tropical' latitudes do water masses exist with such high temperatures near the surface (see figure 3.3). There are also two other weak warm cells: one at the surface ∼5-10°C, and one at a depth of ∼2 km near 13°C.

By using a temperature threshold, we define the 'cool cell' as all negative stream function values with $\theta < 20$°C, and the 'tropical cell' as all negative values with $\theta > 20$°C. The 'warm cell' is defined as all positive stream function values where $\theta > 15$°C. This decomposition is shown in figure 3.5. Choosing this stream function decomposition simplifies the analysis, but neglects the other two weak warm cells seen in figure 3.4c. We associate the weak warm cell at the surface with the southern ocean, and the deep warm cell ∼2 km depth with a SB/SO exchange associated with the SBMOC (seen later).

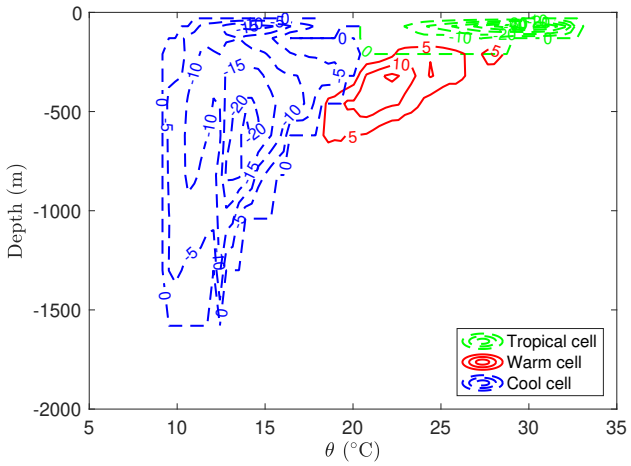



**Figure 3.5:** DDrake global net control thermal overturning circulation ($\Psi_{\theta z}$, in Sv), decomposed into a warm cell (red solid, for $\theta > 15$°C), a cool cell (blue dashed, for $\theta < 20$°C), and a tropical cell (green dashed, for $\theta > 20$°C). Dashed lines denote negative values and circulate anti-clockwise, while solid lines denote positive values and circulate clockwise. Only the top 2 km are shown.

We now proceed to identify the cells in figure 3.5 with particular ocean circulation features seen in figure 3.3. In order to geographically locate the warm, cool, and tropical cells, we repeat the $M^z_\theta$ calculation basin-wise. A similar procedure was done by [Saenko et al., 2018], who calculated $\Psi_{\theta z}$ for the Northern and Southern

Hemispheres separately, using the Nucleus for European Modelling of the Ocean (NEMO) version 3.4 ocean model [Madec et al., 2017]. Such a partitioning does not ensure closed circulation cells when considering the different ocean basins separately, and so it cannot be used to rigorously attribute heat transport to a particular circulation. However, it does provide insight into the individual basin contributions to the global $\Psi_{\theta z}$ picture (figures 3.4c and 3.5). These net thermal overturning circulations for each of the DDrake basins are shown in figure 3.6.

From figure 3.6, we see that the global thermal overturning structure is dominated by the large basin. This is in contrast to figure 3.3 where, in geographical coordinates, the global overturning structure is dominated by the small basin. Comparing panels a and d in figure 3.6 makes clear that the warm cell in figure 3.5 is almost exclusively made up of circulations in the large basin. Referring back to figure 3.3d, we thus attribute the warm cell to a wind-driven inter-gyre communication between the subtropical and subpolar gyres in the large basin. Warm water (∼25°C) downwells at the poleward side of the subtropical gyre near 40°N, crossing isotherms to reach ∼15-20°C water at a depth of approximately 750 m. This water subsequently upwells in the subpolar gyre ∼50°N, before warming back up to 25°C again as it approaches the convergence north of the centre of the subtropical gyre once more.

For the tropical cell, we compare panels a, c, and d in figure 3.6 and thus attribute it to shallow circulations existing in both the small and large basins. In figures 3.3c and d, these shallow circulations are the tropical overturning cells already identified, associated with downwelling at the centres of the subtropical gyres at approximately 30°S and 30°N and subsequent upwelling at the equator.

The cool cell in figure 3.5 from 10-20°C is trickier to identify as, from figures 3.6c and d, we see that it is a combination of different circulations in the small and large basins. The small basin thermal circulation (figure 3.6c) penetrates almost the full ocean depth, downwelling at ∼13°C. This is coincident with the SBMOC (figure 3.3c) where water downwells at approximately 14°C and must cool to ∼13°C and colder, poleward of 60°N. This water keeps its temperature throughout much of the ocean interior below 1 km depth. It then warms along its upwelling branch as it returns northwards, before finally cooling again as it approaches the small basin

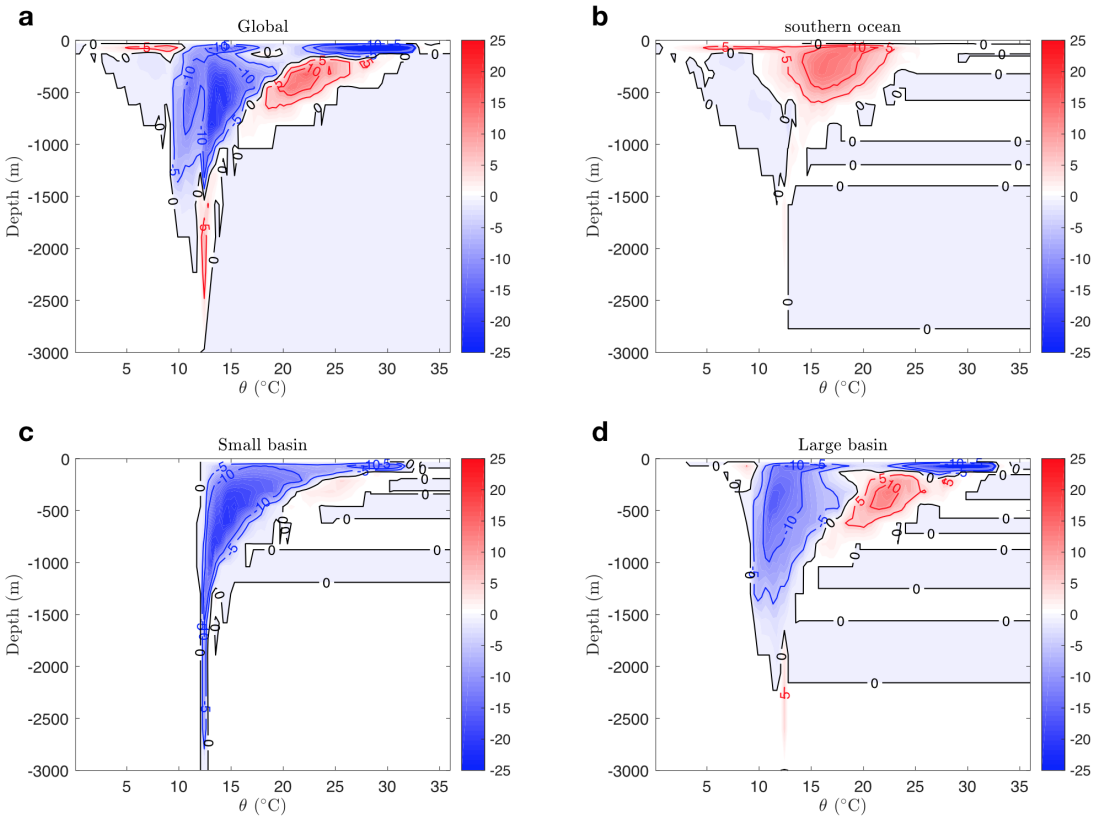



**Figure 3.6:** DDrake net control thermal overturning circulations ($\Psi_{\theta z}$, in Sv) calculated for the (a) global, (b) southern ocean, (c) small basin, and (d) large basin regions. The large basin dominates the global $\Psi_{\theta z}$ structure. Red cells circulate clockwise while blue cells circulate anti-clockwise.

northern high latitudes.

The large basin thermal circulation (figure 3.6d) penetrates to ∼2 km and not the full depth, so we rule out the 'abyssal upwelling' anti-clockwise cell seen in figure 3.3d as part of the cool cell. The fact that, in the LB, $\Psi_{res}^{ctrl}$ reaches the full depth (figure 3.3d) but $\Psi_{\theta z}$ only reaches ∼2 km depth (figure 3.6d) indicates that water parcels circulating below 2 km depth in the LB hold their temperature (i.e. do not warm up or cool down). So, these deep water parcels do not contribute to the LB thermal overturning.

The only other candidate for the cool cell in the LB is the deep clockwise cell associated with the subpolar gyre at the large basin northern high latitudes (figure 3.3d). Here, cool ∼10°C water downwells at the highest northern latitudes (∼70°N) due to polar easterly winds encircling the North Pole. The weak stratification enables the water to plunge to depths of 1-2 km before subsequently upwelling and warming to ∼15°C in the subpolar gyre near 50°N.

In the DDrake southern ocean, there is a single warm cell at ∼15-20°C (figure 3.6b), coincident with the clockwise 'Deacon cell'-like circulation seen in figure 3.3b. Relatively warm water near 20°C downwells in the circumpolar convergence ∼30°S and cools to around 15°C, before upwelling due to Ekman suction near 55°S. The water then warms during the northward Ekman transport before downwelling again. This clockwise Ekman overturning is counteracted by the parameterised eddies, whose collective action induces an anti-clockwise circulation that acts to slump the isopycnal surfaces. The resultant clockwise overturning in the DDrake southern ocean (figure 3.3b) is thus approximately half as strong as it would be without the eddies.

The southern ocean warm cell does not affect the global $\Psi_{\theta z}$ structure much, apart from the weak extension into 5-10°C water, which explains the weak surface warm cell (figure 3.6a). The weak deep warm cell ∼2 km depth remains to be explained fully.

We have now identified the tropical, warm, and cool cells in figure 3.5 with particular ocean circulation features in the small and large basins. In summary:

- Tropical cell: Shallow overturning circulations in both the small and large basins confined to the top ∼200 m, associated with downwelling in the subtropical gyres at approximately 30°S and 30°N and subsequent upwelling at the equator.

- Warm cell: A wind-driven inter-gyre circulation in the large basin associated with downwelling in the subtropical gyre ∼40°N and upwelling in the subpolar gyre ∼50°N.

- Cool cell: A combination of the deep interhemispheric MOC in the small basin and an overturning gyre circulation in the large basin where polar waters downwell ∼70°N and upwell in the subpolar gyre ∼50°N.

This type of thermal overturning decomposition has only been done for a handful of other ocean circulation models. In the intermediate complexity climate model UVic ESM, [Zika et al., 2013] did a similar three-cell decomposition for the global $\Psi_{\theta z}$ into 'surface', 'deep', and 'bottom' cells. They identify the surface cell with shallow overturning circulations associated with the subtropical gyres, just as we have done with the tropical cell of DDrake. Their deep cell is found to be a combination of the AMOC, the Southern Ocean overturning, and an Antarctic Intermediate Water circulation in the Pacific. The bottom cell is identified with the AABW circulation, but no such circulation exists in DDrake.

In a follow-up study, [Zika et al., 2015] calculated $\Psi_{\theta z}$ for the coupled climate model CCSM4 [Gent et al., 2011] and identified 'cold' and 'warm' cells, similar to the 'bottom' and 'deep' cells found in UVic ESM. Like in [Zika et al., 2013], they identify the cold cell with AABW formation and the warm cell with the AMOC and Southern Ocean overturning. In addition to these cold and warm cells, they again find a cool surface cell (similar to the surface cell in UVic ESM and the tropical cell in DDrake), but also a secondary warm cell below this at ∼500 m depth. This secondary warm cell is similar to the warm cell identified in DDrake in figure 3.5 and so is possibly linked to wind-driven gyre circulations in CCSM4, however this is not commented on in their paper.

The deep cell in [Zika et al., 2013] and the warm cell in [Zika et al., 2015] are both

linked to the AMOC, and both flux heat *downwards*. An AMOC that contributes to the net downward transport of heat was also reiterated by [Saenko et al., 2018] for the NEMOv3.4 ocean model [Madec et al., 2017]. This is in contrast to DDrake, whose AMOC analogue (the SBMOC) fluxes heat *upwards* (figure 3.6c), contributing to the cool cell in figure 3.5. The only cell in DDrake that fluxes heat downwards is the warm cell, which we conclude is almost entirely due to wind-driven circulations in the large basin (see section 3.3.3 and figure 3.6d).

A consensus may be emerging that model AMOC cells in fact flux heat downwards, however, this kind of analysis will need to be done for more coupled climate models before any firm conclusions can be made. Whether a control model AMOC cell fluxes heat downwards or upwards may directly impact transient ocean heat storage responses (we touch on this in the next chapter).

Since most of the ocean's density variations are controlled by temperature, fluxing heat downwards is synonymous to pushing light fluid downwards or lifting dense fluid upwards. This requires mechanical forcing from the winds or tides, for example (see section 3.3.3). The theory of [Nikurashin and Vallis, 2012] suggests that the AMOC is primarily driven by winds over the Southern Ocean, given typical parameter ranges for the present-day ocean. This depends on the adiabaticity of the AMOC, and requires a set of isopycnals to outcrop in both the Southern Ocean and Northern Hemisphere (i.e. in the upwelling and downwelling regions) [Wolfe and Cessi, 2011, Johnson et al., 2019].

However, dynamical theories such as [Nikurashin and Vallis, 2012] and those reviewed in [Johnson et al., 2019] are based on density (buoyancy), so we cannot separate the roles of temperature and salinity. This makes it difficult to infer the vertical *heat* transport associated with the AMOC. In particular, the key downwelling regions of the AMOC may occur in 'beta oceans' where the upper-ocean stratification is controlled by salinity, not temperature (e.g. [Carmack, 2007, Petit et al., 2020, Caneill et al., 2022]). So, it is not especially clear that even a wind-driven, adiabatic AMOC should transport heat downwards.

Whether the real-world AMOC is essentially adiabatic, and whether it advectively fluxes heat downwards (warm cell) or upwards (cool cell) in the net is still an open

question [Johnson et al., 2019]. Vertical heat fluxes estimated from observations show that the dominant contribution is a downward heat flux in the Southern Ocean from the upwelling of Circumpolar Deep Water [Cummins et al., 2016]. This estimate neglects the convective downwelling from NADW formation, however. So, even if we assume that the dominant downward heat flux in the Southern Ocean is solely associated with the AMOC, the estimate from [Cummins et al., 2016] doesn't tell us whether the upward heat flux associated with NADW formation would cancel this. Furthermore, the connection between the downwelling and upwelling regions of the AMOC is unclear due to complex interbasin pathways (e.g. [Talley, 2013]).

So, it is unclear whether the real-world AMOC is thermally direct or indirect. Establishing this fact is important for projections of transient climate change, as the AMOC is projected to weaken with global surface warming (e.g. [Gregory et al., 2005, Weaver et al., 2012, Weijer et al., 2020]). Recent proxy observations are also consistent with a weakening response (e.g. [Rahmstorf et al., 2015, Caesar et al., 2018, Zhu and Liu, 2020]). How this weakening affects the corresponding warm or cool cell in temperature space is particularly uncertain; it is possible that the weakening may not even affect the vertical heat transport, as the heat transport depends on the *temperature structure* as well as the strength of the circulation.

In the next chapter, we will show that the SBMOC heat flux is well described by the control overturning, as the SBMOC weakening terms contributing to the heat flux cancel each other out [Shatwell et al., 2020]. A similar result was found by [Zika et al., 2015] for CCSM4 under a global warming scenario. They well approximated the heat transport carried by the warm cell considering only the changing temperature difference between the downwelling and upwelling branches and assuming *no* weakening. We will explore the $CO_2$-doubling vertical heat transport (VHT) responses for DDrake in section 3.4. We will look not just at the SBMOC (which is only a part of the cool cell), but at all the DDrake thermal overturning cells. But first, we examine how the $\Psi_{\theta z}$ cells flux heat vertically in the control climate.

### 3.3.2 Vertical heat transports

Having identified the cells in $\Psi_{\theta z}$ with particular ocean circulations, we now look at the vertical heat transports $\mathcal{H}^z_\theta$ carried by each of them (equation 3.7). These are shown in figure 3.7.

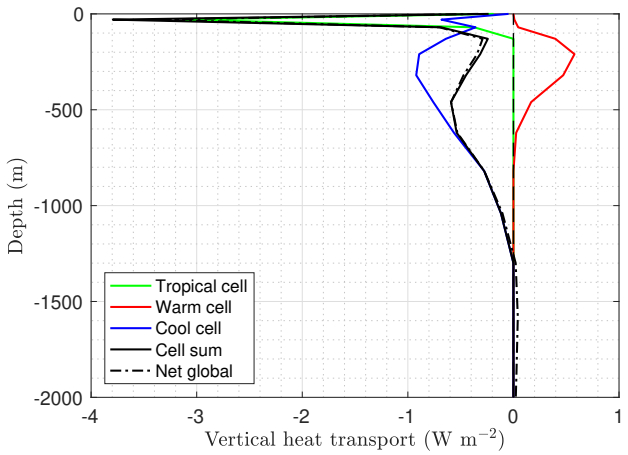



**Figure 3.7:** Vertical heat transport profiles for the three thermal overturning cells of DDrake in the control climate (in W m$^{-2}$). Here, a positive heat transport is directed downwards. The solid black line is the sum of the red, blue, and green lines. The dash-dotted black line is the total global advective VHT, accounting for cells not included in the $\Psi_{\theta z}$ three cell decomposition. Only the top 2 km are shown.

As expected, the warm cell fluxes heat downwards, while the cool and tropical cells flux heat upwards. The warm cell VHT peaks at $\sim$0.6 W m$^{-2}$ at 200 m depth. The cool cell VHT is almost twice as strong, peaking at $\sim -1$ W m$^{-2}$ a little deeper, near 300 m depth. The deeper vertical extent of the cool cell means that below around 600 m depth, the net advective vertical heat transport is supplied almost entirely by it. The tropical cell completely dominates the upward vertical heat transport near the surface, peaking near $-3$ W m$^{-2}$.

The solid black line in figure 3.7 is the total VHT supplied by the tropical, warm, and cool cells. Also plotted is the net global advective VHT (black dash-dotted line, equivalent to the red dash-dotted line in figure 3.2). Below around 1.5 km depth, there is actually a net downward VHT, not captured by the cell sum. Nevertheless, the differences between the black solid and dash-dotted lines are negligible, lending support to our chosen $\Psi_{\theta z}$ three-cell decomposition.

### 3.3.3 Thermally or mechanically driven?

Before assessing how the three DDrake thermal overturning cells respond to an abrupt radiative forcing in the $CO_2$-doubling experiment, we first take a brief foray into their possible driving mechanisms. Knowing whether a cell is primarily thermally or mechanically driven greatly aids a physical description of its response.

It's been over a hundred years since Sandström first postulated his famous theorem [Sandström, 1908]. He concluded that a thermally-forced, steady, overturning circulation could only be maintained if the heating occurred at a greater depth (pressure) than the cooling. In this way, the circulation is able to generate the mechanical energy necessary to overcome frictional dissipation. The fact that a vigorous overturning circulation is observed in the ocean, which is primarily heated and cooled at the surface, stands in flat contradiction to this theorem.

For a long time oceanographers assumed that a significant part of the MOC was forced by buoyancy fluxes at the surface, namely, localised surface cooling feeding the downwelling branch, and surface heating and subsequent diffusion feeding the upwelling branch (e.g. [Wyrtki, 1961, Munk, 1966]). The problem with cold, denser water going down and warm, lighter water going up is that this results in a lowering of the centre-of-mass and hence a release of gravitational potential energy (GPE). This sink of GPE requires an external energy source to sustain it, or else the circulation would slow to a halt with cold, dense water filling the abyss (see, for example, Chapter 5 in [Huang, 2010]).

As discussed in Chapter 1, there are two main upwelling pathways by which dense water can be brought back to the surface: one facilitated by surface winds, and one facilitated by deep diapycnal mixing. For the first pathway, it is the winds that provide the mechanical (kinetic) energy source, drawing deep waters up adiabatically along density surfaces via Ekman suction (e.g. [Toggweiler and Samuels, 1998, Webb and Suginohara, 2001, Wolfe and Cessi, 2011, Marshall and Speer, 2012]). But there is a wider array of mechanical energy sources involved that drive diapycnal mixing, including the winds, tides, and geothermal heating (e.g. [Munk and Wunsch, 1998, Wunsch and Ferrari, 2004]), and possibly marine life (e.g. [Dewar et al., 2006]).

This array of mechanical energy sources then generates internal waves through a variety of mechanisms (see, for example, the review by [Whalen et al., 2020]), including wind-driven near-inertial waves (e.g. [Plueddemann and Farrar, 2006]), internal tides (e.g. [Nycander, 2005]), and lee waves from abyssal flows impinging on topography (e.g. [Wright et al., 2014]). Although the breaking of internal waves provides a significant portion of the energy needed to lift dense waters upwards (e.g [Nikurashin and Ferrari, 2013, Kunze, 2017]), observations reveal that mixing is strongly enhanced above rough bottom topography (e.g. [Polzin et al., 1997, Garabato et al., 2004, Waterhouse et al., 2014]). This last fact is crucial, as bottom-enhanced mixing drives sinking and not upwelling in the stratified ocean interior [Ferrari et al., 2016].

The new paradigmatic view is that diapycnal upwelling of waters does not occur in the interior, but instead is confined to thin, turbulent, boundary layers along sloping bottom topography [Ferrari et al., 2016]. This has led to new studies investigating the influence of topography on the abyssal overturning circulation (e.g. [McDougall and Ferrari, 2017, Mashayek et al., 2017, Holmes et al., 2018, Drake et al., 2022]). These developments are not especially relevant for DDrake, as the configuration has no bottom topography. As such, we limit the discussion to the top 2 km, so the relevant source of diapycnal mixing represented in DDrake is the breaking of internal waves in the ocean interior.

Nevertheless, this new paradigm (that bottom-enhanced diapycnal mixing drives sinking not rising in the interior) does not say anything about the fundamental driver/energy source of the diapycnal mixing. The mechanical energy source is still likely partitioned between the winds and tides, for the most part (e.g. [Munk and Wunsch, 1998, Wunsch and Ferrari, 2004, Kuhlbrodt et al., 2007, Ferrari and Wunsch, 2009]).

However, it is still not settled whether the ocean circulation is essentially a mechanically driven system, and the buoyancy-driven view may be making a comeback. For example, [Saenz et al., 2012] show in an idealised MITgcm configuration that buoyancy forcing and wind forcing each have a positive feedback on the other, so neither forcing can be isolated completely. In relation to GPE, [Butler et al., 2013]

find that surface buoyancy fluxes are a comparable GPE source to diapycnal mixing in HadCM3, while [Zemskova et al., 2015] find that diapycnal mixing contributes negligibly to GPE in ECCO2.

Idealised simulations have revealed that important circulation features such as the ACC [Hogg, 2010] and ocean gyres [Hogg and Gayen, 2020] can be driven by surface buoyancy forcing. It's possible that buoyancy forcing is a comparable driver of the ocean circulation as the winds and tides (see, for example, the recent review by [Gayen and Griffiths, 2022]), a suggestion that has been supported by theoretical energetic arguments (e.g. [Hughes et al., 2009, Tailleux, 2009, Tailleux, 2010]).

So, the current picture surrounding drivers of ocean circulation is nuanced and complex, and we are certainly not going to solve it here. But a useful diagnostic for ocean models was put forward by [Nycander et al., 2007]. They suggest using a stream function in depth-density coordinates as an analysis tool to help identify the driving mechanisms of overturning cells. They show that the integral of this stream function gives the work $W$ performed by the circulation:

$$W = g \int \int \Psi_{\rho' z} \, dz \, d\rho' \tag{3.8}$$

where $g$ is the acceleration due to gravity and $\rho'$ is the density anomaly away from a reference density $\rho_0$. For stationary circulations, they show that $W$ is essentially equivalent to the rate of conversion from potential (GPE) to kinetic energy (KE). This means that if the sign of an overturning cell is *positive*, potential energy is being converted into kinetic energy. The cell is termed 'thermally direct', and could be partly thermally driven and partly mechanically driven. However, if the sign of a cell is *negative*, kinetic energy is being converted into potential energy, and thus work is being performed *on* the fluid. Here, the cell is termed 'thermally indirect' and it is purely mechanically driven.

We thus calculated $M^z_{\sigma_0}$ (using the potential density $\sigma_0$) to find the global $\Psi_{\sigma_0 z}$ overturning for the DDrake control climate. This is shown in figure 3.8a. Comparing with figure 3.5, we again identify the same 'tropical', 'warm', and 'cool' cells as found in the $\Psi_{\theta z}$ overturning (figure 3.8b). We define the tropical cell as all positive values with $\sigma_0 < 24$ kg m$^{-3}$, the cool cell as all positive values with $\sigma_0 > 24$ kg m$^{-3}$,

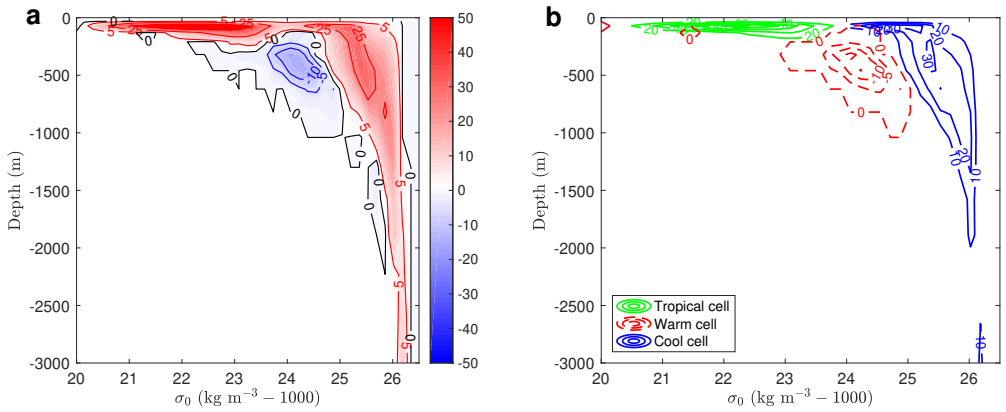



**Figure 3.8:** DDrake control global net overturning circulation in depth-density coordinates, as a function of potential density $\sigma_0$. (a) The net $\Psi_{\sigma_0 z}$ overturning (in Sv) and (b) its decomposition into a warm cell (red dashed, for $\sigma_0 < 25.2$ kg m$^{-3}$), a cool cell (blue solid, for $\sigma_0 > 24$ kg m$^{-3}$), and a tropical cell (green solid, for $\sigma_0 < 24$ kg m$^{-3}$). In panel a, red cells circulate clockwise and blue cells circulate anti-clockwise. In panel b, solid lines denote positive values and circulate clockwise, while dashed lines denote negative values and circulate anti-clockwise.

and the warm cell as all negative values where $\sigma_0 < 25.2$ kg m$^{-3}$ (this last choice eliminates the aforementioned 'deep warm cell' near 2 km depth).

Being negative, the warm cell in figure 3.8b is unambiguously mechanically driven, which supports our previous conclusion that this is a wind-driven inter-gyre circulation in the large basin. Here, wind-driven Ekman pumping pushes light fluid down in the subtropics, and pulls dense fluid up in subpolar latitudes. Such a circulation is put forward as the mean contribution to energy transfer from KE to GPE in the upper ocean in [Ferrari and Wunsch, 2009].

By integrating over each of the cells in figure 3.8b, we find estimates for the work performed (or rate of energy conversion) by each corresponding circulation (equation 3.8). The warm cell performs −38 GW of work i.e. it requires 38 GW of external mechanical forcing in order to sustain it. The tropical cell converts GPE to KE at a rate of 129 GW, and the cool cell at a rate of 250 GW. The total GPE to KE conversion rate (including the 'deep warm cell') is 337 GW. This is significantly larger than what [Nycander et al., 2007] found (94 GW) for the eddy-resolving Ocean Circulation and Climate Advanced Model (OCCAM), but there are too many model differences with DDrake to find a clear reason for this.

We note that the expression for the work performed in equation 3.8 is strictly only correct for the in-situ density and not the potential density, although the choice

of potential density gives a much clearer visualisation of the circulation [Nycander et al., 2007]. Hence, our calculated energy conversion rates for the warm and cool cells may be underestimates and so shouldn't be taken at face value. Nevertheless, their sign tell you whether they are purely or partly mechanically-driven, and their value give a qualitative indication of their relative importance within the global circulation.

## 3.4 Perturbed climate vertical heat balance

We now turn our attention to the change in the vertical heat balance after 200 years due to an abrupt $CO_2$-doubling in the DDrake perturbed climate. The strong increase in net surface heat flux must lead to ocean heat uptake (OHU), but how this heat uptake is partitioned between the various processes is far from obvious. The profiles for the advective and diffusive OHU processes (along with shortwave penetration) for both the DDrake control and perturbed climates are shown in figure 3.9a. The difference between the perturbed and control climates, i.e. the anomalous vertical heat flux, is shown in figure 3.9b.

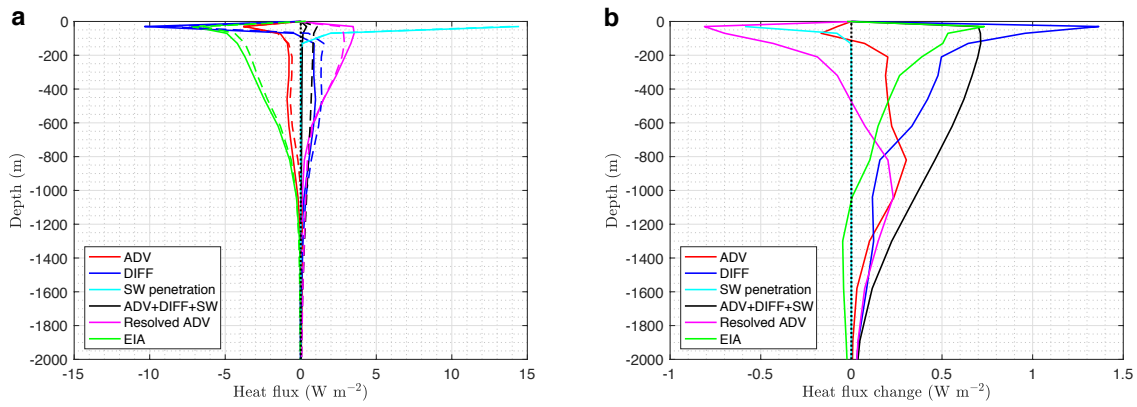



**Figure 3.9:** (a) DDrake control climate (solid lines) and perturbed climate (dashed lines) vertical heat balance for advective (ADV) processes split into resolved and eddy-induced advection (EIA), diffusive (DIFF) processes and shortwave (SW) radiation penetration (in W m$^{-2}$). (b) Change in vertical heat flux due to the $CO_2$-doubling perturbation (difference between the dashed and solid lines in panel a). A downward heat flux is positive. Only the top 2 km are shown.

The anomalous vertical heat fluxes are approximately an order of magnitude smaller than the control climate values, with the total peaking near +0.7 W m$^{-2}$ in the top 200 m (figure 3.9b). They are overwhelmingly positive i.e. downward, as expected,

with the sharpest responses close to the surface. Changes in diffusion (including convective mixing) dominate over most of the water column; only in a slim band near 1 km depth do the advective processes outcompete the diffusive processes.

Interestingly, the resolved advection (magenta line) shows a cooling response in the upper ocean. It changes sign at around 500 m, peaking near 1 km depth. This contribution from the resolved circulation means that the shape of the advective response (red line) is markedly different from the diffusive response (blue line), having an almost flat profile near $+0.25$ W m$^{-2}$ between 200 m and 1 km depth. We now seek to explain the shape of this advective response using the thermal overturning circulations.

### 3.4.1 Changes in ocean circulations and the associated vertical heat transports

#### Thermal overturning responses

Figure 3.10 shows the control climate, perturbed climate, and difference plots for the DDrake global thermal overturning circulation. The $\Delta$-notation in these difference plots refers to a difference between the perturbed and control climate 5-year time-means (200 years apart from each other). The figure shows a clear strengthening of the warm cell, and a weakening of the cool cell. There is also a marked strengthening of the deep warm cell, now near 1.5 km depth (figure 3.10b).

The weakening of the cool cell is not limited to either the small basin or the large basin. The weakening is due to a combination of the small basin MOC weakening (explored further in Chapter 4), and a weakening of the large basin subpolar gyre overturning. The small basin MOC weakening (figure 3.11) is caused by a weakening of the deep convection at high latitudes. This less vigorous convection is due to an increasingly stable stratification due to the amplified warming over polar regions. The weakening of the subpolar gyre overturning in the large basin (figure 3.12) is likely related to a weakening of the polar easterly winds near 60°N.

A plot of the zonally-averaged zonal surface wind stress, and its response throughout the 200 years, is shown in figure 3.14. Each of the curves corresponds to a 50-year

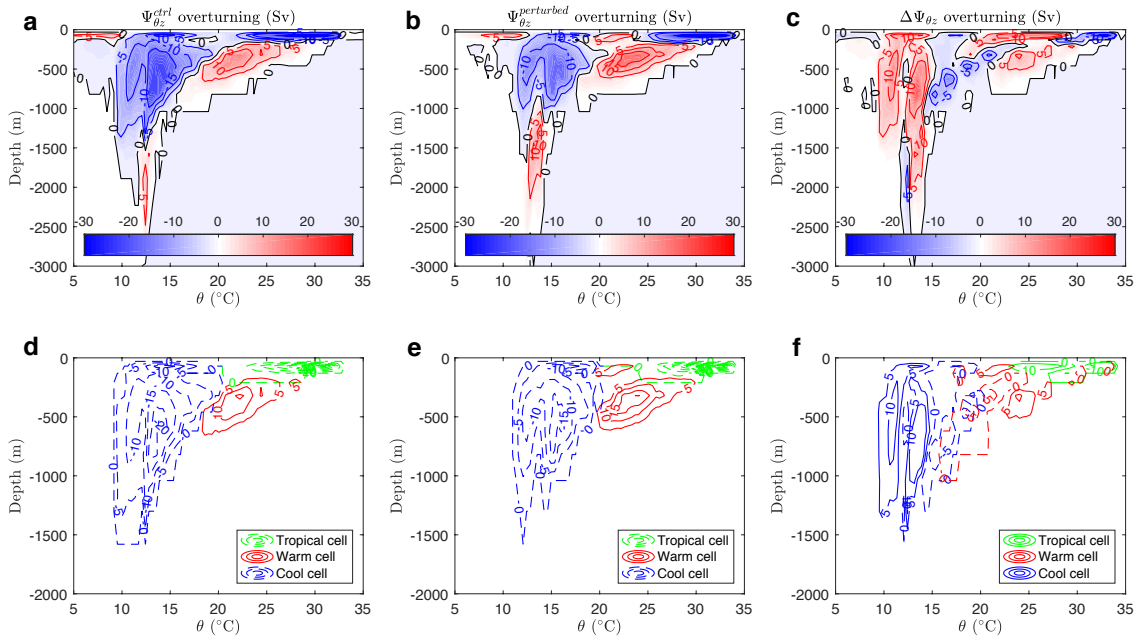



**Figure 3.10:** Response of the DDrake global thermal overturning circulation to an abrupt $CO_2$-doubling (in Sv). Top row: (a) control climate thermal overturning $\Psi_{\theta z}^{ctrl}$, (b) perturbed climate thermal overturning $\Psi_{\theta z}^{perturbed}$, (c) their difference $\Delta\Psi_{\theta z} = \Psi_{\theta z}^{perturbed} - \Psi_{\theta z}^{ctrl}$. Red cells circulate clockwise while blue cells circulate anticlockwise. Bottom row: same as the top row but decomposed into the tropical, warm, and cool thermal overturning cells as defined in the text. Here, solid lines circulate clockwise and dashed lines circulate anticlockwise.

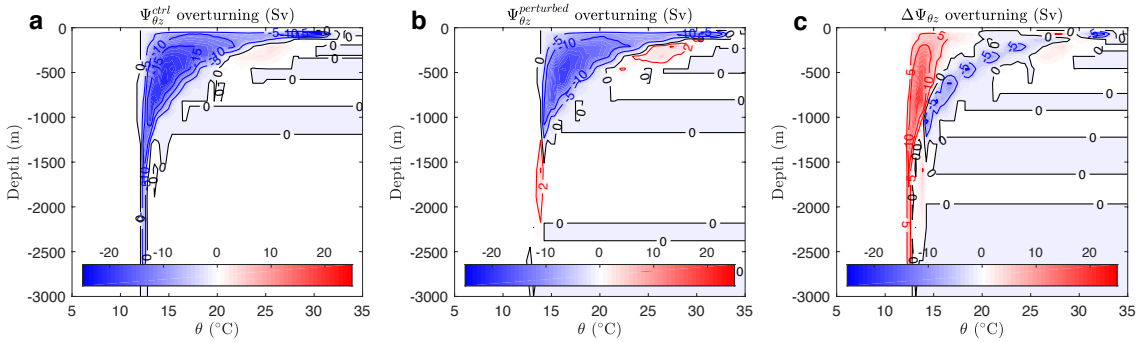



**Figure 3.11:** Small basin thermal overturning circulation response to an abrupt $CO_2$-doubling. (a) control climate thermal overturning $\Psi_{\theta z}^{ctrl}$, (b) perturbed climate thermal overturning $\Psi_{\theta z}^{perturbed}$, (c) their difference $\Delta\Psi_{\theta z} = \Psi_{\theta z}^{perturbed} - \Psi_{\theta z}^{ctrl}$. Red cells circulate clockwise while blue cells circulate anticlockwise.

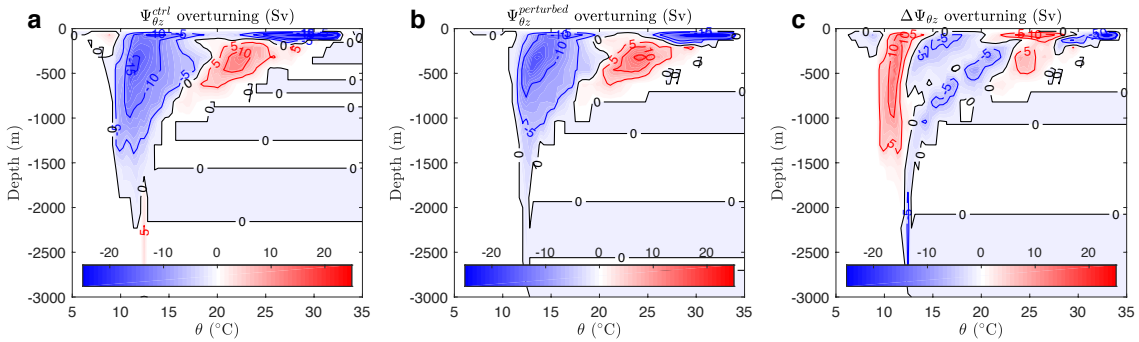



**Figure 3.12:** Large basin thermal overturning circulation response to an abrupt $CO_2$-doubling. (a) control climate thermal overturning $\Psi_{\theta z}^{ctrl}$, (b) perturbed climate thermal overturning $\Psi_{\theta z}^{perturbed}$, (c) their difference $\Delta\Psi_{\theta z} = \Psi_{\theta z}^{perturbed} - \Psi_{\theta z}^{ctrl}$. Red cells circulate clockwise while blue cells circulate anticlockwise.

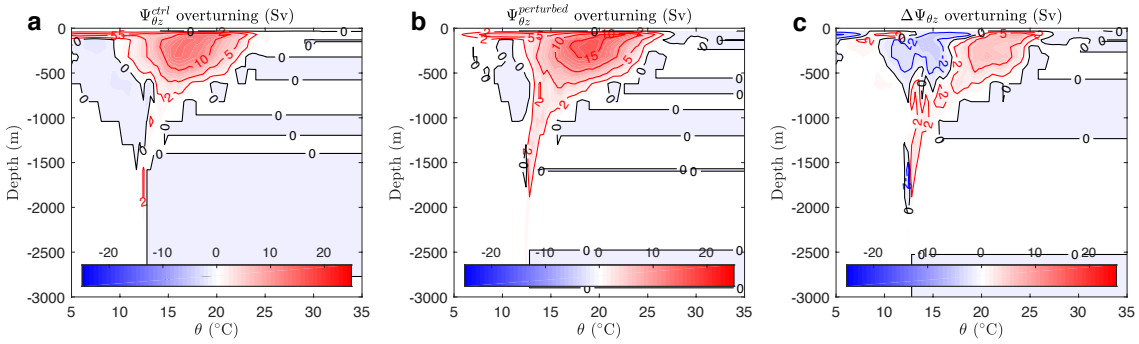



**Figure 3.13:** Southern ocean thermal overturning circulation response to an abrupt $CO_2$-doubling. (a) control climate thermal overturning $\Psi_{\theta z}^{ctrl}$, (b) perturbed climate thermal overturning $\Psi_{\theta z}^{perturbed}$, (c) their difference $\Delta\Psi_{\theta z} = \Psi_{\theta z}^{perturbed} - \Psi_{\theta z}^{ctrl}$. Red cells circulate clockwise while blue cells circulate anticlockwise.

time-mean. The dashed response curves are anomalies away from the control zonal-average, i.e. the black solid curve subtracted from the coloured solid curves. The figure shows that in response to a $CO_2$-doubling, there is a poleward shift and *weakening* of both the midlatitude westerlies and polar easterlies. The positive bulge in the response near 60°N highlights the weaker northern polar easterly. It is our understanding that this weakening signal is responsible for the weakening cool cell in the large basin (figure 3.12).

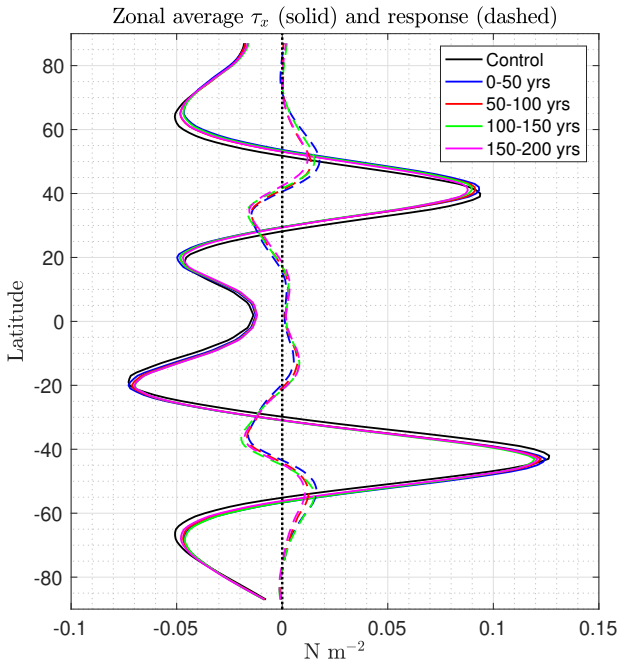



**Figure 3.14:** Zonally-averaged zonal surface wind stress $\tau_x$ (solid lines) and its response to an abrupt $CO_2$-doubling (dashed lines) (in N m$^{-2}$). Solid coloured lines correspond to 50-year time-means throughout the 200 year experiment. Dashed lines are equivalent to the solid coloured lines with the control zonal-average subtracted.

Other coupled climate models show a poleward shift and *strengthening* of the Southern Hemisphere (SH) midlatitude westerlies in response to anthropogenic forcing scenarios (e.g. [Bouttes et al., 2012, Swart and Fyfe, 2012, Goyal et al., 2021]). The SH surface westerly wind-stress response (after 70 years) to a 1% yr$^{-1}$ $CO_2$-increase scenario in CMIP3 and CMIP5 models is $\mathcal{O}(10^{-2})$ N m$^{-2}$ [Swart and Fyfe, 2012] (their figure 4d), which is comparable to the magnitude of the response in DDrake (dashed lines in 3.14). We note, however, that this CMIP3/CMIP5 model response is a strengthening, not a weakening.

The lack of a strengthening surface wind-stress response in DDrake is in contrast to the observed strengthening of the Southern Hemisphere westerlies by ∼20% over the last few decades (e.g. [Thompson and Solomon, 2002, Swart and Fyfe, 2012, Perren et al., 2020]). This strengthening has been attributed to both greenhouse gas (GHG) forcing (e.g. [Kushner et al., 2001]) and ozone depletion (e.g. [Gillett and Thompson, 2003]) in model simulations. Our experiment does not include the effects of ozone depletion, however, and this may be the primary cause of the observed wind changes [Polvani et al., 2011].

The strengthening of the warm cell in figure 3.10e is mostly confined to the large basin (figure 3.12), however there is an appearance of a shallow extension near 200 m depth caused by a strengthening of the southern ocean thermal overturning (figure 3.13). The Ekman pumping velocity $W_{Ek}$ is given by:

$$W_{Ek} = \frac{1}{\rho_0} \operatorname{curl}_z\left(\frac{\tau_{\mathbf{s}}}{f}\right) \tag{3.9}$$

where $\tau_{\mathbf{s}}$ is the wind stress on the ocean surface and $f$ is the Coriolis parameter. The $\operatorname{curl}_z$ operator is defined on a vector $\mathbf{A}$ by $\operatorname{curl}_z \mathbf{A} \equiv \partial_x A_y - \partial_y A_x$. The poleward shift and weakening of the winds in response to the $CO_2$-doubling (figure 3.14) leads to a similar poleward shift and weakening of the Ekman pumping velocities. A plot of the zonally-averaged $W_{Ek}$ and its response is shown in figure 3.15 (The calculation has been omitted for values between 5°S and 5°N where $f$ is close to zero).

Previously, we identified the warm cell circulation with a wind-driven inter-gyre circulation in the large basin, where warmer subtropical water downwells near 40°N, cools, and subsequently upwells near 50°N (see figures 3.3d and 3.5d). From figure 3.15, we find that the Ekman pumping response serves to reinforce this circulation. There is a strengthening of approximately $-8$ m yr$^{-1}$ in the downwelling $W_{Ek}$ near 40°N, and there is a modest strengthening of the upwelling $W_{Ek}$ near 50°N of ∼3 m yr$^{-1}$. Both these signals support a strengthening of the warm cell circulation as seen in figure 3.10e.

The poleward shift of the Southern Hemisphere winds also leads to a modest strengthening of the southern ocean overturning circulation in the top 1 km. This results in a strengthening of the southern ocean's thermal overturning, seen in figure 3.13b. It

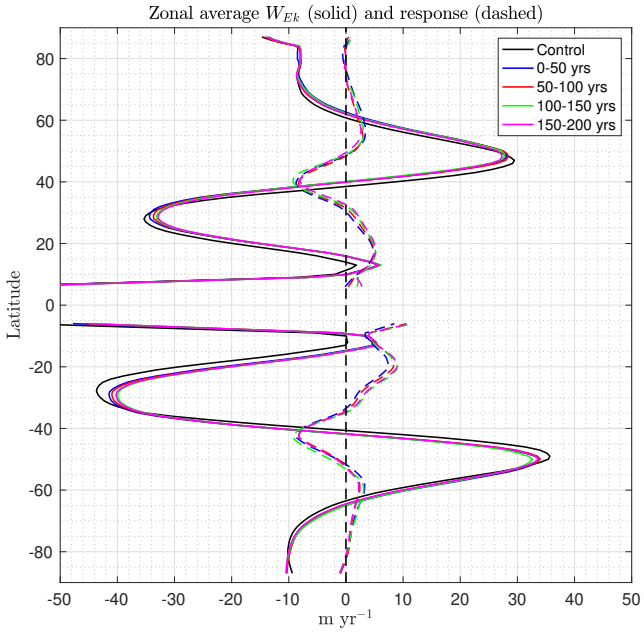



**Figure 3.15:** Zonally-averaged Ekman pumping velocity $W_{Ek}$ (solid lines) and its response to an abrupt $CO_2$-doubling (dashed lines) (in m yr$^{-1}$). Solid coloured lines correspond to 50-year time-means throughout the 200 year experiment. Dashed lines are equivalent to the solid coloured lines with the control zonal-average subtracted.

is this strengthening in the southern ocean that is responsible for the shallow warm cell extension near 200 m depth, as seen in figure 3.10e.

The relationship between the winds and the Southern Ocean MOC has been studied extensively in models (e.g. [Saenko et al., 2005, Abernathey et al., 2011, Gent, 2016]). The general current understanding is that the resolved (or mean) MOC strength increases linearly with the maximum of the Southern Hemisphere zonal surface wind stress (e.g. [Nikurashin and Vallis, 2012]). There might also be a dependence on the bottom drag, as it was found by [Marshall et al., 2017] that an increase in the bottom friction leads to an increase in the ACC transport. Although, this assumes that the Southern Ocean MOC and ACC transport are closely dynamically linked, which may not be the case (e.g. [Morrison and Hogg, 2013]).

More importantly, however, is that an increase in the Southern Hemisphere winds also leads to an increase in the eddy-induced MOC (e.g. [Viebahn and Eden, 2010, Abernathey et al., 2011]). The eddy-induced MOC compensates the increase in the resolved MOC, and the degree of compensation varies among models (e.g. [Downes

and Hogg, 2013]). This 'eddy compensation' effect means that the overall increase in overturning strength is reduced. Nevertheless, it is expected that the net Southern Ocean MOC will intensify in response to an intensification of the winds.

The relationship between this strengthening of the Southern Ocean MOC and vertical heat transport is less clear, however. In the study by [Nycander et al., 2007], they found that only with non-zero wind forcing was there significant downward vertical heat transport in an idealised model using the MITgcm. A similar result was found by [Zika et al., 2013], where they varied the wind stress south of 30°S in UVic ESM. The downward vertical heat transport increased almost linearly with the strength of the wind forcing. The implication here is that an increase in the wind forcing leads to a more vigorous Southern Ocean MOC, which in turn leads to stronger downward vertical heat transport.

However, DDrake lacks a representation of an abyssal cell associated with AABW formation. Such a cell might weaken with increased wind forcing (e.g. [Nikurashin and Vallis, 2012]), and this could additionally contribute to a downward vertical heat transport, as the abyssal cell has been found to be thermally direct in other models (e.g. [Zika et al., 2013, Zika et al., 2015, Saenko et al., 2018]).

We observe intensified warm cells in both the southern ocean and large basin of DDrake (figures 3.12b and 3.13b), however, this is not due to a significant increase in the wind forcing (figure 3.14). The key driver is really a change in the curl of the surface wind stress (equation 3.9), leading to changes in the Ekman pumping velocities that reinforce the downwelling and upwelling branches of the cell circulations (figure 3.15). We should note that as our simulation keeps $\kappa_{GM}$ a constant, we cannot capture the effects of eddy compensation (e.g. [Gent, 2016]), so the response of the DDrake warm cells to the surface winds is likely exaggerated.

The southern ocean strengthening in figure 3.13b also provides us with one clue for the deep warm cell near 1.5 km depth, seen most prominently in figure 3.10b. A similar deep warm cell strengthening is seen in the small basin (figure 3.11b), so we are led to believe that the deep warm cell must be associated with a deep SB/SO exchange, associated with the deep SBMOC. But it is unclear what the physical structure of this circulation might be.

The Ekman pumping response (figure 3.15) also supports our previous conclusion that part of the weakening cool cell response is wind-driven. Before, we pointed to the weakening polar easterly near 60°N in figure 3.14. In figure 3.15, the changing pattern of the high-latitude surface winds contributes to an upwelling $W_{Ek}$ response poleward of 60°N. This increase in high-latitude upwelling damps the downwelling of polar waters in the large basin, leading to a weakening of the cool cell.

Notably, the overall $\Psi_{\theta z}$ structure remains remarkably resilient to the $CO_2$-doubling perturbation (figure 3.10). This is especially clear when comparing the three-cell decompositions in panels d and e. However, there is a translational shift of ∼1-2°C to the right in panel e, owing to the wholesale warming of the ocean. This shift makes the $\Delta\Psi_{\theta z}$ structure more difficult to interpret. In the difference plot in panel f, solid lines denote a clockwise response and dashed lines denote an anticlockwise response. The cool and warm cells are 'cut in half' by opposing clockwise/anticlockwise responses, owing to this shift. Rather than attempting to explain this difference plot in panel f (and in panel c), it may be easier to explain the vertical heat transport (VHT) responses resulting from this change in the thermal overturning. This should serve as an explanation of the total advective VHT response as plotted in figure 3.9b.

### Vertical heat transport responses

We now investigate the advective VHT responses resulting from the changes in thermal overturning for the tropical, warm, and cool cells (equation 3.7). The control climate VHT profiles were explored in section 3.3.2. These profiles are plotted again in figure 3.16a (solid lines) alongside the perturbed climate profiles (dashed lines). Figure 3.16b shows the difference between the perturbed and control climate VHT profiles, i.e. the VHT responses.

The total VHT response is downward, as expected, peaking at +0.45 W $m^{-2}$ at 200 m depth (the average forcing at the ocean surface is 4.44 W $m^{-2}$ (Chapter 5)). This sharp peak is absent in the model-outputted advective response in figure 3.9b. But we should not expect these two profiles to match, owing to discrepancies between the two calculations, as shown in figure 3.2. Nevertheless, the values in figure 3.16b are of the correct size, and the net global shape below 500 m depth is well-captured.

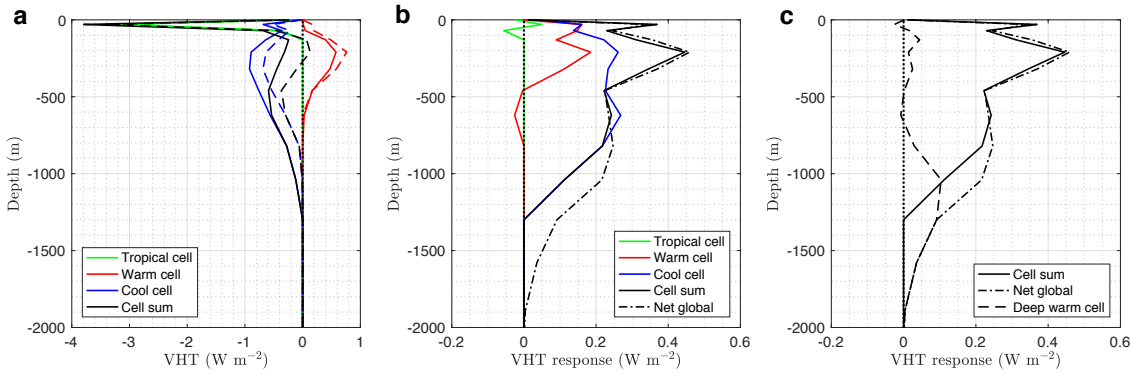



**Figure 3.16:** Changes in vertical heat transports (VHTs) carried by the tropical, warm, and cool cells of the DDrake thermal overturning circulation. Positive = downward. (a) Control climate (solid lines) and perturbed climate (dashed lines) VHT profiles. (b) VHT responses due to the $CO_2$-doubling. The black dash-dotted line is the net global advective VHT response. The net global response takes into account circulations not included in the three-cell decomposition of the thermal overturning. (c) Comparison of the three-cell sum and net global VHT responses. Their difference (black dashed) is attributed to the deep warm cell.

We find that the cool cell dominates the VHT response in the top 1 km, peaking near +0.25 W m$^{-2}$ through 250-750 m depth. The warm cell response supplies an additional $\sim$ +0.1 W m$^{-2}$ in the top 500 m. These increases in downward VHT are due to a weakening of the cool cell (transporting less heat upwards) and a strengthening of the warm cell (transporting more heat downwards), as explored in the previous section. Changes in the tropical cell overturning are unimportant for the VHT response. In [Zika et al., 2015], using $\Psi_{\theta z}$ for CCSM4, they found that their 'cold cell' collapsed while their 'warm cell' strengthened in a global warming scenario. This is a similar response to the cool and warm cells in DDrake; both cell responses contribute to an increase in downward VHT. There is no compensation here. This is bad news for fish, as it suggests that changes in ocean circulation will enable even more warming of the ocean.

We have plotted both the cell sum and the net global VHT responses in figure 3.16b. The net global response (black dash-dotted) takes into account circulations not captured by our chosen three-cell decomposition of the DDrake net global $\Psi_{\theta z}$. This was not a problem for the control climate VHT profiles (see figure 3.1), however, a strengthening of the deep warm cell now leads to a discrepancy between the two black curves. This discrepancy is plotted in figure 3.16c as the black dashed curve, which we attribute to the deep warm cell. As noted in the previous section, we suspect that the deep warm cell is related to the deep interhemispheric overturning

linking the small basin and southern ocean (see figures 3.11b and 3.13b). Thus, our chosen three-cell decomposition neglects this deep circulation, and we miss an additional $\sim$0.1 W m$^{-2}$ of downward VHT below 1 km depth.

A plot of changes in only the peak (positive or negative) VHT for each of the thermal overturning cells is shown in figure 3.17. Panel a reiterates that the response is positive (downwards) for all three cells. The percentage changes relative to the control climate values in panel b are more revealing. The plot shows that the largest proportional response comes from the warm cell, whose peak (downward) VHT increases by 32%. This is followed not too far behind by the cool cell, whose peak (upward) VHT decreases by 25%. Again, the change in VHT due to the tropical cell is negligible.

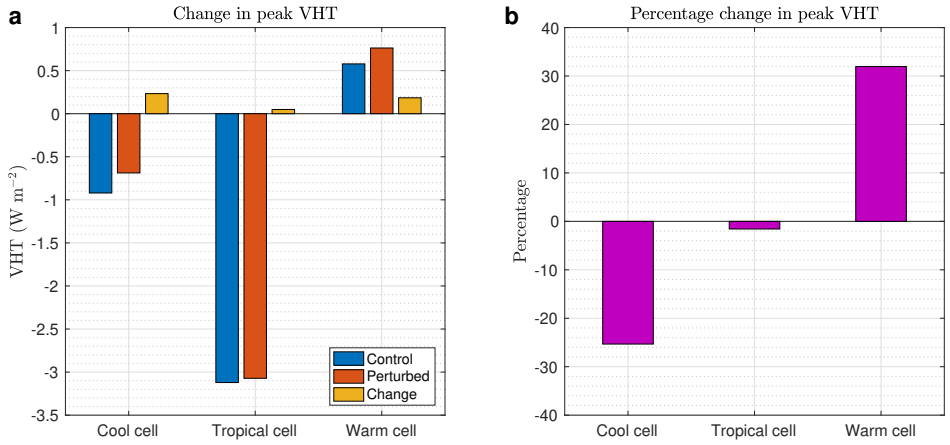



**Figure 3.17:** Changes in the peak (positive or negative) VHT carried by the tropical, warm, and cool cells of the DDrake thermal overturning, in response to the $CO_2$-doubling. (a) Control and perturbed climate values, and their difference (in W m$^{-2}$), (b) percentage changes.

### 3.4.2 Changes in energetics

Before concluding, we take a brief look at the changes in work performed by the DDrake ocean circulation, using the overturning in potential density space, as introduced in section 3.3.3. There, we linked the tropical, warm, and cool cells of $\Psi_{\theta z}$ to similar features in $\Psi_{\sigma_0 z}$ (figure 3.8). Here, we integrate over each of these cells in both the control and perturbed climates to find the work performed by these circulation features (equation 3.8). These are shown in figure 3.18.

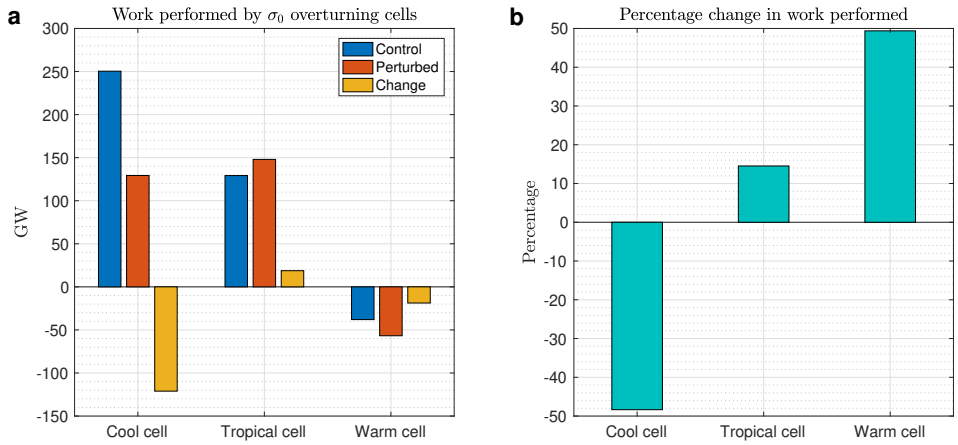



**Figure 3.18:** Changes in the work performed by the tropical, warm, and cool cells of the DDrake thermal overturning, in response to the $CO_2$-doubling (using equation 3.8 with $\Psi_{\sigma_0 z}$). (a) Control and perturbed climate values, and their difference (in GW), (b) percentage changes.

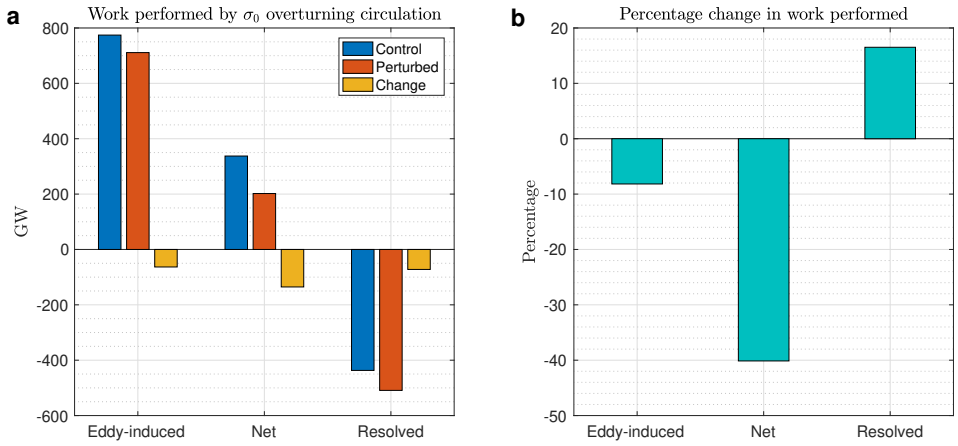



**Figure 3.19:** Changes in the work performed by the global resolved and eddy-induced circulations, and their sum (net circulation), in response to a $CO_2$-doubling (using equation 3.8 with $\Psi_{\sigma_0 z}$). (a) Control and perturbed climate values, and their difference (in GW), (b) percentage changes.

There is a 48% decrease in the work performed by the cool cell as a result of the $CO_2$-doubling. This means much less gravitational potential energy (GPE) is being converted into kinetic energy (KE), which reflects the weakening of the (mostly buoyancy-driven) small basin MOC. However, there is a commensurate 49% increase in the (negative) work performed by the warm cell. This means more kinetic energy is being converted into potential energy, which is supplied by the winds. This is consistent with our use of the surface winds in explaining the strengthening of the warm cell. There is a modest increase of almost 15% in the work performed by the tropical cell, which may reflect the pattern of surface buoyancy forcing, with greater warming at the equator than in the subtropics.

Again, the analysis in [Nycander et al., 2007] and equation 3.8 are only formally correct for the in-situ density, not the potential density. So, the precise values for the work performed in the control and perturbed climates may be underestimates. Nevertheless, this underestimation cancels out when viewing the *changes* in the work performed, so the most meaningful values in figures 3.18 and 3.19 are these changes.

We performed the same calculation for the global $\Psi_{\sigma_0 z}$ overturning, decomposed into resolved and eddy-induced components. This is shown in figure 3.19. This plot reveals an important difference between the resolved and eddy-induced circulations. Resolved circulations perform *negative* work, eddy-induced circulations perform *positive* work. While resolved circulations convert KE into GPE, eddy-induced circulations counteract this by converting GPE into KE (this is expected, as the Gent-McWilliams parameterisation explicitly serves to flatten isopycnal surfaces).

In response to the $CO_2$-doubling, there is a weakening of the eddy-induced circulation ($-8\%$), and a strengthening of the resolved circulation ($+17\%$). Perhaps most interesting is that both these changes result in a much more substantial weakening of the net circulation ($-40\%$). Figure 3.19 provides a definitive answer to the question: "Does the DDrake ocean circulation weaken in response to a $CO_2$-doubling?" The answer is yes. So, despite weakening by 40%, the circulation response still leads to an increase in downward VHT by $\sim$0.2 W m$^{-2}$ in the top 1 km (figure 3.16).

Note, however, that it is still unclear whether the real-world ocean circulation will weaken or strengthen with global warming. Many modelling studies (e.g. [Gregory

et al., 2005, Weaver et al., 2012, Weijer et al., 2020]) and observational studies (e.g. [Caesar et al., 2018, Rahmstorf et al., 2015, Smeed et al., 2018]) point to a weakening of the AMOC (with an implied concomitant weakening of the global ocean circulation). Recent observations, however, reveal a wholesale strengthening of the global ocean circulation since 1990, accompanied by an increase in the global-mean sea-surface wind speed [Hu et al., 2020]. The authors in [Hu et al., 2020] also note that the CMIP5 ensemble mean sea-surface wind speed displays a significant increasing trend in the RCP8.5 scenario, indicating that ocean circulation may also increase commensurately with $CO_2$ emissions. A follow-up study, however, finds that surface warming, not the winds, is the main driver of intensified currents in the upper 200 m in an abrupt $4\times CO_2$ experiment [Peng et al., 2022].

## 3.5 Conclusion

### 3.5.1 Summary

In this chapter, we have examined the advective vertical heat transport response of the top 2 km of the global DDrake ocean circulation using the thermal overturning stream function $\Psi_{\theta z}$. We decomposed the global thermal overturning into particular circulation features — a warm cell, a cool cell, and a tropical cell — and connected these with physical processes and circulations in geographical coordinates. We found that, in response to a $CO_2$-doubling, the warm cell strengthens and the cool cell weakens (the tropical cell response is negligible) (figure 3.10). Both these responses increase the downward vertical heat transport, enabling greater warming of the ocean interior (figure 3.16).

The warm cell circulation is identified with a wind-driven, subtropical-subpolar inter-gyre circulation in the large basin (figure 3.3d), and its strengthening is linked to changing patterns in the surface winds. The surface wind response reinforces the downwelling and upwelling regions of this overturning cell via changes in Ekman pumping (figure 3.15). The cool cell is identified partly with a wind-driven circulation in the large basin, and partly with a buoyancy-driven circulation in the small basin. The wind-driven circulation is a subpolar gyre overturning (figure 3.3d),

whose weakening is associated with damped Ekman pumping at high latitudes (figure 3.15). The buoyancy-driven circulation is the deep small basin MOC (figure 3.3c), whose weakening is due to reduced deep convection at northern high latitudes resulting from amplified polar warming (see Chapter 4).

### 3.5.2 Discussion and Conclusions

The DDrake warm and cool cells have similar-sized VHT responses (figure 3.17), which suggests that both wind- and buoyancy-driven circulation changes are of comparable importance in transient climate change. However, there is a robust weakening of the net global circulation in response to the $CO_2$-doubling (figure 3.19), which is largely due to the weakening of the (buoyancy-driven) small basin MOC (figure 3.11).

This weakening of the small basin MOC is similar to the weakening AMOC response seen in models (e.g. [Gregory et al., 2005, Weaver et al., 2012, Cheng et al., 2013, Weijer et al., 2020]), proxy observations (e.g. [Rahmstorf et al., 2015, Caesar et al., 2018, Zhu and Liu, 2020, Caesar et al., 2021]), and possibly direct observations (e.g. [Smeed et al., 2018]). As the small basin MOC in DDrake is thermally direct, the weakening contributes to an increase in downward VHT. This is in contrast to other models, where a thermal overturning cell coincident with the AMOC has been found to be thermally *indirect* (e.g. [Zika et al., 2013, Zika et al., 2015, Saenko et al., 2018, Savita et al., 2021]).

The VHT response also depends on the temperature structure, however, and not just the strength of the circulation in geographical coordinates [Shatwell et al., 2020], so it is not obvious that a weakening circulation would result in a weakening VHT (upwards or downwards). It would be valuable to link the AMOC weakening and thermal overturning responses in other models. Following the spirit of the AMOC observing arrays RAPID [McCarthy et al., 2015] and SAMBA [Meinen et al., 2018] in both hemispheres, a greater observational focus on the downwelling and upwelling branches of the AMOC would also help answer the question of whether the circulation is thermally direct or indirect.

In CMIP5 historical simulations, the Southern Ocean takes up as much as 75% of

the global ocean heat gain [Frölicher et al., 2015]. This is partly associated with a wind-driven upwelling of cold deep water, which delays the surface warming response [Armour et al., 2016]. The relatively cool sea-surface temperature (SST) enables a large amount of excess heat to be taken up from the atmosphere, which is then advected northward and downward by the MOC. A strengthening of the Southern Ocean overturning and its associated thermal overturning (as seen in figure 3.13b) could possibly further secure the Southern Ocean's dominance in global OHU. However, recent considerations of the projected relative changes in GHG and, particularly, *aerosol* forcings reveal that the Southern Ocean's importance may decrease substantially in the future, with the North Atlantic becoming a comparable player in global OHU [Shi et al., 2018].

However, we should be careful about making any strong inferences from DDrake about the North Atlantic or Southern Ocean circulation (and hence VHT) responses. DDrake lacks a realistic representation of diapycnal mixing, especially its bottom-enhancement, as seen in many observations (e.g. [Polzin et al., 1997, Garabato et al., 2004, Waterhouse et al., 2014]). Although we have focussed on advective transports, the magnitude and profile of diapycnal mixing can affect the strength and structure of the MOC (e.g. [Saenko and Merryfield, 2005, Ito and Marshall, 2008, Nikurashin and Vallis, 2011, Mashayek et al., 2015]), which has implications for the thermal overturning.

Admittedly, diapycnal mixing is more important for the abyssal circulation or Lower Cell of the MOC, which DDrake does not realistically represent. So, we have limited the discussion to the top 2 km, relevant to the Upper Cell of the MOC. But this does not completely solve the issue, as the Upper and Lower Cells are connected, and the strength of their coupling through interbasin transports is a topic of ongoing research (e.g. [Talley, 2013, Thompson et al., 2016, Ferrari et al., 2017, Newsom and Thompson, 2018, Johnson et al., 2019]).

In addition, the depth of the DDrake ocean is only 3 km, so we cannot address the deep ocean's role in the heat budget. This is not a major issue, as warming below 2 km is mainly due to warming of AABW (e.g. [Purkey and Johnson, 2013]), which DDrake does not represent, and the contribution to global OHU below 2 km is

probably only ∼10% (e.g. [Desbruyères et al., 2016, Meyssignac et al., 2019]). The ocean below 2 km also responds on a multi-centennial to millennial timescale (e.g. [Yang and Zhu, 2011, Li et al., 2013]), so our 200 year $CO_2$-doubling simulation is not long enough to capture the deep response. Nevertheless, the ocean below 2 km would become more relevant at longer timescales, and so the relevance of DDrake would become increasingly tenuous.

These caveats aside, our results demonstrate that the thermal overturning circulation $\Psi_{\theta z}$ is a powerful model diagnostic for analysing both circulation and VHT responses in transient climate change. Particularly, when addressed regionally (figure 3.6), and in comparison with the geographical overturning (figure 3.3), thermal overturning cells can be linked to physical circulations. The overturning in depth-density coordinates (figure 3.8) can then also indicate the driving mechanisms for these physical circulations [Nycander et al., 2007].

Our calculation of $\Psi_{\theta z}$ incorporates the resolved and parameterised eddy advection terms, capturing the residual circulation. A new diagnostic, called the 'super residual circulation' (SRC), was recently put forward by [Savita et al., 2021] incorporating subgridscale isopycnal mixing due to mesoscale eddies i.e. 'residual circulation + isopycnal mixing'. Previous studies find that the residual circulation transports heat downward overall (e.g. [Kuhlbrodt et al., 2015, Griffies et al., 2015]). Adding the effect of isopycnal mixing leads to the SRC transporting heat *upward* overall [Savita et al., 2021] (although the residual circulation in DDrake already transports heat upward overall, (figure 3.1)).

The study of [Savita et al., 2021] combines efforts from [Dias et al., 2020a] by extending the concept of 'super residual transport' (originally suggested by [Kuhlbrodt et al., 2015]), and from [Holmes et al., 2019] by combining the residual circulation with the effects of local temperature tendencies to construct a 'diathermal' circulation (crossing temperature surfaces).

The SRC has the advantage that it allows models with different grid resolutions and eddy process parameterisations to be compared in a consistent framework. A high-resolution model (say, 1/12°) might not need parameterisations for eddy advection or isopycnal mixing. For such a model, the residual and resolved circulations are

equivalent, and the residual circulation implicitly contains effects due to isopycnal mixing. As such, comparing this model's residual circulation with a lower-resolution model's that *does* parameterise isopycnal mixing is problematic, as pointed out in [Kuhlbrodt et al., 2015]. Whereas, comparing these two models' SRCs would be more consistent.

We have not considered such intricacies for the DDrake (residual) thermal overturning, so a direct comparison with the thermal overturning circulations in other models (e.g. [Zika et al., 2013, Zika et al., 2015, Saenko et al., 2018]) may not be especially meaningful. We encourage efforts like [Savita et al., 2021] to enable more meaningful model intercomparison, and for researchers to compute thermal overturning diagnostics for a greater range of coupled climate models in order to gain a better understanding of the structure and response of the global ocean circulation under continued global warming.

### 3.5.3 Key points

1. Overturning stream functions in thermodynamic coordinates can be used to decompose the global ocean overturning into particular circulation features, defined by whether they pump heat downward (warm cell) or upward (cool cell).

2. In response to an abrupt $CO_2$-doubling in DDrake, the warm cell strengthens and the cool cell weakens, resulting in an *increase* in the downward advective vertical heat transport of $\sim$0.2 W m$^{-2}$ in the top 2 km. The circulation response does not 'resist' the warming.

3. The warm cell strengthening is linked to changes in the surface winds, while the cool cell weakening is linked to both changes in surface winds and surface buoyancy forcing.

*"I perceive I have not really understood any thing, not a single object, and that no man ever can,*
*Nature here in sight of the sea taking advantage of me to dart upon me and sting me,*
*Because I have dared to open my mouth to sing at all."*
*From As I Ebb'd with the Ocean of Life*

Walt Whitman, 1860

# 4

# Ocean heat storage response to an AMOC slowdown

In this chapter*, we use the DDrake model to explore the role of the Atlantic meridional overturning circulation (AMOC) in transient climate change, likening the small basin MOC (SBMOC) to the AMOC. We introduce the concept of a heat storage contrast: the difference between the small and large basins' heat storage rates. Over the simulated 200 years following the $CO_2$-doubling, we find that the small basin stores heat at a faster rate than the large basin by $0.6 \pm 0.2$ W m$^{-2}$. We argue that this is due to the SBMOC. However, we also find that as the SBMOC weakens significantly, it has little impact on the heat storage contrast. We suggest this is due to the effects of compensating warming patterns and interbasin heat transports. Thus, although the presence of the SBMOC is important for the small basin's enhanced heat storage, the SBMOC weakening is surprisingly unimportant.

*Note this chapter is an adapted and extended version of an article originally published in *Geophysical Research Letters* [Shatwell et al., 2020]. This work has been reviewed by Martha Buckley, Yavor Kostov, an anonymous reviewer, and GRL editor Kathleen Donohue.

## 4.1 Introduction

The AMOC plays a central role in global climate. It is an important conduit in sequestering anthropogenic heat into the ocean interior (e.g. [Chen and Tung, 2014, Kostov et al., 2014]), and its interhemispheric reach is responsible for a northward meridional heat transport in both hemispheres (e.g. [Trenberth and Caron, 2001]). This latter feature results in a global non-zero cross-equatorial heat transport ($\sim$0.5 PW), contributing to the Northern Hemisphere being slightly warmer (by $\sim$2°C) than the Southern Hemisphere [Marshall et al., 2014b].

The AMOC's role in global climate is especially interesting due to the possibility of it weakening in the future. A weakening response of the AMOC with global surface warming is seen across coupled climate models (e.g. [Weaver et al., 2012, Cheng et al., 2013, Weijer et al., 2020]), and indirect proxy observations point to the AMOC having weakened since the mid-twentieth century (e.g. [Caesar et al., 2018, Zhu and Liu, 2020]), with one study suggesting that the AMOC is in its weakest state in over a thousand years [Caesar et al., 2021]. Model biases may favour a stable AMOC, and it is still a concern that the AMOC could collapse in the future, leading to abrupt changes in global climate (e.g. [Liu et al., 2017, Caesar et al., 2018]).

A shutdown of the AMOC could potentially lead to a colder Northern Hemisphere with more extensive Arctic sea-ice [Vellinga and Wood, 2008], an equatorward shift of the ITCZ [Stouffer et al., 2006], and significantly colder winters in Europe [Liu et al., 2017]. Large-scale reorganisations and transitions between different AMOC states have previously been invoked to explain past abrupt paleoclimatic shifts (e.g. [Broecker, 1997, Alley and Clark, 1999]).

The basis for the concern of an AMOC collapse is the potential existence of these different stable AMOC states, in particular, the possibility that the AMOC is bistable with 'on' and 'off' states. Such bistable behaviour originates from Stommel's early work with an idealised two-box model [Stommel, 1961]. Bistable behaviour has subsequently been found in a range of other idealised climate models (e.g. [Manabe and Stouffer, 1988, Rahmstorf, 1995, Johnson et al., 2007]). The presence of multiple equilibria depends critically on the existence of a destabilising salt advection feed-

back, whereby, if the AMOC were to weaken, less salt would be transported to the North Atlantic, encouraging further weakening and so on (e.g. [Rahmstorf, 1996]).

Although multiple equilibrium climate states have been found in very similar modelling set-ups to the DDrake configuration [Ferreira et al., 2011, Ferreira et al., 2018b], the states are not caused by bistability of the overturning circulation, but instead by an ice-albedo feedback modified by meridional ocean heat transport [Ferreira et al., 2018b]. As such, we are not concerned with a complete collapse of the overturning circulation in DDrake, but we are still interested in a substantial weakening of the circulation. A weakening of the AMOC is still projected over the 21st century (e.g. [Kirtman et al., 2013]). For example, CMIP6 models project an AMOC decline of 34-45% by 2100 [Weijer et al., 2020], although the true strength of the future decline is highly uncertain (e.g. [Reintges et al., 2017]). It is also uncertain what effect this will have on ocean heat storage and surface climate in the future (e.g. [Bellomo et al., 2021]).

As discussed in Chapter 1, a weakening of the AMOC is expected as a result of positive buoyancy forcing in the northern high latitudes from a combination of positive heat and freshwater fluxes. Anomalous heat fluxes are largely the result of Arctic amplification — enhanced surface warming in the Arctic relative to the rest of the world (e.g. [Cohen et al., 2014]). Multiple closely related processes are responsible for Arctic amplification, such as changes in atmospheric and oceanic heat transports, sea-ice extent, cloud cover, water vapour, and black carbon aerosols (e.g. [Serreze and Barry, 2011, Previdi et al., 2021]).

However, it's been argued that Arctic sea-ice loss is the dominant contributor to Arctic amplification [Dai et al., 2019]. The key mechanism put forward is an increase in absorbed solar radiation over larger ice-free ocean regions from May to September, and a subsequent release to the atmosphere from October to April (through outgoing longwave radiation, latent, and sensible heat fluxes) [Serreze and Barry, 2011]. The warmer atmosphere will then radiate more strongly back to the surface.

Arctic sea-ice loss also increases the freshwater flux, further contributing to a weakening of the AMOC (e.g. [Jahn and Holland, 2013, Sévellec et al., 2017]). Freshwater fluxes from melting of the Greenland Ice Sheet (e.g. [Lenaerts et al., 2015, Van den

Broeke et al., 2016]) and increased high-latitude precipitation and river runoff (e.g. [Stouffer et al., 2006]) also play a role.

Both the anomalous heat and freshwater fluxes act to reduce the surface density in the North Atlantic, although the relative importance of each type of flux still remains to be determined (e.g. [Kostov et al., 2019, Haskins et al., 2020]). The reduction in surface density suppresses deep convection at the sites of NADW formation, leading to a commensurate reduction in the AMOC strength (e.g. [Thornalley et al., 2018]), and also reduces the meridional density gradient, which is thought to scale with the AMOC strength (e.g. [Stommel, 1961, Griesel and Maqueda, 2006, Gregory and Tailleux, 2011, Ragen et al., 2022]).

The depth and strength of the AMOC positively correlates with the depth of global ocean heat storage (OHS) across CMIP5 models [Kostov et al., 2014]. Multidecadal variability of the AMOC has been linked to periods of enhanced global surface warming and cooling [Chen and Tung, 2018]. It is possible that the presence of the AMOC gives the Atlantic its enhanced heat storage rate compared to the Pacific, as seen in observations (e.g. [Chen and Tung, 2014, Desbruyeres et al., 2017, Zanna et al., 2019, Johnson and Lyman, 2020]).

A weakening AMOC results in a weakening of the northward oceanic meridional heat transport (MHT), which may explain the conspicuous region of cooling ('warming hole') in the subpolar North Atlantic found in observational maps of temperature trends (e.g. [Rahmstorf et al., 2015]) and model projections (e.g. [Gervais et al., 2018]). It has been suggested that this North Atlantic surface cooling reduces the annual-mean sea-air temperature difference, and so reduces the sensible heat flux from the ocean to the atmosphere, leading to an increase in OHU (e.g. [Winton et al., 2013, Drijfhout et al., 2014]). It should be emphasised that the OHU and OHS responses are distinct in this context. Here, a *local increase* in OHU could possibly be accompanied by a *global decrease* in OHS, even though both responses are associated with a weaker AMOC.

Recent work [Saenko et al., 2018] has cast doubt on the observed model correlation between AMOC strength and heat storage [Kostov et al., 2014], suggesting that the eddy parameterisation affects both AMOC strength and global OHU efficiency,

thus causing a spurious correlation between the two quantities. But without a better conceptual grasp on how the AMOC affects OHS, it is unclear whether this correlation is spurious or not. Furthermore, these studies [Kostov et al., 2014, Saenko et al., 2018] establish a link between the AMOC and *global* OHS, while it may be easier to first consider the AMOC's influence on heat storage within the Atlantic basin itself. Given the importance of constraining and monitoring Earth's energy imbalance through OHC observations (e.g. [Von Schuckmann et al., 2016]), and the possibility that the AMOC may continue to weaken into the future, it is imperative to better understand the AMOC's role in ocean heat uptake and storage as the world continues to warm.

To this end, we examine the ocean response of DDrake over 200 years, after an abrupt doubling of atmospheric $CO_2$. We first define the overturning circulation in section 4.2. The small basin exhibits an overturning circulation akin to the AMOC, while the large basin does not. We look at the basins' individual responses, and suggest isolating the effect of the small basin MOC by focusing on small–large basin differences. In section 4.3, we present results where we find and define a heat storage contrast between the small and large basins. We explore the role of the small basin's MOC (SBMOC) in establishing this contrast, particularly its time-evolution as the SBMOC weakens. We also present preliminary results from four CMIP5 models demonstrating the existence of a heat storage contrast between the Atlantic and Pacific basins in abrupt $CO_2$-quadrupling experiments, which parallels the contrast between our model's small and large basins. Conclusions are presented in section 4.4.

## 4.2 Control climate overturning circulations

In this chapter, an overturning stream function is defined as the zonally-integrated meridional volume transport:

$$\Psi(y,z) = \frac{1}{\Delta t}\int_{t}^{t+\Delta t}\int_{z}^{0}\int_{x_W}^{x_E} v\; dx\; dz\; dt \tag{4.1}$$

where $v$ is the meridional velocity averaged over some period of time $\Delta t$, and $x_W$ and $x_E$ define the longitudinal positions of the meridional boundaries enclosing the basin. A positive stream function circulates clockwise, with northward flow at the surface and southward flow at depth. The strength of the circulation can be defined as the maximum of this stream function over particular depth and latitude ranges depending on one's focus. For our purposes, we define the small basin MOC strength as the maximum over all depths and latitudes within the basin i.e. $-3000$ m $< z <$ 0 m, 35°S $< y <$ 90°N. This picks up only the deep overturning cell as the shallow subtropical overturning cells do not dominate in the small basin (figure 4.1a).

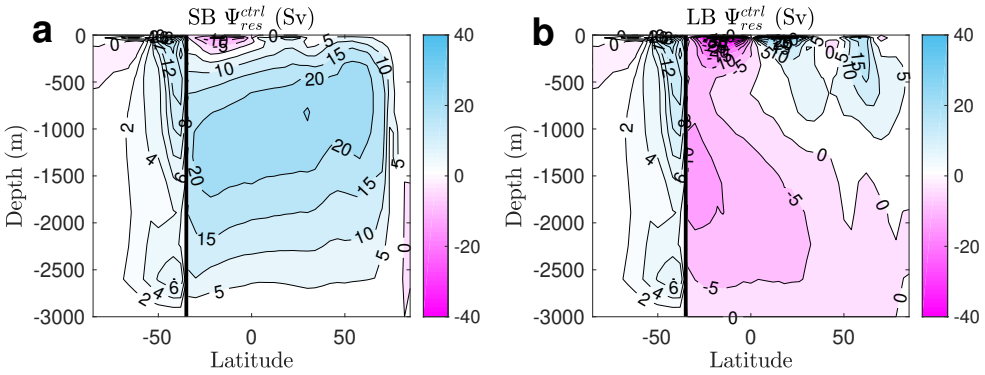



**Figure 4.1:** Control residual overturning stream functions $\Psi^{ctrl}_{res}$ for the (a) small basin, and (b) large basin (in Sv, 1 Sv $\equiv 10^6$ m$^3$ s$^{-1}$). The southern ocean residual overturning is shown south of 35°S (thick black line).

In the DDrake model, the effects due to mesoscale eddies are parameterised by means of a 'bolus velocity' $\mathbf{u}_b$, which depends on the slope of the isopycnal surfaces [Gent and Mcwilliams, 1990] (see Appendix A). As we did in Chapter 3 for the thermal overturning, in order to capture eddy effects in the overturning circulation defined in equation 4.1, we use a 'residual velocity' $v_{res}$, which is a sum of the resolved velocity $v$ and the eddy bolus velocity $v_b$. This defines a residual overturning stream function given by:

$$\Psi_{res}(y,z) = \frac{1}{\Delta t}\int_z^0 \int_{x_W}^{x_E} v_{res}\, dx\, dz\, dt = \frac{1}{\Delta t}\int_z^0 \int_{x_W}^{x_E} (v + v_b)\, dx\, dz\, dt \qquad (4.2)$$

Calculations for the small basin (SB) and large basin (LB) $\Psi_{res}$ in the DDrake control climate (where $\Delta t = 50$ years) are shown in figure 4.1. The maximum of the

SB stream function is defined as the SBMOC strength, and it is the weakening of $\max(\Psi_{res})$ with time that characterises the SBMOC weakening in response to the $CO_2$-doubling.

## 4.3 Results

### 4.3.1 Small and Large Basin Heat Storage Rates

In response to the $CO_2$-doubling, an arbitrary quantity $C = C(t, x, y, z)$ in the model changes from its control value $\overline{C}(x, y, z)$ to a perturbed value $C^{pert}(t, x, y, z)$ by an amount $\Delta C(t, x, y, z) = C^{pert} - \overline{C}$, where $\overline{C}$ is a 50-year time-average. The SB stores heat at a faster rate than the LB, and both heat storage rates decrease with time, reflecting the adjustment to a new equilibrium (figure 4.2a). The large basin's surface area is three times larger than that of the small basin, yet it only takes up 2.21 times more heat energy in joules over the course of the simulation. By considering areal proportions of the total global OHC increase, we find that this is due to a combination of the SB taking up more heat than expected for its size, and the LB taking up less than expected (figure 4.3). We also note that the southern ocean starts out overperforming for its size, but this discrepancy decreases to almost zero over the rest of the 200 years.

To compare the two basins' efficiencies in storing heat, we look at basin OHC changes divided by the respective basin's surface area (in J $m^{-2}$). Here, a change in OHC is calculated as $\Delta OHC = \int_V \rho_0 c_p \Delta\theta \, dV$, where the integral is taken over the entire basin volume, $\rho_0$ is the seawater density, $c_p$ is the specific heat capacity of seawater, and $\theta$ is the potential temperature.

After 200 years' warming, the final anomalous OHC difference, $\Delta\text{OHC}_{SB} - \Delta\text{OHC}_{LB}$, is $3.45 \times 10^9$ J $m^{-2}$ (figure 4.2b), and in terms of heat storage *rates* in W $m^{-2}$, this translates to a time-mean heat storage contrast of $0.6 \pm 0.2$ W $m^{-2}$ (figure 4.2c, the difference between the red and blue curves in figure 4.2a). There is large inter-annual variability in the heat storage rates, and the heat storage contrast shows no discernible trend over the 200 years. At the same time, we see that the SBMOC strength (stream function maximum) weakens rapidly by ∼25% during the first 30

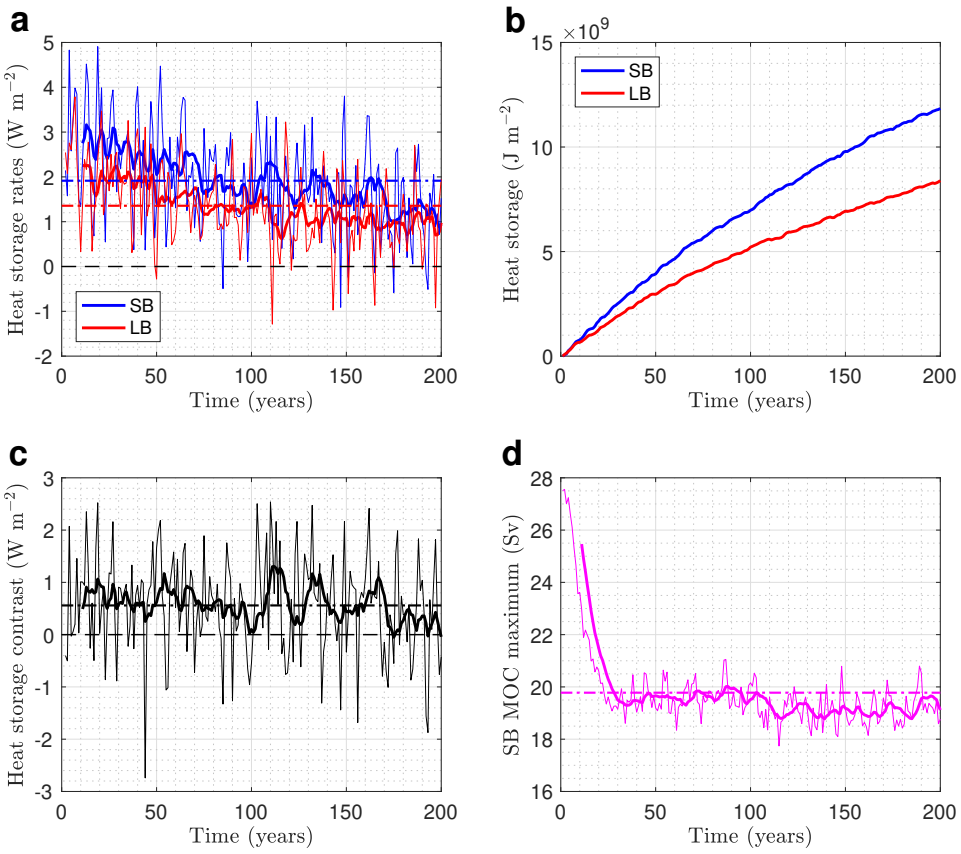



**Figure 4.2:** Time series of annually-averaged (a) SB and LB heat storage rates ($\partial_t(\Delta\text{OHC})$, in W m$^{-2}$); (b) OHC anomalies ($\Delta$OHC, in J m$^{-2}$); (c) the difference in heat storage rates i.e. the heat storage contrast ($\partial_t(\Delta\text{OHC}_{SB} - \Delta\text{OHC}_{LB})$, in W m$^{-2}$); and (d) SBMOC strength (max($\Psi_{res}^{pert}$), in Sv) following an abrupt doubling of $CO_2$. Thick lines are decadal running means and horizontal dash-dot lines indicate time-mean values. The time-mean heat storage contrast is 0.6 $\pm$ 0.2 W m$^{-2}$ (standard error, assuming 20 degrees of freedom accounting for decadal oscillations).

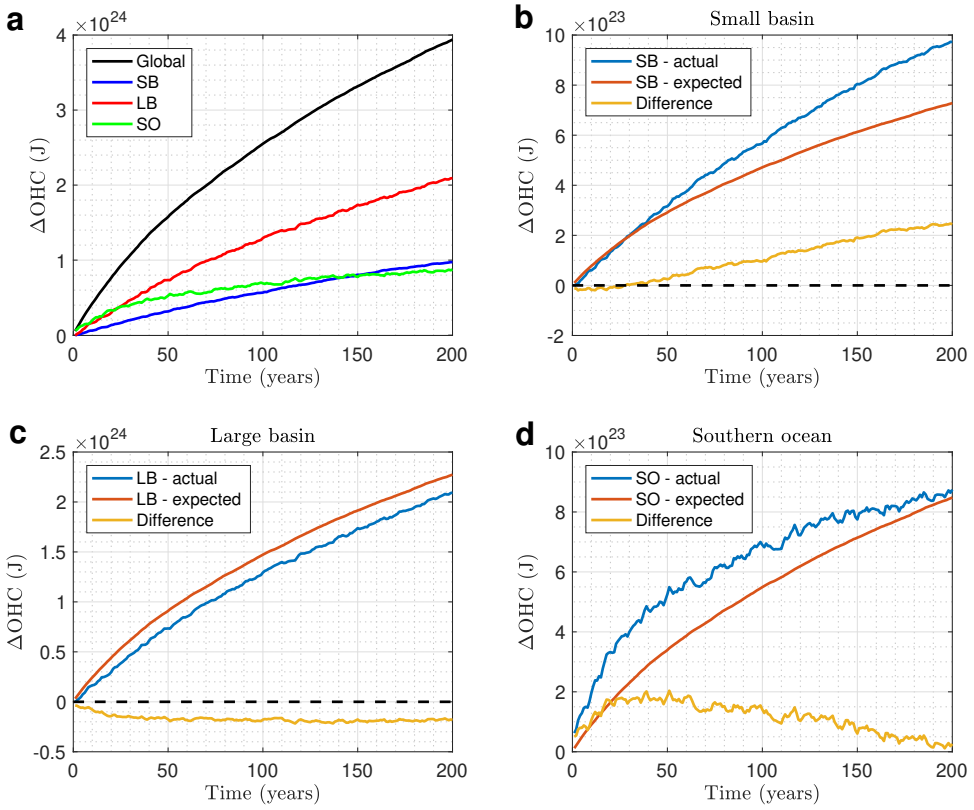



**Figure 4.3:** (a) Time-series of heat storage responses (in J) for all DDrake basins. (b-d) Comparison of actual versus expected heat storage responses (in J) considering the fractional coverage of the total surface area for (b) the small basin (SB), (c) the large basin (LB), and (d) the southern ocean (SO) of DDrake. For each basin B, the 'expected' curves are (B's surface-area/global surface-area)*(global response) i.e. the surface-area-weighted fraction of the black curve in (a). From this perspective, we see that the SB overperforms (while the LB underperforms) with respect to its size.

years (figure 4.2d), after which it remains quite stable at ∼19 Sv (1 Sv ≡ $10^6$ $m^3$ $s^{-1}$), with small oscillations of ∼1 Sv which likely reflect internal oscillations of the system (see [Buckley et al., 2012]).

Figure 4.4 shows the anomalous horizontal-mean temperature response $\Delta\theta$ as a function of depth and time for the two basins. The SB temperature signal penetrates into the ocean interior more quickly than the LB signal. The 0.1 K contour reaches the sea floor in the SB within 150 years, whereas in the LB it only extends down to ∼2 km depth after the full 200 years. The vertical structures of the two basins' temperature responses are significantly different. While the upper-ocean responses (∼top 500 m) are similar, the differences at depth are substantial. This is expected as the depth to which the wind-driven circulation penetrates is similar in both basins.

At a depth of ∼800 m in figure 4.4, there is an abrupt change in the SB response where heat is taken up more rapidly. The gradient of $\Delta\theta$ with depth reveals that, in this region, deeper waters' warming is *preceding* that of the waters above it. This suggests that temperature anomalies are being advected downwards to depths below 800 m faster than that allowed by diffusion, Ekman pumping, and other processes associated with the waters above. Rapid downward advection of temperature anomalies points to deep convection [Marshall and Schott, 1999], which we take to be closely associated with the downwelling branch of the small basin's MOC.

### 4.3.2 Role of the Small Basin MOC

To make the connection between ocean heat storage and the SBMOC more explicit, we look at the spatial pattern of the vertically-averaged potential temperature response $\Delta\theta$ for different depth intervals (figure 4.5a, b). The upper 1 km reveals pronounced warming at high latitudes in every basin, a conspicuous pool of warming at 40-60°N in the SB, and enhanced warming at 40°S where there is zonal circumpolar flow, a feature reminiscent of the warming behaviour along the Antarctic Circumpolar Current (ACC) [Armour et al., 2016]. Below 1 km depth, the temperature anomaly in the SB flows along the deep western boundary current, coincident with the lower limb of its MOC. Note there are no large temperature anomalies at depth in the LB or southern ocean regions.

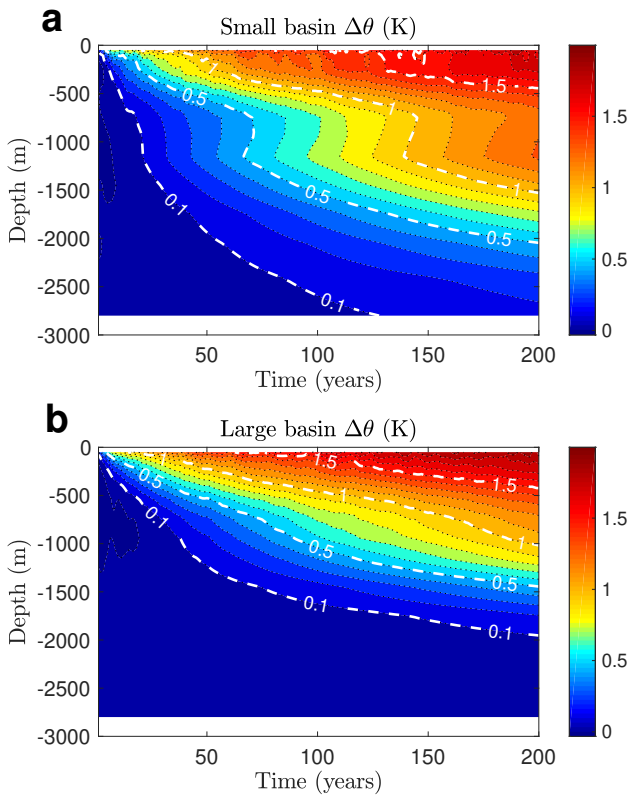



**Figure 4.4:** Depth-time plots of the anomalous temperature response (in K) in the (a) small and (b) large basins of DDrake following an abrupt $CO_2$-doubling. The contour interval is 0.1 K, and the 0.1, 0.5, 1.0, and 1.5 K contours are highlighted. The upper ocean responses are similar, but the differences at depth are substantial.

The SBMOC's role is made even clearer when we plot the control residual overturning ($\overline{\Psi_{res}}$) on top of the final zonally-averaged $\Delta\theta$ in the SB (figure 4.5c). There is distinctive deep warming at 60-80°N, collocated with the downwelling branch of $\overline{\Psi_{res}}$. The $\Delta\theta$ structure also approximates the pattern of the streamlines, and we see an isolated pool of warm water between 1 and 1.5 km depth near the equator, suggesting the equatorward advection of temperature anomalies into this region away from the high latitudes of deep water formation.

Figures 4.2 and 4.5 together highlight that the key process governing the enhanced heat storage rate in the SB is the rapid advection of surface temperature anomalies into the interior by the SBMOC. This relationship between the small basin's MOC and heat storage rate highlights the importance of the present-climate AMOC, which could help explain the Atlantic's observed enhanced warming rate compared to the Pacific (e.g. [Chen and Tung, 2014, Desbruyeres et al., 2017, Zanna et al., 2019]).

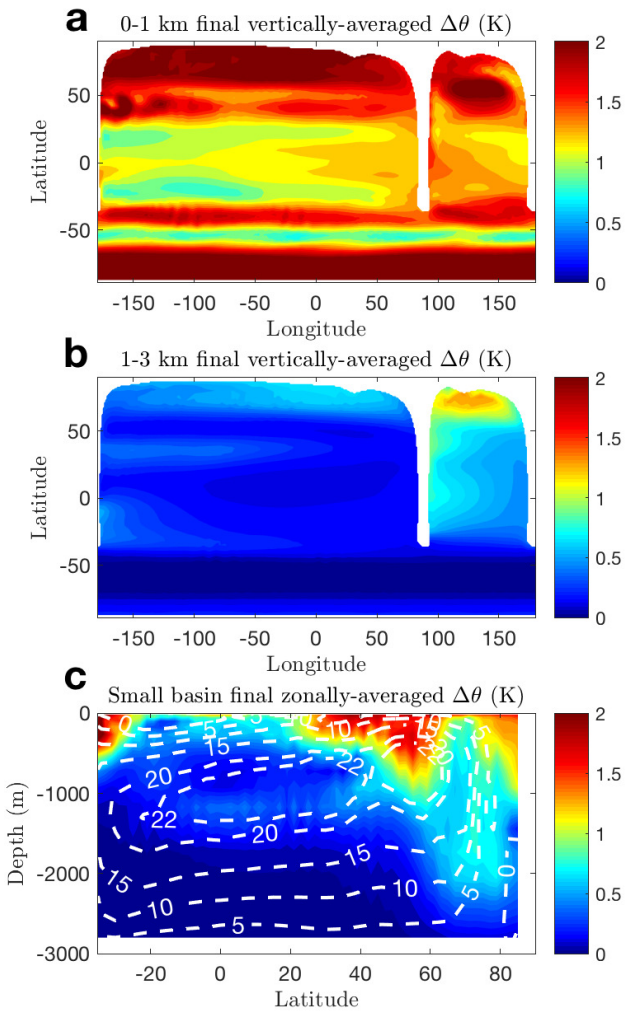



**Figure 4.5:** Vertically-averaged $\Delta\theta$ (in K) after 200 years following an abrupt doubling of atmospheric $CO_2$ in DDrake for the depth intervals (a) 0-1 km and (b) 1-3 km. The temperature anomaly at depth follows a deep western boundary current in the small basin. (c) Zonally-averaged $\Delta\theta$ (colour, in K) in the small basin after 200 years' warming, and streamlines (white dashed contours, in Sv) for the control residual overturning $\overline{\Psi_{res}}$.

### 4.3.3 Role of the southern ocean region

In DDrake, the large basin dominates global ocean heat uptake, while the southern ocean and small basin are comparable (figure 4.3a). In the real-world, the Southern Ocean dominates global ocean heat uptake in CMIP5 models [Frölicher et al., 2015] and observations (e.g. [Desbruyeres et al., 2017]). From the historical simulations in [Frölicher et al., 2015], approximately half of the heat taken up by the Southern Ocean is exported northwards. This northward transport is also supported by observations, which results in a delayed warming of the Southern Ocean [Armour et al., 2016]. Thus, another possibility is that the SB–LB heat storage contrast is due to a difference in northward heat transports from the southern ocean region of DDrake.

However, if we plot the integrated net air-sea heat flux (OHU) compared with the heat storage (OHS) for the DDrake basins, we find that the southern ocean *gains* heat rather than exporting heat northwards. The heat storage in the SB is consistently *less* than the heat uptake (figure 4.6a). This implies that the SB actually *leaks* heat across 35°S to the southern ocean region in DDrake. At the same time, there is little difference between heat uptake and heat storage in the LB, and although it starts out losing heat to the southern ocean, it ends up *gaining* heat from it after about 100 years. Thus, the SB–LB contrast cannot be explained by heat transports with the southern ocean. For this to be the case, we would need the LB to leak heat to the SB. Currently, the opposite is observed.

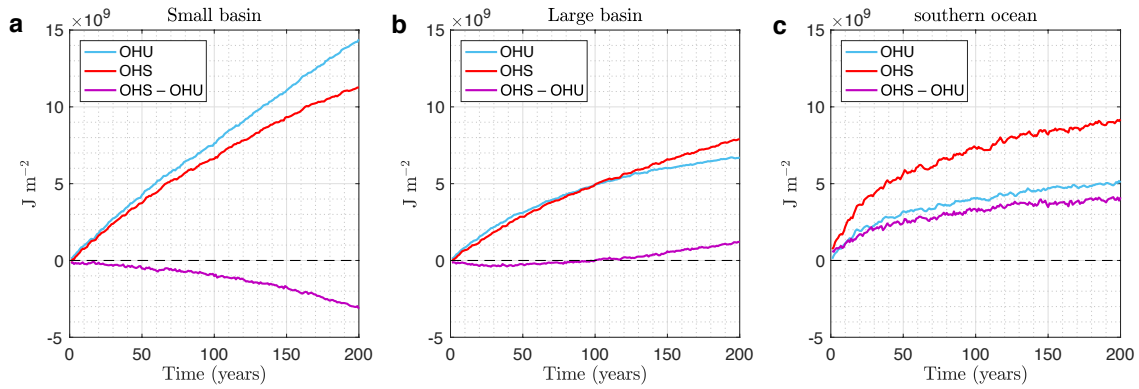



**Figure 4.6:** Time series of time-integrated net surface heat flux (OHU) and changes in OHC (OHS), and their difference (OHS−OHU) (in J $m^{-2}$) for the (a) small basin, (b) large basin, and (c) southern ocean regions of DDrake.

### 4.3.4 Heat storage response to SBMOC Weakening

It is now clear that the SBMOC plays an important role in setting the heat storage contrast between the two basins of DDrake. However, the SBMOC strength weakens rapidly by ∼25% during the first 30 years, after which it remains stable between 18 and 20 Sv (figure 4.2d). As has been suggested in other modelling studies (e.g. [Gregory, 2000, Gregory et al., 2005, Liu et al., 2017]), this weakening is primarily a result of a thermally-forced buoyancy increase in the northern high latitudes (we have not investigated salinity-forced changes in buoyancy due to freshwater fluxes). Figure 4.7 shows the time-mean sea surface temperature (SST) trend during the period of SBMOC weakening (first 30 years). The warming pattern shows a clear polar amplification in both hemispheres.

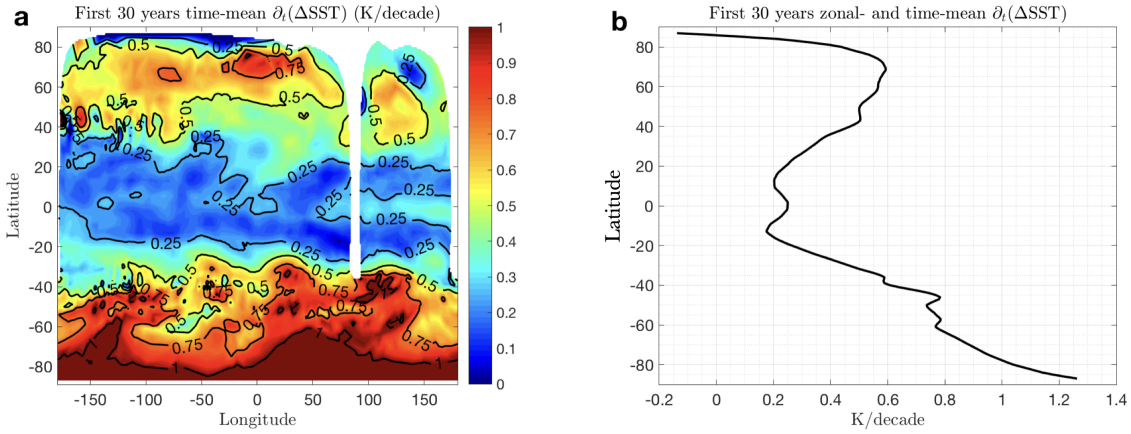



**Figure 4.7:** (a) Map of time-mean SST warming trends during the first 30 years (i.e. SBMOC weakening regime) of the $CO_2$-doubling experiment (in K/decade), (b) Zonally-averaged time-mean SST warming trends over the same period.

There is also a distinctive 'dipole-like' pattern in the SB northern high latitudes, reminiscent of the AMOC weakening 'fingerprint' described in [Caesar et al., 2018] (although we should emphasise that this is not a dipole *per se* as all the trends are positive; the blue spot near 70°N merely indicates *less warming*, not cooling). The SB blue spot resembles the 'warming hole', a region of surface cooling observed in the subpolar North Atlantic that is linked to a weakening of the AMOC (e.g. [Drijfhout et al., 2012, Rahmstorf et al., 2015]). The superficial resemblance of this pattern in DDrake is consistent with the SBMOC decline (figure 4.2d).

The amplified warming at the northern high latitudes leads to a reduction in con-

vection at the sites of deep water formation. The reduction in deep water formation rates feeding the downwelling branch of the SBMOC leads to a commensurate reduction in the SBMOC strength. This is demonstrated in figure 4.8 where we plot the vertically-averaged convective index for the control climate (panel a) and over the first 50 years following the $CO_2$-doubling (panel b). The index measures the percentage of time over which convective adjustment is active. There is a marked reduction in the average convective index of $\sim$30% over the first 50 years, consistent with the reduction in the SBMOC strength.

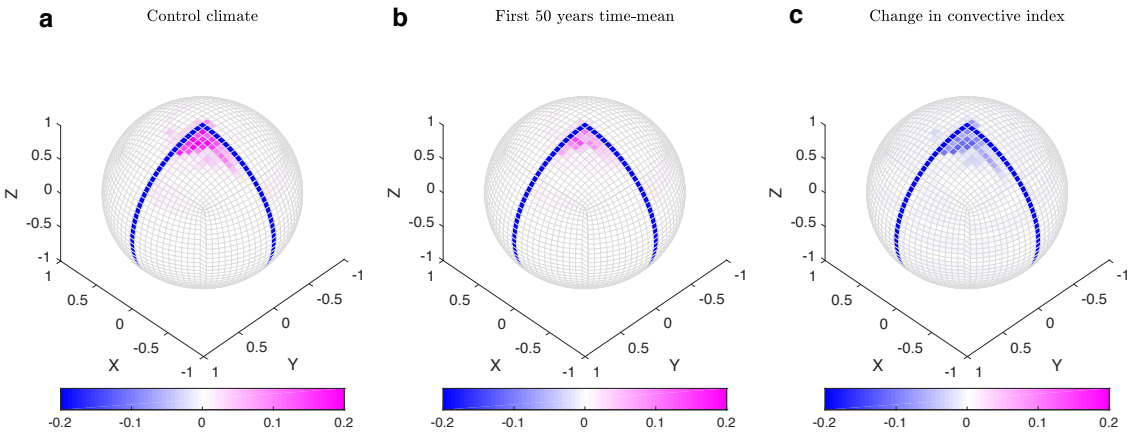



**Figure 4.8:** Time-mean vertically-averaged convective index for (a) the control climate, (b) the first 50 years following the $CO_2$-doubling, and (c) their difference. The dark blue lines indicate the meridional barriers enclosing the small basin (they don't contribute to the convection).

Despite the clear reduction in the SBMOC strength, the heat storage contrast, however, remains approximately constant over the 200 years (figure 4.2c). Thus, we find that the SBMOC weakening has little, if any, impact on the heat storage contrast. To explain this counter-intuitive result, consider the vertical heat flux associated with the SBMOC, approximated by $\rho_0 c_p \Psi_{res} \delta\theta$ (in W), where $\rho_0 = 1030$ kg m$^{-3}$ is a reference seawater density, $c_p = 3994$ J K$^{-1}$ kg$^{-1}$ is the specific heat capacity of seawater (at constant pressure), and $\delta\theta$ is the temperature difference (in K) across the downwelling and upwelling branches of the circulation i.e. $\theta_\downarrow - \theta_\uparrow$. This choice is motivated by similar scaling arguments used to represent the MHT associated with the AMOC (e.g. [Buckley and Marshall, 2016]). We take vertically-averaged $\theta$ values in the latitude bands 60-80°N and 30-50°S in the SB sector for $\theta_\downarrow$ and $\theta_\uparrow$, respectively. Following the $CO_2$-doubling, we consider the change in the SBMOC heat flux, $\Delta\mathcal{H}_{MOC} = \rho_0 c_p \Delta(\Psi_{res}\delta\theta)$. This is given by (see Appendix B):

$$\frac{\Delta\mathcal{H}_{MOC}}{\rho_0 c_p} \approx \underbrace{\overline{\Psi_{res}}\Delta(\delta\theta)}_{>0} + \underbrace{\Delta\Psi_{res}\overline{\delta\theta}}_{>0} + \underbrace{\Delta\Psi_{res}\Delta(\delta\theta)}_{<0} \tag{4.3}$$

where we take the convention that a downward heat flux is positive. There are two processes to consider: one due to $\Delta\Psi_{res}$ (SBMOC weakening) and one due to $\Delta(\delta\theta)$ (differential warming). We find that $\theta_{\downarrow}$ warms at a faster rate than $\theta_{\uparrow}$, so that $\Delta(\delta\theta) > 0$ (figure 4.9). The first term in equation 4.3 is then positive, leading to an increase in the anomalous downward heat flux.

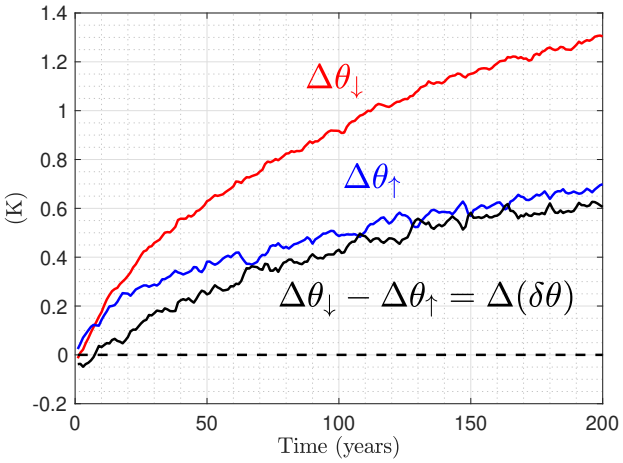



**Figure 4.9:** Time series of warming responses for the small basin MOC downwelling ($\Delta\theta_{\downarrow}$, red) and upwelling ($\Delta\theta_{\uparrow}$, blue) regions, and their difference ($\Delta(\delta\theta)$, black) (in K). The downwelling region warms at a faster rate than the upwelling region.

Now, we know that the SBMOC weakens ($\Delta\Psi_{res} < 0$), so one might think that this process compensates the differential warming (as $\Delta(\delta\theta) > 0$). Importantly, however, in the control integration, $\overline{\delta\theta} = -0.70$ K ($< 0$), indicating that the SBMOC is thermally direct and transports heat *upwards*. So, the second term in equation 4.3 is in fact *positive*. We also concluded this more directly in Chapter 3, where we projected the circulation into depth-temperature coordinates, demonstrating that the downwelling occurs at a cooler temperature than the upwelling.

Both the differential warming *and* the SBMOC weakening processes thus contribute to an *increase* in the anomalous downward heat flux. Only their interaction $\Delta\Psi_{res}\Delta(\delta\theta)$ is negative, leading to an upward heat flux. This is because the zonally-averaged $\Delta\Psi_{res}$ circulates counterclockwise, with upwelling at the northern end of the SB and downwelling at the southern end (figure 4.10). Thus, combined with an increase in

$\delta\theta$, this leads to warmer water being upwelled than downwelled.

Overall, this means that $\Delta\mathcal{H}_{MOC} > 0$. These terms are plotted (in W m$^{-2}$) in figure 4.11a. Notably, the two terms involving $\Delta\Psi_{res}$ (i.e. SBMOC weakening) compensate each other, while the dominant term is $\overline{\Psi_{res}}\Delta(\delta\theta)$, so it is the control overturning that plays the prominent role. We acknowledge that equation 4.3 assumes that the latitudinal structures of $\Delta\Psi_{res}$ and $\overline{\Psi_{res}}$ are similar, and this assumption is not entirely appropriate during the period of SBMOC weakening (figure 4.10b). However, it is appropriate during the non-weakening regime (figure 4.10d), so our results — the $\Delta\Psi_{res}\overline{\delta\theta}$ and $\Delta\Psi_{res}\Delta(\delta\theta)$ terms compensate each other, and $\Delta\mathcal{H}_{MOC}$ increases with time — are robust.

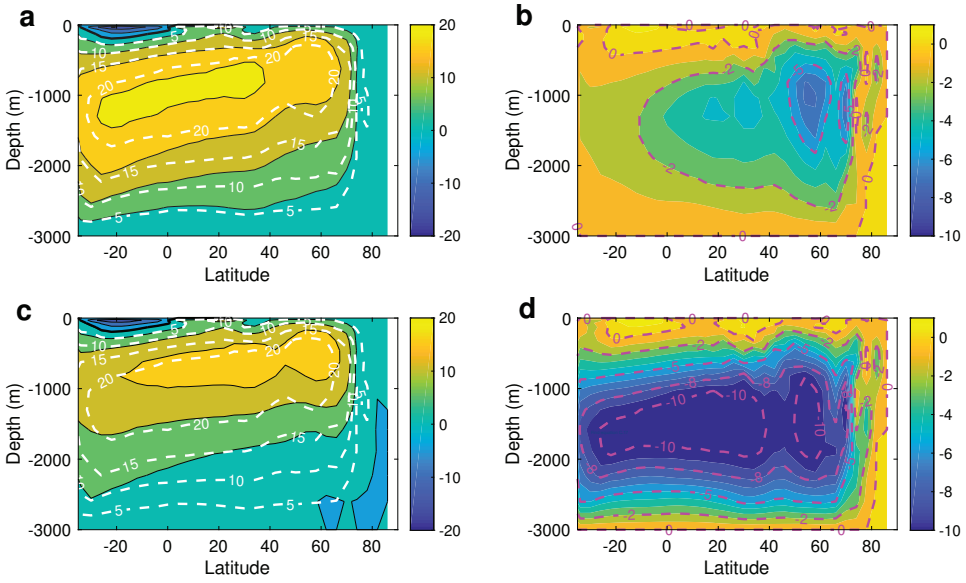



**Figure 4.10:** Zonal-mean structures of the SBMOC response. (a) 0-30 years time-mean $\Psi_{res}^{pert}$ (colour), and $\overline{\Psi_{res}}$ (white dashed contours) overturning in the small basin (in Sv) during the weakening regime; (b) 0-30 years time-mean $\Delta\Psi_{res} = \Psi_{res}^{pert} - \overline{\Psi_{res}}$ overturning response (colour and pink dashed contours) in the small basin (in Sv) during the weakening regime; (c-d) same as panels (a) and (b) except time-means are taken over the period 30-200 years during the non-weakening regime. In panels (a) and (c), the contour interval is 5 Sv and the zero contour is highlighted in black.

The anomalous downward SBMOC heat flux increases with time, and most rapidly during the SBMOC weakening. Why this increase in $\Delta\mathcal{H}_{MOC}$ does not lead to an increase in the heat storage contrast remains to be explained. As noted previously in section 4.3.3, if we consider the increase in air-sea heat flux (heat uptake) compared to the increase in OHC (heat storage) in the small basin, we find that the small basin *leaks heat* across 35°S to the southern ocean region at a rate of ∼0.5 W m$^{-2}$,

and this leakage rate increases with time (figure 4.11b). For a change in OHC in the small basin, we can write:

$$\partial_t(\Delta \mathrm{OHC}_{SB}) = \Delta \mathcal{F}_s^{SB} \underbrace{+\rho_0 c_p \int_{\text{at } 35°\mathrm{S}} \int_{-H_{SB}}^{0} \Delta(v\theta_{SB})\, dz\, dx}_{\Delta \mathcal{H}_{leak}} \tag{4.4}$$

where $\Delta \mathcal{F}_s^{SB}$ is the change in net surface heat flux over the small basin, $H_{SB}$ is the small basin depth, and we define $\Delta \mathcal{H}_{leak}$ as the SB heat leakage rate across 35°S. From figure 4.11b, we see that $\Delta \mathcal{H}_{leak}$ and $\Delta \mathcal{H}_{MOC}$ compensate each other, especially on long timescales (see dashed lines). This is made even clearer in an energy budget sense, where we find that $\partial_t(\Delta \mathrm{OHC}_{SB}) + \Delta \mathcal{H}_{MOC} \approx \Delta \mathcal{F}_s^{SB}$ (light blue, dashed), which implies that $\Delta \mathcal{H}_{MOC} \approx -\Delta \mathcal{H}_{leak}$. So, as the SBMOC heat flux increases, this permits more heat to penetrate the ocean surface, causing an increase in the net surface heat flux $\Delta \mathcal{F}_s^{SB}$. However, this additional heat input is then lost to the southern ocean, which ensures that the heat storage contrast remains stationary.

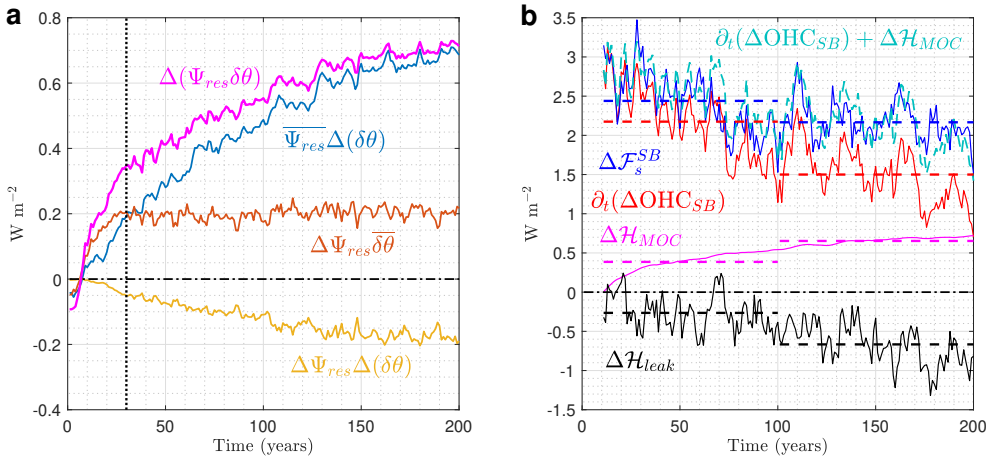



**Figure 4.11:** (a) Decomposition of the change in SB downward (positive) MOC heat flux ($\Delta(\Psi_{res}\delta\theta)$, magenta) into differential warming ($\overline{\Psi_{res}}\Delta(\delta\theta)$, blue), SBMOC weakening ($\Delta\Psi_{res}\overline{\delta\theta}$, orange), and nonlinear ($\Delta\Psi_{res}\Delta(\delta\theta)$, yellow) terms (annual averages, in W m$^{-2}$). A vertical dotted line is plotted at 30 years to separate the weakening and non-weakening SBMOC regimes. (b) Decadal running means of the SB heat uptake rate ($\Delta \mathcal{F}_s^{SB}$, blue), heat storage rate ($\partial_t(\Delta \mathrm{OHC}_{SB})$, red), SBMOC heat flux ($\Delta \mathcal{H}_{MOC}$, magenta), and leakage rate to the southern ocean ($\Delta \mathcal{H}_{leak} = \partial_t(\Delta OHC_{SB}) - \Delta \mathcal{F}_s^{SB}$, black) (in W m$^{-2}$). Note that the sum of the heat storage rate and SBMOC heat flux (light blue, dashed) almost matches the heat uptake rate. Horizontal dashed lines are centennial time-means.

This heat loss to the southern ocean is similar to the 'redistribution temperature' response seen in [Xie and Vallis, 2012] where, in an idealised model of the Atlantic ocean, the AMOC weakening serves to transport heat from the Northern Hemisphere high latitudes towards the Southern Hemisphere. We noted previously that, across CMIP5 models, under historical simulations, the Southern Ocean dominates ocean heat uptake and exports approximately half of the energy it takes up *northwards* [Frölicher et al., 2015]. However, a weakening of this northward heat transport (perhaps as a result of ozone hole recovery in the near future) could manifest as an anomalous southward transport from the Atlantic basin to the Southern Ocean, which is consistent with our results (figures 4.6 and 4.11b).

### 4.3.5 Parallels with CMIP5 Models

Our analysis suggests new ways to look at the AMOC's role in ocean heat storage in observations and more complex climate models. We performed a preliminary analysis of four CMIP5 models, and show that there is a heat storage contrast between the Atlantic and Pacific basins (defined from 30°S to 65°N) in abrupt $CO_2$-quadrupling experiments (figure 4.12). Under this more intense forcing scenario, the multi-model time-mean heat storage contrast is 2.2 W $m^{-2}$. Looking at individual models, the contrast persists in the models CANESM2 and NASA-GISS-E2-H, but weakens in MIROC-ESM and GFDL-ESM2M (figure 4.12b).

This could be due to different model AMOC responses and, particularly, whether the control model AMOC cells are thermally direct (flux heat upward, like the SBMOC) or indirect (flux heat downward). For example, [Zika et al., 2013] diagnosed overturning cells in UVic ESM and found that the cell coincident with the AMOC was thermally indirect. Additionally, model AMOC cells have been found to transport heat downwards in CCSM4 [Zika et al., 2015], NEMOv3.4 [Saenko et al., 2018], and ACCESS-OM2 [Savita et al., 2021]. So, our results might not apply to these models. However, it is still an open question whether the real-world AMOC is thermally direct or indirect (see Chapter 3). Nevertheless, we suggest that the AMOC is at least responsible for the existence of a contrast in each of these CMIP5 models, just as the SBMOC is responsible for the contrast in DDrake.

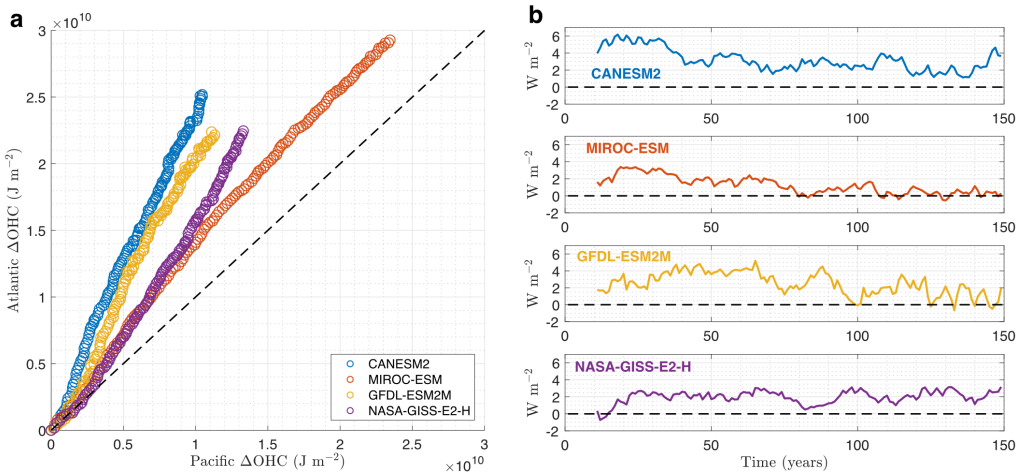



**Figure 4.12:** (a) Atlantic vs. Pacific top-3 km column-averaged annual OHC anomalies (in J m$^{-2}$) immediately following an abrupt quadrupling of atmospheric $CO_2$ in CMIP5 models (each dot represents one year). Atlantic and Pacific basins defined from 30°S to 65°N. The deviation from the identity line (black dashed) highlights the Atlantic's enhanced warming rate relative to the Pacific in these experiments. (b) Decadal running means of individual model Atlantic–Pacific heat storage contrasts $\partial_t(\Delta\text{OHC}_{Atl} - \Delta\text{OHC}_{Pac})$ (in W m$^{-2}$).

## 4.4 Discussion and Conclusions

In this study, we have used the DDrake model, where the small basin is endowed with an overturning circulation akin to that of the present-day Atlantic Ocean, to study the transient response of the ocean to an abrupt doubling of atmospheric $CO_2$. We find that the small basin experiences an enhanced heat storage rate due to a rapid advection of surface temperature anomalies into its interior. Similar to [Kostov et al., 2014], who found no significant correlations between the AMOC weakening and the depth of heat storage in CMIP5 models, we find no significant relationship between the small basin's MOC weakening and its weakening heat storage rate in our set-up. Moreover, we find that the SB–LB heat storage contrast remains almost constant during the period of SBMOC weakening, and throughout the rest of the simulated 200 years on multidecadal timescales (figure 4.2c).

Weakening of the AMOC has been seen in proxy observations (e.g. [Rahmstorf et al., 2015, Caesar et al., 2018, Zhu and Liu, 2020, Caesar et al., 2021]) and climate models (e.g. [Gregory et al., 2005, Weaver et al., 2012, Cheng et al., 2013, Kirtman et al., 2013, Weijer et al., 2020]), and recent observations from RAPID are consistent with a declining AMOC response predicted from coupled climate models [Smeed et al.,

2018]. However, large interannual and decadal variability in the AMOC make the detection of long-term trends difficult (e.g. [Frajka-Williams et al., 2019, Jackson et al., 2022, Latif et al., 2022]), and it's still unclear whether the suggested weakening from proxies is reliable (e.g. [Kilbourne et al., 2022]).

It has been suggested that a weakening of the AMOC in the future could lead to a reduction in deep ocean heat storage, resulting in an accelerated warming of surface temperatures [Chen and Tung, 2018]. However, this view perhaps focuses too narrowly on $\Delta\Psi_{res}$ and, as we have found in our experiments, considering $\Delta(\Psi_{res}\delta\theta)$ paints a more complicated picture, by introducing differential warming as an additional process to AMOC weakening (equation 4.3). Additionally, positive correlations between the global-mean surface temperature and AMOC strength have been found in observations [Caesar et al., 2020] and simulations [Bonnet et al., 2021], implying that a weakening of the AMOC should lead to a reduction in surface warming, not an acceleration.

This is consistent with our results as, contrary to expectations, we find that the anomalous downward SBMOC heat flux $\Delta\mathcal{H}_{MOC}$ increases as the SBMOC weakens. Furthermore, we find that the dominant term in its decomposition is from differential warming, with the control overturning playing the prominent role (figure 4.11a). Finally, although $\Delta\mathcal{H}_{MOC}$ increases, this does not lead to an increase in the heat storage contrast, as this additional heat input is subsequently lost to the southern ocean region (figure 4.11b). Thus, although the presence of the SBMOC is important for the small basin's enhanced heat storage rate, the change in SBMOC strength is surprisingly unimportant during the simulated 200 years in our experiment. It is not known whether this SBMOC weakening affects the difference in $\Delta$OHC at equilibrium between the small and large basins; further simulations would be needed to address this.

We emphasise that, like all modelling studies, our results are model-dependent. The compensation we found between the $\Delta\Psi_{res}$ terms in figure 4.11a very likely depends on model-specific AMOC states and responses. It should also be underlined that this is an idealised model: there is no bottom topography, no representation of Antarctic Bottom Water formation, and the control SBMOC strength is 26 Sv,

which is ∼40% stronger than the real-world AMOC (e.g. [Buckley and Marshall, 2016, Danabasoglu et al., 2021]), although this is not outside the CMIP5 and CMIP6 model ranges [Weaver et al., 2012, Weijer et al., 2020].

Observational estimates of the AMOC strength vary. Transport estimates from RAPID at 26.5°N [McCarthy et al., 2015] give values ∼18 Sv (e.g. [Smeed et al., 2018]), while estimates from the Meridional Overturning Variability Experiment (MOVE) at 16°N [Send et al., 2011] give values ∼24 Sv (e.g. [Frajka-Williams et al., 2018, Danabasoglu et al., 2021]). Although, the MOVE array is designed to measure variability rather than the absolute value.

The control SBMOC strength is quite high. Nevertheless, our results rest on the SBMOC weakening and not its initial value. Many studies have shown a relationship between the control AMOC strength and the subsequent AMOC weakening in climate change simulations, with a stronger AMOC generally leading to greater weakening (e.g. [Gregory et al., 2005, Gregory and Tailleux, 2011, Weaver et al., 2012, Winton et al., 2014, Weijer et al., 2020]). Thus, an overprediction of the SBMOC strength likely means that the SBMOC weakening is also an overprediction. This lends further support to our results, as the weakening doesn't impact the SB–LB heat storage contrast despite being significantly large.

Finally, the real-world MOC is three-dimensional, spanning multiple basins with interbasin transports (e.g. [Talley, 2013, Ferrari et al., 2017, Newsom and Thompson, 2018]). This may also be true for the DDrake MOC, but, in our analysis, we've implicitly assumed that the overturning circulations in the small and large basins are not strongly connected. In section 4.3.3, we found that the SB leaks heat to the LB. This is similar to a recent study from [Sun et al., 2022] who found that the Atlantic leaks heat to the Indo-Pacific as a result of AMOC weakening in a $CO_2$-quadrupling experiment in the CCSM4 model. They attribute this result specifically to an interbasin overturning circulation, and the same explanation could apply to our result.

If so, this points to an interbasin overturning circulation connecting the small and large basins in DDrake, which makes it difficult to attribute the existence of the SB–LB heat storage contrast solely to the SBMOC. However, as we saw in section

4.3.2, we associated the SB's enhanced heat storage rate with deep convection at the northern high latitudes i.e. the downwelling branch of the SBMOC. If the DDrake MOC is interbasin, it might take thousands of years for a heat anomaly from the SB northern high latitudes to traverse the SB and enter the LB (e.g. transit times through overturning circulation components reach ∼3600 years in ECCOv4 [Rousselet et al., 2021]). So, our simulation length of 200 years is likely too short for this interbasin effect to have an impact on the heat storage contrast.

To conclude, in this simplified set-up, we were able to provide a conceptual grasp on how a deep overturning circulation affects a basin's heat storage rate, and the comparison with CMIP5 models in figure 4.12 is encouraging. A key conclusion that extends beyond the specifics of DDrake is that the impact of the AMOC on OHS is driven not only by the AMOC's strength. The temperature structure and its changes must also be considered for a complete evaluation of the AMOC's role.

Our results underline the importance of the AMOC in ocean heat storage, and for its accurate representation in other, predictive climate models. Continued observational monitoring efforts such as RAPID [McCarthy et al., 2015], MOVE [Send et al., 2011], the South Atlantic MOC Basin-wide Array (SAMBA) [Meinen et al., 2018], and the Overturning in the Subpolar North Atlantic Program (OSNAP) [Lozier et al., 2019], in conjunction with more advanced high-resolution climate models, should drive a deeper understanding of the AMOC. But we are also encouraged by the use of simpler, more conceptual models such as DDrake in order to make sense of this increasing complexity.

### 4.4.1 Key points

1. A deep meridional overturning circulation (MOC) connects the ocean surface to its interior, enhancing heat storage rate under global warming.
2. This circulation in the Atlantic (AMOC) may enable its enhanced heat storage rate relative to the Pacific in recent decades.
3. AMOC weakening may not necessarily impact ocean heat storage rate due to compensating physical processes.

*"Essentially all models are wrong, but some are useful."*

George Box, 1979

# 5

# Representation of OHU in Two-Layer EBMs

Current two-layer energy-balance models (EBMs) successfully emulate the global-mean surface air temperature responses of CMIP5 models in abrupt $4\times CO_2$ experiments [Geoffroy et al., 2013b], yet little attention has been paid to how well they emulate the subsurface ocean temperature response. Using the fitting procedure outlined in [Geoffroy et al., 2013b], we fit a two-layer EBM to the temperature responses of the DDrake configuration under an abrupt $CO_2$-doubling. We find that we can interpret the fitted EBM parameters physically, in light of what we know about OHU processes in DDrake from Chapters 3 and 4. Unlike in previous approaches, which focus primarily on surface warming, we assess both the upper- and lower-layer EBM-fitted responses, and find that the fits for the lower-layer (subsurface ocean) are poor. This indicates that the current EBM formulation is unsatisfactory, and any inferred subsurface ocean warming from the EBM is misleading.

We attempt to improve the representation of subsurface warming in the traditional two-layer EBM by adjusting the power-law dependence of the heat exchange between the two layers. Increasing or decreasing this power-law dependence conceptually in-

creases or decreases the sensitivity of OHU to the stratification in the EBM. We find that increasing the sensitivity (quadratic power-law) improves the representation of subsurface warming in DDrake and in 4 out of 5 CMIP5 models analysed under abrupt $CO_2$-increase experiments. Decreasing the sensitivity (2/3 power-law) leads to a poorer representation of subsurface warming across all models analysed. This difference in behaviour between the quadratic and 2/3 power-laws might highlight the importance of the stratification for OHU, but why a quadratic power-law should fare better than a linear one remains to be explained.

## 5.1 Introduction

Coupled atmosphere-ocean general circulation models (AOGCMs) have grown greatly in complexity, commensurate with advances in computing technologies over the last few decades. They are tremendously useful and comprehensive tools to study the climate and perform projections, yet they are computationally very expensive. Furthermore, the resulting overwhelming complexity of state-of-the-art AOGCMs means that no single person can wholly understand what one of these models is doing. As we've seen in Chapters 3 and 4, even a greatly simplified, highly idealised aquaplanet model like DDrake still exhibits rich, complex behaviour, with multiple distinct circulation processes playing an important role in OHU. An alternative is to use simple climate models to emulate the AOGCM responses. These are far simpler to understand, and can cover a wider range of potential climate scenarios with negligible computational cost.

One branch of simple climate models encompasses physically-based energy balance models (EBMs). Energy balance models have been used extensively in climate science to aid the understanding of heat transfers within the climate system (e.g. [Budyko, 1969, Sellers, 1969, Hoffert et al., 1980, Murphy, 1995]). Alongside the advancement of AOGCMs, EBMs have been used to emulate and make sense of AOGCM results (e.g. [Schlesinger and Jiang, 1990, Raper and Cubasch, 1996, Raper et al., 2001]) and, more recently, to help identify and quantify the sources of spread in climate change projections (e.g. [Padilla et al., 2011, Geoffroy et al., 2012, Bodman and Jones, 2016, Colman and Soldatenko, 2020]).

EBMs provide a useful framework for summarising and comparing bulk physical properties of different AOGCMs (e.g. [Raper et al., 2002, Gregory and Forster, 2008, Geoffroy et al., 2013b]), and the parameters describing these properties can be interpreted in terms of physical processes (e.g. [Kostov et al., 2014]) so may provide insight into the underlying physics.

A recent popular EBM is a form of two-layer EBM, which is capable of capturing the 'two-timescale' surface temperature response seen in abruptly-forced AOGCM experiments [Held et al., 2010, Geoffroy et al., 2013b]. In this two-layer EBM, the climate system is aggregated and split into two vertical layers: the first layer represents the atmosphere, land-surface, and oceanic mixed-layer; and the second layer represents the deeper ocean below.

Due to the ocean's overwhelming heat capacity compared to that of the atmosphere and land-surface, one can approximate the upper-layer as simply representing the oceanic mixed-layer, making the EBM an ocean-only model (as was done previously in [Kostov et al., 2014]). We will do the same in this chapter. This allows us to concentrate on physical processes within the ocean, transferring energy from the mixed-layer to the thermocline and deeper waters below.

The state of each layer is described by the temperature perturbations $T$ and $T_0$, and these change according to a net surface heat flux at the ocean surface and a heat exchange between the two layers. Following [Geoffroy et al., 2013b], the temperature perturbations obey the equations:

$$\begin{aligned} C\frac{dT}{dt} &= \mathcal{F} - \alpha T - \gamma(T - T_0) \\ C_0\frac{dT_0}{dt} &= \gamma(T - T_0) \end{aligned} \tag{5.1}$$

Here, $\mathcal{F}$ is an effective forcing at the ocean surface (in W m$^{-2}$); for an abrupt $CO_2$-doubling, the resulting forcing $\mathcal{F}$ is, to a good approximation, a constant. The parameter $\alpha$ encompasses different radiative feedbacks of the system, and $\gamma$ parameterises the heat exchange (or thermal coupling) between the two layers. The constants $C$ and $C_0$ are effective heat capacities for each layer (in J m$^{-2}$ K$^{-1}$). A

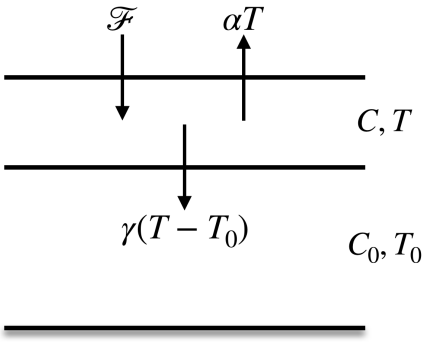



**Figure 5.1:** Diagram of the simple two-layer energy balance model. Arrows represent energy fluxes. $\mathcal{F}$ is the effective forcing at the ocean surface, $\alpha$ is the globally-averaged climate feedback parameter, $\gamma$ is the heat exchange parameter, $T$ and $T_0$ are temperature perturbations, and $C$ and $C_0$ are effective heat capacities.

diagram of the energy fluxes in the EBM is shown in figure 5.1.

Equations 5.1 can be solved to give (see Appendix C for derivation):

$$\begin{aligned} T(t) &= T_{eq}(1 - a_f e^{-t/\tau_f} - a_s e^{-t/\tau_s}) \\ T_0(t) &= T_{eq}(1 - \phi_f a_f e^{-t/\tau_f} - \phi_s a_s e^{-t/\tau_s}) \end{aligned} \tag{5.2}$$

where $T_{eq} = \mathcal{F}/\alpha$ is the temperature at equilibrium, and the parameters $a_f, a_s, \tau_f, \tau_s$, $\phi_f$, and $\phi_s$ are as defined in [Geoffroy et al., 2013b]. The parameters $\tau_f$ and $\tau_s$ are distinct fast and slow timescales, respectively. The fast timescale corresponds to the timescale of adjustment of the upper-layer to the equilibrium temperature (a few years to a decade), while the slow timescale corresponds to a joint adjustment of the upper and lower layers (order of centuries). These roughly correspond to timescales of adjustment for the oceanic mixed-layer and the top 2-3 km of the ocean, respectively.

The parameters $a_f, a_s, \phi_f$, and $\phi_s$ are 'mode parameters' that partition the adjustment towards equilibrium into the fast and slow components such that $a_f + a_s = 1$ and $\phi_f a_f + \phi_s a_s = 1$. As $t \to \infty$, both $T$ and $T_0$ tend towards the equilibrium temperature $T_{eq}$, under the two timescales.

Can we accurately emulate OHU in DDrake using this EBM (equation 5.1)? The EBM has found success in emulating the forced *surface* temperature response in other AOGCMs (e.g. [Held et al., 2010, Geoffroy et al., 2013b, Rohrschneider et al.,

2019]), but the emulated *subsurface* temperature response (i.e. the OHU) has received less attention. The problem of subsurface warming emulation was recently highlighted by [Nadiga and Urban, 2019], who found that this EBM could not simultaneously reproduce both the surface and subsurface ocean warming of an AOGCM under an abrupt $4\times CO_2$ forcing. If the two-layer EBM is to be used as a physically-based emulator, we would like it to be able to reproduce both the surface *and subsurface* warming.

We first use the two-layer EBM in equations 5.1 (the 'Geoffroy EBM') to fit the surface and subsurface temperature responses of DDrake forced by an abrupt $CO_2$-doubling. The fitting procedure is briefly described in section 5.2.1, and section 5.2.2 presents results using this traditional EBM framework. We find that we can interpret the fitted EBM parameters physically, in light of what we know about DDrake from Chapters 3 and 4. However, we also find that the Geoffroy EBM is unable to represent the subsurface warming in DDrake, confirming the shortcoming of this EBM highlighted by [Nadiga and Urban, 2019].

We attempt to improve the representation of subsurface warming by modifying the power-law for the heat exchange between the two layers, $\gamma^*(T - T_0)^\zeta$, in section 5.3. In the Geoffroy EBM, the heat exchange is linear i.e. $\zeta = 1$. By increasing the power-law dependence to $\zeta = 2$, we improve the representation of subsurface warming for DDrake and 4 out of 5 other CMIP5 models under abrupt $CO_2$-increase experiments. Decreasing the power-law dependence to $\zeta = 2/3$ (suggested from quasigeostrophic theory [Rhines and Young, 1982b]) worsens the representation of subsurface warming across all models. Some conclusions are offered in section 5.4.

## 5.2 The traditional EBM framework

### 5.2.1 Fitting procedure

To begin our investigation, we follow the same procedure as in [Geoffroy et al., 2013b], where they successfully fit this two-layer EBM (equations 5.1) to CMIP5 model surface air temperature (SAT) responses to an abrupt $CO_2$-quadrupling. Here, we fit to annually-averaged SAT anomalies relative to the DDrake control

climate rather than monthly snapshots. This does not impact our results.

The radiative parameters $\mathcal{F}$ and $\alpha$ are found by linearly regressing the first 50 years of the net radiative imbalance against the global mean surface air temperature response, following the method of [Gregory et al., 2004]. The mode parameters are found making use of the solutions (equations 5.2), and $C, C_0$, and $\gamma$ are then found through analytical relationships between the fitted parameters (see [Geoffroy et al., 2013b] for the full procedure):

$$C = \frac{\alpha}{a_f/\tau_f + a_s/\tau_s} \tag{5.3}$$

$$C_0 = \alpha(\tau_f a_f + \tau_s a_s) - C \tag{5.4}$$

$$\gamma = \frac{C_0}{\tau_f a_s + \tau_s a_f} \tag{5.5}$$

Throughout this procedure, only the global mean *surface air temperature* response is used. The EBM radiative and mode parameters are fitted to each CMIP5 model output in order to reproduce the SAT response. Arguably, this is a practical choice as humans live in the atmospheric surface boundary layer, so the SAT is most relevant to us when making climate projections. However, if we wish to be consistent with the *meaning* of the symbols in the two-layer EBM, $T$ is not the SAT response; it is the upper-layer temperature response, which in this case is the oceanic mixed-layer temperature.

The logic is thus flawed here, as the authors in [Geoffroy et al., 2013b] conflate the EBM's predicted mixed-layer temperature with a surface air temperature, and these are quite different things (if they were the same, there would be no atmosphere-ocean sensible heat fluxes). Moreover, the EBM-predicted $T_0$ and its correspondence with the deep temperature response in the CMIP5 models is not examined in [Geoffroy et al., 2013b].

### 5.2.2 Results with traditional EBM: DDrake fitted responses

Here, we present results for the two-layer 'Geoffroy EBM' fits to the DDrake temperature responses to an abrupt $CO_2$-doubling. The fitting procedure is performed for the globally-averaged response, and also for the basin-average responses for the small and large basins, and the model southern ocean. The effective layer heat capacities $C$ and $C_0$ (in W yr m$^{-2}$ K$^{-1}$) are found using equations 5.3 and 5.4, and the corresponding upper- and lower-layer thicknesses ($h$ and $H$, respectively) can thus be found using:

$$\begin{aligned} h &= \frac{86400 \times 360 \times C}{\rho_0 c_p} \\ H &= \frac{86400 \times 360 \times C_0}{\rho_0 c_p} \end{aligned} \tag{5.6}$$

where $\rho_0$ is a reference seawater density (kg m$^{-3}$), and $c_p$ the specific heat capacity of seawater at constant pressure (J kg$^{-1}$ K$^{-1}$). In this way, the fitted EBM parameters give 'predictions' for the mixed-layer depth ($h$) and the depth to which the deep-ocean is thermally involved over the 200 years ($h + H$).

Note that it is difficult to pin down what the lower-layer in the EBM specifically represents, as it is simply treated as a large heat sink. The lower-layer thickness $H$ merely arises from the fitting procedure, and the fitted parameters are optimised to the SAT. In [Geoffroy et al., 2013b] (and in many other studies e.g. [Gregory, 2000, Held et al., 2010, Kostov et al., 2014, Rohrschneider et al., 2019]), the lower-layer is simply called the 'deep ocean' or 'lower ocean'. We will continue using the language 'deep ocean' to refer to the lower-layer, which we can take to mean 'all ocean layers below the mixed-layer'.

A key aim of this chapter is to critically evaluate the upper- and lower-layer temperature responses given by the EBM, and hence the representation of OHU. We do this by plotting the vertically-averaged DDrake temperature responses that correspond to the predicted layer thicknesses (equation 5.6). Using these plots, we can assess how well the EBM actually captures the subsurface ocean warming i.e. the transfer of heat from the mixed-layer to the thermocline and deeper waters below.

This transfer is characterised by the heat transfer coefficient $\gamma$ (in W m$^{-2}$ K$^{-1}$), calculated using equation 5.5. The thermal physical parameters (along with the fitted slow and fast timescales) are displayed in table 5.1. Radiative parameters and corresponding equilibrium temperatures are shown in table 5.2.

| | $C$ (W yr m$^{-2}$ K$^{-1}$) | $C_0$ (W yr m$^{-2}$ K$^{-1}$) | $h$ (m) | $H$ (m) | $\gamma$ (W m$^{-2}$ K$^{-1}$) | $\tau_s$ (yr) | $\tau_f$ (yr) |
|---|---|---|---|---|---|---|---|
| Global | 20.3 | 108.1 | 153 | 817 | 1.02 | 185 | 7.9 |
| SB | 21.5 | 113.6 | 163 | 859 | 1.48 | 141 | 6.1 |
| LB | 21.3 | 109.0 | 161 | 824 | 1.39 | 141 | 6.3 |
| SO | 14.7 | 98.8 | 111 | 747 | 0.55 | 313 | 10.7 |

**Table 5.1:** Upper-layer heat capacity $C$, lower-layer heat capacity $C_0$, the corresponding upper- and lower-layer thicknesses $h$ and $H$, heat exchange coefficient $\gamma$, and fitted slow and fast timescales $\tau_s$ and $\tau_f$ for each of the DDrake basins, following the fitting procedure in [Geoffroy et al., 2013b].

| | $\mathcal{F}$ (W m$^{-2}$) | $\alpha$ (W m$^{-2}$ K$^{-1}$) | $T_{eq}$ (K) |
|---|---|---|---|
| Global | 4.44 | 1.48 | 3.00 |
| SB | 4.64 | 1.92 | 2.42 |
| LB | 4.73 | 1.90 | 2.49 |
| SO | 3.93 | 0.79 | 4.97 |

**Table 5.2:** Calculated radiative parameters for each of the DDrake basins using the SAT, following the fitting procedure in [Geoffroy et al., 2013b]: the radiative forcing $\mathcal{F}$, the climate feedback $\alpha$, and the corresponding equilibrium temperature $T_{eq}$.

The global value for $h + H$ gives a total ocean depth of 970 m, close to the CMIP5 ensemble mean found in [Geoffroy et al., 2013b] of 1182 m. The fitted physical parameters in table 5.1 are largely consistent with our findings from previous chapters. The stratification in the SB is weaker than in the LB (Chapter 2). We know that deep convection is localised to the SB northern high latitudes, which enables an overturning circulation in the SB akin to the AMOC (SBMOC, Chapter 4). These results suggest that the fitted mixed-layer and deep-ocean layer thicknesses ($h$ and $H$) should be largest in the SB. This is what we see in table 5.1 (columns 3 and 4).

In Chapter 4, we determined that the SBMOC is responsible for the small basin's enhanced heat storage rate, as it connects the SB surface to its interior. We also attributed the existence of the SBMOC to the heat storage contrast between the small and large basins. The heat exchange coefficient $\gamma$ characterises the coupling between the two layers in the EBM. As the surface and interior are more strongly

connected in the SB due to the SBMOC, this suggests that the fitted $\gamma$ should be largest for the SB, which is what we see in table 5.1 (column 5).

This is also consistent with our findings from Chapter 3. There, we associated the SBMOC with a deep thermal overturning circulation ($\Psi_{\theta z}$) that spans the full depth of the basin. Thermal overturning circulations in the LB reach approximately mid-depth, while the thermal circulation in the SO reaches ∼500 m depth (figure 3.6). If we view the $\Psi_{\theta z}$ depths as a measure of $H$, then we expect that the order of $H$ from largest to smallest should go: SB, LB, SO. If we view the $\Psi_{\theta z}$ depths as a measure of the thermal coupling between the mixed-layer and deeper ocean, then we expect that $\gamma$ from largest to smallest should also go: SB, LB, SO. This is precisely what we see in table 5.1 (columns 4 and 5).

Notably, the longest adjustment timescales are seen for the SO — almost twice as long as those for the small and large basins (table 5.1 columns 6 and 7). This is consistent with the relatively slow response of the real-world Southern Ocean (e.g. [Li et al., 2013, Marshall et al., 2014a]), due to wind-driven upwelling of old, unmodified deep water dampening the surface warming around Antarctica [Armour et al., 2016]. It's possible that a similar mechanism exists in DDrake, but the lack of an AABW mass or a realistic Lower Cell of the MOC makes this unlikely. Further analysis would be needed to address this.

Nevertheless, we can interpret the fitted EBM parameters in terms of the DDrake ocean circulation. The fitted parameters thus have physical meaning, and this lends further support to the EBM's use as a physically-based emulator. In spite of this, however, the resulting fitted temperature responses are poor.

Figure 5.2 shows the fitted EBM temperature responses. The EBM (black dashed lines) reproduces the DDrake SAT response not only globally, but also regionally for each basin. This is unsurprising as the SAT response is what the EBM radiative and mode parameters were fitted to. However, if we compare the EBM fits to the SST responses, a good fit is only seen for the southern ocean (figure 5.2, panel d), where the SST and SAT are comparable. Globally, and in the small and large basins, the SAT is $\approx 0.2$ K warmer than the SST.

Even worse, the vertically-averaged temperature responses corresponding to the

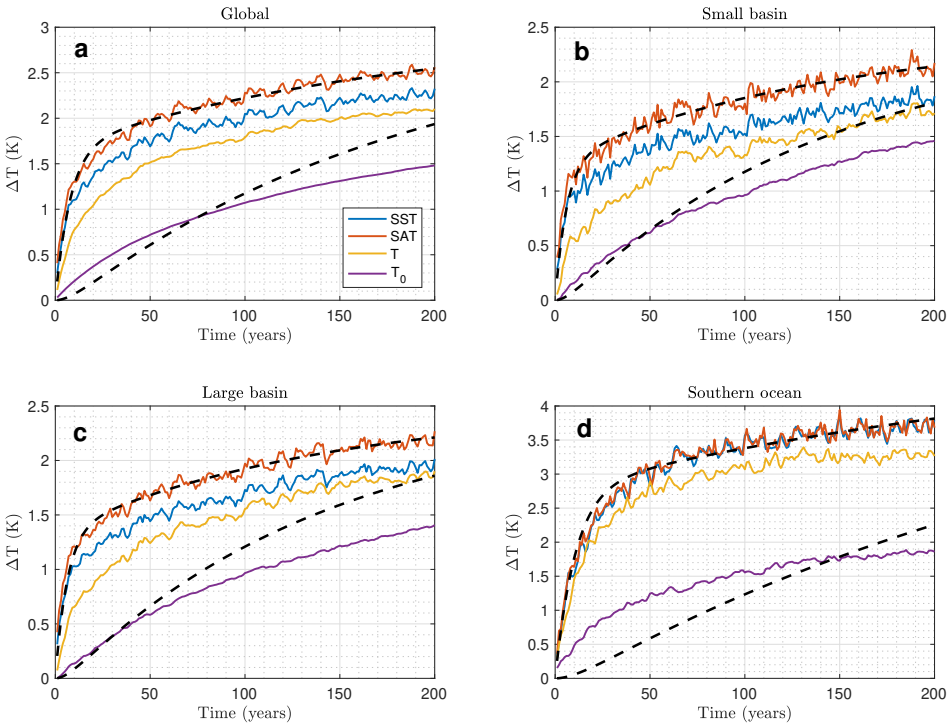



**Figure 5.2:** Time-series of annually-averaged surface air temperature (SAT, orange line) and sea surface temperature (SST, blue line); and vertically-averaged upper-layer temperature ($T$, yellow line) and lower-layer temperature ($T_0$, purple line) corresponding to the derived layer thicknesses presented in table 5.1 for the (a) global, (b) small basin, (c) large basin, and (d) southern ocean regions of DDrake, relative to the control climate state. The fitted Geoffroy EBM responses for $T$ and $T_0$ are shown as black dashed lines.

EBM-predicted upper-layer thicknesses $h$ as presented in table 5.1 (yellow lines) show very little correspondence with the upper-layer black dashed fits. The same is true for the lower-layer responses, corresponding to the EBM-predicted lower-layer thicknesses $H$ (purple lines). As mentioned in section 5.2.1, if we wish to be consistent with the original formulation of the two-layer EBM, the fitted black dashed lines for $T$ and $T_0$ should correspond to the yellow and purple lines respectively in figure 5.2. Evidently, they do not. So, although the SAT response is well-reproduced, the other curves suggest this two-layer EBM poorly represents OHU in DDrake.

Root mean-square errors for each of these fits are shown in table 5.3. The upper-layer fit is evaluated against the upper-layer $T$ response (yellow lines), as well as the SAT response (orange lines) for comparison. The lower-layer fit is evaluated against the lower-layer $T_0$ response (purple lines). The small basin and southern

ocean span the extremes; the small basin has the poorest upper-layer fit, but the best lower-layer fit, while the southern ocean is the opposite. Taking both layers together, the EBM captures the small and large basin responses almost equally well, with the worst overall fit found for the southern ocean.

| | SAT RMSE (K) | Upper-layer $T$ RMSE (K) | Lower-layer $T_0$ RMSE (K) | Total (Upper + Lower) RMSE (K) |
|---|---|---|---|---|
| Global | 0.07 | 0.45 | 0.23 | 0.68 |
| SB | 0.07 | 0.47 | 0.21 | 0.68 |
| LB | 0.06 | 0.39 | 0.28 | 0.67 |
| SO | 0.12 | 0.37 | 0.40 | 0.77 |

**Table 5.3:** Root mean-square errors (RMSEs) for the EBM fits for the upper- and lower-layer temperature responses $T$ and $T_0$ for each basin of DDrake. The RMSE for the upper-layer EBM fit is also evaluated against the SAT response, shown in the left-most column for comparison.

## 5.3 A new EBM framework

We've now seen that the traditional two-layer EBM (equations 5.1) cannot represent the subsurface warming in DDrake (e.g. figure 5.2). To remedy this, we suggest modifying the heat exchange between the two layers by introducing a power, $\zeta$:

$$\begin{aligned} C\frac{dT}{dt} &= \mathcal{F} - \alpha T - \gamma^*(T - T_0)^\zeta \\ C_0\frac{dT_0}{dt} &= \gamma^*(T - T_0)^\zeta \end{aligned} \tag{5.7}$$

Here, we've recast $\gamma$ as $\gamma^*$ to reflect the change in dimensions this coefficient will have (dependent on $\zeta$). In the traditional Geoffroy EBM (equations 5.1), the heat exchange is linear, so $\zeta = 1$.

The temperature difference between the two layers $(T - T_0)$ can be interpreted as a crude representation of the change in stratification. A stronger/weaker temperature difference might indicate a stronger/weaker stratification. In the real ocean, a stronger stratification further isolates the upper ocean from waters below the pycnocline, thus hindering OHU (e.g. [Kuhlbrodt and Gregory, 2012, Marshall and Zanna, 2014, Bourgeois et al., 2022]).

If the upper-layer in the EBM represented the pycnocline and the lower-layer represented the deeper ocean below (like in the model of [Gnanadesikan, 1999]), then an increase in the temperature difference would entail an increase in the stratification. But this is not the case. In the two-layer EBM, the upper-layer represents the mixed-layer, and the lower-layer represents the ocean below the mixed-layer, which includes the pycnocline. So, we cannot simply link a stronger/weaker temperature difference with a stronger/weaker stratification in the EBM.

In the EBM, a stronger temperature difference results in a larger heat exchange between the two layers (for constant $\gamma^*$), thus enhancing OHU. For the Geoffroy EBM solution to a step-function forcing (equations 5.2), this temperature difference grows to a peak on the fast timescale $\tau_f$ and decays to zero over the slow timescale $\tau_s$. It is thus the decrease in the temperature difference over the slow timescale that hinders OHU in the EBM, mimicking the effect of an increasing stratification.

Going back to equations 5.7, increasing or decreasing $\zeta$ conceptually increases or decreases the sensitivity of OHU to the stratification. Given that a *decrease* in the layer temperature difference mimics the effect of an *increase* in the stratification, it is not clear whether increasing $\zeta$ or decreasing $\zeta$ will improve the EBM's performance in emulating the DDrake subsurface warming. We will try both, first increasing the sensitivity with $\zeta = 2$, and then decreasing the sensitivity with $\zeta = 2/3$.

### 5.3.1 New fitting procedure

In section 5.2.1, the fitting of the mode parameters for the Geoffroy EBM relies on prior knowledge of the analytical solution to equations 5.1, but we do not know what the analytical solution is for equations 5.7 with an arbitrary $\zeta$. Also, in order to compare the two different EBM formulations, we should use the same fitting procedure for both; hence we cannot follow the same procedure as in section 5.2.1. Instead, we take a more pragmatic approach.

The radiative parameters $\mathcal{F}$ and $\alpha$ are still found in the same way using the method outlined in [Gregory et al., 2004], but fitting to the mean SST rather than the SAT response. For a given value of $\zeta$, we co-vary the other model parameters $\gamma^*$, $h$, and $H$ aiming to minimise the RMSE of the fit to the SST response, using an interior

point algorithm [Byrd et al., 2000]. These three parameters are subject to lower and upper bounds to eliminate unphysical solutions: $0 < \gamma^*$ (W m$^{-2}$ K$^{-\zeta}$) $< 10$, $10 < h$ (m) $< 500$, and $100 < H$ (m) $< 3000$. The optimal triple $(\gamma^*, h, H)$ that minimises the RMSE is then taken along with the radiative parameters $\mathcal{F}$ and $\alpha$ to define the fit.

This fitting method is in keeping with the spirit of the initial fitting procedure as outlined in section 5.2.1, as the calibration data used comprises only the surface warming (SST) response and net radiative imbalance. The effective heat capacities $C$ and $C_0$ (and hence the layer thicknesses) are determined *a posteriori*, as before. This approach allows for a direct assessment of the EBM's ability in inferring the deep ocean response, as $C_0$ arises from the fitting procedure; no information about the true deep ocean response is given.

### 5.3.2 Increasing the sensitivity ($\zeta = 2$)

We first try increasing the sensitivity to $(T - T_0)$ by setting $\zeta = 2$. This makes the heat exchange in the EBM quadratic, rather than linear, giving the new 'quadratic EBM':

$$\begin{aligned} C\frac{dT}{dt} &= \mathcal{F} - \alpha T - \gamma^*(T - T_0)^2 \\ C_0\frac{dT_0}{dt} &= \gamma^*(T - T_0)^2 \end{aligned} \tag{5.8}$$

#### Fitted parameters

Using the fitting procedure outlined in section 5.3.1, we fit both the Geoffroy and quadratic EBMs to the DDrake temperature responses. The five fitted model parameters (and corresponding layer thicknesses) for each DDrake basin, for both the Geoffroy and quadratic EBMs, can be found in table E.1 in Appendix E. The fitted parameters are qualitatively very similar to what was found before. The upper-layer heat capacities are approximately an order of magnitude smaller than the lower-layer, however the $C$ and $C_0$ values are systematically larger for the quadratic

EBM compared to the Geoffroy EBM, with the ratio $C/C_0$ being slightly smaller (except in the southern ocean). Again, the largest values of $\gamma^{(*)}$ and $H$ are found for the small basin where there is a deep overturning circulation, consistent with the small basin's enhanced heat storage rate (Chapter 4).

### DDrake fitted responses

A comparison of the newly fitted Geoffroy and quadratic EBM responses for DDrake from the interior point algorithm method is shown in figure 5.3. Clearly, the quadratic EBM does a better job than the Geoffroy EBM at capturing the deep-ocean temperature response globally, and for the small and large basins (blue lines in figure 5.3, panels a-c). It is less clear whether a cost is incurred with regard to the upper-layer responses.

Root mean-square errors for each of these fits are shown in table 5.4. The upper-layer fits are evaluated against the implied upper-layer responses (red lines) as well as the SST responses (magenta lines) for comparison. The lower-layer fits are evaluated against the implied lower-layer responses (blue lines). Almost no cost is incurred upon moving from the Geoffroy EBM to the quadratic EBM as the RMSEs for the upper-layer $T$ responses are identical for each EBM (to two significant figures). At the same time, large gains are made for the lower-layer $T_0$ responses (except in the southern ocean).

| | SST RMSE (K) | Upper-layer $T$ RMSE (K) | Lower-layer $T_0$ RMSE (K) | Total (Upper + Lower) RMSE (K) |
|---|---|---|---|---|
| Global | 0.07; 0.07 | 0.23; 0.23 | 0.19; 0.10 | 0.42; 0.33 |
| SB | 0.06; 0.06 | 0.20; 0.20 | 0.12; 0.05 | 0.32; 0.25 |
| LB | 0.05; 0.05 | 0.14; 0.14 | 0.23; 0.09 | 0.37; 0.23 |
| SO | 0.12; 0.13 | 0.41; 0.41 | 0.57; 0.59 | 0.98; 1.00 |

**Table 5.4:** Root mean-square errors (RMSEs) for the (Geoffroy; quadratic) EBM fits for the upper- and lower-layer temperature responses $T$ and $T_0$ for each basin of DDrake. The RMSE for the upper-layer EBM fit evaluated against the SST response is also shown in the left-most column for comparison.

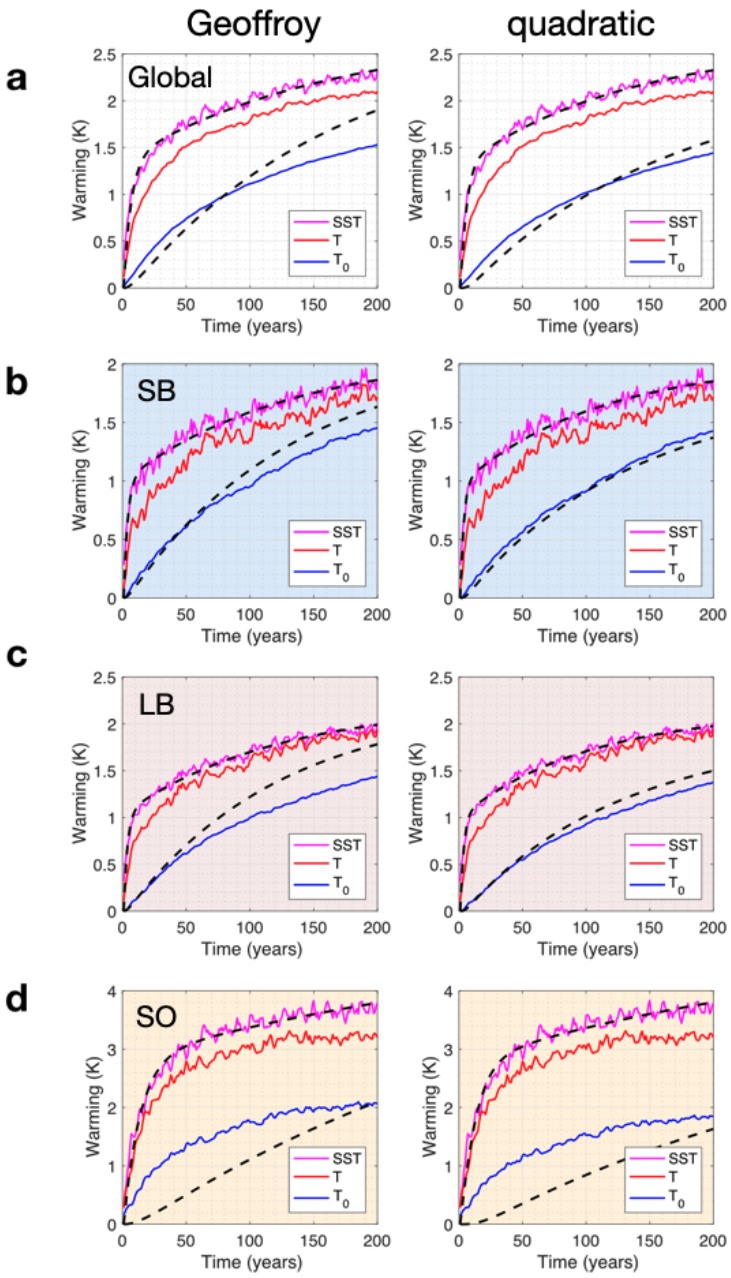



**Figure 5.3:** Comparison of fitted EBM responses (black dashed) for the Geoffroy EBM (left column) and quadratic EBM (right column). Presented are time-series of annually-averaged SST responses (magenta), and vertically-averaged upper-layer (red, $T$) and lower-layer (blue, $T_0$) temperature responses corresponding to the layer thicknesses $h$ and $H$ implied by the EBM (see table E.1), for the DDrake $CO_2$-doubling experiment. Panels (a-d) correspond to the different basins of DDrake: (a) Global responses, (b) Small basin responses (blue shading), (c) Large basin responses (red shading), and (d) southern ocean responses (yellow shading).

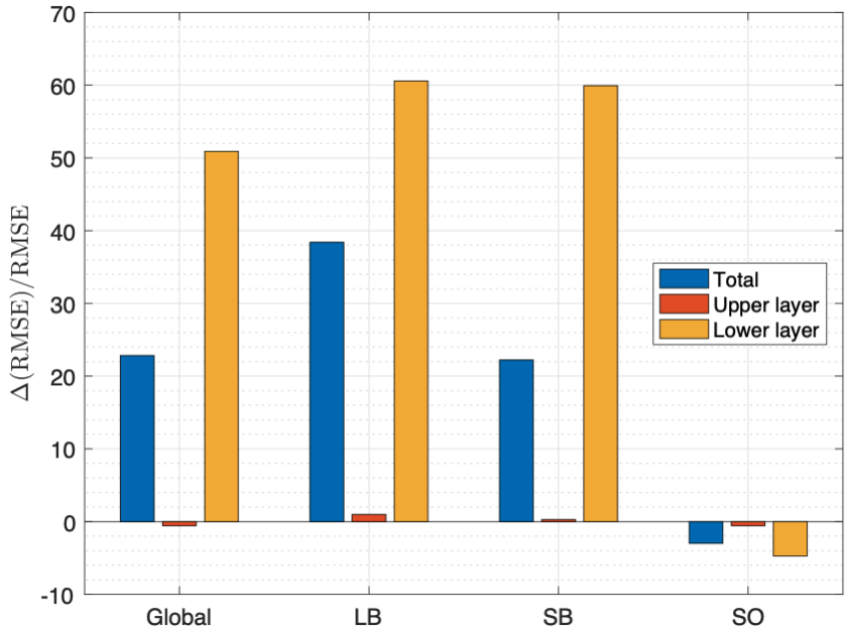



**Figure 5.4:** Percentage improvement in the RMSE of the fitted DDrake temperature responses after changing from the Geoffroy EBM to the quadratic EBM. The change improves fits for all basins but the southern ocean. A substantial increase ($> 50\%$) is seen for the global lower-layer temperature response.

It is more instructive to see the percentage change improvement in the RMSE of the fits upon moving from the Geoffroy EBM to the quadratic EBM (using the same fitting procedure):

$$\text{Improvement} = \frac{\text{RMSE}_{Geoffroy} - \text{RMSE}_{quadratic}}{\text{RMSE}_{Geoffroy}} = \frac{\Delta\text{RMSE}}{\text{RMSE}} \tag{5.9}$$

This performance improvement is shown in figure 5.4. As deduced from table 5.4, almost no change is seen for the upper-layer fits. However, large and substantial improvements are seen for the lower-layer fits. Notably, the switch to the quadratic EBM improves the global-average fits, as well as fits for the small and large basins. Only in the southern ocean is no improvement seen (actually, there is a small decline). Switching to the quadratic EBM leads to a global improvement of $+23\%$, with a striking improvement of $+51\%$ for the lower-layer response. The largest increases ($\sim$+60%) are seen for the lower-layer responses of the small and large basins, with the large basin enjoying the largest overall improvement of $+38\%$.

Note that we have also introduced an improvement in the lower-layer fits simply by changing the fitting procedure. For example, comparing tables 5.3 and 5.4, we see

that the global lower-layer RMSE has changed from 0.23 to 0.19 — same Geoffroy EBM, different fitting procedure. This is only an improvement of +17%, so pales in comparison to the (further) +51% improvement we find upon moving from the Geoffroy EBM to the quadratic EBM (0.19 to 0.10 in table 5.4). Nevertheless, this concealed improvement due to the change in fitting procedure is worth mentioning.

### Results with CMIP5 models

We see large improvements for the lower-layer fits upon moving to the quadratic EBM (increasing $\zeta$ from 1 to 2) for DDrake (figure 5.4). However, this is only for an idealised configuration of the MITgcm. We now test the quadratic EBM on fitting the temperature responses from a suite of five CMIP5 models under abrupt $4\times CO_2$ experiments. We take the radiative parameters $\mathcal{F}$ and $\alpha$ from [Kostov et al., 2014], who tabulated their fitted EBM parameters in their supporting information. Like us, they conceptualised the two-layer EBM as an ocean-only model, and so their radiative forcing values $\mathcal{F}$ include a contribution from the heat exchange between the land and ocean domains. This is not the case for the fitted values for CMIP5 models found in [Geoffroy et al., 2013b], so we do not use their fitted parameters.

We find the other model parameters $\gamma^{(*)}, h$, and, $H$ in the same way as described in section 5.3.1, by co-varying each of them using an interior point algorithm, with the aim to minimise the RMSE of the fit to the CMIP5 model SST response. The parameters $\gamma^{(*)}$ and $h$ are subject to the same upper and lower bounds as before; $H$ is now allowed to vary between 100 and 5000 m, on account of 3000 m no longer being the maximum depth, as is the case in DDrake. Our fitted parameter values can be found in table E.2 in Appendix E. As found before when fitting to the different basins of DDrake (table E.1), the quadratic EBM produces $C$ and $C_0$ values that are systematically larger than those found using the Geoffroy EBM.

We note that the $C$ and $C_0$ values (for both EBMs) are unusually large, with very thick corresponding layer thicknesses. The ensemble mean $C$ and $C_0$ (as well as $\gamma$) are $\sim$5 times larger than those found in [Geoffroy et al., 2013b]. We suggest this is due to methodological differences. However, there is also large intermodel spread in the fitted thermal parameters $(\gamma^{(*)}, h, H)$. We note that the model MRI-CGCM3

is an outlier with regard to our fitting method, as the fitted $h$ from the quadratic EBM is the maximum allowed by the procedure (500 m), and the fitted $H$ from both EBMs is the maximum of 5000 m. This gives this particular model especially high values for $C$ and $C_0$.

Using these fitted parameters, we first check whether the quadratic EBM can skilfully represent the surface warming (SST) response. As mentioned in section 5.2.1, we note this is logically inconsistent as we should be comparing the upper-layer $T$ responses, but this is how two-layer EBMs have typically been used (e.g. [Held et al., 2010, Geoffroy et al., 2013b, Kostov et al., 2014]).

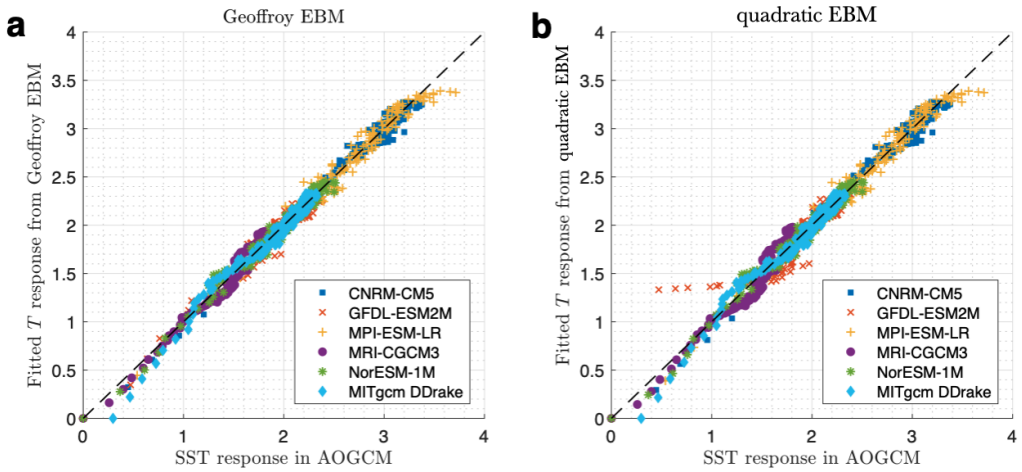



**Figure 5.5:** Comparison between the annual-average global-mean SST response from CMIP5 model abrupt $4\times CO_2$ experiments, and the upper-layer $T$ responses fitted from the two-layer (a) Geoffroy and (b) quadratic EBMs. Points for the abrupt $CO_2$-doubling experiment in DDrake are also plotted for comparison.

Figure 5.5 plots the fitted $T$ responses from both the Geoffroy and quadratic EBMs against the global mean SST responses from abrupt $4\times CO_2$ CMIP5 model experiments. Panel (a) confirms the findings of [Geoffroy et al., 2013b], demonstrating the Geoffroy EBM's skill in reproducing an AOGCM's global surface temperature response (SST rather than SAT, in this case). Panel (b) shows a similar performance for the quadratic EBM, apart from a few points in GFDL-ESM2M with overestimated warming (red crosses).

Comparing the actual AOGCM vertically-averaged layer temperature responses, corresponding to the inferred layer thicknesses $h$ and $H$ in table E.2, paints a different picture. This is shown in figure 5.6, and we see that both EBMs systematically over-

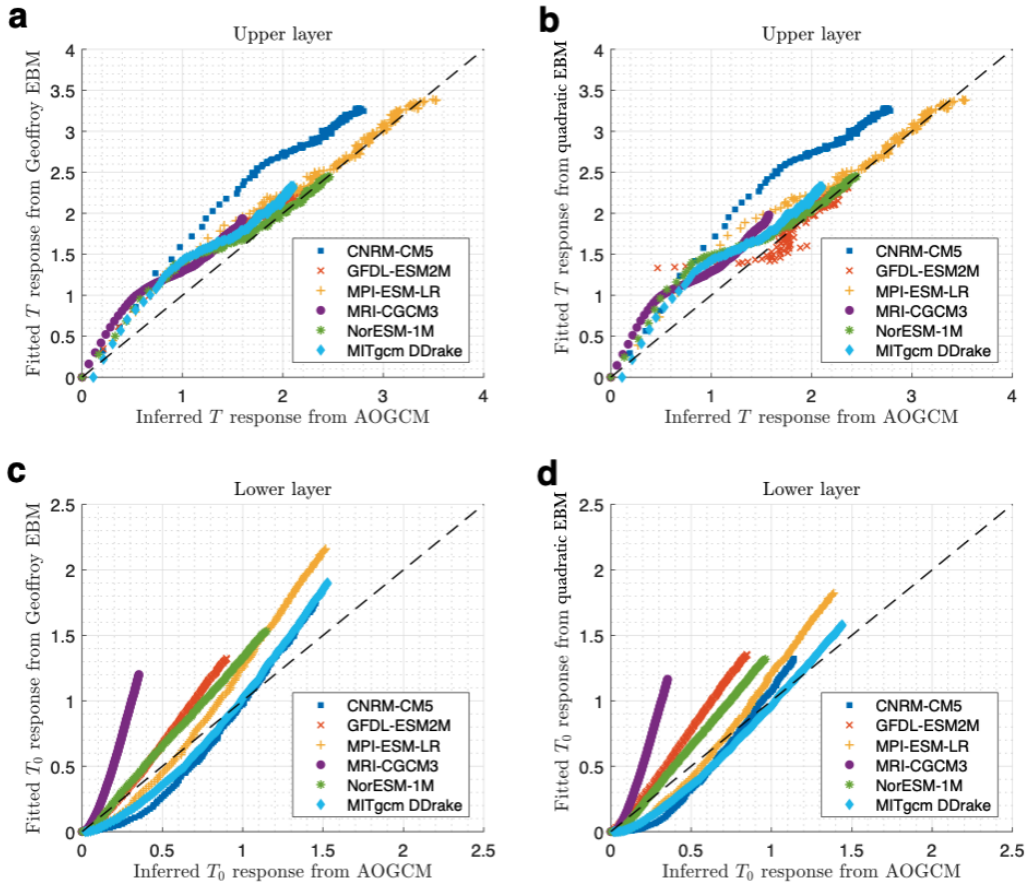



**Figure 5.6:** Comparison between the inferred upper-layer $T$ responses (top row) and lower-layer $T_0$ responses (bottom row) from CMIP5 models with the corresponding fitted responses from both the Geoffroy (left column) and quadratic (right column) two-layer EBMs. Points for the abrupt $CO_2$-doubling experiment in DDrake are also plotted for comparison.

estimate the AOGCM warming response in both the upper and lower layers. It is unclear from this plot whether the quadratic EBM better represents the upper-layer response (top row of figure 5.6), but there is a subtle shift of the curves towards the black dashed line in panel (d) (comparing with panel (c)), indicating that the quadratic EBM better represents the lower-layer temperature response.

To see this more directly, we tabulate the RMSEs for each of these fits in table 5.5, just as we did for the DDrake basin fits in table 5.4. The upper-layer EBM fits are again evaluated against the inferred upper-layer AOGCM responses, as well as the AOGCM SST responses for comparison. The lower-layer EBM fits are evaluated against the inferred lower-layer AOGCM responses.

The RMSEs for each EBM are plotted against each other in figure 5.7, and the

| | SST RMSE (K) | Upper-layer $T$ RMSE (K) | Lower-layer $T_0$ RMSE (K) | Total (Upper + Lower) RMSE (K) |
|---|---|---|---|---|
| CNRM-CM5 | 0.08; 0.08 | 0.59; 0.62 | 0.17; 0.13 | 0.76; 0.75 |
| GFDL-ESM2M | 0.09; 0.15 | 0.21; 0.15 | 0.24; 0.31 | 0.45; 0.46 |
| MPI-ESM-LR | 0.09; 0.10 | 0.15; 0.18 | 0.34; 0.22 | 0.49; 0.40 |
| MRI-CGCM3 | 0.09; 0.11 | 0.30; 0.34 | 0.48; 0.46 | 0.79; 0.80 |
| NorESM-1M | 0.06; 0.07 | 0.15; 0.21 | 0.22; 0.20 | 0.37; 0.41 |
| MITgcm DDrake | 0.07; 0.07 | 0.23; 0.23 | 0.19; 0.10 | 0.42; 0.33 |
| Ensemble mean | 0.08; 0.10 | 0.28; 0.30 | 0.29; 0.26 | 0.57; 0.56 |
| Std. dev. | 0.01; 0.03 | 0.18; 0.19 | 0.12; 0.13 | 0.19; 0.19 |

**Table 5.5:** Root mean-square errors (RMSEs) for the (Geoffroy; quadratic) EBM fits for the upper- and lower-layer temperature responses $T$ and $T_0$ from CMIP5 abrupt 4×$CO_2$ experiments. The RMSE for the upper-layer EBM fit evaluated against the SST response is also shown in the left-most column for comparison. Equivalent RMSEs for DDrake (same as the 'Global' row in table 5.4) are shown in the bottom row for reference. Note that the ensemble means and standard deviations don't include the DDrake values.

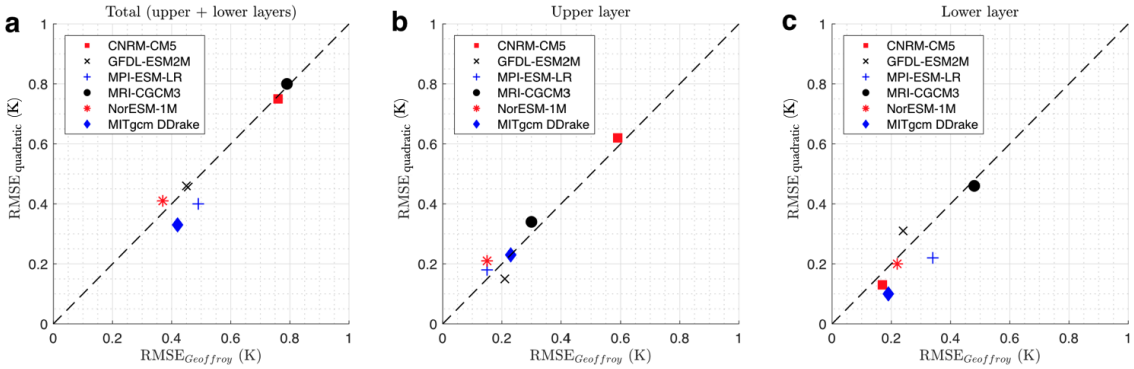



**Figure 5.7:** Comparison between the RMSEs of the fits found from the Geoffroy and quadratic two-layer EBMs for CMIP5 model temperature responses in abrupt 4×$CO_2$ experiments. The (a) total, (b) upper-layer, and (c) lower-layer RMSEs are shown. Points corresponding to the abrupt $CO_2$-doubling experiment in DDrake are also shown as blue diamonds.

percentage improvements (equation 5.9) are shown in figure 5.8 (as was done for the basins of DDrake in figure 5.4). From figure 5.7c, we see that DDrake plus 4 out of the 5 CMIP5 models lie below the black dashed line, showing that the quadratic EBM provides a better fit for the lower-layer temperature response (this can also be seen from table 5.5).

In section 5.3.2, we found that no cost was incurred for the DDrake upper-layer fit in moving to the quadratic EBM. We can see this from figure 5.7b, as DDrake (blue diamond) lies almost exactly on the black dashed line. This is not the case for the CMIP5 models; those models that lay *below* the line for the lower-layer fit (panel c) now lie *above* the line for the upper-layer fit (panel b). This demonstrates that

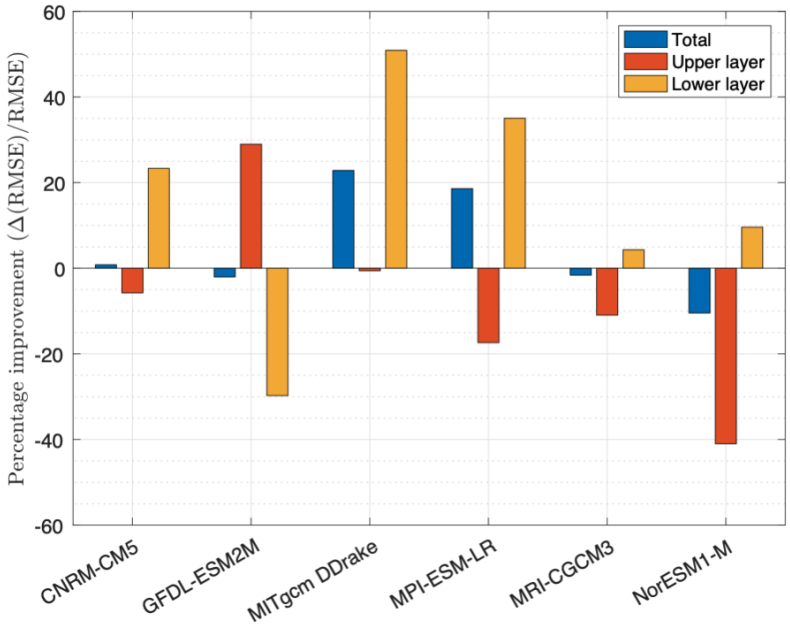



**Figure 5.8:** Percentage improvement in the RMSE of the fitted CMIP5 model (and DDrake) temperature responses after changing from the Geoffroy EBM to the quadratic EBM. The change improves fits for the lower-layer response for 4 out of the 5 CMIP5 models analysed.

a trade-off in the goodness of fits from the upper to the lower layers takes place when moving from the Geoffroy EBM to the quadratic EBM (GFDL-ESM2M being the exception, where the opposite occurs). As the quadratic EBM produces $C$ and $C_0$ values that are systematically larger (table E.2), the inferred warming for both layers is smaller. So, a previous overestimate for the lower-layer warming becomes a better fit, but the upper-layer warming may now be an underestimate, becoming a worse fit.

This is more easily seen in figure 5.8 — where the lower-layer improvements are positive, the upper-layer improvements are negative (and vice versa for GFDL-ESM2M). The results in figure 5.4 for the individual DDrake basins were quite striking. Upon looking at other AOGCMs, we see that the results are mixed. Apart from DDrake, only CNRM-CM5 and MPI-ESM-LR show >10% improvement in the lower-layer fits, and it is only MPI-ESM-LR that shows an overall improvement >10%. Nevertheless, the quadratic EBM improves the lower-layer fits for 4 out of 5 of the CMIP5 models chosen (by an average of 21%), demonstrating that this effect is not limited to the idealised DDrake configuration.

### 5.3.3 Decreasing the sensitivity ($\zeta = 2/3$)

We've now seen that increasing the sensitivity of OHU to the stratification in the two-layer EBM (i.e. increasing $\zeta$ from 1 to 2) improves the representation of subsurface warming in AOGCMs (e.g. figure 5.8). This suggests that decreasing the sensitivity will lead to the opposite effect, but we still need to test this.

First, we need to choose a value for $\zeta < 1$. When we increased the sensitivity, there was a natural progression from linear ($\zeta = 1$) to quadratic ($\zeta = 2$). Here, however, there is no natural progression from linear to sublinear guiding our decision. But we can look to a physical justification for why we might decrease the sensitivity to the stratification.

Overlapping with the mixed-layer in the top ~50 m is the surface Ekman layer. In the subtropical gyres, convergence of Ekman transport leads to downwelling, or 'Ekman pumping'. Surface heat anomalies can thus be pumped down into the ocean interior by the surface winds. Such a mechanism has been found in many modelling studies (e.g. [Zhang and Vallis, 2013, Exarchou et al., 2015, Kuhlbrodt et al., 2015, Saenko et al., 2021]). This is also consistent with our findings from Chapter 3, where we showed that heat is transported downwards by the large-scale wind-driven circulation in DDrake.

We can describe the effect of this Ekman pumping OHU process using the quasi-geostrophic (QG) theory of [Rhines and Young, 1982b] for the wind-driven circulation. Starting with the assumption that potential vorticity is homogenised within the gyre [Rhines and Young, 1982a] (and ignoring relative vorticity), we can derive an expression for the vertical buoyancy transport ($wb$) as a function of the Ekman pumping velocity $w_{Ek}$ and the stratification $\partial b/\partial z$:

$$wb|_{z=0} = \left[\frac{6f_0^2}{\beta}(x - x_E)\right]^{1/3} w_{Ek}^{4/3} \left(\frac{\partial b}{\partial z}\right)^{2/3} \tag{5.10}$$

where $f_0$ is a reference value for the Coriolis parameter, $\beta$ is the variation of the Coriolis parameter with latitude, and $x_E$ is the eastern boundary of the gyre. The full derivation of this equation can be found in Appendix F.

Equation 5.10 shows that the vertical buoyancy transport is proportional to $w_{Ek}^{4/3}$, which is consistent with the idea that a stronger wind stress curl should lead to greater OHU. But the key result here is that $wb$ is also proportional to the 2/3-power of the stratification i.e. the relationship is sublinear.

We can liken the vertical buoyancy transport to the vertical heat exchange in the EBM, where $\gamma^*$ captures the effects of $w_{Ek}$, and $(T - T_0)$ is analogous to $\partial b/\partial z$. This motivates a choice of $\zeta = 2/3$, giving us the new 'Rhines and Young EBM' or 'RY EBM':

$$\begin{aligned} C\frac{dT}{dt} &= \mathcal{F} - \alpha T - \gamma^*(T - T_0)^{2/3} \\ C_0\frac{dT_0}{dt} &= \gamma^*(T - T_0)^{2/3} \end{aligned} \tag{5.11}$$

Fitted parameters

Like before, we fit the RY EBM to the DDrake temperature responses, using the fitting procedure outlined in section 5.3.1. The fitted parameters for each DDrake basin can be found in table E.3 in Appendix E. Similar to the Geoffroy and quadratic EBMs, the RY EBM gives the small basin the largest value for $\gamma^*$, consistent with the SB's enhanced heat storage rate (Chapter 4).

Unlike the other EBMs, however, the RY EBM gives the large basin the largest value for $H$ (1000 m). This is inconsistent with the relative $\Psi_{\theta z}$ depths we found in Chapter 3, as we expect $H$ to be largest for the small basin. Processes scaling with $(T - T_0)^{2/3}$ might be more pronounced in the large basin, which is consistent with a dominance of wind-driven circulations and Ekman pumping there (Chapter 3). This could explain why the fitted $H$ is larger for the LB than for the SB, but this is very speculative.

### DDrake fitted responses

A comparison of the fitted Geoffroy and RY EBM responses for DDrake are shown in figure 5.9. Changing to the RY EBM leads to consistently poorer fits. Initially, the Geoffroy EBM overestimates the DDrake subsurface warming ($T_0$ curves). Changing to the quadratic EBM reduces this overestimation, leading to an improvement in the fits (figure 5.3). Changing to the RY EBM, however, increases this overestimation, leading to even poorer fits than before.

This can be seen more clearly from the RMSEs for each of the fits in table 5.6, and from the percentage change improvement in figure 5.10. There is actually a slight improvement in the fits for the LB and SO, but this is overwhelmed by the especially poor fit for the SB leading to poorer fits overall. The difference in the RY EBM performance between the SB and LB is consistent with their respective mean circulations. Wind-driven circulations dominate in the LB (most relevant to the RY EBM scaling), while the convectively-driven SBMOC dominates the SB (Chapter 3). So, we expect that the RY EBM would work better for the LB than for the SB, and this is what we see in figure 5.10.

| | SST RMSE (K) | Upper-layer $T$ RMSE (K) | Lower-layer $T_0$ RMSE (K) | Total (Upper + Lower) RMSE (K) |
|---|---|---|---|---|
| Global | 0.06; 0.07 | 0.23; 0.23 | 0.19; 0.28 | 0.42; 0.51 |
| SB | 0.06; 0.06 | 0.20; 0.20 | 0.12; 0.20 | 0.32; 0.40 |
| LB | 0.05; 0.08 | 0.14; 0.13 | 0.23; 0.23 | 0.37; 0.36 |
| SO | 0.12; 0.12 | 0.41; 0.33 | 0.57; 0.63 | 0.97; 0.96 |

**Table 5.6:** Root mean-square errors (RMSEs) for the (Geoffroy; RY) EBM fits for the upper- and lower-layer temperature responses $T$ and $T_0$ for each basin of DDrake. The RMSE for the upper-layer EBM fit evaluated against the SST response is also shown in the left-most column for comparison.

### Results with CMIP5 models

Just as we did for the quadratic EBM in section 5.3.2, we now test the RY EBM on fitting temperature responses from the same suite of five CMIP5 models under abrupt $4\times CO_2$ experiments. We take the radiative parameters $\mathcal{F}$ and $\alpha$ from [Kostov et al., 2014] like before, and the thermal parameters $\gamma^{(*)}$, $h$, and $H$ are again found by co-varying each of them using an interior point algorithm, minimising the RMSE

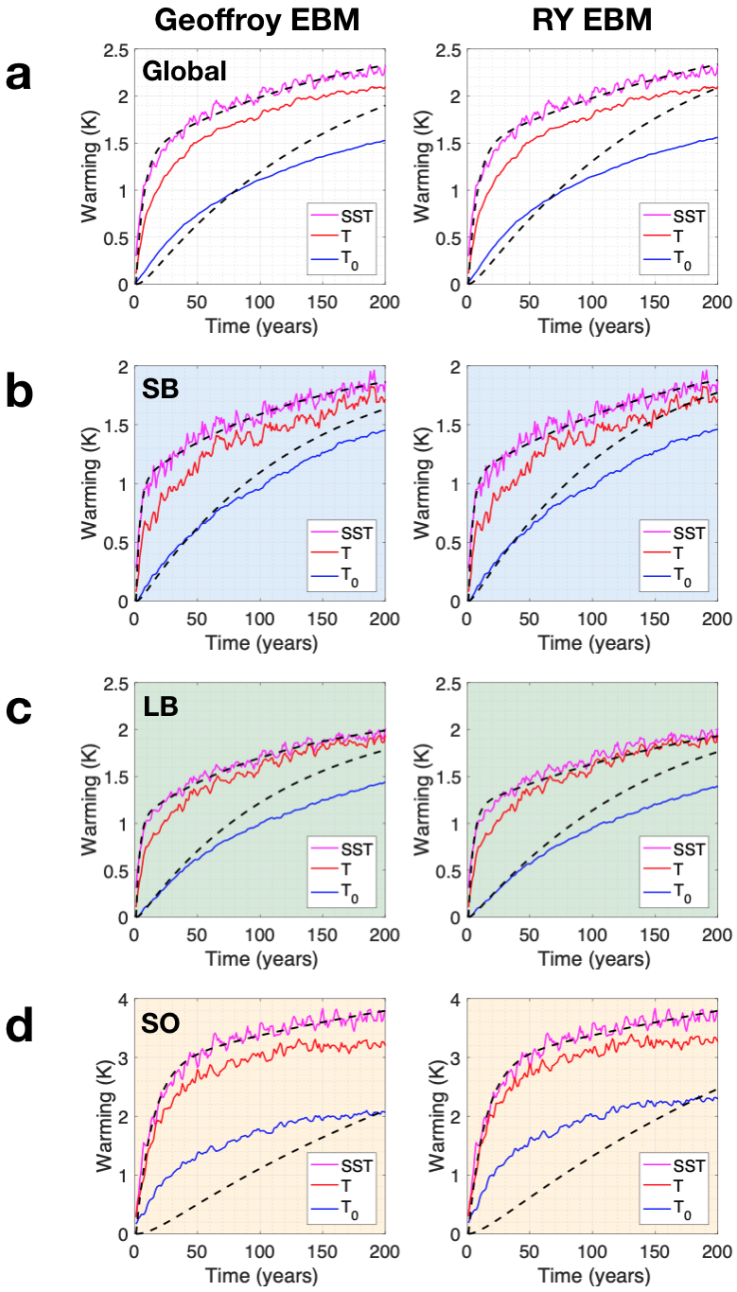



**Figure 5.9:** Comparison of fitted EBM responses (black dashed) for the Geoffroy EBM (left column) and RY EBM (right column). Presented are time-series of annually-averaged SST responses (magenta), and vertically-averaged upper-layer (red, $T$) and lower-layer (blue, $T_0$) temperature responses corresponding to the layer thicknesses $h$ and $H$ implied by the EBM (see table E.3), for the DDrake $CO_2$-doubling experiment. Panels (a-d) correspond to the different basins of DDrake: (a) Global responses, (b) Small basin responses (blue shading), (c) Large basin responses (green shading), and (d) southern ocean responses (yellow shading).

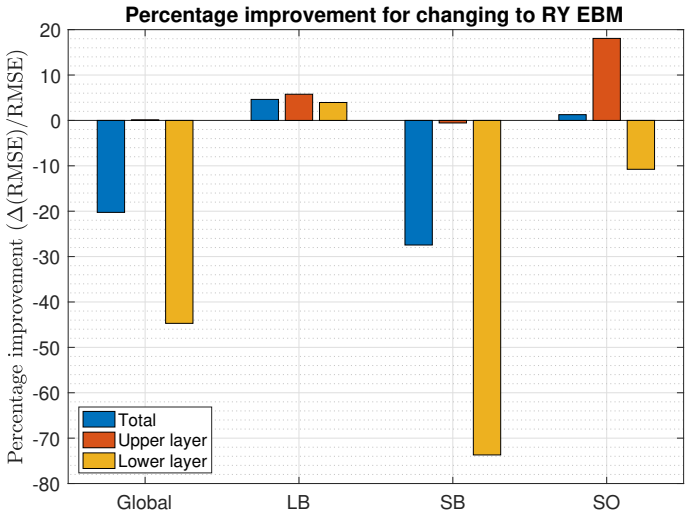



**Figure 5.10:** Percentage improvement in the RMSE of the fitted DDrake temperature responses after changing from the Geoffroy EBM to the RY EBM. The change worsens fits overall, mainly due to the especially poor fit for the SB.

of the fit to the CMIP5 model SST response (subject to the same upper and lower bounds as before).

The fitted parameter values can be found in table E.4 in Appendix E. Whereas the quadratic EBM produced $C$ and $C_0$ values that were systematically larger than those found using the Geoffroy EBM, the RY EBM produces $C$ and $C_0$ values that are systematically *smaller*. This leads to an overestimate of the subsurface warming, resulting in poorer fits overall, as we found for DDrake in the previous section. This can be seen from the RMSEs for each of the fits in table 5.7, and from the percentage change improvement in figure 5.11.

From the SST column in table 5.7, we see that the RY EBM has a similar skill to the Geoffroy EBM in reproducing an AOGCM's surface temperature response. However, the RY EBM gives poorer fits than the Geoffroy EBM across the board (by an average of 10%), except for the model MRI-CGCM3 (blue bars in figure 5.11). Furthermore, the RY EBM worsens the lower-layer fits for all the models analysed by an average of 29% (yellow bars in figure 5.11). So, changing to the RY EBM (i.e. decreasing the sensitivity of OHU to the stratification) does *not* improve the emulation of subsurface warming.

| | SST RMSE (K) | Upper-layer $T$ RMSE (K) | Lower-layer $T_0$ RMSE (K) | Total (Upper + Lower) RMSE (K) |
|---|---|---|---|---|
| CNRM-CM5 | 0.08; 0.08 | 0.59; 0.59 | 0.17; 0.23 | 0.76; 0.82 |
| GFDL-ESM2M | 0.09; 0.08 | 0.21; 0.19 | 0.24; 0.33 | 0.45; 0.52 |
| MPI-ESM-LR | 0.09; 0.09 | 0.15; 0.14 | 0.34; 0.42 | 0.49; 0.56 |
| MRI-CGCM3 | 0.09; 0.07 | 0.30; 0.25 | 0.48; 0.50 | 0.79; 0.75 |
| NorESM-1M | 0.06; 0.06 | 0.15; 0.11 | 0.22; 0.29 | 0.37; 0.40 |
| MITgcm DDrake | 0.06; 0.07 | 0.23; 0.23 | 0.19; 0.28 | 0.42; 0.51 |
| Ensemble mean | 0.08; 0.08 | 0.28; 0.26 | 0.29; 0.35 | 0.57; 0.61 |
| Std. dev. | 0.01; 0.01 | 0.18; 0.19 | 0.12; 0.11 | 0.19; 0.17 |

**Table 5.7:** Root mean-square errors (RMSEs) for the (Geoffroy; RY) EBM fits for the upper- and lower-layer temperature responses $T$ and $T_0$ from CMIP5 abrupt 4×$CO_2$ experiments. The RMSE for the upper-layer EBM fit evaluated against the SST response is also shown in the left-most column for comparison. Equivalent RMSEs for DDrake (same as the 'Global' row in table 5.4) are shown in the bottom row for reference. Note that the ensemble means and standard deviations don't include the DDrake values.

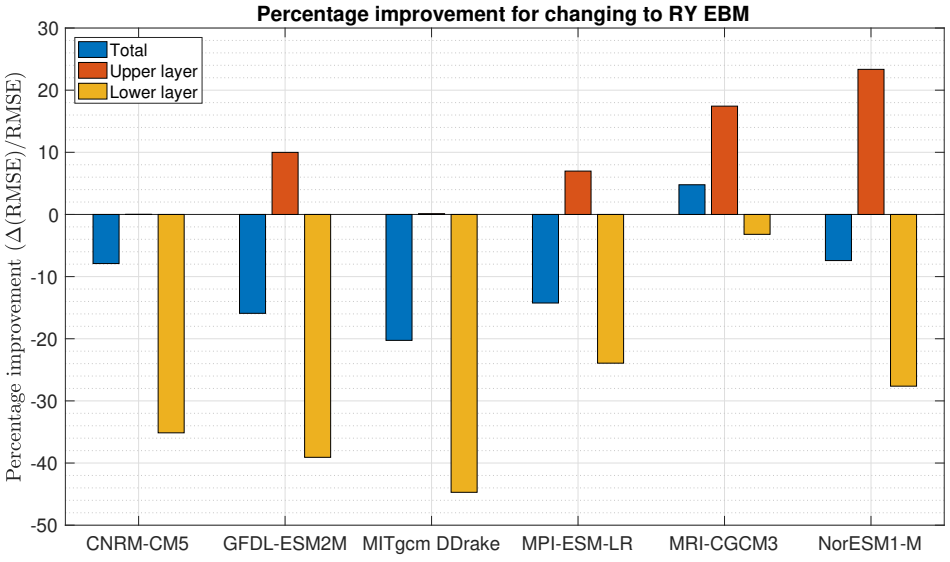



**Figure 5.11:** Percentage improvement in the RMSE of the fitted CMIP5 model (and DDrake) temperature responses after changing from the Geoffroy EBM to the RY EBM. The change leads to poorer fits across the board apart from MRI-CGCM3.

## 5.4 Conclusions

Using the two-layer EBM framework of [Geoffroy et al., 2013b] (equations 5.1), we successfully fitted surface air temperature (SAT) responses for each of the DDrake basins under an abrupt $CO_2$-doubling (figure 5.2). This skill in reproducing surface warming has typically been taken as good evidence for the EBM accurately representing the climate system (e.g. [Held et al., 2010, Geoffroy et al., 2012, Geoffroy et al., 2013b, Kostov et al., 2014]). However, these studies neglect the subsurface warming (i.e. the OHU).

We found that we could interpret the Geoffroy EBM fitted parameters physically, in terms of the DDrake ocean circulation (section 5.2.2). But despite this, the Geoffroy EBM poorly represents the subsurface warming in DDrake (figure 5.2). Work from [Nadiga and Urban, 2019] found that this EBM poorly represents the subsurface warming in the AOGCM CCSM4. From the work in this chapter, we find poor representation of subsurface warming in DDrake and in a suite of five other CMIP5 models (figure 5.6c). We believe that this poor representation should extend to other AOGCMs if probed by other researchers.

We attempted to improve the representation of subsurface warming by proposing a new EBM framework (equations 5.7), which modifies the power law for the heat exchange between the two layers. Increasing or decreasing the power law dependence ($\zeta$) conceptually increases or decreases the sensitivity of OHU to the stratification in the two-layer EBM.

We found that increasing the sensitivity ($\zeta = 1 \rightarrow \zeta = 2$) improves the representation of subsurface warming in DDrake by 51% (figure 5.4), and in 4 other CMIP5 models by an average of 21% (figure 5.8). Decreasing the sensitivity ($\zeta = 1 \rightarrow \zeta = 2/3$) leads to a poorer representation of subsurface warming across all models analysed, however, by an average of 29% (figure 5.11).

We suggested $\zeta = 2/3$ by likening the vertical heat exchange in the EBM to the vertical buoyancy transport within a wind-driven gyre, using the theory of [Rhines and Young, 1982b] (equation 5.10, derived in Appendix F). The derivation of equation 5.10 rests on the assumption that potential vorticity is homogenised within the

gyres [Rhines and Young, 1982a]. Although large regions of homogenisation have been observed in the Atlantic and Pacific Oceans (see e.g. Chapter 20 in [Vallis, 2017]), this may not be the case for the AOGCMs we analysed. Additionally, it is the Southern Ocean, and not the Atlantic and Pacific Oceans, that dominates OHU in models and observations (e.g. [Frölicher et al., 2015, Wijffels et al., 2016, Durack et al., 2018]). These reasons help explain why the RY EBM may not be applicable, and so leads to poorer fits across the board.

The improvement in the fits using $\zeta = 2$ is more puzzling, however. The increased sensitivity to $(T - T_0)$ in the quadratic EBM might highlight the importance of the stratification for OHU. But it is unclear why processes scaling with $(T - T_0)^2$ should be dominant, leading to improvements in the lower-layer fits (although the improvement is quite small). We have no physical justification for the choice of $\zeta = 2$; it was a simply a natural progression from $\zeta = 1$. Clearly, why the quadratic EBM better represents subsurface warming (especially so in DDrake) demands a physical explanation. I hope that future researchers might explore this.

Although we do see improvements in the fits using the quadratic EBM, these improvements are marginal. Previous EBMs have treated $\gamma$ as a constant (e.g. [Gregory, 2000, Held et al., 2010, Geoffroy et al., 2013b, Kostov et al., 2014, Rohrschneider et al., 2019]), and so cannot represent ocean circulation *change*. The quadratic and RY EBMs also suffer from this limitation, despite changes in ocean circulation greatly affecting ocean heat uptake (e.g. [Banks and Gregory, 2006, Xie and Vallis, 2012, Winton et al., 2013, Garuba and Klinger, 2016, Dias et al., 2020b]). (See also Chapters 3 and 4.) Introducing a time-dependent $\gamma$ may be a more fruitful approach to better represent subsurface warming.

The use of only two layers for the EBM should also be questioned. To properly represent subsurface ocean warming, a third layer might be added to account for abyssal warming. (Although, the contribution below 2 km to global OHU is likely less than 10% (e.g. [Desbruyères et al., 2016, Meyssignac et al., 2019])). This would necessarily introduce a millennial timescale in addition to the fast and slow timescales found previously. The model runs used in this study only last 200 years (for DDrake) and 150 years (for the CMIP5 models), so a millennial timescale would

probably not impact our results significantly. But a three-layer model would become more relevant if investigating longer-term warming.

### 5.4.1 Key points

1. Current two-layer energy-balance models (EBMs) poorly represent subsurface warming.
2. Increasing the sensitivity of OHU to the stratification in the EBM improves the representation of subsurface warming in 5 out of 6 AOGCMs analysed.
3. Decreasing the sensitivity worsens the representation of subsurface warming across all AOGCMs analysed.

*"The search for the truth is in one way hard and in another easy — for it is evident that no one of us can master it fully, nor miss it wholly. Each one of us adds a little to our knowledge of nature, and from all the facts assembled arises a certain grandeur."*

Aristotle, c. 350 BCE

# 6

# Conclusion

## 6.1 Summary

In this thesis, I have presented the first study of the response of the DDrake model to an abrupt atmospheric $CO_2$-doubling. Noting that a better understanding of OHU processes is crucial to reduce our uncertainty in climate projections, I have attempted to address this by focussing on OHU processes in DDrake. The model's idealised geometry favours a clear separation of ocean basins with distinct circulation processes. This allows for an evaluation of the role of different circulations for ocean heat storage under transient climate change.

In Chapter 3, we projected the DDrake control-climate ocean circulation onto depth-temperature coordinates to reveal thermal overturning cells. We identified three distinct cells: a warm cell fluxing heat downward, a cool cell fluxing heat upward, and a shallow tropical cell fluxing heat upward (figure 3.5).

Unlike in [Zika et al., 2013], who only looked at the global structure of the thermal overturning, we performed the same calculation regionally for each of the DDrake basins, exploiting the model's simple geometry (figure 3.6). By carefully comparing the SB, LB, and SO thermal overturning structures with the global picture, and with

the overturning in geographical coordinates, we identified the circulation features responsible for the warm, cool, and tropical cells. The warm cell is a wind-driven subtropical-subpolar inter-gyre circulation in the large basin. The cool cell is a combination of the deep small basin MOC and a polar gyre circulation in the large basin. And the tropical cell consists of the shallow Ekman overturning cells in the small and large basins, with upwelling at the equator. We were able to conclude that the warm cell is primarily wind-driven by identifying it in depth-density coordinates as thermally indirect.

We examined how these circulations and their associated vertical heat transports (VHTs) responded to an abrupt $CO_2$-doubling. We demonstrated that a shift in the zonal surface wind stress leads to an Ekman pumping response that serves to reinforce the large basin warm cell circulation (figure 3.15), supporting our conclusion that this cell is wind-driven. This leads to an increase in the downward advective VHT (figure 3.16). At the same time, amplified warming at northern high latitudes results in less vigorous convection feeding the downwelling branch of the SBMOC. The resultant SBMOC weakening is the dominant contributor to a weaker cool cell circulation (figure 3.11). A weaker cool cell also results in an increase in the downward VHT, and both the warm and cool cell responses sum to give $\sim +0.2$ W m$^{-2}$ in the top 2 km (figure 3.16).

This is similar to results from [Zika et al., 2015] for CCSM4, who also found a stronger warm cell and weaker cool cell in a global warming scenario. The key takeaway is that the DDrake circulation response does not 'resist' the warming, but rather permits even greater warming of the ocean interior. This interior ocean warming most likely delays the surface temperature response (e.g. [Gregory, 2000]), making the circulation changes a negative climate feedback. Notably, the interior warming response occurs in spite of the fact that the DDrake ocean circulation also *weakens* substantially by 40% (figure 3.19). This chapter provides a link between ocean circulation and heat storage, drawing a direct correspondence between circulation features and vertical heat transports using thermal overturning cells.

In Chapter 4, we focussed on the SBMOC weakening response, drawing a comparison with the possible weakening of the AMOC in the future (e.g. [Kirtman et al.,

2013, Weijer et al., 2020]). Noting the absence of such a deep overturning circulation in the large basin, we introduced the concept of a 'heat storage contrast' (defined as the difference between the SB and LB heat storage rates) to quantify the difference between the two basins, and perhaps isolate the role of the SBMOC. We found that the small basin warms at a faster rate than the large basin by $0.6 \pm 0.2$ W m$^{-2}$ (figure 4.2). This resembles the Atlantic warming at a faster than the Pacific in observations (by $\sim$0.3 W m$^{-2}$ [Desbruyeres et al., 2017]). We also demonstrated the existence of this Atlantic-Pacific contrast in four CMIP5 models in $CO_2$-quadrupling runs (figure 4.12).

We showed how a rapid advection of surface temperature anomalies into the interior associated with the SBMOC enhances the heat storage rate. The temperature response below 1 km depth in the small basin follows a deep western boundary current, and a plume of deep warming is collocated with the downwelling branch of the SBMOC (figure 4.5). We also ruled out the possibility of heat exchanges with the southern ocean setting the heat storage contrast, as the small basin actually *leaks heat* to the large basin via the southern ocean (figure 4.6). We thus concluded that the reason why the small basin warms at a faster rate than the large basin is due to the presence of the SBMOC. This suggests that the reason why the Atlantic warms at a faster rate than the Pacific is due to the presence of the AMOC.

The more interesting finding, however, is that the SB-LB heat storage contrast remains approximately constant during the simulated 200 years, despite the fact that the SBMOC weakens substantially by $\sim$25%. The weakening thus has little or no impact on the heat storage contrast. We derived a simple expression for the vertical heat flux associated with the SBMOC (Appendix B), enabling us to decompose the response into SBMOC weakening and differential warming components. This decomposition highlighted the dominant role of the control climate overturning, as the terms involving SBMOC weakening compensate each other (figure 4.11). The SBMOC heat flux does actually *increase* with time however, but this additional heat input is lost to the southern ocean, ensuring that the heat storage contrast does not increase in concert. The surprising takeaway is that the *presence* of the SBMOC is important for setting the heat storage contrast, but its subsequent weakening does not lead to a weakening of the contrast. This chapter gives a second link between

ocean circulation and heat storage, finding a counterintuitive relationship for the SBMOC.

Finally, in Chapter 5, we asked whether we could emulate OHU in DDrake using a two-layer energy-balance model (EBM) [Geoffroy et al., 2013b]. We found that we could interpret the fitted EBM parameters physically, and that we could reproduce the DDrake surface warming following a $CO_2$-doubling both globally and basin-wise. However, we were unable to accurately represent the subsurface warming in DDrake, confirming a shortcoming of this EBM pointed out by [Nadiga and Urban, 2019].

We attempted to improve the subsurface warming representation by modifying the power-law dependence $\zeta$ of the heat exchange between the two layers in the EBM, $\gamma^*(T - T_0)^\zeta$. We noted that increasing or decreasing $\zeta$ was analogous to increasing or decreasing the sensitivity of OHU to the stratification in the EBM. We found that increasing the sensitivity from $\zeta = 1 \rightarrow \zeta = 2$ improved the representation of subsurface warming in DDrake by 51% (figure 5.4) and in 4 out of 5 other CMIP5 models by an average of 21% (figure 5.8). Whereas decreasing the sensitivity from $\zeta = 1 \rightarrow \zeta = 2/3$ worsened the subsurface warming representation across all models by an average of 29% (figure 5.11).

The suggestion of $\zeta = 2/3$ came from likening the vertical heat exchange in the EBM to the vertical buoyancy transport within a wind-driven gyre (see Appendix F). The fact that this choice leads to poorer subsurface warming representation suggests that wind-driven gyres do not dominate OHU in the models we analysed. The suggestion of $\zeta = 2$, however, had no physical justification. Why this choice improves on the original EBM remains to be explained.

This final results chapter presents a third link between ocean circulation and heat storage, as we found we could interpret the fitted EBM parameters in terms of the DDrake ocean circulation. But a stronger link may be within grasp, if a robust physical explanation concerning the circulation were offered to explain the improvement upon changing $\zeta = 1 \rightarrow \zeta = 2$.

## 6.2 Conclusions and Outlook

An important finding from Chapter 5 is that current evaluation of two-layer EBMs is physically inconsistent, where the EBM's success is judged by how well the upper-layer (mixed-layer) $T$ reproduces an AOGCM's surface air temperature response. If we are to use this EBM as a physics-based emulator, future studies need to acknowledge this inconsistency and compare like for like quantities. In addition, as pointed out by [Nadiga and Urban, 2019], we should ask of a physics-based emulator to reproduce both the surface *and subsurface* warming. They found that the two-layer EBM could not adequately represent the subsurface warming in CCSM4.

This subsurface warming representation has been neglected by other researchers, who have instead chosen to focus on the two-timescale nature of the surface warming response (e.g. [Held et al., 2010, Geoffroy et al., 2013b, Geoffroy et al., 2013a]). This is surprising, as it neglects consideration of OHU processes. Given an AOGCM's surface warming response (from an abrupt $CO_2$-increase, for example), the two-layer EBM tells you what the corresponding mixed-layer $T$ and deep ocean $T_0$ should be for that AOGCM. If we reduce the AOGCM's ocean into the two layers that correspond to the EBM's predictions (by vertically averaging), we can verify whether the AOGCM is actually behaving as the EBM tells us. The key idea is that if the EBM predictions for $T$ and $T_0$ are poor, then the energy transfer parameterisations in the EBM are likely inaccurate.

We did this procedure for DDrake and five other CMIP5 models in Chapter 5. Rather than focussing on bettering the fit for the surface warming response, we wanted to interrogate the EBM formulation itself. Does heat really transfer from the mixed-layer to the ocean below as $\gamma(T - T_0)$? Other researchers have probably neglected this question for the obvious answer being "no". But it is a question worth asking. Why choose $\gamma(T - T_0)$ otherwise? We hope our suggestion of $\gamma^*(T - T_0)^\zeta$ has at least opened up this discussion. And I hope that future researchers might explain why a choice of $\zeta = 2$ leads to broad improvements in subsurface warming emulation.

I'm not sure if it is possible to solve the RY or quadratic EBM equations analytically.

A nice feature of the Geoffroy EBM equations is that exact expressions for the fast and slow response timescales can be derived in terms of the radiative and thermal properties of the system (see Appendix C). It would be helpful if a similar two-timescale decomposition existed for the quadratic EBM equations' solution, but this is not known. If this were found, this would lend further support for adopting the quadratic EBM equations in emulating AOGCM results, and would bring these equations into the discussion surrounding two-timescale approaches.

The key original finding from Chapter 3 is that the DDrake ocean circulation response permits *more* heat to enter the ocean interior, not less. This happens at the same time as the circulation *weakening* by 40%. The response is due to a strengthening of the warm cell and a weakening of the cool cell, both contributing to an increase in the downward advective heat flux. This complements findings from [Zika et al., 2015], who found a strengthening warm cell and weakening cool cell in a global warming scenario for the model CCSM4. Notably, the circulations responsible for the warm and cool cells in CCSM4 are most likely very different to those in DDrake.

For the CCSM4 warm and cool cells, [Zika et al., 2015] draw a comparison with the thermal overturning found for UVic ESM in [Zika et al., 2013]. They do not analyse the circulations or driving mechanisms responsible for specific cells in CCSM4, but instead assume them to be the same as those diagnosed in UVic ESM because of the close correspondence between their thermal overturning structures. Hence, the warm cell is linked to the Southern Ocean and Atlantic MOC maintained by Southern Hemisphere winds, and the cool cell is linked to AABW formation (as in UVic ESM [Zika et al., 2013]). In DDrake, the warm cell is a wind-driven inter-gyre circulation in the large basin. No such AABW mass exists in DDrake, and the cool cell is a combination of the small basin MOC and a gyre circulation in the large basin.

Due to the very different circulations responsible for the warm and cool cells in DDrake compared to those for UVic ESM, it is perhaps inaccurate to assume that the thermal overturning circulations in UVic ESM and CCSM4 should correspond (as do the authors in [Zika et al., 2015]). Arguably, these two more realistic coupled climate models should bear more resemblance with each other than they do with the

idealised DDrake model, but they do have distinct ocean component models. (UVic ESM uses GFDL's Modular Ocean Model (MOM) [Pacanowski and Griffies, 1996] while CCSM4 uses the Los Alamos Parallel Ocean Program (POP) [Smith et al., 2010]).

Nevertheless, perhaps there are some unifying physical processes shared between the DDrake, UVic ESM, and CCSM4 thermal overturning circulations. In each of these models, the 'warm cell' is identified as wind-driven, and the 'cool cell' is at least partly buoyancy-driven. In response to global warming, increasing surface stratification (e.g. [Li et al., 2020]) should hinder deep water formation (see e.g. [Heuzé et al., 2020] pre-print) and thus weaken cool cell circulations. Additionally, an intensification and poleward shift of the winds (e.g. [Yin, 2005, Swart and Fyfe, 2012, Hu et al., 2020, Goyal et al., 2021]) may lead to a strengthening of (wind-driven) warm cell circulations.

So, irrespective of the specific geographical circulations responsible for the warm and cool cells in each of these models, their driving mechanisms may still provide a clue to their response under transient climate change. The notion that downward advective VHT in the ocean should *increase* in the future is plausible, as we expect warm cells to strengthen and cool cells to weaken. Of course, future process-based analyses of the thermal overturning circulations for other climate models should provide more support for this hypothesis.

Perhaps the key difference between DDrake and these other models is the lack of a realistic Lower MOC Cell, associated with AABW formation. From the depth-density overturning (figure 3.8 in Chapter 3), we deduce that water masses with $\sigma_0 \approx 26.5$ kg m$^{-3}$ sink in the SB northern high-latitudes and fuel the downwelling branch of the SBMOC. In figure 6.1, I plot an inventory of the DDrake control climate ocean volume in temperature-salinity coordinates, both globally and basin-wise. Overlaid are contours of potential density $\sigma_0$.

From the figure, it is clear that no denser water masses exist in the SO (panel b) that 'SB deep water' (panel c) could mix with during its upwelling. In the real world, mixing takes place between North Atlantic Deep Water (NADW) and AABW along the upwelling branch of the AMOC (e.g. [Talley, 2013]). There is thus a densification

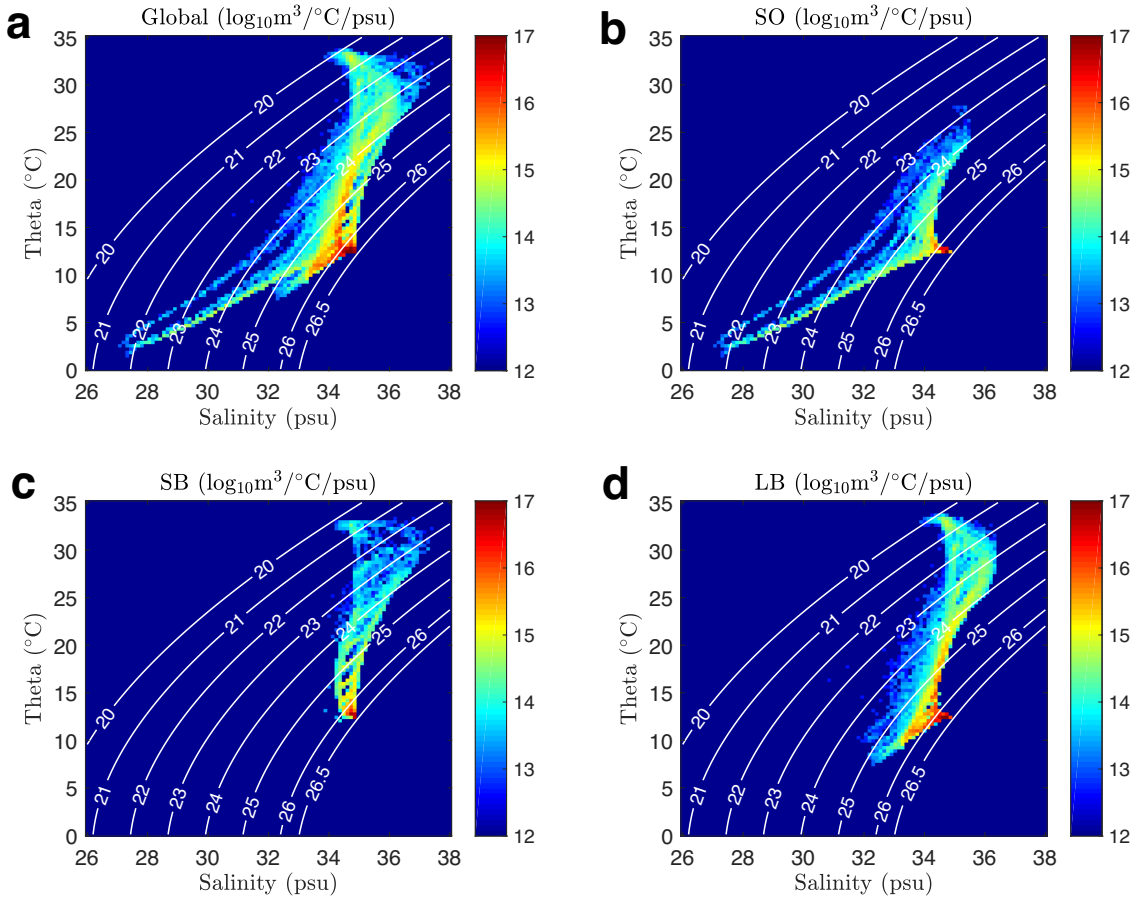



**Figure 6.1:** Census of water masses for the DDrake control climate in temperature-salinity coordinates for (a) global, (b) southern ocean, (c) small basin, and (d) large basin regions (colour, in $\log_{10}$m$^3$/°C/psu). In white are contours of potential density $\sigma_0$ (kg m$^{-3}$).

of the upwelling waters sourced from the North Atlantic high-latitudes, making the upwelling AMOC branch denser than the downwelling branch. This leads to the AMOC cell being thermally indirect in depth-temperature coordinates, as found in [Zika et al., 2013, Saenko et al., 2018, Savita et al., 2021], which suggests it must be driven by the Southern Hemisphere winds (ignoring haline effects). The lack of an analogous AABW mass in DDrake means that no such mixing takes place during the SBMOC upwelling, and so the water cannot become any denser. Hence, the SBMOC cell ends up being thermally direct rather than indirect (as found in Chapter 3).

Staying within the simple aquaplanet modelling framework, a natural next step would be to introduce a circular Antarctic continent at the South Pole of DDrake, with a suitable choice of continental slope. An increase in the model sea ice thickness diffusion would promote formation and equatorward transport of sea ice near the South Pole. This should hopefully encourage brine rejection, bottom water formation, and the development of an AABW-like overturning cell. (The introduction of the Antarctic land mass would also eliminate the easterly current running counter-clockwise around the South Pole of DDrake.) Projecting again the resultant circulation state onto depth-temperature (or depth-sigma) coordinates would help assess the role of the AABW circulation.

It would be most interesting to see if this changed the character of the SBMOC from thermally direct to thermally indirect. The introduction of this AABW circulation might then bring the DDrake thermal overturning structure into line with the more sophisticated climate models, and provide avenues to explore the influence of Lower Cell MOC weakening on transient climate change (e.g. [Suzuki et al., 2022]), rather than Upper Cell (AMOC) weakening (as we did in Chapter 4).

A major theme of this thesis has been to try and find a mechanistic link between ocean circulation and heat storage. Following on from the data presented in figure 6.1, another future direction is to use the 'water mass transformation' (WMT) framework first introduced by [Walin, 1982]. In this framework, the ocean is partitioned into conceptually distinct water masses characterised by particular scalar properties (such as temperature and salinity). Changes in water masses are caused

by property exchanges at boundary layers (e.g. air-sea fluxes, geothermal heating) or interior mixing processes. Defining water masses by buoyancy (approximated by potential density) gives a direct connection to circulation. The approach thus offers measures of the ocean circulation within the WMT phase space without needing any direct measures of the circulation itself (see review by [Groeskamp et al., 2019]).

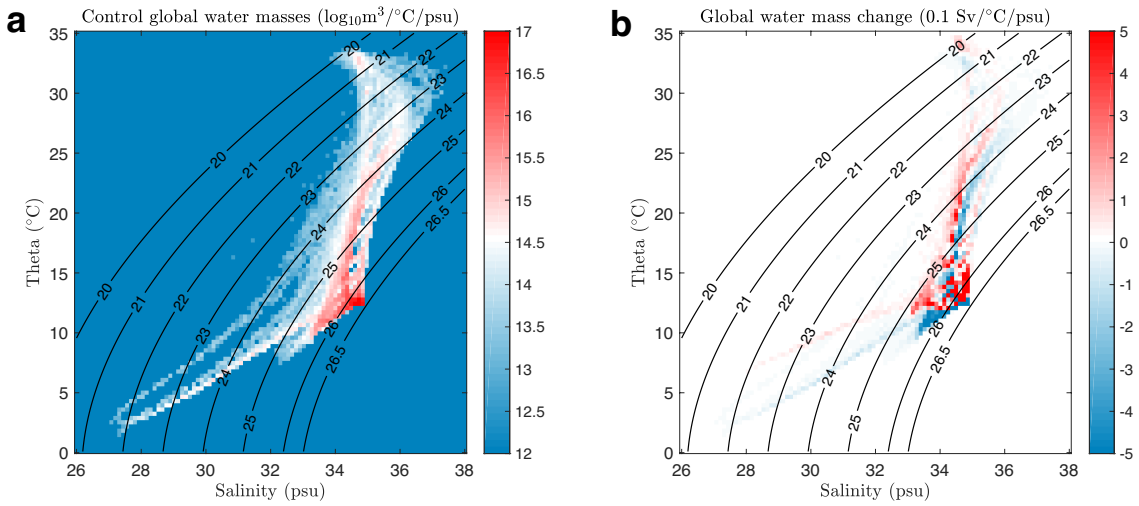



**Figure 6.2:** (a) Global water mass census for the DDrake control climate in temperature-salinity coordinates in $\log_{10}$m$^3$/°C/psu (equivalent to panel a from figure 6.1). (b) Average water mass transformation rate between the control climate and year 200 of the $CO_2$-doubling run in 0.1 Sv/°C/psu. Black lines are contours of potential density $\sigma_0$ (kg m$^{-3}$).

In figure 6.2, I plot the water mass change between the control climate and year 200 of the $CO_2$-doubling experiment, divided by the 200 years (to give a WMT rate). Water masses are eroded from the blue regions and created in the red regions in panel b. The challenge is to estimate the 'map' from the blue regions to the red regions, and infer the mechanisms associated with those water mass transformations. For example, we can already see that for water masses with temperatures below ~12°C, there appears to be a shift 'upward' in temperature space from the blue arm of water masses to the red arm (possibly along isopycnals). This indicates strong radiative/sensible heating without much role for evaporation/precipitation, and this must be occurring in the southern ocean region (compare with figure 6.1b).

A recent paper from [Zika et al., 2020] attempted to infer mechanisms of OHC change in this way, only considering changes in water masses from 11 years of observational estimates from the EN4 data set [Good et al., 2013]. They estimate such a map from 'early' water masses (2006-2011) to 'late' water masses (2012-2017) in temperature-

salinity (T-S) space using an Earth Mover Distance (EMD) algorithm [Pele and Werman, 2009]. This minimises the 'distance' in T-S space a water mass has to move to go from the 'early' to the 'late' states. As advection plays no role in T-S space (assuming it does no mixing), the method allows an estimation of the *material* warming added to the ocean (distinct from warming caused by the redistribution of background OHC due to changes in ocean circulation).

The role of circulation in the *redistribution* warming can be found as a residual between the total warming and the inferred material warming due to water mass changes (i.e. $\Delta T_{redistribution} = \Delta T_{total} - \Delta T_{material}$). This is similar to the 'added' and 'redistributed' heat components seen in previous studies (e.g. [Banks and Gregory, 2006, Xie and Vallis, 2012, Garuba and Klinger, 2016]). Plotting maps of the material and redistributed warming components, they find that the redistributed signal is very heterogenous, while the material warming shows a coherent increase over the entire globe [Zika et al., 2020]. Notably, the material OHC change peaks at 35°S and 35°N, collocated with peaks of Ekman downwelling. This is consistent with the theme of wind-driven OHU for the warm cell in Chapter 3.

Another striking feature from their results is the clear Atlantic-Pacific contrast in the material OHC change. They find that the North Atlantic ($< 44$°N) stores 24% of the global material OHC change despite representing less than 12% of the global surface area. A similar calculation for DDrake finds that, 200 years after the $CO_2$-doubling, the SB is responsible for 24% of the global OHC increase despite covering 18% of the global surface area.

In Chapter 4 we defined a heat storage contrast between the small and large basins of DDrake, finding the SB to warm at a faster rate than the LB by $0.6 \pm 0.2$ W m$^{-2}$. Using the total OHC change data from Table 1 in [Zika et al., 2020], there is an Atlantic-Pacific contrast of $\sim$1 W m$^{-2}$. (The Atlantic OHC increase is 135 TW, and the Pacific increase is 49 TW. I take the Atlantic and Pacific surface areas to be 81.8 million km$^2$ and 161.8 million km$^2$, respectively*.) Notably, if we perform the same calculation using only the *material* OHC change data, we still find an Atlantic-Pacific contrast of $\sim$0.5 W m$^{-2}$. This crude calculation highlights that the contrast

*Using estimates from NOAA at https://www.ngdc.noaa.gov/mgg/global/etopo1_ocean_volumes.html.

is not simply due to circulation changes (e.g. AMOC weakening). It suggests the importance of background ocean circulations in setting the heat storage contrast, which we argued for in Chapter 4 with the case of the SBMOC setting the contrast between the small and large basins of DDrake.

Performing a similar WMT analysis for DDrake would help isolate the role of circulation *changes* through the material/redistributed decomposition. Although there exist other methods to form such a decomposition, either through the use of passive tracers (e.g. [Banks and Gregory, 2006]) or by 'fixing' currents to their control climate state [Winton et al., 2013], the added information from the water mass changes could also help shed light on the *causes* of those circulation changes. The method used in [Zika et al., 2020] is also novel and understudied, so applying it to a simple model such as DDrake brings with it the benefits of easier evaluation and interpretation.

The key message from Chapter 4 is that the Atlantic punches above its weight in terms of ocean heat storage. This is seen in models in $CO_2$-increase experiments (e.g. [Kuhlbrodt and Gregory, 2012, Shatwell et al., 2020]), and in observations (e.g. [Desbruyeres et al., 2017, Zika et al., 2020]). We argued that the analogous enhanced SB heat storage in DDrake was due to the presence of the SBMOC. However, it's been suggested that enhanced ocean heat storage in the Atlantic is in fact due to an enhanced inter-ocean heat transport from the Indian to the Atlantic basin via Agulhas leakage [Lee et al., 2011]. This contradicts our findings from Chapter 4, where we showed that the SB-LB heat storage contrast persists despite the fact that heat actually leaks from the SB to the LB via the SO, and not the other way around (figure 4.6).

We did not show the pathways of this SB-LB heat exchange. Different Agulhas-like leakages were found by [Nilsson et al., 2013] in a very similar modelling set-up to DDrake. Here, however, the leakage depended on the meridional boundary extents being equatorward or poleward of the zero wind line. Only if the 'African' continent (i.e. the Eastern boundary of the basin with deep water formation) were equatorward of the zero wind line would this permit an Agulhas-like leakage just south of this boundary. In DDrake, both meridional boundaries extend to 35°S, *poleward* of the

zero wind line near 30°S. We therefore do not expect such an Agulhas-like leakage from the LB to the SB in DDrake. There could instead be an 'anti-Agulhas-like' leakage slipping under the SB's eastern boundary into the LB (explaining the SB-to-LB heat leakage), but this would mean the analogous Atlantic/Indian basin roles would be reversed.

So, although we showed the SB leaking heat to the LB (via the SO) in Chapter 4, it is not clear exactly what causes this. It is worth noting that the redistribution component in [Zika et al., 2020] shows an anomalous *southward* transport of heat from the Atlantic into the Southern Ocean (in contrast to the northward heat transport from Agulhas leakage assumed in [Lee et al., 2011]). The role of Agulhas leakage in transient climate change is thus another open question that could be explored using the DDrake configuration (perhaps with higher resolution, due to the key role of mesoscale eddies).

Agulhas leakage is expected to increase with a poleward shift of the Southern Hemisphere winds (e.g. [Biastoch et al., 2009]). This also directly impinges on AMOC weakening, as an increase in warm, salty water from the Indian Ocean entering the Atlantic could help *strengthen* the AMOC [Beal et al., 2011], thus counteracting weakening due to increased surface buoyancy forcing from Arctic amplification and sea ice melt (e.g. [Sévellec et al., 2017, Dai et al., 2019, Dai, 2022]). Future Lagrangian studies with simulated virtual particles may help better reveal the circulation pathways in DDrake (see review by [Van Sebille et al., 2018]), and perhaps shed light on the interplay between Agulhas-like leakage, the heat storage contrast, and MOC weakening.

The work in this thesis has provided the first results revealing the DDrake model's response to an abrupt $CO_2$-doubling. It has also hopefully put this model on the map for its utility in answering fundamental climate dynamics questions related to transient climate change. As mentioned in Chapter 1, this thesis provides a contribution to the hierarchical approach to climate modelling (as exhorted by [Held, 2005]), where DDrake occupies an intermediate position in the model hierarchy, between simple climate models (e.g. EBMs) on one end, and high-resolution Earth system models (ESMs) on the other. I have attempted to connect DDrake to these

other models spanning the hierarchy through Chapters 3 to 5. I hope the unique insights garnered from using an intermediate model, aided by its simple geometry and clean circulation decomposition, clearly reveal its utility.

I hope this thesis builds towards a stronger, process-based understanding of OHU, and helps to underpin a link between ocean circulation and heat storage. Only by having a clear understanding of circulation changes and their effect on OHU can we make more confident projections of future climate changes.

# Bibliography

[Abernathey et al., 2011] Abernathey, R., Marshall, J., and Ferreira, D. (2011). The dependence of southern ocean meridional overturning on wind stress. *Journal of Physical Oceanography*, 41(12):2261–2278.

[Abernathey and Marshall, 2013] Abernathey, R. P. and Marshall, J. (2013). Global surface eddy diffusivities derived from satellite altimetry. *Journal of Geophysical Research: Oceans*, 118(2):901–916.

[Adcroft and Campin, 2004] Adcroft, A. and Campin, J.-M. (2004). Rescaled height coordinates for accurate representation of free-surface flows in ocean circulation models. *Ocean Modelling*, 7(3-4):269–284.

[Adcroft et al., 2004a] Adcroft, A., Campin, J.-M., Hill, C., and Marshall, J. (2004a). Implementation of an atmosphere–ocean general circulation model on the expanded spherical cube. *Monthly Weather Review*, 132(12):2845–2863.

[Adcroft et al., 2004b] Adcroft, A., Hill, C., Campin, J.-M., Marshall, J., and Heimbach, P. (2004b). Overview of the formulation and numerics of the mit gcm. In *Proceedings of the ECMWF seminar series on Numerical Methods, Recent developments in numerical methods for atmosphere and ocean modelling*, pages 139–149.

[Alley et al., 2001] Alley, R., Anandakrishnan, S., and Jung, a. P. (2001). Stochastic resonance in the north atlantic. *Paleoceanography*, 16(2):190–198.

[Alley and Clark, 1999] Alley, R. B. and Clark, P. U. (1999). The deglaciation of the northern hemisphere: a global perspective. *Annual Review of Earth and Planetary Sciences*, 27(1):149–182.

[Andrews et al., 2012] Andrews, T., Gregory, J. M., Forster, P. M., and Webb, M. J. (2012). Cloud adjustment and its role in co2 radiative forcing and climate sensitivity: A review. *Surveys in geophysics*, 33(3):619–635.

[Armour et al., 2016] Armour, K. C., Marshall, J., Scott, J. R., Donohoe, A., and Newsom, E. R. (2016). Southern ocean warming delayed by circumpolar upwelling and equatorward transport. *Nature Geoscience*, 9(7):549.

[Arrhenius, 1896] Arrhenius, S. (1896). Xxxi. on the influence of carbonic acid in the air upon the temperature of the ground. *The London, Edinburgh, and Dublin Philosophical Magazine and Journal of Science*, 41(251):237–276.

[Banks and Gregory, 2006] Banks, H. T. and Gregory, J. M. (2006). Mechanisms of ocean heat uptake in a coupled climate model and the implications for tracer based predictions of ocean heat uptake. *Geophysical Research Letters*, 33(7).

[Beal et al., 2011] Beal, L. M., De Ruijter, W. P., Biastoch, A., and Zahn, R. (2011). On the role of the agulhas system in ocean circulation and climate. *Nature*, 472(7344):429–436.

[Bellomo et al., 2021] Bellomo, K., Angeloni, M., Corti, S., and von Hardenberg, J. (2021). Future climate change shaped by inter-model differences in atlantic meridional overturning circulation response. *Nature Communications*, 12(1):1–10.

[Biastoch et al., 2009] Biastoch, A., Böning, C. W., Schwarzkopf, F. U., and Lutjeharms, J. (2009). Increase in agulhas leakage due to poleward shift of southern hemisphere westerlies. *Nature*, 462(7272):495–498.

[Blunden et al., 2018] Blunden, J., Hartfield, G., Arndt, D., DUNN, R., TYE, M., Blenkinsop, S., Donat, M., Durre, I., Ziese, M., Cooper, O., et al. (2018). State of the climate in 2017. *Bulletin of the American Meteorological Society*, 99(8):Si–S310.

[Bodman and Jones, 2016] Bodman, R. W. and Jones, R. N. (2016). Bayesian estimation of climate sensitivity using observationally constrained simple climate models. *Wiley Interdisciplinary Reviews: Climate Change*, 7(3):461–473.

[Bonnet et al., 2021] Bonnet, R., Swingedouw, D., Gastineau, G., Boucher, O., Deshayes, J., Hourdin, F., Mignot, J., Servonnat, J., and Sima, A. (2021). Increased risk of near term global warming due to a recent amoc weakening. *Nature communications*, 12(1):1–9.

[Bourgeois et al., 2022] Bourgeois, T., Goris, N., Schwinger, J., and Tjiputra, J. F. (2022). Stratification constrains future heat and carbon uptake in the southern ocean between 30° s and 55° s. *Nature Communications*, 13(1):1–8.

[Bouttes et al., 2012] Bouttes, N., Gregory, J., Kuhlbrodt, T., and Suzuki, T. (2012). The effect of windstress change on future sea level change in the southern ocean. *Geophysical Research Letters*, 39(23).

[Boyer et al., 2018] Boyer, T. P., Garcia, H. E., Locarnini, R. A., Zweng, M. M., Mishonov, A. V., Reagan, J. R., Weathers, K. A., Baranova, O. K., Seidov, D., and Smolyar, I. V. (2018). World ocean atlas 2018. https://www.ncei.noaa.gov/archive/accession/NCEI-WOA18.

[Broecker, 1997] Broecker, W. S. (1997). Thermohaline circulation, the achilles heel of our climate system: Will man-made co2 upset the current balance? *Science*, 278(5343):1582–1588.

[Bryan and Cox, 1967] Bryan, K. and Cox, M. D. (1967). A numerical investigation of the oceanic general circulation. *Tellus*, 19(1):54–80.

[Bryden and Imawaki, 2001] Bryden, H. L. and Imawaki, S. (2001). Ocean heat transport. *International Geophysics*, 77:455–474.

[Buckley et al., 2012] Buckley, M. W., Ferreira, D., Campin, J.-M., Marshall, J., and Tulloch, R. (2012). On the relationship between decadal buoyancy anomalies and variability of the atlantic meridional overturning circulation. *Journal of climate*, 25(23):8009–8030.

[Buckley and Marshall, 2016] Buckley, M. W. and Marshall, J. (2016). Observations, inferences, and mechanisms of the atlantic meridional overturning circulation: A review. *Reviews of Geophysics*, 54(1):5–63.

[Budyko, 1969] Budyko, M. I. (1969). The effect of solar radiation variations on the climate of the earth. *tellus*, 21(5):611–619.

[Butler et al., 2013] Butler, E., Oliver, K., Gregory, J. M., and Tailleux, R. (2013). The ocean's gravitational potential energy budget in a coupled climate model. *Geophysical Research Letters*, 40(20):5417–5422.

[Byrd et al., 2000] Byrd, R. H., Gilbert, J. C., and Nocedal, J. (2000). A trust region method based on interior point techniques for nonlinear programming. *Mathematical programming*, 89(1):149–185.

[Byrne and Goldblatt, 2014] Byrne, B. and Goldblatt, C. (2014). Radiative forcing at high concentrations of well-mixed greenhouse gases. *Geophysical Research Letters*, 41(1):152–160.

[Caesar et al., 2021] Caesar, L., McCarthy, G., Thornalley, D., Cahill, N., and Rahmstorf, S. (2021). Current atlantic meridional overturning circulation weakest in last millennium. *Nature Geoscience*, 14(3):118–120.

[Caesar et al., 2020] Caesar, L., Rahmstorf, S., and Feulner, G. (2020). On the relationship between atlantic meridional overturning circulation slowdown and global surface warming. *Environmental Research Letters*, 15(2):024003.

[Caesar et al., 2018] Caesar, L., Rahmstorf, S., Robinson, A., Feulner, G., and Saba, V. (2018). Observed fingerprint of a weakening atlantic ocean overturning circulation. *Nature*, 556(7700):191–196.

[Callendar, 1938] Callendar, G. S. (1938). The artificial production of carbon dioxide and its influence on temperature. *Quarterly Journal of the Royal Meteorological Society*, 64(275):223–240.

[Campin et al., 2008] Campin, J.-M., Marshall, J., and Ferreira, D. (2008). Sea ice–ocean coupling using a rescaled vertical coordinate z$*$. *Ocean Modelling*, 24(1-2):1–14.

[Caneill et al., 2022] Caneill, R., Roquet, F., Madec, G., and Nycander, J. (2022). The polar transition from alpha to beta regions set by a surface buoyancy flux inversion. *Journal of Physical Oceanography*.

[Carmack, 2007] Carmack, E. C. (2007). The alpha/beta ocean distinction: A perspective on freshwater fluxes, convection, nutrients and productivity in high-latitude seas. *Deep Sea Research Part II: Topical Studies in Oceanography*, 54(23-26):2578–2598.

[Cessi, 2019] Cessi, P. (2019). The global overturning circulation. *Annual review of marine science*, 11:249–270.

[Cessi and Jones, 2017] Cessi, P. and Jones, C. S. (2017). Warm-route versus cold-route interbasin exchange in the meridional overturning circulation. *Journal of Physical Oceanography*, 47(8):1981–1997.

[Charney et al., 1979] Charney, J. et al. (1979). *Carbon Dioxide and Climate: A Scientific Assessment: Report of an Ad Hoc Study Group on Carbon Dioxide and Climate, Woods Hole, Massachusetts, July 23-27, 1979 to the Climate Research Board, Assembly of Mathematical and Physical Sciences, National Research Council*. National Academies.

[Chen et al., 2008] Chen, G., Lu, J., and Frierson, D. M. (2008). Phase speed spectra and the latitude of surface westerlies: Interannual variability and global warming trend. *Journal of Climate*, 21(22):5942–5959.

[Chen and Tung, 2014] Chen, X. and Tung, K.-K. (2014). Varying planetary heat sink led to global-warming slowdown and acceleration. *Science*, 345(6199):897–903.

[Chen and Tung, 2018] Chen, X. and Tung, K.-K. (2018). Global surface warming enhanced by weak atlantic overturning circulation. *Nature*, 559(7714):387–391.

[Cheng et al., 2019] Cheng, L., Abraham, J., Hausfather, Z., and Trenberth, K. E. (2019). How fast are the oceans warming? *Science*, 363(6423):128–129.

[Cheng et al., 2017] Cheng, L., Trenberth, K. E., Fasullo, J., Boyer, T., Abraham, J., and Zhu, J. (2017). Improved estimates of ocean heat content from 1960 to 2015. *Science Advances*, 3(3):e1601545.

[Cheng et al., 2013] Cheng, W., Chiang, J. C., and Zhang, D. (2013). Atlantic meridional overturning circulation (amoc) in cmip5 models: Rcp and historical simulations. *Journal of Climate*, 26(18):7187–7197.

[Church et al., 2013] Church, J. A., White, N. J., Domingues, C. M., Monselesan, D. P., and Miles, E. R. (2013). Sea-level and ocean heat-content change. In *International Geophysics*, volume 103, pages 697–725. Elsevier.

[Cohen et al., 2014] Cohen, J., Screen, J. A., Furtado, J. C., Barlow, M., Whittleston, D., Coumou, D., Francis, J., Dethloff, K., Entekhabi, D., Overland, J., et al. (2014). Recent arctic amplification and extreme mid-latitude weather. *Nature geoscience*, 7(9):627–637.

[Colman and Soldatenko, 2020] Colman, R. and Soldatenko, S. (2020). Understanding the links between climate feedbacks, variability and change using a two-layer energy balance model. *Climate Dynamics*, 54(7):3441–3459.

[Craig et al., 2017] Craig, P. M., Ferreira, D., and Methven, J. (2017). The contrast between atlantic and pacific surface water fluxes. *Tellus A: Dynamic Meteorology and Oceanography*, 69(1):1330454.

[Cummins et al., 2016] Cummins, P. F., Masson, D., and Saenko, O. A. (2016). Vertical heat flux in the ocean: Estimates from observations and from a coupled general circulation model. *Journal of Geophysical Research: Oceans*, 121(6):3790–3802.

[Dai, 2022] Dai, A. (2022). Arctic amplification is the main cause of the atlantic meridional overturning circulation weakening under large co2 increases. *Climate Dynamics*, pages 1–17.

[Dai et al., 2019] Dai, A., Luo, D., Song, M., and Liu, J. (2019). Arctic amplification is caused by sea-ice loss under increasing co2. *Nature communications*, 10(1):1–13.

[Danabasoglu et al., 2021] Danabasoglu, G., Castruccio, F. S., Small, R. J., Tomas, R., Frajka-Williams, E., and Lankhorst, M. (2021). Revisiting amoc transport estimates from observations and models. *Geophysical Research Letters*, 48(10):e2021GL093045.

[Dansgaard et al., 1993] Dansgaard, W., Johnsen, S. J., Clausen, H. B., Dahl-Jensen, D., Gundestrup, N., Hammer, C., Hvidberg, C., Steffensen, J., Sveinbjörnsdottir, A., Jouzel, J., et al. (1993). Evidence for general instability of past climate from a 250-kyr ice-core record. *Nature*, 364(6434):218–220.

[De Lavergne et al., 2016a] De Lavergne, C., Madec, G., Le Sommer, J., Nurser, A. G., and Garabato, A. C. N. (2016a). The impact of a variable mixing efficiency on the abyssal overturning. *Journal of Physical Oceanography*, 46(2):663–681.

[De Lavergne et al., 2016b] De Lavergne, C., Madec, G., Le Sommer, J., Nurser, A. G., and Naveira Garabato, A. C. (2016b). On the consumption of antarctic bottom water in the abyssal ocean. *Journal of Physical Oceanography*, 46(2):635–661.

[Desbruyeres et al., 2017] Desbruyeres, D., McDonagh, E. L., King, B. A., and Thierry, V. (2017). Global and full-depth ocean temperature trends during the early twenty-first century from argo and repeat hydrography. *Journal of Climate*, 30(6):1985–1997.

[Desbruyères et al., 2016] Desbruyères, D. G., Purkey, S. G., McDonagh, E. L., Johnson, G. C., and King, B. A. (2016). Deep and abyssal ocean warming from 35 years of repeat hydrography. *Geophysical Research Letters*, 43(19):10–356.

[Dewar et al., 2006] Dewar, W. K., Bingham, R. J., Iverson, R., Nowacek, D. P., St Laurent, L. C., and Wiebe, P. H. (2006). Does the marine biosphere mix the ocean? *Journal of Marine Research*, 64(4):541–561.

[Dias et al., 2020a] Dias, F. B., Domingues, C. M., Marsland, S. J., Griffies, S., Rintoul, S., Matear, R., and Fiedler, R. (2020a). On the superposition of mean advective and eddy-induced transports in global ocean heat and salt budgets. *Journal of Climate*, 33(3):1121–1140.

[Dias et al., 2020b] Dias, F. B., Fiedler, R., Marsland, S., Domingues, C., Clément, L., Rintoul, S., Mcdonagh, E., Mata, M., and Savita, A. (2020b). Ocean heat storage in response to changing ocean circulation processes. *Journal of Climate*, 33(21):9065–9082.

[Doddridge et al., 2019] Doddridge, E. W., Marshall, J., Song, H., Campin, J.-M., Kelley, M., and Nazarenko, L. (2019). Eddy compensation dampens southern ocean sea surface temperature response to westerly wind trends. *Geophysical Research Letters*, 46(8):4365–4377.

[Domingues et al., 2008] Domingues, C. M., Church, J. A., White, N. J., Gleckler, P. J., Wijffels, S. E., Barker, P. M., and Dunn, J. R. (2008). Improved estimates of upper-ocean warming and multi-decadal sea-level rise. *Nature*, 453(7198):1090–1093.

[Döös et al., 2012] Döös, K., Nilsson, J., Nycander, J., Brodeau, L., and Ballarotta, M. (2012). The world ocean thermohaline circulation. *Journal of Physical Oceanography*, 42(9):1445–1460.

[Döös et al., 2008] Döös, K., Nycander, J., and Coward, A. C. (2008). Lagrangian decomposition of the deacon cell. *Journal of Geophysical Research: Oceans*, 113(C7).

[Döös and Webb, 1994] Döös, K. and Webb, D. J. (1994). The deacon cell and the other meridional cells of the southern ocean. *Journal of Physical Oceanography*, 24(2):429–442.

[Downes and Hogg, 2013] Downes, S. M. and Hogg, A. M. (2013). Southern ocean circulation and eddy compensation in cmip5 models. *Journal of Climate*, 26(18):7198–7220.

[Drake et al., 2022] Drake, H. F., Ruan, X., Callies, J., Ogden, K., Thurnherr, A. M., and Ferrari, R. (2022). Dynamics of eddying abyssal mixing layers over sloping rough topography. *Journal of Physical Oceanography*.

[Drijfhout et al., 2012] Drijfhout, S., Van Oldenborgh, G. J., and Cimatoribus, A. (2012). Is a decline of amoc causing the warming hole above the north atlantic in observed and modeled warming patterns? *Journal of Climate*, 25(24):8373–8379.

[Drijfhout et al., 2014] Drijfhout, S. S., Blaker, A. T., Josey, S. A., Nurser, A., Sinha, B., and Balmaseda, M. (2014). Surface warming hiatus caused by in-

creased heat uptake across multiple ocean basins. *Geophysical Research Letters*, 41(22):7868–7874.

[Durack et al., 2018] Durack, P. J., Gleckler, P. J., Purkey, S. G., Johnson, G. C., Lyman, J. M., and Boyer, T. P. (2018). Ocean warming: From the surface to the deep in observations and models. *Oceanography*, 31(2):41–51.

[Eden and Greatbatch, 2008] Eden, C. and Greatbatch, R. J. (2008). Diapycnal mixing by meso-scale eddies. *Ocean Modelling*, 23(3-4):113–120.

[Exarchou et al., 2015] Exarchou, E., Kuhlbrodt, T., Gregory, J. M., and Smith, R. S. (2015). Ocean heat uptake processes: a model intercomparison. *Journal of Climate*, 28(2):887–908.

[Eyring et al., 2016] Eyring, V., Bony, S., Meehl, G. A., Senior, C. A., Stevens, B., Stouffer, R. J., and Taylor, K. E. (2016). Overview of the coupled model intercomparison project phase 6 (cmip6) experimental design and organization. *Geoscientific Model Development*, 9(5):1937–1958.

[Ferrari, 2014] Ferrari, R. (2014). What goes down must come up. *Nature*, 513(7517):179–180.

[Ferrari and Ferreira, 2011] Ferrari, R. and Ferreira, D. (2011). What processes drive the ocean heat transport? *Ocean Modelling*, 38(3-4):171–186.

[Ferrari et al., 2016] Ferrari, R., Mashayek, A., McDougall, T. J., Nikurashin, M., and Campin, J.-M. (2016). Turning ocean mixing upside down. *Journal of Physical Oceanography*, 46(7):2239–2261.

[Ferrari et al., 2017] Ferrari, R., Nadeau, L.-P., Marshall, D. P., Allison, L. C., and Johnson, H. L. (2017). A model of the ocean overturning circulation with two closed basins and a reentrant channel. *Journal of Physical Oceanography*, 47(12):2887–2906.

[Ferrari and Wunsch, 2009] Ferrari, R. and Wunsch, C. (2009). Ocean circulation kinetic energy: Reservoirs, sources, and sinks. *Annual Review of Fluid Mechanics*, 41:253–282.

[Ferreira et al., 2018a] Ferreira, D., Cessi, P., Coxall, H. K., De Boer, A., Dijkstra, H. A., Drijfhout, S. S., Eldevik, T., Harnik, N., McManus, J. F., Marshall, D. P., et al. (2018a). Atlantic-pacific asymmetry in deep water formation. *Annual Review of Earth and Planetary Sciences*.

[Ferreira et al., 2010] Ferreira, D., Marshall, J., and Campin, J.-M. (2010). Localization of deep water formation: Role of atmospheric moisture transport and geometrical constraints on ocean circulation. *Journal of Climate*, 23(6):1456–1476.

[Ferreira et al., 2018b] Ferreira, D., Marshall, J., Ito, T., and McGee, D. (2018b). Linking glacial-interglacial states to multiple equilibria of climate. *Geophysical Research Letters*, 45(17):9160–9170.

[Ferreira et al., 2011] Ferreira, D., Marshall, J., and Rose, B. (2011). Climate determinism revisited: Multiple equilibria in a complex climate model. *Journal of Climate*, 24(4):992–1012.

[Foote, 1856] Foote, E. N. (1856). Circumstances affecting the heat of the sun's rays. *The American Journal of Science and Arts*, 53(31):382–383.

[Forget et al., 2015] Forget, G., Campin, J.-M., Heimbach, P., Hill, C. N., Ponte, R. M., and Wunsch, C. (2015). Ecco version 4: An integrated framework for non-linear inverse modeling and global ocean state estimation. *Geoscientific Model Development*, 8(10):3071–3104.

[Forget and Ferreira, 2019] Forget, G. and Ferreira, D. (2019). Global ocean heat transport dominated by heat export from the tropical pacific. *Nature Geoscience*, 12(5):351–354.

[Frajka-Williams et al., 2019] Frajka-Williams, E., Ansorge, I. J., Baehr, J., Bryden, H. L., Chidichimo, M. P., Cunningham, S. A., Danabasoglu, G., Dong, S., Donohue, K. A., Elipot, S., et al. (2019). Atlantic meridional overturning circulation: Observed transport and variability. *Frontiers in Marine Science*, page 260.

[Frajka-Williams et al., 2018] Frajka-Williams, E., Lankhorst, M., Koelling, J., and Send, U. (2018). Coherent circulation changes in the deep north atlantic from 16 n

and 26 n transport arrays. *Journal of Geophysical Research: Oceans*, 123(5):3427–3443.

[Frederikse et al., 2020] Frederikse, T., Landerer, F., Caron, L., Adhikari, S., Parkes, D., Humphrey, V. W., Dangendorf, S., Hogarth, P., Zanna, L., Cheng, L., et al. (2020). The causes of sea-level rise since 1900. *Nature*, 584(7821):393–397.

[Frölicher et al., 2015] Frölicher, T. L., Sarmiento, J. L., Paynter, D. J., Dunne, J. P., Krasting, J. P., and Winton, M. (2015). Dominance of the southern ocean in anthropogenic carbon and heat uptake in cmip5 models. *Journal of Climate*, 28(2):862–886.

[Fyfe et al., 2007] Fyfe, J. C., Saenko, O. A., Zickfeld, K., Eby, M., and Weaver, A. J. (2007). The role of poleward-intensifying winds on southern ocean warming. *Journal of Climate*, 20(21):5391–5400.

[Gao et al., 2018] Gao, L., Rintoul, S. R., and Yu, W. (2018). Recent wind-driven change in subantarctic mode water and its impact on ocean heat storage. *Nature Climate Change*, 8(1):58–63.

[Garabato et al., 2004] Garabato, A. C. N., Polzin, K. L., King, B. A., Heywood, K. J., and Visbeck, M. (2004). Widespread intense turbulent mixing in the southern ocean. *Science*, 303(5655):210–213.

[Garuba and Klinger, 2016] Garuba, O. A. and Klinger, B. A. (2016). Ocean heat uptake and interbasin transport of the passive and redistributive components of surface heating. *Journal of Climate*, 29(20):7507–7527.

[Gayen and Griffiths, 2022] Gayen, B. and Griffiths, R. W. (2022). Rotating horizontal convection. *Annual Review of Fluid Mechanics*, 54:105–132.

[Gent, 2016] Gent, P. R. (2016). Effects of southern hemisphere wind changes on the meridional overturning circulation in ocean models. *Annu. Rev. Mar. Sci*, 8:79–94.

[Gent et al., 2011] Gent, P. R., Danabasoglu, G., Donner, L. J., Holland, M. M., Hunke, E. C., Jayne, S. R., Lawrence, D. M., Neale, R. B., Rasch, P. J., Verten-

stein, M., et al. (2011). The community climate system model version 4. *Journal of climate*, 24(19):4973–4991.

[Gent and Mcwilliams, 1990] Gent, P. R. and Mcwilliams, J. C. (1990). Isopycnal mixing in ocean circulation models. *Journal of Physical Oceanography*, 20(1):150–155.

[Geoffroy et al., 2013a] Geoffroy, O., Saint-Martin, D., Bellon, G., Voldoire, A., Olivié, D., and Tytéca, S. (2013a). Transient climate response in a two-layer energy-balance model. part ii: Representation of the efficacy of deep-ocean heat uptake and validation for cmip5 aogcms. *Journal of Climate*, 26(6):1859–1876.

[Geoffroy et al., 2013b] Geoffroy, O., Saint-Martin, D., Olivié, D. J., Voldoire, A., Bellon, G., and Tytéca, S. (2013b). Transient climate response in a two-layer energy-balance model. part i: Analytical solution and parameter calibration using cmip5 aogcm experiments. *Journal of Climate*, 26(6):1841–1857.

[Geoffroy et al., 2012] Geoffroy, O., Saint-Martin, D., and Ribes, A. (2012). Quantifying the sources of spread in climate change experiments. *Geophysical research letters*, 39(24).

[Gervais et al., 2018] Gervais, M., Shaman, J., and Kushnir, Y. (2018). Mechanisms governing the development of the north atlantic warming hole in the cesm-le future climate simulations. *Journal of Climate*, 31(15):5927–5946.

[Gill, 1982] Gill, A. (1982). *Atmosphere-ocean dynamics*, volume 30. Academic press.

[Gillett and Thompson, 2003] Gillett, N. P. and Thompson, D. W. (2003). Simulation of recent southern hemisphere climate change. *Science*, 302(5643):273–275.

[Gnanadesikan, 1999] Gnanadesikan, A. (1999). A simple predictive model for the structure of the oceanic pycnocline. *Science*, 283(5410):2077–2079.

[Gnanadesikan et al., 2015] Gnanadesikan, A., Pradal, M.-A., and Abernathey, R. (2015). Isopycnal mixing by mesoscale eddies significantly impacts oceanic anthropogenic carbon uptake. *Geophysical Research Letters*, 42(11):4249–4255.

[Gnanadesikan et al., 2005] Gnanadesikan, A., Slater, R. D., Swathi, P., and Vallis, G. K. (2005). The energetics of ocean heat transport. *Journal of climate*, 18(14):2604–2616.

[Good et al., 2013] Good, S. A., Martin, M. J., and Rayner, N. A. (2013). En4: Quality controlled ocean temperature and salinity profiles and monthly objective analyses with uncertainty estimates. *Journal of Geophysical Research: Oceans*, 118(12):6704–6716.

[Gould et al., 2013] Gould, J., Sloyan, B., and Visbeck, M. (2013). In situ ocean observations: A brief history, present status, and future directions. *International Geophysics*, 103:59–81.

[Goyal et al., 2021] Goyal, R., Sen Gupta, A., Jucker, M., and England, M. H. (2021). Historical and projected changes in the southern hemisphere surface westerlies. *Geophysical Research Letters*, 48(4):e2020GL090849.

[Gregg et al., 2003] Gregg, M. C., Sanford, T. B., and Winkel, D. P. (2003). Reduced mixing from the breaking of internal waves in equatorial waters. *Nature*, 422(6931):513–515.

[Gregory et al., 2005] Gregory, J., Dixon, K., Stouffer, R., Weaver, A., Driesschaert, E., Eby, M., Fichefet, T., Hasumi, H., Hu, A., Jungclaus, J., et al. (2005). A model intercomparison of changes in the atlantic thermohaline circulation in response to increasing atmospheric co2 concentration. *Geophysical Research Letters*, 32(12).

[Gregory and Forster, 2008] Gregory, J. and Forster, P. (2008). Transient climate response estimated from radiative forcing and observed temperature change. *Journal of Geophysical Research: Atmospheres*, 113(D23).

[Gregory and Webb, 2008] Gregory, J. and Webb, M. (2008). Tropospheric adjustment induces a cloud component in co 2 forcing. *Journal of Climate*, 21(1):58–71.

[Gregory, 2000] Gregory, J. M. (2000). Vertical heat transports in the ocean and their effect on time-dependent climate change. *Climate Dynamics*, 16(7):501–515.

[Gregory et al., 2004] Gregory, J. M., Ingram, W., Palmer, M., Jones, G., Stott, P., Thorpe, R., Lowe, J., Johns, T., and Williams, K. (2004). A new method for

diagnosing radiative forcing and climate sensitivity. *Geophysical research letters*, 31(3).

[Gregory and Mitchell, 1997] Gregory, J. M. and Mitchell, J. F. (1997). The climate response to co2 of the hadley centre coupled aogcm with and without flux adjustment. *Geophysical Research Letters*, 24(15):1943–1946.

[Gregory and Tailleux, 2011] Gregory, J. M. and Tailleux, R. (2011). Kinetic energy analysis of the response of the atlantic meridional overturning circulation to co2-forced climate change. *Climate dynamics*, 37(5):893–914.

[Griesel and Maqueda, 2006] Griesel, A. and Maqueda, M. A. M. (2006). The relation of meridional pressure gradients to north atlantic deep water volume transport in an ocean general circulation model. *Climate Dynamics*, 26(7):781–799.

[Griffies, 2018] Griffies, S. (2018). Fundamentals of ocean climate models. In *Fundamentals of Ocean Climate Models*. Princeton university press.

[Griffies, 1998] Griffies, S. M. (1998). The gent–mcwilliams skew flux. *Journal of Physical Oceanography*, 28(5):831–841.

[Griffies et al., 2000] Griffies, S. M., Pacanowski, R. C., and Hallberg, R. W. (2000). Spurious diapycnal mixing associated with advection in a z-coordinate ocean model. *Monthly Weather Review*, 128(3):538–564.

[Griffies et al., 2015] Griffies, S. M., Winton, M., Anderson, W. G., Benson, R., Delworth, T. L., Dufour, C. O., Dunne, J. P., Goddard, P., Morrison, A. K., Rosati, A., et al. (2015). Impacts on ocean heat from transient mesoscale eddies in a hierarchy of climate models. *Journal of Climate*, 28(3):952–977.

[Groeskamp et al., 2019] Groeskamp, S., Griffies, S. M., Iudicone, D., Marsh, R., Nurser, A. G., and Zika, J. D. (2019). The water mass transformation framework for ocean physics and biogeochemistry. *Annual review of marine science*, 11:271–305.

[Groeskamp et al., 2020] Groeskamp, S., LaCasce, J. H., McDougall, T. J., and Rogé, M. (2020). Full-depth global estimates of ocean mesoscale eddy mixing from observations and theory. *Geophysical Research Letters*, 47(18):e2020GL089425.

[Groeskamp et al., 2017] Groeskamp, S., Sloyan, B. M., Zika, J. D., and McDougall, T. J. (2017). Mixing inferred from an ocean climatology and surface fluxes. *Journal of Physical Oceanography*, 47(3):667–687.

[Grootes et al., 1993] Grootes, P. M., Stuiver, M., White, J., Johnsen, S., and Jouzel, J. (1993). Comparison of oxygen isotope records from the gisp2 and grip greenlandice cores. *Nature*, 366(6455):552–554.

[Hallberg and Gnanadesikan, 2006] Hallberg, R. and Gnanadesikan, A. (2006). The role of eddies in determining the structure and response of the wind-driven southern hemisphere overturning: Results from the modeling eddies in the southern ocean (meso) project. *Journal of Physical Oceanography*, 36(12):2232–2252.

[Hansen et al., 1985] Hansen, J., Russell, G., Lacis, A., Fung, I., Rind, D., and Stone, P. (1985). Climate response times: Dependence on climate sensitivity and ocean mixing. *Science*, 229(4716):857–859.

[Hansen et al., 2011] Hansen, J., Sato, M., Kharecha, P., and Schuckmann, K. v. (2011). Earth's energy imbalance and implications. *Atmospheric Chemistry and Physics*, 11(24):13421–13449.

[Hartmann et al., 2013] Hartmann, D., Tank, A., Rusticucci, M., Alexander, L., Brönnimann, S., Charabi, Y., Dentener, F., Dlugokencky, E., Easterling, D., Kaplan, A., et al. (2013). Observations: Atmosphere and surface: Climate change 2013 the physical science basis: Working group i contribution to the fifth assessment report of the intergovernmental panel on climate change. *Cambridge University Press*, page 159.

[Haskins et al., 2020] Haskins, R. K., Oliver, K. I., Jackson, L. C., Wood, R. A., and Drijfhout, S. S. (2020). Temperature domination of amoc weakening due to freshwater hosing in two gcms. *Climate Dynamics*, 54(1):273–286.

[Hay, 2008] Hay, W. W. (2008). Evolving ideas about the cretaceous climate and ocean circulation. *Cretaceous Research*, 29(5-6):725–753.

[Held, 2005] Held, I. M. (2005). The gap between simulation and understanding in climate modeling. *Bulletin of the American Meteorological Society*, 86(11):1609–1614.

[Held et al., 2010] Held, I. M., Winton, M., Takahashi, K., Delworth, T., Zeng, F., and Vallis, G. K. (2010). Probing the fast and slow components of global warming by returning abruptly to preindustrial forcing. *Journal of Climate*, 23(9):2418–2427.

[Herweijer et al., 2005] Herweijer, C., Seager, R., Winton, M., and Clement, A. (2005). Why ocean heat transport warms the global mean climate. *Tellus A: Dynamic Meteorology and Oceanography*, 57(4):662–675.

[Heuzé et al., 2020] Heuzé, C., Mohrmann, M., Andersson, E., and Crafoord, E. (2020). Global decline of deep water formation with increasing atmospheric co2. *EarthArXiv*.

[Hieronymus and Nycander, 2013] Hieronymus, M. and Nycander, J. (2013). The budgets of heat and salinity in nemo. *Ocean Modelling*, 67:28–38.

[Hoffert et al., 1980] Hoffert, M. I., Callegari, A. J., and Hsieh, C.-T. (1980). The role of deep sea heat storage in the secular response to climatic forcing. *Journal of Geophysical Research: Oceans*, 85(C11):6667–6679.

[Hoffman et al., 1998] Hoffman, P. F., Kaufman, A. J., Halverson, G. P., and Schrag, D. P. (1998). A neoproterozoic snowball earth. *science*, 281(5381):1342–1346.

[Hogg, 2010] Hogg, A. M. (2010). An antarctic circumpolar current driven by surface buoyancy forcing. *Geophysical Research Letters*, 37(23).

[Hogg and Gayen, 2020] Hogg, A. M. and Gayen, B. (2020). Ocean gyres driven by surface buoyancy forcing. *Geophysical Research Letters*, 47(16):e2020GL088539.

[Holmes et al., 2018] Holmes, R. M., de Lavergne, C., and McDougall, T. J. (2018). Ridges, seamounts, troughs, and bowls: Topographic control of the dianeutral circulation in the abyssal ocean. *Journal of Physical Oceanography*, 48(4):861–882.

[Holmes et al., 2019] Holmes, R. M., Zika, J. D., and England, M. H. (2019). Diathermal heat transport in a global ocean model. *Journal of Physical Oceanography*, 49(1):141–161.

[Hu et al., 2020] Hu, S., Sprintall, J., Guan, C., McPhaden, M. J., Wang, F., Hu, D., and Cai, W. (2020). Deep-reaching acceleration of global mean ocean circulation over the past two decades. *Science advances*, 6(6):eaax7727.

[Huang et al., 2003] Huang, B., Stone, P. H., Sokolov, A. P., and Kamenkovich, I. V. (2003). The deep-ocean heat uptake in transient climate change. *Journal of climate*, 16(9):1352–1363.

[Huang, 2010] Huang, R. X. (2010). *Ocean circulation: wind-driven and thermohaline processes*. Cambridge University Press.

[Huber and Zanna, 2017] Huber, M. B. and Zanna, L. (2017). Drivers of uncertainty in simulated ocean circulation and heat uptake. *Geophysical Research Letters*, 44(3):1402–1413.

[Hughes et al., 2009] Hughes, G. O., Hogg, A. M. C., and Griffiths, R. W. (2009). Available potential energy and irreversible mixing in the meridional overturning circulation. *Journal of Physical Oceanography*, 39(12):3130–3146.

[Imbrie et al., 1993] Imbrie, J., Berger, A., Boyle, E., Clemens, S., Duffy, A., Howard, W., Kukla, G., Kutzbach, J., Martinson, D., McIntyre, A., et al. (1993). On the structure and origin of major glaciation cycles 2. the 100,000-year cycle. *Paleoceanography*, 8(6):699–735.

[Ishii et al., 2017] Ishii, M., Fukuda, Y., Hirahara, S., Yasui, S., Suzuki, T., and Sato, K. (2017). Accuracy of global upper ocean heat content estimation expected from present observational data sets. *Sola*, 13:163–167.

[Ishii and Kimoto, 2009] Ishii, M. and Kimoto, M. (2009). Reevaluation of historical ocean heat content variations with time-varying xbt and mbt depth bias corrections. *Journal of Oceanography*, 65(3):287–299.

[Ito and Marshall, 2008] Ito, T. and Marshall, J. (2008). Control of lower-limb overturning circulation in the southern ocean by diapycnal mixing and mesoscale eddy transfer. *Journal of Physical Oceanography*, 38(12):2832–2845.

[Jackett and Mcdougall, 1995] Jackett, D. R. and Mcdougall, T. J. (1995). Minimal adjustment of hydrographic profiles to achieve static stability. *Journal of Atmospheric and Oceanic Technology*, 12(2):381–389.

[Jackson et al., 2022] Jackson, L. C., Biastoch, A., Buckley, M. W., Desbruyères, D. G., Frajka-Williams, E., Moat, B., and Robson, J. (2022). The evolution of the north atlantic meridional overturning circulation since 1980. *Nature Reviews Earth & Environment*, pages 1–14.

[Jahn and Holland, 2013] Jahn, A. and Holland, M. M. (2013). Implications of arctic sea ice changes for north atlantic deep convection and the meridional overturning circulation in ccsm4-cmip5 simulations. *Geophysical Research Letters*, 40(6):1206–1211.

[Johnson and Lyman, 2020] Johnson, G. C. and Lyman, J. M. (2020). Warming trends increasingly dominate global ocean. *Nature Climate Change*, 10(8):757–761.

[Johnson et al., 2019] Johnson, H. L., Cessi, P., Marshall, D. P., Schloesser, F., and Spall, M. A. (2019). Recent contributions of theory to our understanding of the atlantic meridional overturning circulation. *Journal of Geophysical Research: Oceans*, 124(8):5376–5399.

[Johnson et al., 2007] Johnson, H. L., Marshall, D. P., and Sproson, D. A. (2007). Reconciling theories of a mechanically driven meridional overturning circulation with thermohaline forcing and multiple equilibria. *Climate Dynamics*, 29(7-8):821–836.

[Jones and Abernathey, 2019] Jones, C. and Abernathey, R. P. (2019). Isopycnal mixing controls deep ocean ventilation. *Geophysical Research Letters*, 46(22):13144–13151.

[Josey et al., 2013] Josey, S. A., Gulev, S., and Yu, L. (2013). Exchanges through the ocean surface. In *International Geophysics*, volume 103, pages 115–140. Elsevier.

[Katzav and Parker, 2015] Katzav, J. and Parker, W. S. (2015). The future of climate modeling. *Climatic Change*, 132(4):475–487.

[Keil et al., 2020] Keil, P., Mauritsen, T., Jungclaus, J., Hedemann, C., Olonscheck, D., and Ghosh, R. (2020). Multiple drivers of the north atlantic warming hole. *Nature Climate Change*, 10(7):667–671.

[Kilbourne et al., 2022] Kilbourne, K. H., Wanamaker, A. D., Moffa-Sanchez, P., Reynolds, D. J., Amrhein, D. E., Butler, P. G., Gebbie, G., Goes, M., Jansen, M. F., Little, C. M., et al. (2022). Atlantic circulation change still uncertain. *Nature Geoscience*, 15(3):165–167.

[Kirtman et al., 2013] Kirtman, B., Power, S. B., Adedoyin, A. J., Boer, G. J., Bojariu, R., Camilloni, I., Doblas-Reyes, F., Fiore, A. M., Kimoto, M., Meehl, G., et al. (2013). Near-term climate change: Projections and predictability. In *Climate Change 2013 the Physical Science Basis: Working Group I Contribution to the Fifth Assessment Report of the Intergovernmental Panel on Climate Change*, pages 953–1028. Cambridge University Press.

[Klinger et al., 1996] Klinger, B. A., Marshall, J., and Send, U. (1996). Representation of convective plumes by vertical adjustment. *Journal of Geophysical Research: Oceans*, 101(C8):18175–18182.

[Klymak et al., 2006] Klymak, J. M., Moum, J. N., Nash, J. D., Kunze, E., Girton, J. B., Carter, G. S., Lee, C. M., Sanford, T. B., and Gregg, M. C. (2006). An estimate of tidal energy lost to turbulence at the hawaiian ridge. *Journal of Physical Oceanography*, 36(6):1148–1164.

[Kostov et al., 2014] Kostov, Y., Armour, K. C., and Marshall, J. (2014). Impact of the atlantic meridional overturning circulation on ocean heat storage and transient climate change. *Geophysical Research Letters*, 41(6):2108–2116.

[Kostov et al., 2019] Kostov, Y., Johnson, H. L., and Marshall, D. P. (2019). Amoc sensitivity to surface buoyancy fluxes: the role of air-sea feedback mechanisms. *Climate Dynamics*, 53(7):4521–4537.

[Kuhlbrodt and Gregory, 2012] Kuhlbrodt, T. and Gregory, J. (2012). Ocean heat uptake and its consequences for the magnitude of sea level rise and climate change. *Geophysical Research Letters*, 39(18).

[Kuhlbrodt et al., 2015] Kuhlbrodt, T., Gregory, J., and Shaffrey, L. (2015). A process-based analysis of ocean heat uptake in an aogcm with an eddy-permitting ocean component. *Climate Dynamics*, 45(11):3205–3226.

[Kuhlbrodt et al., 2007] Kuhlbrodt, T., Griesel, A., Montoya, M., Levermann, A., Hofmann, M., and Rahmstorf, S. (2007). On the driving processes of the atlantic meridional overturning circulation. *Reviews of Geophysics*, 45(2).

[Kuhlbrodt et al., 2012] Kuhlbrodt, T., Smith, R. S., Wang, Z., and Gregory, J. M. (2012). The influence of eddy parameterizations on the transport of the antarctic circumpolar current in coupled climate models. *Ocean Modelling*, 52:1–8.

[Kunze, 2017] Kunze, E. (2017). Internal-wave-driven mixing: Global geography and budgets. *Journal of Physical Oceanography*, 47(6):1325–1345.

[Kushner et al., 2001] Kushner, P. J., Held, I. M., and Delworth, T. L. (2001). Southern hemisphere atmospheric circulation response to global warming. *Journal of Climate*, 14(10):2238–2249.

[LaCasce et al., 2014] LaCasce, J., Ferrari, R., Marshall, J., Tulloch, R., Balwada, D., and Speer, K. (2014). Float-derived isopycnal diffusivities in the dimes experiment. *Journal of Physical Oceanography*, 44(2):764–780.

[Large and Yeager, 2009] Large, W. and Yeager, S. (2009). The global climatology of an interannually varying air–sea flux data set. *Climate dynamics*, 33(2-3):341–364.

[Latif et al., 2022] Latif, M., Sun, J., Visbeck, M., and Hadi Bordbar, M. (2022). Natural variability has dominated atlantic meridional overturning circulation since 1900. *Nature Climate Change*, pages 1–6.

[Ledwell et al., 2000] Ledwell, J., Montgomery, E., Polzin, K., St Laurent, L., Schmitt, R., and Toole, J. (2000). Evidence for enhanced mixing over rough topography in the abyssal ocean. *Nature*, 403(6766):179–182.

[Ledwell et al., 2011] Ledwell, J. R., St. Laurent, L. C., Girton, J. B., and Toole, J. M. (2011). Diapycnal mixing in the antarctic circumpolar current. *Journal of Physical Oceanography*, 41(1):241–246.

[Ledwell et al., 1993] Ledwell, J. R., Watson, A. J., and Law, C. S. (1993). Evidence for slow mixing across the pycnocline from an open-ocean tracer-release experiment. *Nature*, 364(6439):701–703.

[Ledwell et al., 1998] Ledwell, J. R., Watson, A. J., and Law, C. S. (1998). Mixing of a tracer in the pycnocline. *Journal of Geophysical Research: Oceans*, 103(C10):21499–21529.

[Lee et al., 2011] Lee, S.-K., Park, W., Van Sebille, E., Baringer, M. O., Wang, C., Enfield, D. B., Yeager, S. G., and Kirtman, B. P. (2011). What caused the significant increase in atlantic ocean heat content since the mid-20th century? *Geophysical Research Letters*, 38(17).

[Legg et al., 2009] Legg, S., Briegleb, B., Chang, Y., Chassignet, E. P., Danabasoglu, G., Ezer, T., Gordon, A. L., Griffies, S., Hallberg, R., Jackson, L., et al. (2009). Improving oceanic overflow representation in climate models: the gravity current entrainment climate process team. *Bulletin of the American Meteorological Society*, 90(5):657–670.

[Lenaerts et al., 2015] Lenaerts, J. T., Le Bars, D., Van Kampenhout, L., Vizcaino, M., Enderlin, E. M., and Van Den Broeke, M. R. (2015). Representing greenland ice sheet freshwater fluxes in climate models. *Geophysical Research Letters*, 42(15):6373–6381.

[Levitus et al., 2012] Levitus, S., Antonov, J. I., Boyer, T. P., Baranova, O. K., Garcia, H. E., Locarnini, R. A., Mishonov, A. V., Reagan, J., Seidov, D., Yarosh, E. S., et al. (2012). World ocean heat content and thermosteric sea level change (0–2000 m), 1955–2010. *Geophysical Research Letters*, 39(10).

[Li et al., 2013] Li, C., von Storch, J.-S., and Marotzke, J. (2013). Deep-ocean heat uptake and equilibrium climate response. *Climate Dynamics*, 40(5):1071–1086.

[Li et al., 2020] Li, G., Cheng, L., Zhu, J., Trenberth, K. E., Mann, M. E., and Abraham, J. P. (2020). Increasing ocean stratification over the past half-century. *Nature Climate Change*, pages 1–8.

[Liu et al., 2017] Liu, W., Xie, S.-P., Liu, Z., and Zhu, J. (2017). Overlooked possibility of a collapsed atlantic meridional overturning circulation in warming climate. *Science Advances*, 3(1):e1601666.

[Lozier et al., 2019] Lozier, M., Li, F., Bacon, S., Bahr, F., Bower, A., Cunningham, S., De Jong, M., De Steur, L., Deyoung, B., Fischer, J., et al. (2019). A sea change in our view of overturning in the subpolar north atlantic. *Science*, 363(6426):516–521.

[Lucarini and Ragone, 2011] Lucarini, V. and Ragone, F. (2011). Energetics of climate models: Net energy balance and meridional enthalpy transport. *Reviews of Geophysics*, 49(1).

[Lumpkin et al., 2020] Lumpkin, R., Baringer, M., Bif, M. B., Boyer, T., Bushinsky, S. M., Carter, B. R., Cetinić, I., Chambers, D. P., Cheng, L., Chiba, S., et al. (2020). Global oceans. *Bulletin of the American Meteorological Society*, 101(8):S129–S184.

[Lumpkin and Speer, 2007] Lumpkin, R. and Speer, K. (2007). Global ocean meridional overturning. *Journal of Physical Oceanography*, 37(10):2550–2562.

[Macdonald and Baringer, 2013] Macdonald, A. M. and Baringer, M. O. (2013). Ocean heat transport. In *International Geophysics*, volume 103, pages 759–785. Elsevier.

[Madec et al., 2017] Madec, G., Bourdallé-Badie, R., Bouttier, P.-A., Bricaud, C., Bruciaferri, D., Calvert, D., Chanut, J., Clementi, E., Coward, A., Delrosso, D., et al. (2017). Nemo ocean engine. *Notes du Pôle de modélisation de l'Institut Pierre-Simon Laplace (IPSL)*, 27.

[Manabe and Stouffer, 1988] Manabe, S. and Stouffer, R. (1988). Two stable equilibria of a coupled ocean-atmosphere model. *Journal of Climate*, 1(9):841–866.

[Manabe and Wetherald, 1975] Manabe, S. and Wetherald, R. T. (1975). The effects of doubling the co2 concentration on the climate of a general circulation model. *Journal of the Atmospheric Sciences*, 32(1):3–15.

[Marshall and Zanna, 2014] Marshall, D. P. and Zanna, L. (2014). A conceptual model of ocean heat uptake under climate change. *Journal of Climate*, 27(22):8444–8465.

[Marshall et al., 2004] Marshall, J., Adcroft, A., Campin, J.-M., Hill, C., and White, A. (2004). Atmosphere–ocean modeling exploiting fluid isomorphisms. *Monthly Weather Review*, 132(12):2882–2894.

[Marshall et al., 1997a] Marshall, J., Adcroft, A., Hill, C., Perelman, L., and Heisey, C. (1997a). A finite-volume, incompressible navier stokes model for studies of the ocean on parallel computers. *Journal of Geophysical Research: Oceans*, 102(C3):5753–5766.

[Marshall et al., 2014a] Marshall, J., Armour, K. C., Scott, J. R., Kostov, Y., Hausmann, U., Ferreira, D., Shepherd, T. G., and Bitz, C. M. (2014a). The ocean's role in polar climate change: asymmetric arctic and antarctic responses to greenhouse gas and ozone forcing. *Philosophical Transactions of the Royal Society A: Mathematical, Physical and Engineering Sciences*, 372(2019):20130040.

[Marshall et al., 2014b] Marshall, J., Donohoe, A., Ferreira, D., and McGee, D. (2014b). The ocean's role in setting the mean position of the inter-tropical convergence zone. *Climate Dynamics*, 42(7-8):1967–1979.

[Marshall et al., 1997b] Marshall, J., Hill, C., Perelman, L., and Adcroft, A. (1997b). Hydrostatic, quasi-hydrostatic, and nonhydrostatic ocean modeling. *Journal of Geophysical Research: Oceans*, 102(C3):5733–5752.

[Marshall and Radko, 2003] Marshall, J. and Radko, T. (2003). Residual-mean solutions for the antarctic circumpolar current and its associated overturning circulation. *Journal of Physical Oceanography*, 33(11):2341–2354.

[Marshall and Schott, 1999] Marshall, J. and Schott, F. (1999). Open-ocean convection: Observations, theory, and models. *Reviews of Geophysics*, 37(1):1–64.

[Marshall et al., 2015] Marshall, J., Scott, J. R., Armour, K. C., Campin, J.-M., Kelley, M., and Romanou, A. (2015). The ocean's role in the transient response of climate to abrupt greenhouse gas forcing. *Climate Dynamics*, 44(7-8):2287–2299.

[Marshall et al., 2017] Marshall, J., Scott, J. R., Romanou, A., Kelley, M., and Leboissetier, A. (2017). The dependence of the ocean's moc on mesoscale eddy diffusivities: A model study. *Ocean Modelling*, 111:1–8.

[Marshall and Speer, 2012] Marshall, J. and Speer, K. (2012). Closure of the meridional overturning circulation through southern ocean upwelling. *Nature Geoscience*, 5(3):171–180.

[Mashayek et al., 2017] Mashayek, A., Ferrari, R., Merrifield, S., Ledwell, J. R., St Laurent, L., and Garabato, A. N. (2017). Topographic enhancement of vertical turbulent mixing in the southern ocean. *Nature communications*, 8(1):1–12.

[Mashayek et al., 2015] Mashayek, A., Ferrari, R., Nikurashin, M., and Peltier, W. (2015). Influence of enhanced abyssal diapycnal mixing on stratification and the ocean overturning circulation. *Journal of Physical Oceanography*, 45(10):2580–2597.

[Mashayek et al., 2013] Mashayek, A., Ferrari, R., Vettoretti, G., and Peltier, W. (2013). The role of the geothermal heat flux in driving the abyssal ocean circulation. *Geophysical Research Letters*, 40(12):3144–3149.

[Masson-Delmotte et al., 2021] Masson-Delmotte, V., Zhai, P., Pirani, A., Connors, S. L., Péan, C., Berger, S., Caud, N., Chen, Y., Goldfarb, L., Gomis, M., et al. (2021). Climate change 2021: the physical science basis. *Contribution of working group I to the sixth assessment report of the intergovernmental panel on climate change*, page 2.

[McCarthy et al., 2015] McCarthy, G. D., Smeed, D. A., Johns, W. E., Frajka-Williams, E., Moat, B. I., Rayner, D., Baringer, M. O., Meinen, C. S., Collins,

J., and Bryden, H. L. (2015). Measuring the atlantic meridional overturning circulation at 26 n. *Progress in Oceanography*, 130:91–111.

[McDougall and Ferrari, 2017] McDougall, T. J. and Ferrari, R. (2017). Abyssal upwelling and downwelling driven by near-boundary mixing. *Journal of Physical Oceanography*, 47(2):261–283.

[Meehl et al., 2011] Meehl, G. A., Arblaster, J. M., Fasullo, J. T., Hu, A., and Trenberth, K. E. (2011). Model-based evidence of deep-ocean heat uptake during surface-temperature hiatus periods. *Nature Climate Change*, 1(7):360–364.

[Meehl et al., 2007] Meehl, G. A., Covey, C., Delworth, T., Latif, M., McAvaney, B., Mitchell, J. F., Stouffer, R. J., and Taylor, K. E. (2007). The wcrp cmip3 multimodel dataset: A new era in climate change research. *Bulletin of the American meteorological society*, 88(9):1383–1394.

[Meinen et al., 2018] Meinen, C. S., Speich, S., Piola, A. R., Ansorge, I., Campos, E., Kersalé, M., Terre, T., Chidichimo, M. P., Lamont, T., Sato, O. T., et al. (2018). Meridional overturning circulation transport variability at 34.5 s during 2009–2017: Baroclinic and barotropic flows and the dueling influence of the boundaries. *Geophysical Research Letters*, 45(9):4180–4188.

[Meinshausen et al., 2011] Meinshausen, M., Raper, S. C., and Wigley, T. M. (2011). Emulating coupled atmosphere-ocean and carbon cycle models with a simpler model, magicc6–part 1: Model description and calibration. *Atmospheric Chemistry and Physics*, 11(4):1417–1456.

[Meyssignac et al., 2019] Meyssignac, B., Boyer, T., Zhao, Z., Hakuba, M. Z., Landerer, F. W., Stammer, D., Köhl, A., Kato, S., L'Ecuyer, T., Ablain, M., et al. (2019). Measuring global ocean heat content to estimate the earth energy imbalance. *Frontiers in Marine Science*, 6:432.

[Millero and Poisson, 1981] Millero, F. J. and Poisson, A. (1981). International one-atmosphere equation of state of seawater. *Deep Sea Research Part A. Oceanographic Research Papers*, 28(6):625–629.

[Molteni, 2003] Molteni, F. (2003). Atmospheric simulations using a gcm with simplified physical parametrizations. i: Model climatology and variability in multi-decadal experiments. *Climate Dynamics*, 20(2-3):175–191.

[Morrison et al., 2013] Morrison, A., Saenko, O., Hogg, A. M., and Spence, P. (2013). The role of vertical eddy flux in southern ocean heat uptake. *Geophysical Research Letters*, 40(20):5445–5450.

[Morrison and Hogg, 2013] Morrison, A. K. and Hogg, A. (2013). On the relationship between southern ocean overturning and acc transport. *Journal of Physical Oceanography*, 43(1):140–148.

[Munday et al., 2013] Munday, D. R., Johnson, H. L., and Marshall, D. P. (2013). Eddy saturation of equilibrated circumpolar currents. *Journal of Physical Oceanography*, 43(3):507–532.

[Munk and Wunsch, 1998] Munk, W. and Wunsch, C. (1998). Abyssal recipes ii: Energetics of tidal and wind mixing. *Deep-sea research. Part I, Oceanographic research papers*, 45(12):1977–2010.

[Munk, 1966] Munk, W. H. (1966). Abyssal recipes. *Deep Sea Research*, 13:707–730.

[Murphy, 1995] Murphy, J. (1995). Transient response of the hadley centre coupled ocean-atmosphere model to increasing carbon dioxide. part iii: analysis of global-mean response using simple models. *Journal of Climate*, 8(3):496–514.

[Myhre et al., 1998] Myhre, G., Highwood, E. J., Shine, K. P., and Stordal, F. (1998). New estimates of radiative forcing due to well mixed greenhouse gases. *Geophysical research letters*, 25(14):2715–2718.

[Nadiga and Urban, 2019] Nadiga, B. T. and Urban, N. M. (2019). Improved representation of ocean heat content in energy balance models. *Climatic Change*, 152(3-4):503–516.

[Newsom et al., 2016] Newsom, E. R., Bitz, C. M., Bryan, F. O., Abernathey, R., and Gent, P. R. (2016). Southern ocean deep circulation and heat uptake in a high-resolution climate model. *Journal of Climate*, 29(7):2597–2619.

[Newsom and Thompson, 2018] Newsom, E. R. and Thompson, A. F. (2018). Reassessing the role of the indo-pacific in the ocean's global overturning circulation. *Geophysical Research Letters*, 45(22):12–422.

[Nikurashin and Ferrari, 2013] Nikurashin, M. and Ferrari, R. (2013). Overturning circulation driven by breaking internal waves in the deep ocean. *Geophysical Research Letters*, 40(12):3133–3137.

[Nikurashin and Vallis, 2011] Nikurashin, M. and Vallis, G. (2011). A theory of deep stratification and overturning circulation in the ocean. *Journal of Physical Oceanography*, 41(3):485–502.

[Nikurashin and Vallis, 2012] Nikurashin, M. and Vallis, G. (2012). A theory of the interhemispheric meridional overturning circulation and associated stratification. *Journal of Physical Oceanography*, 42(10):1652–1667.

[Nilsson et al., 2013] Nilsson, J., Langen, P. L., Ferreira, D., and Marshall, J. (2013). Ocean basin geometry and the salinification of the atlantic ocean. *Journal of Climate*, 26(16):6163–6184.

[Nurser and Lee, 2004] Nurser, A. G. and Lee, M.-M. (2004). Isopycnal averaging at constant height. part i: The formulation and a case study. *Journal of physical oceanography*, 34(12):2721–2739.

[Nycander, 2005] Nycander, J. (2005). Generation of internal waves in the deep ocean by tides. *Journal of Geophysical Research: Oceans*, 110(C10).

[Nycander et al., 2015] Nycander, J., Hieronymus, M., and Roquet, F. (2015). The nonlinear equation of state of sea water and the global water mass distribution. *Geophysical Research Letters*, 42(18):7714–7721.

[Nycander et al., 2007] Nycander, J., Nilsson, J., Döös, K., and Broström, G. (2007). Thermodynamic analysis of ocean circulation. *Journal of physical oceanography*, 37(8):2038–2052.

[Pacanowski and Griffies, 1996] Pacanowski, R. and Griffies, S. (1996). Mom 2 version 2, documentation, user's guide and reference manual. *Geophysical Fluid Dynamics Laboratory/NOAA, GFDL Ocean Tech. Rep*, 32.

[Padilla et al., 2011] Padilla, L. E., Vallis, G. K., and Rowley, C. W. (2011). Probabilistic estimates of transient climate sensitivity subject to uncertainty in forcing and natural variability. *Journal of Climate*, 24(21):5521–5537.

[Palmer et al., 2007] Palmer, M., Haines, K., Tett, S., and Ansell, T. (2007). Isolating the signal of ocean global warming. *Geophysical Research Letters*, 34(23).

[Park and Bryan, 2000] Park, Y.-G. and Bryan, K. (2000). Comparison of thermally driven circulations from a depth-coordinate model and an isopycnal-layer model. part i: Scaling-law sensitivity to vertical diffusivity. *Journal of Physical Oceanography*, 30(3):590–605.

[Paulson and Simpson, 1977] Paulson, C. A. and Simpson, J. J. (1977). Irradiance measurements in the upper ocean. *Journal of Physical Oceanography*, 7(6):952–956.

[Pauluis et al., 2008] Pauluis, O., Czaja, A., and Korty, R. (2008). The global atmospheric circulation on moist isentropes. *Science*, 321(5892):1075–1078.

[Pauluis et al., 2011] Pauluis, O., Shaw, T., and Laliberté, F. (2011). A statistical generalization of the transformed eulerian-mean circulation for an arbitrary vertical coordinate system. *Journal of the atmospheric sciences*, 68(8):1766–1783.

[Pele and Werman, 2009] Pele, O. and Werman, M. (2009). Fast and robust earth mover's distances. In *2009 IEEE 12th International Conference on Computer Vision*, pages 460–467. IEEE.

[Peng et al., 2022] Peng, Q., Xie, S.-P., Wang, D., Huang, R. X., Chen, G., Shu, Y., Shi, J.-R., and Liu, W. (2022). Surface warming–induced global acceleration of upper ocean currents. *Science advances*, 8(16):eabj8394.

[Perren et al., 2020] Perren, B. B., Hodgson, D. A., Roberts, S. J., Sime, L., Van Nieuwenhuyze, W., Verleyen, E., and Vyverman, W. (2020). Southward migration of the southern hemisphere westerly winds corresponds with warming climate over centennial timescales. *Communications Earth & Environment*, 1(1):1–8.

[Petit et al., 2020] Petit, T., Lozier, M. S., Josey, S. A., and Cunningham, S. A. (2020). Atlantic deep water formation occurs primarily in the iceland basin and irminger sea by local buoyancy forcing. *Geophysical Research Letters*, 47(22):e2020GL091028.

[Plueddemann and Farrar, 2006] Plueddemann, A. and Farrar, J. (2006). Observations and models of the energy flux from the wind to mixed-layer inertial currents. *Deep Sea Research Part II: Topical Studies in Oceanography*, 53(1-2):5–30.

[Polvani et al., 2011] Polvani, L. M., Waugh, D. W., Correa, G. J., and Son, S.-W. (2011). Stratospheric ozone depletion: The main driver of twentieth-century atmospheric circulation changes in the southern hemisphere. *Journal of Climate*, 24(3):795–812.

[Polzin et al., 1997] Polzin, K., Toole, J., Ledwell, J., and Schmitt, R. (1997). Spatial variability of turbulent mixing in the abyssal ocean. *Science*, 276(5309):93–96.

[Pradal and Gnanadesikan, 2014] Pradal, M.-A. and Gnanadesikan, A. (2014). How does the redi parameter for mesoscale mixing impact global climate in an earth system model? *Journal of Advances in Modeling Earth Systems*, 6(3):586–601.

[Previdi et al., 2021] Previdi, M., Smith, K. L., and Polvani, L. M. (2021). Arctic amplification of climate change: a review of underlying mechanisms. *Environmental Research Letters*.

[Purkey and Johnson, 2010] Purkey, S. G. and Johnson, G. C. (2010). Warming of global abyssal and deep southern ocean waters between the 1990s and 2000s: Contributions to global heat and sea level rise budgets. *Journal of Climate*, 23(23):6336–6351.

[Purkey and Johnson, 2013] Purkey, S. G. and Johnson, G. C. (2013). Antarctic bottom water warming and freshening: Contributions to sea level rise, ocean freshwater budgets, and global heat gain. *Journal of Climate*, 26(16):6105–6122.

[Qu et al., 2019] Qu, T., Fukumori, I., and Fine, R. A. (2019). Spin-up of the southern hemisphere super gyre. *Journal of Geophysical Research: Oceans*, 124(1):154–170.

[Ragen et al., 2022] Ragen, S., Armour, K. C., Thompson, L., Shao, A., and Darr, D. (2022). The role of atlantic basin geometry in meridional overturning circulation. *Journal of Physical Oceanography*.

[Rahmstorf, 1995] Rahmstorf, S. (1995). Bifurcations of the atlantic thermohaline circulation in response to changes in the hydrological cycle. *Nature*, 378(6553):145–149.

[Rahmstorf, 1996] Rahmstorf, S. (1996). On the freshwater forcing and transport of the atlantic thermohaline circulation. *Climate Dynamics*, 12(12):799–811.

[Rahmstorf, 2002] Rahmstorf, S. (2002). Ocean circulation and climate during the past 120,000 years. *Nature*, 419(6903):207–214.

[Rahmstorf et al., 2015] Rahmstorf, S., Box, J. E., Feulner, G., Mann, M. E., Robinson, A., Rutherford, S., and Schaffernicht, E. J. (2015). Exceptional twentieth-century slowdown in atlantic ocean overturning circulation. *Nature climate change*, 5(5):475.

[Rančić et al., 1996] Rančić, M., Purser, R., and Mesinger, F. (1996). A global shallow-water model using an expanded spherical cube: Gnomonic versus conformal coordinates. *Quarterly Journal of the Royal Meteorological Society*, 122(532):959–982.

[Raper and Cubasch, 1996] Raper, S. and Cubasch, U. (1996). Emulation of the results from a coupled general circulation model using a simple climate model. *Geophysical Research Letters*, 23(10):1107–1110.

[Raper et al., 2001] Raper, S., Gregory, J. M., and Osborn, T. (2001). Use of an upwelling-diffusion energy balance climate model to simulate and diagnose a/ogcm results. *Climate Dynamics*, 17(8):601–613.

[Raper et al., 2002] Raper, S. C., Gregory, J. M., and Stouffer, R. J. (2002). The role of climate sensitivity and ocean heat uptake on aogcm transient temperature response. *Journal of Climate*, 15(1):124–130.

[Raymo et al., 2004] Raymo, M. E., Oppo, D. W., Flower, B. P., Hodell, D. A., McManus, J. F., Venz, K., Kleiven, K., and McIntyre, K. (2004). Stability of

north atlantic water masses in face of pronounced climate variability during the pleistocene. *Paleoceanography*, 19(2).

[Redi, 1982] Redi, M. H. (1982). Oceanic isopycnal mixing by coordinate rotation. *Journal of Physical Oceanography*, 12(10):1154–1158.

[Reintges et al., 2017] Reintges, A., Martin, T., Latif, M., and Keenlyside, N. S. (2017). Uncertainty in twenty-first century projections of the atlantic meridional overturning circulation in cmip3 and cmip5 models. *Climate Dynamics*, 49(5):1495–1511.

[Rhein et al., 2013] Rhein, M., Rintoul, S., Aoki, S., Campos, E., Chambers, D., Feely, R., Gulev, S., Johnson, G., Josey, S., Kostianoy, A., et al. (2013). Observations: ocean. in 'climate change 2013: the physical science basis. contribution of working group i to the fifth assessment report of the intergovernmental panel on climate change'. *Cambridge University Press, Cambridge, United Kingdom and New York, NY, USA*.

[Rhines and Young, 1982a] Rhines, P. B. and Young, W. R. (1982a). Homogenization of potential vorticity in planetary gyres. *Journal of Fluid Mechanics*, 122:347–367.

[Rhines and Young, 1982b] Rhines, P. B. and Young, W. R. (1982b). A theory of the wind-driven circulation. i. mid-ocean gyres. *J. Mar. Res*, 40(3):559–596.

[Ridgway and Dunn, 2007] Ridgway, K. and Dunn, J. (2007). Observational evidence for a southern hemisphere oceanic supergyre. *Geophysical Research Letters*, 34(13).

[Roemmich, 2007] Roemmich, D. (2007). Super spin in the southern seas. *Nature*, 449(7158):34–35.

[Roemmich et al., 2015] Roemmich, D., Church, J., Gilson, J., Monselesan, D., Sutton, P., and Wijffels, S. (2015). Unabated planetary warming and its ocean structure since 2006. *Nature climate change*, 5(3):240–245.

[Rohrschneider et al., 2019] Rohrschneider, T., Stevens, B., and Mauritsen, T. (2019). On simple representations of the climate response to external radiative forcing. *Climate Dynamics*, 53(5):3131–3145.

[Rousselet et al., 2021] Rousselet, L., Cessi, P., and Forget, G. (2021). Coupling of the mid-depth and abyssal components of the global overturning circulation according to a state estimate. *Science Advances*, 7(21):eabf5478.

[Sachs and Lehman, 1999] Sachs, J. P. and Lehman, S. J. (1999). Subtropical north atlantic temperatures 60,000 to 30,000 years ago. *Science*, 286(5440):756–759.

[Saenko and Merryfield, 2005] Saenko, O. and Merryfield, W. (2005). On the effect of topographically enhanced mixing on the global ocean circulation. *Journal of Physical Oceanography*, 35(5):826–834.

[Saenko et al., 2005] Saenko, O. A., Fyfe, J. C., and England, M. H. (2005). On the response of the oceanic wind-driven circulation to atmospheric co 2 increase. *Climate dynamics*, 25(4):415–426.

[Saenko et al., 2021] Saenko, O. A., Gregory, J. M., Griffies, S. M., Couldrey, M. P., and Dias, F. B. (2021). Contribution of ocean physics and dynamics at different scales to heat uptake in low-resolution aogcms. *Journal of Climate*, 34(6):2017–2035.

[Saenko et al., 2018] Saenko, O. A., Yang, D., and Gregory, J. M. (2018). Impact of mesoscale eddy transfer on heat uptake in an eddy-parameterizing ocean model. *Journal of Climate*, 31(20):8589–8606.

[Saenz et al., 2012] Saenz, J., Hogg, A., Hughes, G., and Griffiths, R. (2012). Mechanical power input from buoyancy and wind to the circulation in an ocean model. *Geophysical research letters*, 39(13).

[Salas-Mélia et al., 2005] Salas-Mélia, D., Chauvin, F., Déqué, M., Douville, H., Gueremy, J., Marquet, P., Planton, S., Royer, J., and Tyteca, S. (2005). Description and validation of the cnrm-cm3 global coupled model. *CNRM working note*, 103:36.

[Salehipour et al., 2015] Salehipour, H., Peltier, W., and Mashayek, A. (2015). Turbulent diapycnal mixing in stratified shear flows: the influence of prandtl number on mixing efficiency and transition at high reynolds number. *Journal of Fluid Mechanics*, 773:178–223.

[Sandström, 1908] Sandström, J. W. (1908). Dynamische versuche mit meerwasser. *Ann. Hydrodyn. Mar. Meteor.*, 36:6–23.

[Sarnthein et al., 1994] Sarnthein, M., Winn, K., Jung, S. J., Duplessy, J.-C., Labeyrie, L., Erlenkeuser, H., and Ganssen, G. (1994). Changes in east atlantic deepwater circulation over the last 30,000 years: Eight time slice reconstructions. *Paleoceanography*, 9(2):209–267.

[Savita et al., 2021] Savita, A., Zika, J. D., Domingues, C. M., Marsland, S. J., Evans, G. D., Dias, F. B., Holmes, R. M., and McC. Hogg, A. (2021). Super residual circulation: A new perspective on ocean vertical heat transport. *Journal of Physical Oceanography*, 51(8):2443–2462.

[Schlesinger and Jiang, 1990] Schlesinger, M. E. and Jiang, X. (1990). Simple model representation of atmosphere-ocean gcms and estimation of the time scale of c02-induced climate change. *Journal of climate*, 3(12):1297–1315.

[Schlesinger and Mitchell, 1987] Schlesinger, M. E. and Mitchell, J. F. (1987). Climate model simulations of the equilibrium climatic response to increased carbon dioxide. *Reviews of Geophysics*, 25(4):760–798.

[Schlitzer, 2000] Schlitzer, R. (2000). Electronic atlas of woce hydrographic and tracer data. *EOS Trans. Am. Geophys. Un.*, 81(5).

[Sellers, 1969] Sellers, W. D. (1969). A global climatic model based on the energy balance of the earth-atmosphere system. *Journal of Applied Meteorology*, 8(3):392–400.

[Send et al., 2011] Send, U., Lankhorst, M., and Kanzow, T. (2011). Observation of decadal change in the atlantic meridional overturning circulation using 10 years of continuous transport data. *Geophysical Research Letters*, 38(24).

[Serreze and Barry, 2011] Serreze, M. C. and Barry, R. G. (2011). Processes and impacts of arctic amplification: A research synthesis. *Global and planetary change*, 77(1-2):85–96.

[Sévellec et al., 2017] Sévellec, F., Fedorov, A. V., and Liu, W. (2017). Arctic sea-ice decline weakens the atlantic meridional overturning circulation. *Nature Climate Change*, 7(8):604–610.

[Shatwell et al., 2020] Shatwell, P., Czaja, A., and Ferreira, D. (2020). Ocean heat storage rate unaffected by moc weakening in an idealized climate model. *Geophysical Research Letters*, 47(16).

[Shi et al., 2018] Shi, J.-R., Xie, S.-P., and Talley, L. D. (2018). Evolving relative importance of the southern ocean and north atlantic in anthropogenic ocean heat uptake. *Journal of Climate*, 31(18):7459–7479.

[Smeed et al., 2018] Smeed, D., Josey, S., Beaulieu, C., Johns, W. E., Moat, B., Frajka-Williams, E., Rayner, D., Meinen, C., Baringer, M., Bryden, H., et al. (2018). The north atlantic ocean is in a state of reduced overturning. *Geophysical Research Letters*, 45(3):1527–1533.

[Smith et al., 2015] Smith, D. M., Allan, R. P., Coward, A. C., Eade, R., Hyder, P., Liu, C., Loeb, N. G., Palmer, M. D., Roberts, C. D., and Scaife, A. A. (2015). Earth's energy imbalance since 1960 in observations and cmip5 models. *Geophysical research letters*, 42(4):1205–1213.

[Smith and Murphy, 2007] Smith, D. M. and Murphy, J. M. (2007). An objective ocean temperature and salinity analysis using covariances from a global climate model. *Journal of Geophysical Research: Oceans*, 112(C2).

[Smith and Marshall, 2009] Smith, K. S. and Marshall, J. (2009). Evidence for enhanced eddy mixing at middepth in the southern ocean. *Journal of Physical Oceanography*, 39(1):50–69.

[Smith et al., 2010] Smith, R., Jones, P., Briegleb, B., Bryan, F., Danabasoglu, G., Dennis, J., Dukowicz, J., Eden, C., Fox-Kemper, B., Gent, P., et al. (2010). The parallel ocean program (pop) reference manual: ocean component of the

community climate system model (ccsm) and community earth system model (cesm). *LAUR-01853*, 141:1–140.

[Solomon et al., 2007] Solomon, S., Manning, M., Marquis, M., Qin, D., et al. (2007). *Climate change 2007-the physical science basis: Working group I contribution to the fourth assessment report of the IPCC*, volume 4. Cambridge university press.

[Spilhaus, 1983] Spilhaus, A. (1983). World ocean maps: the proper places to interrupt. *Proceedings of the American Philosophical Society*, 127(1):50–60.

[Spilhaus, 1942] Spilhaus, A. F. (1942). Maps of the whole world ocean. *Geographical Review*, 32(3):431–435.

[Stocker et al., 2013] Stocker, T. F., Qin, D., Plattner, G.-K., Tignor, M., Allen, S. K., Boschung, J., Nauels, A., Xia, Y., Bex, V., Midgley, P. M., et al. (2013). Climate change 2013: The physical science basis. *Contribution of working group I to the fifth assessment report of the intergovernmental panel on climate change*, 1535.

[Stommel, 1948] Stommel, H. (1948). The westward intensification of wind-driven ocean currents. *Eos, Transactions American Geophysical Union*, 29(2):202–206.

[Stommel, 1961] Stommel, H. (1961). Thermohaline convection with two stable regimes of flow. *Tellus*, 13(2):224–230.

[Stouffer, 2004] Stouffer, R. J. (2004). Time scales of climate response. *Journal of climate*, 17(1):209–217.

[Stouffer et al., 2006] Stouffer, R. J., Yin, J., Gregory, J., Dixon, K., Spelman, M., Hurlin, W., Weaver, A., Eby, M., Flato, G., Hasumi, H., et al. (2006). Investigating the causes of the response of the thermohaline circulation to past and future climate changes. *Journal of Climate*, 19(8):1365–1387.

[Sun et al., 2022] Sun, S., Thompson, A. F., Xie, S.-P., and Long, S.-M. (2022). Indo-pacific warming induced by a weakening of the atlantic meridional overturning circulation. *Journal of Climate*, 35(2):815–832.

[Suzuki et al., 2022] Suzuki, T., Komuro, Y., Kusahara, K., and Tatebe, H. (2022). Transient influence of the reduction of deepwater formation on ocean heat uptake and heat budgets in the global climate system. *Geophysical Research Letters*, 49(3):e2021GL095179.

[Sverdrup, 1947] Sverdrup, H. U. (1947). Wind-driven currents in a baroclinic ocean; with application to the equatorial currents of the eastern pacific. *Proceedings of the National Academy of Sciences*, 33(11):318–326.

[Swart and Fyfe, 2012] Swart, N. and Fyfe, J. C. (2012). Observed and simulated changes in the southern hemisphere surface westerly wind-stress. *Geophysical Research Letters*, 39(16).

[Tailleux, 2009] Tailleux, R. (2009). On the energetics of stratified turbulent mixing, irreversible thermodynamics, boussinesq models and the ocean heat engine controversy. *Journal of Fluid Mechanics*, 638:339–382.

[Tailleux, 2010] Tailleux, R. (2010). Entropy versus ape production: On the buoyancy power input in the oceans energy cycle. *Geophysical research letters*, 37(22).

[Talley, 2011] Talley, L. D. (2011). *Descriptive physical oceanography: an introduction*. Academic press.

[Talley, 2013] Talley, L. D. (2013). Closure of the global overturning circulation through the indian, pacific, and southern oceans: Schematics and transports. *Oceanography*, 26(1):80–97.

[Taylor et al., 2012] Taylor, K. E., Stouffer, R. J., and Meehl, G. A. (2012). An overview of cmip5 and the experiment design. *Bulletin of the American Meteorological Society*, 93(4):485–498.

[Thompson et al., 2016] Thompson, A. F., Stewart, A. L., and Bischoff, T. (2016). A multibasin residual-mean model for the global overturning circulation. *Journal of Physical Oceanography*, 46(9):2583–2604.

[Thompson and Solomon, 2002] Thompson, D. W. and Solomon, S. (2002). Interpretation of recent southern hemisphere climate change. *Science*, 296(5569):895–899.

[Thornalley et al., 2018] Thornalley, D. J., Oppo, D. W., Ortega, P., Robson, J. I., Brierley, C. M., Davis, R., Hall, I. R., Moffa-Sanchez, P., Rose, N. L., Spooner, P. T., et al. (2018). Anomalously weak labrador sea convection and atlantic overturning during the past 150 years. *Nature*, 556(7700):227–230.

[Toggweiler and Samuels, 1998] Toggweiler, J. and Samuels, B. (1998). On the ocean's large-scale circulation near the limit of no vertical mixing. *Journal of Physical Oceanography*, 28(9):1832–1852.

[Toggweiler and Russell, 2008] Toggweiler, J. R. and Russell, J. (2008). Ocean circulation in a warming climate. *Nature*, 451(7176):286–288.

[Trenberth, 2018] Trenberth, K. E. (2018). Climate change caused by human activities is happening and it already has major consequences. *Journal of energy & natural resources law*, 36(4):463–481.

[Trenberth, 2020] Trenberth, K. E. (2020). Understanding climate change through earth's energy flows. *Journal of the Royal Society of New Zealand*, 50(2):331–347.

[Trenberth and Caron, 2001] Trenberth, K. E. and Caron, J. M. (2001). Estimates of meridional atmosphere and ocean heat transports. *Journal of Climate*, 14(16):3433–3443.

[Trenberth et al., 2014] Trenberth, K. E., Fasullo, J. T., and Balmaseda, M. A. (2014). Earth's energy imbalance. *Journal of Climate*, 27(9):3129–3144.

[Trenberth et al., 2009] Trenberth, K. E., Fasullo, J. T., and Kiehl, J. (2009). Earth's global energy budget. *Bulletin of the American Meteorological Society*, 90(3):311–324.

[Vallis, 2012] Vallis, G. K. (2012). *Climate and the Oceans*. Princeton University Press.

[Vallis, 2017] Vallis, G. K. (2017). *Atmospheric and oceanic fluid dynamics*. Cambridge University Press.

[Van den Broeke et al., 2016] Van den Broeke, M. R., Enderlin, E. M., Howat, I. M., Kuipers Munneke, P., Noël, B. P., Van De Berg, W. J., Van Meijgaard, E., and

Wouters, B. (2016). On the recent contribution of the greenland ice sheet to sea level change. *The Cryosphere*, 10(5):1933–1946.

[Van Sebille et al., 2018] Van Sebille, E., Griffies, S. M., Abernathey, R., Adams, T. P., Berloff, P., Biastoch, A., Blanke, B., Chassignet, E. P., Cheng, Y., Cotter, C. J., et al. (2018). Lagrangian ocean analysis: Fundamentals and practices. *Ocean Modelling*, 121:49–75.

[Vellinga and Wood, 2008] Vellinga, M. and Wood, R. A. (2008). Impacts of thermohaline circulation shutdown in the twenty-first century. *Climatic Change*, 91(1-2):43–63.

[Viebahn and Eden, 2010] Viebahn, J. and Eden, C. (2010). Towards the impact of eddies on the response of the southern ocean to climate change. *Ocean Modelling*, 34(3-4):150–165.

[Vollmer and Eden, 2013] Vollmer, L. and Eden, C. (2013). A global map of mesoscale eddy diffusivities based on linear stability analysis. *Ocean Modelling*, 72:198–209.

[Von Schuckmann et al., 2020] Von Schuckmann, K., Cheng, L., Palmer, M. D., Hansen, J., Tassone, C., Aich, V., Adusumilli, S., Beltrami, H., Boyer, T., Cuesta-Valero, F. J., et al. (2020). Heat stored in the earth system: where does the energy go? *Earth System Science Data*, 12(3):2013–2041.

[Von Schuckmann et al., 2016] Von Schuckmann, K., Palmer, M., Trenberth, K. E., Cazenave, A., Chambers, D., Champollion, N., Hansen, J., Josey, S., Loeb, N., Mathieu, P.-P., et al. (2016). An imperative to monitor earth's energy imbalance. *Nature Climate Change*, 6(2):138–144.

[Walin, 1982] Walin, G. (1982). On the relation between sea-surface heat flow and thermal circulation in the ocean. *Tellus*, 34(2):187–195.

[Wallace et al., 1990] Wallace, J. M., Smith, C., and Jiang, Q. (1990). Spatial patterns of atmosphere-ocean interaction in the northern winter. *Journal of Climate*, 3(9):990–998.

[Warren, 1983] Warren, B. A. (1983). Why is no deep water formed in the north pacific? *Journal of Marine Research*, 41(2):327–347.

[Washington and Meehl, 1984] Washington, W. M. and Meehl, G. A. (1984). Seasonal cycle experiment on the climate sensitivity due to a doubling of co2 with an atmospheric general circulation model coupled to a simple mixed-layer ocean model. *Journal of Geophysical Research: Atmospheres*, 89(D6):9475–9503.

[Watanabe et al., 2013] Watanabe, M., Kamae, Y., Yoshimori, M., Oka, A., Sato, M., Ishii, M., Mochizuki, T., and Kimoto, M. (2013). Strengthening of ocean heat uptake efficiency associated with the recent climate hiatus. *Geophysical Research Letters*, 40(12):3175–3179.

[Watanabe et al., 2010] Watanabe, M., Suzuki, T., O'ishi, R., Komuro, Y., Watanabe, S., Emori, S., Takemura, T., Chikira, M., Ogura, T., Sekiguchi, M., et al. (2010). Improved climate simulation by miroc5: mean states, variability, and climate sensitivity. *Journal of Climate*, 23(23):6312–6335.

[Waterhouse et al., 2014] Waterhouse, A. F., MacKinnon, J. A., Nash, J. D., Alford, M. H., Kunze, E., Simmons, H. L., Polzin, K. L., St. Laurent, L. C., Sun, O. M., Pinkel, R., et al. (2014). Global patterns of diapycnal mixing from measurements of the turbulent dissipation rate. *Journal of Physical Oceanography*, 44(7):1854–1872.

[Watson et al., 2013] Watson, A. J., Ledwell, J. R., Messias, M.-J., King, B. A., Mackay, N., Meredith, M. P., Mills, B., and Naveira Garabato, A. C. (2013). Rapid cross-density ocean mixing at mid-depths in the drake passage measured by tracer release. *Nature*, 501(7467):408–411.

[Weaver et al., 2012] Weaver, A. J., Sedláček, J., Eby, M., Alexander, K., Crespin, E., Fichefet, T., Philippon-Berthier, G., Joos, F., Kawamiya, M., Matsumoto, K., et al. (2012). Stability of the atlantic meridional overturning circulation: A model intercomparison. *Geophysical Research Letters*, 39(20).

[Webb and Suginohara, 2001] Webb, D. and Suginohara, N. (2001). Vertical mixing in the ocean. *Nature*, 409(6816):37–37.

[Weijer et al., 2020] Weijer, W., Cheng, W., Garuba, O. A., Hu, A., and Nadiga, B. (2020). Cmip6 models predict significant 21st century decline of the atlantic meridional overturning circulation. *Geophysical Research Letters*, 47(12):e2019GL086075.

[Whalen et al., 2012] Whalen, C., Talley, L., and MacKinnon, J. (2012). Spatial and temporal variability of global ocean mixing inferred from argo profiles. *Geophysical Research Letters*, 39(18).

[Whalen et al., 2020] Whalen, C. B., De Lavergne, C., Naveira Garabato, A. C., Klymak, J. M., Mackinnon, J. A., and Sheen, K. L. (2020). Internal wave-driven mixing: Governing processes and consequences for climate. *Nature Reviews Earth & Environment*, 1(11):606–621.

[Wigley and Raper, 1987] Wigley, T. M. and Raper, S. (1987). Thermal expansion of sea water associated with global warming. *Nature*, 330(6144):127–131.

[Wijffels et al., 2016] Wijffels, S., Roemmich, D., Monselesan, D., Church, J., and Gilson, J. (2016). Ocean temperatures chronicle the ongoing warming of earth. *Nature Climate Change*, 6(2):116–118.

[Wijffels et al., 1992] Wijffels, S. E., Schmitt, R. W., Bryden, H. L., and Stigebrandt, A. (1992). Transport of freshwater by the oceans. *J. Phys. Oceanogr*, 22(2):155–162.

[Wild et al., 2015] Wild, M., Folini, D., Hakuba, M. Z., Schär, C., Seneviratne, S. I., Kato, S., Rutan, D., Ammann, C., Wood, E. F., and König-Langlo, G. (2015). The energy balance over land and oceans: an assessment based on direct observations and cmip5 climate models. *Climate Dynamics*, 44(11):3393–3429.

[Wills and Schneider, 2015] Wills, R. C. and Schneider, T. (2015). Stationary eddies and the zonal asymmetry of net precipitation and ocean freshwater forcing. *Journal of Climate*, 28(13):5115–5133.

[Winton, 2003] Winton, M. (2003). On the climatic impact of ocean circulation. *Journal of climate*, 16(17):2875–2889.

[Winton et al., 2014] Winton, M., Anderson, W. G., Delworth, T. L., Griffies, S. M., Hurlin, W. J., and Rosati, A. (2014). Has coarse ocean resolution biased simulations of transient climate sensitivity? *Geophysical Research Letters*, 41(23):8522–8529.

[Winton et al., 2013] Winton, M., Griffies, S. M., Samuels, B. L., Sarmiento, J. L., and Frölicher, T. L. (2013). Connecting changing ocean circulation with changing climate. *Journal of climate*, 26(7):2268–2278.

[Wolfe and Cessi, 2011] Wolfe, C. L. and Cessi, P. (2011). The adiabatic pole-to-pole overturning circulation. *Journal of Physical Oceanography*, 41(9):1795–1810.

[Wright et al., 2014] Wright, C. J., Scott, R. B., Ailliot, P., and Furnival, D. (2014). Lee wave generation rates in the deep ocean. *Geophysical Research Letters*, 41(7):2434–2440.

[Wu et al., 2012] Wu, L., Cai, W., Zhang, L., Nakamura, H., Timmermann, A., Joyce, T., McPhaden, M. J., Alexander, M., Qiu, B., Visbeck, M., et al. (2012). Enhanced warming over the global subtropical western boundary currents. *Nature Climate Change*, 2(3):161–166.

[Wunsch, 2020] Wunsch, C. (2020). Is the ocean speeding up? ocean surface energy trends. *Journal of Physical Oceanography*, 50(11):3205–3217.

[Wunsch and Ferrari, 2004] Wunsch, C. and Ferrari, R. (2004). Vertical mixing, energy, and the general circulation of the oceans. *Annu. Rev. Fluid Mech.*, 36:281–314.

[Wunsch and Heimbach, 2013] Wunsch, C. and Heimbach, P. (2013). Two decades of the atlantic meridional overturning circulation: Anatomy, variations, extremes, prediction, and overcoming its limitations. *Journal of Climate*, 26(18):7167–7186.

[Wyrtki, 1961] Wyrtki, K. (1961). The thermohaline circulation in relation to the general circulation in the oceans. *Deep Sea Research (1953)*, 8(1):39–64.

[Xie and Vallis, 2012] Xie, P. and Vallis, G. K. (2012). The passive and active nature of ocean heat uptake in idealized climate change experiments. *Climate Dynamics*, 38(3-4):667–684.

[Yang et al., 2020] Yang, H., Lohmann, G., Krebs-Kanzow, U., Ionita, M., Shi, X., Sidorenko, D., Gong, X., Chen, X., and Gowan, E. J. (2020). Poleward shift of the major ocean gyres detected in a warming climate. *Geophysical Research Letters*, 47(5):e2019GL085868.

[Yang et al., 2016] Yang, H., Lohmann, G., Wei, W., Dima, M., Ionita, M., and Liu, J. (2016). Intensification and poleward shift of subtropical western boundary currents in a warming climate. *Journal of Geophysical Research: Oceans*, 121(7):4928–4945.

[Yang and Zhu, 2011] Yang, H. and Zhu, J. (2011). Equilibrium thermal response timescale of global oceans. *Geophysical research letters*, 38(14).

[Yang et al., 2019] Yang, Q., Nikurashin, M., Sasaki, H., Sun, H., and Tian, J. (2019). Dissipation of mesoscale eddies and its contribution to mixing in the northern south china sea. *Scientific reports*, 9(1):1–9.

[Yin, 2005] Yin, J. H. (2005). A consistent poleward shift of the storm tracks in simulations of 21st century climate. *Geophysical Research Letters*, 32(18).

[Yu and Weller, 2007] Yu, L. and Weller, R. A. (2007). Objectively analyzed air–sea heat fluxes for the global ice-free oceans (1981–2005). *Bulletin of the American Meteorological Society*, 88(4):527–540.

[Zanna et al., 2019] Zanna, L., Khatiwala, S., Gregory, J. M., Ison, J., and Heimbach, P. (2019). Global reconstruction of historical ocean heat storage and transport. *Proceedings of the National Academy of Sciences*, 116(4):1126–1131.

[Zemskova et al., 2015] Zemskova, V. E., White, B. L., and Scotti, A. (2015). Available potential energy and the general circulation: Partitioning wind, buoyancy forcing, and diapycnal mixing. *Journal of Physical Oceanography*, 45(6):1510–1531.

[Zhai et al., 2012] Zhai, X., Johnson, H. L., Marshall, D. P., and Wunsch, C. (2012). On the wind power input to the ocean general circulation. *Journal of Physical Oceanography*, 42(8):1357–1365.

[Zhang et al., 2004] Zhang, Y., Rossow, W. B., Lacis, A. A., Oinas, V., and Mishchenko, M. I. (2004). Calculation of radiative fluxes from the surface to top of atmosphere based on isccp and other global data sets: Refinements of the radiative transfer model and the input data. *Journal of Geophysical Research: Atmospheres*, 109(D19).

[Zhang and Vallis, 2013] Zhang, Y. and Vallis, G. K. (2013). Ocean heat uptake in eddying and non-eddying ocean circulation models in a warming climate. *Journal of physical oceanography*, 43(10):2211–2229.

[Zhu and Liu, 2020] Zhu, C. and Liu, Z. (2020). Weakening atlantic overturning circulation causes south atlantic salinity pile-up. *Nature Climate Change*, pages 1–6.

[Zika et al., 2012] Zika, J. D., England, M. H., and Sijp, W. P. (2012). The ocean circulation in thermohaline coordinates. *Journal of Physical Oceanography*, 42(5):708–724.

[Zika et al., 2020] Zika, J. D., Gregory, J. M., McDonagh, E. L., Marzocchi, A., and Clement, L. (2020). Recent water mass changes reveal mechanisms of ocean warming. *Journal of Climate*, pages 1–52.

[Zika et al., 2015] Zika, J. D., Laliberté, F., Mudryk, L. R., Sijp, W. P., and Nurser, A. (2015). Changes in ocean vertical heat transport with global warming. *Geophysical Research Letters*, 42(12):4940–4948.

[Zika et al., 2013] Zika, J. D., Sijp, W. P., and England, M. H. (2013). Vertical heat transport by ocean circulation and the role of mechanical and haline forcing. *Journal of physical oceanography*, 43(10):2095–2112.

# A

# Eddy parameterisation in MITgcm

As introduced in Chapter 2, mesoscale eddies in the DDrake ocean are parameterised as a combination of an isopycnal diffusion (Redi) [Redi, 1982] and an advective process (GM) [Gent and Mcwilliams, 1990], both with the same transfer coefficient of 1200 $m^2\ s^{-1}$. The 'Redi' scheme mixes tracer properties along isopycnal surfaces, introducing a tendency term on the right-hand side of the tracer equations 2.4 and 2.5 of the form $\nabla \cdot (\kappa_\rho \underline{\underline{\mathbf{K}}}_{Redi} \nabla \tau)$. Here, $\kappa_\rho$ is the isopycnal diffusivity and $\underline{\underline{\mathbf{K}}}_{Redi}$ is a rank 2 tensor that projects the gradient of the tracer $\tau$ onto the isopycnal surface. The $\underline{\underline{\mathbf{K}}}_{Redi}$ tensor has the form:

$$\underline{\underline{\mathbf{K}}}_{Redi} = \frac{1}{1+|\mathbf{S}|^2} \begin{pmatrix} 1+S_y^2 & -S_x S_y & S_x \\ -S_x S_y & 1+S_x^2 & S_y \\ S_x & S_y & |\mathbf{S}|^2 \end{pmatrix} \approx \begin{pmatrix} 1 & 0 & S_x \\ 0 & 1 & S_y \\ S_x & S_y & |\mathbf{S}|^2 \end{pmatrix} \tag{A.1}$$

where $S_x = -\partial_x \sigma / \partial_z \sigma$ and $S_y = -\partial_y \sigma / \partial_z \sigma$ define the components of the slope of the isopycnal surfaces $\sigma$. To get the final expression, we have made the small slope approximation ($|\mathbf{S}| \ll 1$). This is appropriate, as typical slopes in the ocean interior

are very small ($\sim 10^{-4}$–$10^{-2}$).

The GM advective or 'transport' effect of the eddies is parameterised by means of a 'bolus velocity' $\mathbf{u}_b$ which depends on $S_x$ and $S_y$. This adds another term on the right-hand side of the model tracer equations of the form $-\nabla \cdot (\tau \mathbf{u}_b)$. The bolus velocity is defined as the curl of a stream function $\mathbf{F}^*$ (and hence is automatically non-divergent):

$$\mathbf{u}_b = \nabla \times \mathbf{F}^* = \nabla \times \begin{pmatrix} F_x^* \\ F_y^* \\ 0 \end{pmatrix} = \nabla \times \begin{pmatrix} -\kappa_{GM} S_y \\ \kappa_{GM} S_x \\ 0 \end{pmatrix} = \begin{pmatrix} -\partial_z(\kappa_{GM} S_x) \\ -\partial_z(\kappa_{GM} S_y) \\ \partial_x(\kappa_{GM} S_x) + \partial_y(\kappa_{GM} S_y) \end{pmatrix} \tag{A.2}$$

where $\kappa_{GM}$ is the GM eddy transfer coefficient. It was pointed out by [Griffies, 1998] that the eddy bolus flux $\tau \mathbf{u}_b$ could be written as the sum of a non-divergent flux and a skew flux:

$$\begin{aligned} \tau \mathbf{u}_b &= \begin{pmatrix} -\partial_z(\kappa_{GM} S_x)\tau \\ -\partial_z(\kappa_{GM} S_y)\tau \\ (\partial_x(\kappa_{GM} S_x) + \partial_y(\kappa_{GM} S_y))\tau \end{pmatrix} \\ &= \begin{pmatrix} -\partial_z(\kappa_{GM} S_x \tau) \\ -\partial_z(\kappa_{GM} S_y \tau) \\ \partial_x(\kappa_{GM} S_x \tau) + \partial_y(\kappa_{GM} S_y \tau) \end{pmatrix} + \begin{pmatrix} \kappa_{GM} S_x \partial_z \tau \\ \kappa_{GM} S_y \partial_z \tau \\ -\kappa_{GM} S_x \partial_x \tau - \kappa_{GM} S_y \partial_y \tau \end{pmatrix} \end{aligned} \tag{A.3}$$

As the first vector in this decomposition is non-divergent, it has no effect on the tracer field, so it can be dropped. This means that we can redefine $\tau \mathbf{u}_b \equiv \kappa_{GM} \underline{\underline{\mathbf{K}}}_{GM} \nabla \tau$, where $\underline{\underline{\mathbf{K}}}_{GM}$ is an antisymmetric tensor with the form:

$$\underline{\underline{\mathbf{K}}}_{GM} = \begin{pmatrix} 0 & 0 & -S_x \\ 0 & 0 & -S_y \\ S_x & S_y & 0 \end{pmatrix} \tag{A.4}$$

It is this formulation of the GM scheme that is used in the DDrake configuration.

The horizontal eddy buoyancy transfer is equivalent to conventional downgradient diffusion, while the vertical transfer is *upgradient*. The combination of these fluxes acts to rotate and flatten the isopycnal surfaces, extracting kinetic energy from the available potential energy of the flow.

The GM scheme is used in conjunction with the Redi isopycnal mixing scheme so that: $\kappa_\rho \underline{\underline{\mathbf{K}}}_{Redi} \nabla\tau - \tau \mathbf{u}_b = (\kappa_\rho \underline{\underline{\mathbf{K}}}_{Redi} + \kappa_{GM} \underline{\underline{\mathbf{K}}}_{GM}) \nabla\tau$. By choosing the same transfer coefficient ($\kappa_\rho = \kappa_{GM} = \kappa$) for both $\underline{\underline{\mathbf{K}}}_{Redi}$ and $\underline{\underline{\mathbf{K}}}_{GM}$, substantial cancellations take place leaving us with:

$$\kappa_\rho \underline{\underline{\mathbf{K}}}_{Redi} + \kappa_{GM} \underline{\underline{\mathbf{K}}}_{GM} = \kappa(\underline{\underline{\mathbf{K}}}_{Redi} + \underline{\underline{\mathbf{K}}}_{GM}) = \kappa \begin{pmatrix} 1 & 0 & 0 \\ 0 & 1 & 0 \\ 2S_x & 2S_y & |\mathbf{S}|^2 \end{pmatrix} \tag{A.5}$$

This is the essence of the 'GMREDI' scheme used in the MITgcm for the parameterisation of mesoscale oceanic eddies.

# B

# Derivation of the change in SBMOC heat flux

As introduced in Chapter 4, a model quantity $C = C(t, x, y, z)$ changes from its control value $\overline{C}(x, y, z)$ to a perturbed value $C^{pert}(t, x, y, z)$ by an amount $\Delta C$ due to the $CO_2$ perturbation:

$$\Delta C(t, x, y, z) = C^{pert}(t, x, y, z) - \overline{C}(x, y, z) \tag{B.1}$$

where $\overline{C}$ is a 50-year time average taken from the last 50 years of the model spin-up, after it has reached an equilibrated state. We note that we do not analyse instantaneous values in the perturbed climate, but rather annual averages. This detail is unimportant when considering changes in one quantity, but has an impact when considering changes in a combination of quantities. Hence, we first rewrite equation B.1 as a difference between an annually averaged quantity in the perturbed climate, and a 50-year averaged quantity in the control climate:

$$\Delta C(t, x, y, z) = \overline{C}^{1yr}_{pert}(t, x, y, z) - \overline{C}^{50yr}_{ctrl}(x, y, z) \tag{B.2}$$

Then, an instantaneous value of $\Psi_{res}$ in the perturbed simulation is:

$$\Psi_{res} = \overline{\Psi_{res}}^{1yr} + \Psi'_{res} = \Delta\Psi_{res} + \overline{\Psi_{res}}^{50yr} + \Psi'_{res} \tag{B.3}$$

where $\Psi'_{res}$ is the sub-annual variability in $\Psi_{res}$, and the 'ctrl' and 'pert' subscripts have been omitted for clarity. A similar expression can be obtained for $\delta\theta$. Then, a change in the SBMOC heat flux $\mathcal{H}_{MOC}$ is given by:

$$\begin{aligned}
\frac{\Delta\mathcal{H}_{MOC}}{\rho_0 c_p} &= \overline{\Psi_{res}\delta\theta}^{1yr}_{pert} - \overline{\Psi_{res}\delta\theta}^{50yr}_{ctrl} \\
&= \overline{(\Delta\Psi_{res} + \overline{\Psi_{res}}^{50yr} + \Psi'_{res})(\Delta(\delta\theta) + \overline{\delta\theta}^{50yr} + \delta\theta')}^{1yr} - \overline{\Psi_{res}\delta\theta}^{50yr} \\
&= \overline{\Delta\Psi_{res}\Delta(\delta\theta)}^{1yr} + \overline{\Delta\Psi_{res}\overline{\delta\theta}^{50yr}}^{1yr} + \overline{\Delta\Psi_{res}\delta\theta'}^{1yr} \\
&+ \overline{\overline{\Psi_{res}}^{50yr}\Delta(\delta\theta)}^{1yr} + \overline{\overline{\Psi_{res}}^{50yr}\overline{\delta\theta}^{50yr}}^{1yr} + \overline{\overline{\Psi_{res}}^{50yr}\delta\theta'}^{1yr} \\
&+ \overline{\Psi'_{res}\Delta(\delta\theta)}^{1yr} + \overline{\Psi'_{res}\overline{\delta\theta}^{50yr}}^{1yr} + \overline{\Psi'_{res}\delta\theta'}^{1yr} - \overline{\Psi_{res}\delta\theta}^{50yr} \\
&= \Delta\Psi_{res}\Delta(\delta\theta) + \Delta\Psi_{res}\overline{\delta\theta}^{50yr} + \overline{\Psi_{res}}^{50yr}\Delta(\delta\theta) \\
&+ \underbrace{\overline{\Psi_{res}}^{50yr}\overline{\delta\theta}^{50yr} + \overline{\Psi'_{res}\delta\theta'}^{1yr} - \overline{\Psi_{res}\delta\theta}^{50yr}}_{T}
\end{aligned} \tag{B.4}$$

Note that $\overline{\Delta C}^{1yr} = \Delta C$ and $\overline{C'}^{1yr} = 0$ for some quantity $C$. The term $T$ represents the change in variability between the control and perturbed climates:

$$T = \underbrace{\overline{\Psi'_{res}\delta\theta'}^{1yr}}_{T_{pert}} - \underbrace{(\overline{\Psi_{res}\delta\theta}^{50yr} - \overline{\Psi_{res}}^{50yr}\overline{\delta\theta}^{50yr})}_{T_{ctrl}} \tag{B.5}$$

In our analysis, we assume that this term $T$ is small and hence neglect it in our expression for $\Delta\mathcal{H}_{MOC}$. This leaves us with:

$$\frac{\Delta\mathcal{H}_{MOC}}{\rho_0 c_p} \approx \Delta\Psi_{res}\Delta(\delta\theta) + \Delta\Psi_{res}\overline{\delta\theta}^{50yr} + \overline{\Psi_{res}}^{50yr}\Delta(\delta\theta) \tag{B.6}$$

which is our equation 4.3 as stated in Chapter 4.

# C

# Analytical solution of the Geoffroy EBM under a step-forcing

The two-layer EBM utilised in [Geoffroy et al., 2013b] was introduced in Chapter 5 in equation 5.1, which we reprint here for reference:

$$\begin{aligned} C\frac{dT}{dt} &= \mathcal{F} - \alpha T - \gamma(T - T_0) \\ C_0\frac{dT_0}{dt} &= \gamma(T - T_0) \end{aligned} \tag{C.1}$$

For a step-forcing, $\mathcal{F}$ is a constant. We can rewrite these equations as a matrix differential equation in the form $d\mathbf{X}/dt = \mathbb{A}\mathbf{X} + \mathbf{B}$, giving:

$$\frac{d}{dt}\begin{pmatrix} T \\ T_0 \end{pmatrix} = \begin{pmatrix} -(\alpha+\gamma)/C & \gamma/C \\ \gamma/C_0 & -\gamma/C_0 \end{pmatrix}\begin{pmatrix} T \\ T_0 \end{pmatrix} + \begin{pmatrix} \mathcal{F}/C \\ 0 \end{pmatrix} \tag{C.2}$$

The general solution to this system of ODEs is the solution to the homogenous equation, plus a particular solution (or particular integral).

## C.1 Particular solution

For a steady-state solution $\mathbf{X}^*$, $d\mathbf{X}/dt = 0$, which implies that $\mathbb{A}\mathbf{X}^* + \mathbf{B} = 0$. From this, we see that $\mathbf{X}^* = -\mathbb{A}^{-1}\mathbf{B}$ and that $\mathbf{B} = -\mathbb{A}\mathbf{X}^*$. From this last expression, we can rewrite equation C.2 as:

$$\frac{d\mathbf{X}}{dt} = \mathbb{A}(\mathbf{X}(t) - \mathbf{X}^*) \tag{C.3}$$

which reveals that the steady-state solution $\mathbf{X}^*$ is in fact a *particular solution.* Hence, noting that $\det \mathbb{A} = \gamma\alpha/CC_0 \neq 0$, we can invert the matrix $\mathbb{A}$ and evaluate the solution as:

$$\mathbf{X}^* = -\mathbb{A}^{-1}\mathbf{B} = \frac{CC_0}{\gamma\alpha}\begin{pmatrix}\gamma/C_0 & \gamma/C \\ \gamma/C_0 & (\alpha+\gamma)/C\end{pmatrix}\begin{pmatrix}\mathcal{F}/C \\ 0\end{pmatrix} = \begin{pmatrix}\mathcal{F}/\alpha \\ \mathcal{F}/\alpha\end{pmatrix} = \begin{pmatrix}T_{eq} \\ T_{eq}\end{pmatrix} \tag{C.4}$$

So, the steady-state solution is the equilibrium temperature $T_{eq}$, which is to be expected.

## C.2 Solution to the homogeneous equation

We now seek a solution to the homogeneous equation $d\mathbf{X}_h/dt = \mathbb{A}\mathbf{X}_h$. A general form of solution to this equation is:

$$\mathbf{X}_h(t) = c_1 e^{\lambda_1 t}\mathbf{u}_1 + c_2 e^{\lambda_2 t}\mathbf{u}_2 \tag{C.5}$$

where $\lambda_i$ and $\mathbf{u}_i$ are eigenvalues and eigenvectors of $\mathbb{A}$, respectively, and the $c_i$ are constants. We now proceed to find these eigenvalues and eigenvectors.

### C.2.1 Eigenvalues of $\mathbb{A}$

The eigenvalues must obey the characteristic equation $\det(\mathbb{A} - \lambda\mathbb{I}) = 0$:

$$\begin{aligned}
\det(\mathbb{A} - \lambda\mathbb{I}) &= \begin{vmatrix} -(\alpha+\gamma)/C - \lambda & \gamma/C \\ \gamma/C_0 & -\gamma/C_0 - \lambda \end{vmatrix} \\
&= \Big(-\frac{(\alpha+\gamma)}{C} - \lambda\Big)\Big(-\frac{\gamma}{C_0} - \lambda\Big) - \frac{\gamma^2}{CC_0} \\
&= \lambda^2 + \Big(\underbrace{\frac{\alpha+\gamma}{C} + \frac{\gamma}{C_0}}_{b}\Big)\lambda + \frac{\gamma\alpha}{CC_0} \\
&= 0
\end{aligned} \tag{C.6}$$

Following the notation in [Geoffroy et al., 2013b], we define the discriminant $\delta = b^2 - 4\frac{\alpha\gamma}{CC_0}$, which allows us to write the solution:

$$\lambda_\pm = \frac{-b \pm \sqrt{\delta}}{2} \tag{C.7}$$

To preserve the 'two-timescales' approach particular to this EBM, we define $\tau_s = -1/\lambda_-$ and $\tau_f = -1/\lambda_+$, giving:

$$\begin{aligned}
\tau_s &= -\frac{1}{\lambda_-} = \frac{CC_0}{2\alpha\gamma}(b + \sqrt{\delta}) \\
\tau_f &= -\frac{1}{\lambda_+} = \frac{CC_0}{2\alpha\gamma}(b - \sqrt{\delta})
\end{aligned} \tag{C.8}$$

which are the 'slow' and 'fast' timescales that characterise the temperature response to a step-forcing.

### C.2.2 Eigenvectors of $\mathbb{A}$

Having found the eigenvalues $\lambda_\pm$ (equation C.7), we can proceed in finding the eigenvectors of $\mathbb{A}$, which obey $\mathbb{A}\mathbf{u}_\pm = \lambda_\pm\mathbf{u}_\pm$. Firstly, for $\mathbf{u}_- = (\mu_-, \nu_-)$, we have $\mathbb{A}\mathbf{u}_- = \lambda_-\mathbf{u}_-$:

$$\begin{pmatrix} -(\alpha+\gamma)/C & \gamma/C \\ \gamma/C_0 & -\gamma/C_0 \end{pmatrix} \begin{pmatrix} \mu_- \\ \nu_- \end{pmatrix} = \lambda_- \begin{pmatrix} \mu_- \\ \nu_- \end{pmatrix} \tag{C.9}$$

which can be readily solved to give:

$$\mu_- = \Big(1 + \frac{C_0}{\gamma}\lambda_-\Big)\nu_- \tag{C.10}$$

We can rewrite the prefactor for $\nu_-$ as:

$$\begin{aligned} 1 + \frac{C_0}{\gamma}\lambda_- &= -\frac{C_0}{2\gamma}\Big(\underbrace{\frac{\alpha+\gamma}{C} - \frac{\gamma}{C_0}}_{b^*} - \sqrt{\delta}\Big) \\ &= -\frac{C_0}{2\gamma}\Big(b^* - \sqrt{\delta}\Big) = \frac{1}{\phi_s} \end{aligned} \tag{C.11}$$

where we've introduced the quantities $b^*$ and $\phi_s$, following the presentation in [Geoffroy et al., 2013b]. We now choose $\mu_- = 1$, which forces $\nu_- = \phi_s$. Hence, our 'slow' eigenvector is:

$$\mathbf{u}_- = \begin{pmatrix} 1 \\ \phi_s \end{pmatrix} \tag{C.12}$$

Following a similar procedure for $\mathbf{u}_+$, we find:

$$\mu_+ = \Big(1 + \frac{C_0}{\gamma}\lambda_+\Big)\nu_+ \tag{C.13}$$

and we rewrite the $\nu_+$ prefactor:

$$1 + \frac{C_0}{\gamma}\lambda_+ = -\frac{C_0}{2\gamma}\Big(b^* + \sqrt{\delta}\Big) = \frac{1}{\phi_f} \tag{C.14}$$

where, again, we've followed the presentation in [Geoffroy et al., 2013b], introducing the parameter $\phi_f$. As before, if we choose $\mu_+ = 1$, we arrive at our 'fast' eigenvector:

$$\mathbf{u}_+ = \begin{pmatrix} 1 \\ \phi_f \end{pmatrix} \tag{C.15}$$

### C.2.3 Solution

Having found the eigenvalues (equation C.7) and eigenvectors (equations C.12 and C.15) of $\mathbb{A}$, we can now simply substitute these into equation C.5 to find the solution to the homogeneous equation:

$$\mathbf{X}_h = c_- e^{\lambda_- t}\mathbf{u}_- + c_+ e^{\lambda_+ t}\mathbf{u}_+ \tag{C.16}$$

which can be written:

$$\begin{aligned}\begin{pmatrix} T_h(t) \\ T_{0h}(t) \end{pmatrix} &= c_- e^{-t/\tau_s}\begin{pmatrix} 1 \\ \phi_s \end{pmatrix} + c_+ e^{-t/\tau_f}\begin{pmatrix} 1 \\ \phi_f \end{pmatrix} \\ &= \begin{pmatrix} 1 & 1 \\ \phi_s & \phi_f \end{pmatrix}\begin{pmatrix} c_- e^{-t/\tau_s} \\ c_+ e^{-t/\tau_f} \end{pmatrix}\end{aligned} \tag{C.17}$$

### C.3 General solution

The general solution is simply the sum of the solution to the homogeneous equation (equation C.17) and the particular solution (equation C.4). Hence:

$$\begin{aligned} T(t) &= T_{eq} + c_- e^{-t/\tau_s} + c_+ e^{-t/\tau_f} \\ T_0(t) &= T_{eq} + \phi_s c_- e^{-t/\tau_s} + \phi_f c_+ e^{-t/\tau_f} \end{aligned} \tag{C.18}$$

In order to find the constants $c_\pm$, we need the initial conditions. If $T$ and $T_0$ are layer temperature perturbations, we have that at $t = 0$, $T = T_0 = 0$. Substituting in, we eventually find that:

$$c_+ = T_{eq}\frac{(\phi_s - 1)}{(\phi_f - \phi_s)} = -T_{eq}a_f \tag{C.19}$$

where the last equality follows to stay in keeping with the notation in [Geoffroy et al., 2013b]. This allows us to write:

$$a_f = \frac{(\phi_s - 1)}{(\phi_s - \phi_f)} \tag{C.20}$$

Similarly, we find that:

$$c_- = T_{eq}\frac{(1 - \phi_f)}{(\phi_f - \phi_s)} = -T_{eq}a_s \tag{C.21}$$

where, again, the last equality follows in order to be consistent with notation, which implies that:

$$a_s = \frac{(1 - \phi_f)}{(\phi_s - \phi_f)} \tag{C.22}$$

We note that $a_s + a_f = 1$, and $\phi_s a_s + \phi_f a_f = 1$. The $a_i$ and $\phi_i$ are the mode parameters that partition the adjustment towards equilibrium into the fast and slow components. Finally, we can write the full general solution:

$$\boxed{\begin{aligned} T(t) &= T_{eq}(1 - a_f e^{-t/\tau_f} - a_s e^{-t/\tau_s}) \\ T_0(t) &= T_{eq}(1 - \phi_f a_f e^{-t/\tau_f} - \phi_s a_s e^{-t/\tau_s}) \end{aligned}} \tag{C.23}$$

which is the same as equation 5.2 as presented in Chapter 5.

# D

# Non-dimensionalisation of the Geoffroy EBM and Limiting Cases

The two-layer EBM equations utilised in [Geoffroy et al., 2013b] are:

$$\begin{aligned} C\frac{dT}{dt} &= \mathcal{F} - \alpha T - \gamma(T - T_0) \\ C_0\frac{dT_0}{dt} &= \gamma(T - T_0) \end{aligned} \tag{D.1}$$

where $C$ and $C_0$ are effective heat capacities, and $T$ and $T_0$ are temperature perturbations for the mixed-layer ocean and deep ocean layers, respectively. The symbol $\mathcal{F}$ is an effective radiative forcing, $\alpha$ is the climate feedback parameter, and $\gamma$ is the heat exchange parameter.

We can rewrite the effective heat capacities as $C = \rho_0 c_p h$ and $C_0 = \rho_0 c_p H$, where $\rho_0$ is a reference seawater density, $c_p$ the specific heat capacity of seawater (at constant pressure), and $h$ and $H$ are layer thicknesses. We can then define the scalings $h_{scale}$

and $H_{scale}$ for the upper and lower layers, giving $h = h_{scale}\hat{h}$ and $H = H_{scale}\hat{H}$, where hatted variables are non-dimensional.

To isolate parameters affecting the dynamics, we need to non-dimensionalise the time variable by a timescale $t_{scale}$, such that $t = t_{scale}\hat{t}$. There are many natural timescales to choose, but here we choose the 'fast' timescale $\tau_F = (\rho_0 c_p h_{scale})/(\alpha+\gamma)$ as defined in [Held et al., 2010], as this timescale is most immediately relevant to transient climate change. Rewriting the EBM equations in terms of these non-dimensional variables gives us:

$$\begin{aligned} \rho_0 c_p h_{scale}\,\hat{h}\,\frac{1}{t_{scale}}\frac{dT}{d\hat{t}} &= \mathcal{F} - \alpha T - \gamma(T - T_0) \\ \rho_0 c_p H_{scale}\,\hat{H}\,\frac{1}{t_{scale}}\frac{dT_0}{d\hat{t}} &= \gamma(T - T_0) \end{aligned} \tag{D.2}$$

Substituting in $t_{scale} = \tau_F$ and dividing by $\alpha$ results in the equations:

$$\begin{aligned} \frac{\alpha+\gamma}{\alpha}\,\hat{h}\frac{dT}{d\hat{t}} &= \frac{\mathcal{F}}{\alpha} - T - \frac{\gamma}{\alpha}(T - T_0) \\ \frac{\alpha+\gamma}{\alpha}\frac{H_{scale}}{h_{scale}}\,\hat{H}\frac{dT_0}{d\hat{t}} &= \frac{\gamma}{\alpha}(T - T_0) \end{aligned} \tag{D.3}$$

or, equivalently:

$$\begin{aligned} \hat{h}\frac{dT}{d\hat{t}} &= \left(1 + \frac{\gamma}{\alpha}\right)^{-1}\left(\frac{\mathcal{F}}{\alpha} - T - \frac{\gamma}{\alpha}(T - T_0)\right) \\ \hat{H}\frac{dT_0}{d\hat{t}} &= \frac{h_{scale}}{H_{scale}}\left(1 + \frac{\gamma}{\alpha}\right)^{-1}\left(\frac{\gamma}{\alpha}(T - T_0)\right) \end{aligned} \tag{D.4}$$

where it is apparent that the ratio $\gamma/\alpha$ is crucial in controlling the dynamics. This simple procedure highlights that it is not just climate feedbacks that are important in transient climate change. The interplay of climate feedbacks with the efficiency of ocean heat uptake, or ocean vertical heat transports, is key.

## D.1 Limiting cases

### D.1.1 Radiative feedbacks dominate, $\gamma/\alpha << 1$

In this case, we presume that there is very little heat exchange between the two layers, and so the dominant heat flux in the model is that radiated upwards to space from the upper layer. We make use of the notation used in Appendix C, where we derived the analytical solution for the Geoffroy EBM under a step forcing. We first look at the parameters $b$ and $\delta$:

$$\begin{aligned} b &= \frac{\alpha+\gamma}{C} + \frac{\gamma}{C_0} \approx \frac{\alpha}{C} \\ \delta &= b^2 - \frac{4\alpha\gamma}{CC_0} = b^2 - \frac{4\alpha^2(\gamma/\alpha)}{CC_0} \approx b^2 \approx \left(\frac{\alpha}{C}\right)^2 \end{aligned} \tag{D.5}$$

These then feed back into the slow and fast timescales, giving us:

$$\begin{aligned} \tau_s &= \frac{CC_0}{2\alpha\gamma}(b+\sqrt{\delta}) \approx \frac{CC_0}{2\alpha\gamma}\left(\frac{\alpha}{C}+\frac{\alpha}{C}\right) = \frac{C_0}{\gamma} \\ &\implies \tau_f \approx \frac{C}{\alpha} \end{aligned} \tag{D.6}$$

where we've used the fact that $\det \mathbb{A} = \gamma\alpha/CC_0$ is the product of the eigenvalues, i.e. $1/(\tau_f\tau_s)$, in order to find the fast timescale $\tau_f$. Now, like $b$, $b^* \approx \alpha/C$, which means we can find the parameters $\phi_s$ and $\phi_f$ by:

$$\begin{aligned} \phi_s &= \frac{C}{2\gamma}(b^*+\sqrt{\delta}) \approx \frac{C}{2\gamma}\left(\frac{\alpha}{C}+\frac{\alpha}{C}\right) = \frac{\alpha}{\gamma} \\ \phi_f &= \frac{C}{2\gamma}(b^*-\sqrt{\delta}) \approx 0 \end{aligned} \tag{D.7}$$

We can then find the parameters $a_f$ and $a_s$:

$$\begin{aligned} a_f &= \frac{\phi_s - 1}{\phi_s - \phi_f} \approx 1 - \frac{\gamma}{\alpha} \\ a_s &= \frac{1-\phi_f}{\phi_s-\phi_f} \approx \frac{\gamma}{\alpha} \end{aligned} \tag{D.8}$$

Note that the relationships $a_f + a_s = 1$ and $\phi_f a_f + \phi_s a_s = 1$ still hold, which ensures the satisfaction of the initial conditions $T(0) = T_0(0) = 0$. Finally, we can write down the limiting solutions:

$$\boxed{\begin{aligned} T(t) &\approx T_{eq} - \frac{\gamma}{\alpha} T_{eq} e^{-\gamma t/C_0} - \left(1 - \frac{\gamma}{\alpha}\right) T_{eq} e^{-\alpha t/C} \approx T_{eq}\left(1 - e^{-\alpha t/C}\right) \\ T_0(t) &\approx T_{eq}\left(1 - e^{-\gamma t/C_0}\right) \end{aligned}} \tag{D.9}$$

Note that if $\gamma = 0$, then $T_0(t) = 0$ as expected. What's interesting here is that the two-layer EBM has reduced to two separate one-layer EBMs in its behaviour. If $\gamma << \alpha$, the coupling between the two layers disappears. Each layer simply approaches the equilibrium temperature $T_{eq}$ with their respective fast or slow timescale. This decoupling of the two-layer EBM into two one-layer EBMs is shown schematically in figure D.1. The lower layer heat fluxes are of the same form as those of the upper layer, but are scaled by $\gamma/\alpha$ i.e. a very small number.

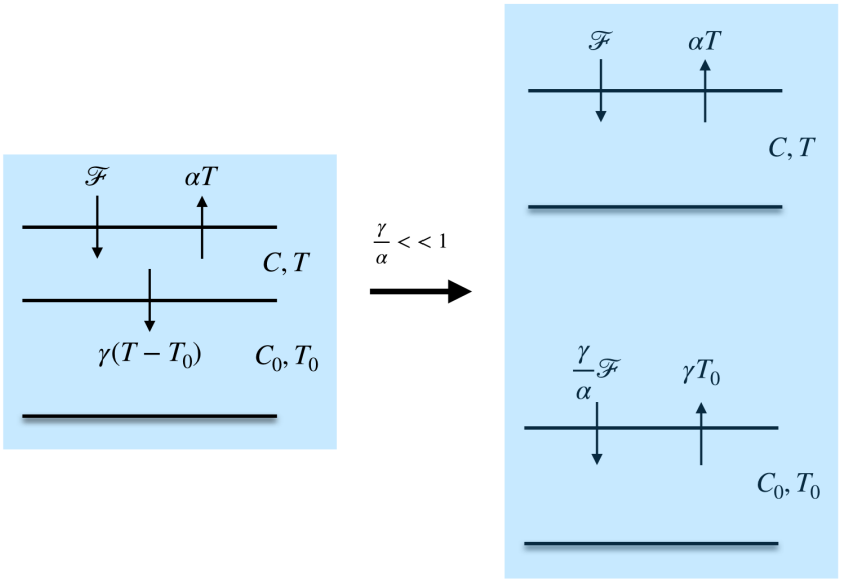



**Figure D.1:** Two-layer EBM reduces to two separate one-layer EBMs in the limit $\gamma << \alpha$.

### D.1.2 Heat exchange dominates, $\gamma/\alpha >> 1$

In this limit case, we presume that heat is much more rapidly transported downwards from the upper layer to the lower layer than is radiated upwards to space, i.e. $\gamma >> \alpha$. Following the procedure in the previous section, we approximate $b$ and $\delta$

first:

$$
\begin{aligned}
b &= \frac{\alpha+\gamma}{C} + \frac{\gamma}{C_0} \approx \frac{\gamma}{C} + \frac{\gamma}{C_0} = \frac{\gamma(C+C_0)}{CC_0} \\
\delta &= b^2 - \frac{4\alpha\gamma}{CC_0} = \frac{(\alpha+\gamma)^2}{C^2} + \frac{2\gamma(\gamma-\alpha)}{CC_0} + \frac{\gamma^2}{C_0^2} \approx \frac{\gamma^2}{C^2} + \frac{2\gamma^2}{CC_0} + \frac{\gamma^2}{C_0^2} = \left(\frac{\gamma}{C} + \frac{\gamma}{C_0}\right)^2
\end{aligned}
\tag{D.10}
$$

We find that $\delta \approx b^2$, as we found for the previous limit case. We now look at the timescales $\tau_s$ and $\tau_f$, giving us:

$$
\begin{aligned}
\tau_s &= \frac{CC_0}{2\alpha\gamma}(b + \sqrt{\delta}) \approx \frac{CC_0}{2\alpha\gamma}\frac{2\gamma(C+C_0)}{CC_0} = \frac{C+C_0}{\alpha} \\
&\implies \tau_f \approx \frac{CC_0}{\gamma(C+C_0)}
\end{aligned}
\tag{D.11}
$$

where, again, we've made use of the fact that $\det \mathbb{A} = 1/(\tau_f \tau_s)$. Note that in this case $\tau_f \approx 1/b$. Similarly, as for $b$, we find the $b^*$ approximation:

$$
b^* = \frac{\alpha+\gamma}{C} - \frac{\gamma}{C_0} \approx \frac{\gamma}{C} - \frac{\gamma}{C_0} = \frac{\gamma(C_0-C)}{CC_0} \tag{D.12}
$$

This, in turn, lets us find the parameters:

$$
\begin{aligned}
\phi_f &= \frac{C}{2\gamma}(b^* - \sqrt{\delta}) \approx \frac{C}{2\gamma}\left(\frac{\gamma(C_0-C)}{CC_0} - \frac{\gamma(C_0+C)}{CC_0}\right) = -\frac{C}{C_0} \\
\phi_s &= \frac{C}{2\gamma}(b^* + \sqrt{\delta}) \approx 1
\end{aligned}
\tag{D.13}
$$

Now, we find approximations for the mode parameters $a_f$ and $a_s$:

$$
\begin{aligned}
a_f &= \frac{\phi_s - 1}{\phi_s - \phi_f} \approx 0 \\
a_s &= \frac{1 - \phi_f}{\phi_s - \phi_f} \approx 1
\end{aligned}
\tag{D.14}
$$

As before, $a_f + a_s = 1$ and $\phi_f a_f + \phi_s a_s = 1$ still hold. Finally, we can write down the limiting solutions for this case as:

$$\boxed{\begin{aligned} T(t) &\approx T_{eq}\left(1 - e^{-\alpha t/(C+C_0)}\right) \\ T_0(t) &\approx T_{eq}\left(1 - e^{-\alpha t/(C+C_0)}\right) \end{aligned}} \tag{D.15}$$

So, $T(t) = T_0(t)$, and both layers in the system behave in exactly the same way. This effectively reduces the two-layer EBM to a well-mixed, one-layer system with an effective heat capacity of $C + C_0$, as shown in figure D.2.

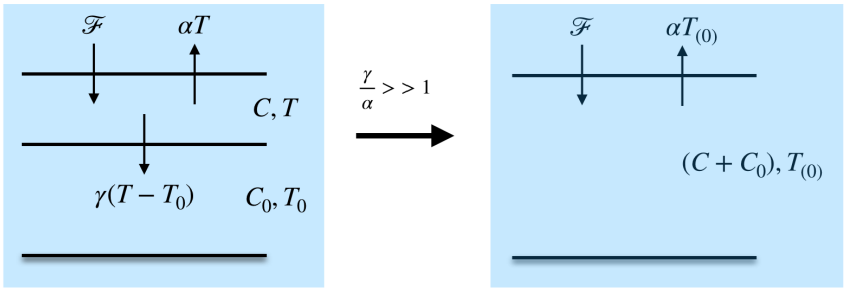



**Figure D.2:** Two-layer EBM reduces to a one-layer system with effective heat capacity $C + C_0$ when $\gamma >> \alpha$.

In the real-world system, $\gamma$ and $\alpha$ are probably comparable, so the oceanic mixed-layer is neither completely decoupled from, nor completely coupled to the deep ocean. The behaviour lies somewhere in between these two limiting cases.

# E

# Fitted parameter values for two-layer EBMs

| | $\mathcal{F}$ (W m$^{-2}$) | $\alpha$ (W m$^{-2}$ K$^{-1}$) | $C$ (W yr m$^{-2}$ K$^{-1}$) | $C_0$ (W yr m$^{-2}$ K$^{-1}$) | $h$ (m) | $H$ (m) | $\gamma^{(*)}$ (W m$^{-2}$ K$^{-1(-2)}$) |
|---|---|---|---|---|---|---|---|
| Global | 4.26 | 1.56 | 17.8; 18.8 | 113.6; 135.0 | 134; 143 | 859; 1021 | 1.36; 1.05 |
| Small basin | 4.50 | 2.14 | 13.6; 15.3 | 135.5; 159.4 | 103; 116 | 1025; 1205 | 2.12; 2.20 |
| Large basin | 4.56 | 2.06 | 12.5; 15.0 | 121.5; 141.4 | 95; 114 | 919; 1070 | 2.10; 2.05 |
| southern ocean | 3.83 | 0.76 | 17.0; 19.2 | 104.0; 128.4 | 128; 145 | 786; 971 | 0.52; 0.18 |

**Table E.1:** Fitted physical parameters for both the (Geoffroy; quadratic) EBMs using an interior point algorithm: the radiative forcing $\mathcal{F}$, radiative feedback $\alpha$, upper-layer heat capacity $C$, lower-layer heat capacity $C_0$, the corresponding upper-layer and lower-layer thicknesses $h$ and $H$, and the heat exchange coefficient $\gamma$ (or $\gamma^*$) for each of the DDrake basins.

| | $\mathcal{F}$ (W m$^{-2}$) | $\alpha$ (W m$^{-2}$ K$^{-1}$) | $C$ (W yr m$^{-2}$ K$^{-1}$) | $C_0$ (W yr m$^{-2}$ K$^{-1}$) | $h$ (m) | $H$ (m) | $\gamma^{(*)}$ (W m$^{-2}$ K$^{-1(-2)}$) |
|---|---|---|---|---|---|---|---|
| CNRM-CM5 | 9.88 | 2.33 | 28.7; 32.4 | 226.3; 292.6 | 217; 245 | 1711; 2212 | 1.40; 0.55 |
| GFDL-ESM2M | 9.69 | 2.76 | 24.7; 1.5 | 463.6; 491.2 | 187; 11 | 3505; 3714 | 3.48; 3.42 |
| MPI-ESM-LR | 11.80 | 2.09 | 23.4; 29.0 | 391.6; 454.2 | 177; 219 | 2961; 3434 | 3.69; 1.84 |
| MRI-CGCM3 | 9.78 | 2.54 | 55.8; 66.1 | 661.3; 661.3 | 422; 500 | 5000; 5000 | 6.24; 6.60 |
| NorESM-1M | 10.85 | 2.48 | 35.3; 43.0 | 538.7; 611.6 | 267; 325 | 4073; 4624 | 4.98; 3.52 |
| MITgcm DDrake | 4.26 | 1.56 | 17.8; 18.8 | 113.6; 135.0 | 134; 143 | 859; 1021 | 1.36; 1.05 |
| Ensemble mean | 10.40 | 2.44 | 33.6; 34.4 | 456.3; 502.2 | 254; 260 | 3450; 3797 | 3.96; 3.19 |
| Std. dev. | 0.91 | 0.25 | 13.3; 23.4 | 162.8; 144.6 | 100; 177 | 1231; 1093 | 1.81; 2.27 |

**Table E.2:** Fitted physical parameters for both the (Geoffroy; quadratic) EBMs using an interior point algorithm. The effective radiative forcing $\mathcal{F}$ and climate feedback $\alpha$ values for CMIP5 models are taken from [Kostov et al., 2014]. Upper-layer heat capacity $C$, lower-layer heat capacity $C_0$, the corresponding upper-layer and lower-layer thicknesses $h$ and $H$, and the heat exchange coefficient $\gamma$ (or $\gamma^*$) estimates for the five CMIP5 models used. The equivalent parameters found for DDrake (same as the 'Global' row in table E.1) are shown in the bottom row for comparison. Ensemble means and standard deviations don't include the values from DDrake.

| | $\mathcal{F}$ (W m$^{-2}$) | $\alpha$ (W m$^{-2}$ K$^{-1}$) | $C$ (W yr m$^{-2}$ K$^{-1}$) | $C_0$ (W yr m$^{-2}$ K$^{-1}$) | $h$ (m) | $H$ (m) | $\gamma^{(*)}$ (W m$^{-2}$ K$^{-1(-2/3)}$) |
|---|---|---|---|---|---|---|---|
| Global | 4.26 | 1.56 | 17.7; 17.6 | 113.6; 103.7 | 134; 133 | 859; 784 | 1.36; 1.43 |
| Small basin | 4.50 | 2.14 | 13.6; 13.2 | 135.6; 125.3 | 103; 100 | 1025; 947 | 2.12; 2.02 |
| Large basin | 4.56 | 2.06 | 12.6; 13.2 | 121.5; 132.3 | 95; 100 | 919; 1000 | 2.10; 1.83 |
| southern ocean | 3.83 | 0.76 | 16.9; 15.7 | 104.0; 90.3 | 128; 119 | 786; 683 | 0.52; 0.74 |

**Table E.3:** Fitted physical parameters for both the (Geoffroy; RY) EBMs using an interior point algorithm: the radiative forcing $\mathcal{F}$, radiative feedback $\alpha$, upper-layer heat capacity $C$, lower-layer heat capacity $C_0$, the corresponding upper-layer and lower-layer thicknesses $h$ and $H$, and the heat exchange coefficient $\gamma$ (or $\gamma^*$) for each of the DDrake basins.

| | $\mathcal{F}$ (W m$^{-2}$) | $\alpha$ (W m$^{-2}$ K$^{-1}$) | $C$ (W yr m$^{-2}$ K$^{-1}$) | $C_0$ (W yr m$^{-2}$ K$^{-1}$) | $h$ (m) | $H$ (m) | $\gamma^{(*)}$ (W m$^{-2}$ K$^{-1(-2/3)}$) |
|---|---|---|---|---|---|---|---|
| CNRM-CM5 | 9.88 | 2.33 | 28.7; 26.6 | 226.3; 191.6 | 217; 201 | 1711; 1449 | 1.40; 1.92 |
| GFDL-ESM2M | 9.69 | 2.76 | 24.7; 22.1 | 463.6; 405.2 | 187; 167 | 3505; 3064 | 3.48; 4.00 |
| MPI-ESM-LR | 11.80 | 2.09 | 23.4; 20.2 | 391.6; 352.1 | 177; 153 | 2961; 2662 | 3.69; 4.65 |
| MRI-CGCM3 | 9.78 | 2.54 | 55.8; 48.0 | 661.3; 661.3 | 422; 363 | 5000; 5000 | 6.24; 6.16 |
| NorESM-1M | 10.85 | 2.48 | 35.3; 30.8 | 538.7; 489.2 | 267; 233 | 4073; 3699 | 4.98; 5.58 |
| MITgcm DDrake | 4.26 | 1.56 | 17.7; 17.6 | 113.6; 103.7 | 134; 133 | 859; 784 | 1.36; 1.43 |
| Ensemble mean | 10.40 | 2.44 | 33.6; 29.5 | 456.3; 419.9 | 254; 223 | 3450; 3175 | 3.96; 4.46 |
| Std. dev. | 0.91 | 0.25 | 13.3; 11.1 | 162.8; 173.2 | 100; 84 | 1231; 1310 | 1.81; 1.65 |

**Table E.4:** Fitted physical parameters for both the (Geoffroy; RY) EBMs using an interior point algorithm. The effective radiative forcing $\mathcal{F}$ and climate feedback $\alpha$ values for CMIP5 models are taken from [Kostov et al., 2014]. Upper-layer heat capacity $C$, lower-layer heat capacity $C_0$, the corresponding upper-layer and lower-layer thicknesses $h$ and $H$, and the heat exchange coefficient $\gamma$ (or $\gamma^*$) estimates for the five CMIP5 models used. The equivalent parameters found for DDrake (same as the 'Global' row in table E.3) are shown in the bottom row for comparison. Ensemble means and standard deviations don't include the values from DDrake.

# F

# Vertical buoyancy transport within a wind-driven gyre

We start with the quasigeostrophic (QG) theory of [Rhines and Young, 1982b] to describe the circulation within a wind-driven gyre. Ignoring relative vorticity (appropriate for basin-scale circulations), the QG potential vorticity $q$ is given by

$$q = \beta y + \frac{f_0^2}{N^2}\frac{\partial^2 \psi}{\partial z^2} \tag{F.1}$$

where $f_0$ is a reference value for the Coriolis parameter, $\beta$ is the variation of the Coriolis parameter with latitude, $N$ is the buoyancy frequency, and $\psi$ is the stream function.

We assume that potential vorticity is homogenised within closed contours of $\psi$ [Rhines and Young, 1982a], so that within the gyre, $q = q_0$ is a constant. And we define a depth $D(x, y)$ that marks the lower boundary of the gyre. This also marks the depth of the wind's influence, so, below this depth, $\psi = 0$. The flow is then given by solving the following equations:

$$\begin{aligned} \frac{\partial^2 \psi}{\partial z^2} = \frac{N^2}{f_0^2}(q_0 - \beta y) \qquad ; \qquad -D(x,y) < z < 0 \\ \psi = 0 \qquad ; \qquad z \leq -D(x,y) \end{aligned} \tag{F.2}$$

At the lower boundary of the gyre, we require $\psi = \psi_z = 0$ to ensure that $\psi$ and $\psi_z$ remain continuous across the boundary. This leads to the solution:

$$\psi = \frac{N^2}{2f_0^2}(z + D)^2(q_0 - \beta y) \qquad ; \qquad -D(x,y) < z < 0 \tag{F.3}$$

Next, we can obtain an expression for $D$ using the QG buoyancy equation and rearranging for $w$ giving:

$$w = -\frac{1}{N^2} J(\psi, b) = -\frac{f_0}{N^2} J(\psi, \psi_z) \tag{F.4}$$

where the perturbation buoyancy $b = f_0 \psi_z$, $J$ denotes the Jacobian, and we have assumed that $b_t = 0$ as we are only interested in statistically-steady solutions.

We assume that at $z = 0$, $w = w_{Ek}$ is the Ekman pumping velocity. Evaluating our expression for $w$ (equation F.4) at $z = 0$ gives:

$$w_{Ek} = w|_{z=0} = \frac{\beta N^2}{2f_0^3} D^2 \frac{\partial D}{\partial x}(q_0 - \beta y) \tag{F.5}$$

We define a barotropic stream function as:

$$\psi_B = \int_x^{x_E} w_{Ek}\, dx' \tag{F.6}$$

where $x_E$ is the eastern boundary of the gyre. Then, integrating the expression for $w_{Ek}$ and rearranging for $D$ gives:

$$D = \left[ \frac{-6f_0^3}{\beta N^2} \frac{\psi_B}{(q_0 - \beta y)} \right]^{1/3} \tag{F.7}$$

If we further assume that $w_{Ek}$ is independent of $x$, then $\psi_B = w_{Ek}(x_E - x)$ and we can rewrite equation F.7 as:

$$D = \left[ \frac{6f_0^3}{\beta N^2} \frac{w_{Ek}(x - x_E)}{(q_0 - \beta y)} \right]^{1/3} \tag{F.8}$$

Substituting either expression for $D$ into equation F.3 then gives the full stream function solution.

Next, we wish to find an expression for the vertical buoyancy transport $wb$. This is:

$$wb = \underbrace{-\frac{f_0}{N^2} J(\psi, \psi_z)}_{w} \cdot \underbrace{f_0 \psi_z}_{b} = \frac{f_0^2}{N^2} \psi_z (\psi_y \psi_{zx} - \psi_x \psi_{zy}) \tag{F.9}$$

After expanding and simplifying, this leads to an expression that reads:

$$wb = \frac{\beta}{2} \left( \frac{N^2}{f_0^2} \right)^2 D_x (z + D)^3 (q_0 - \beta y)^2 \tag{F.10}$$

Noting that $b_z = f_0 \psi_{zz} = \frac{N^2}{f_0}(q_0 - \beta y)$, we can rewrite equation F.10 as:

$$wb = \frac{\beta}{2f_0^2} D_x (z + D)^3 \left( \frac{\partial b}{\partial z} \right)^2 \tag{F.11}$$

And finally, substituting in equation F.8 for $D$ and evaluating at $z = 0$ gives:

$$\boxed{wb|_{z=0} = \left[ \frac{6f_0^2}{\beta} (x - x_E) \right]^{1/3} w_{Ek}^{4/3} \left( \frac{\partial b}{\partial z} \right)^{2/3}} \tag{F.12}$$

which is the same as equation 5.10 as presented in Chapter 5. We thus find that the vertical buoyancy transport at the surface is proportional to the 2/3-power of $\partial b / \partial z$. Further, we find that $wb$ is proportional to $w_{Ek}^{4/3}$, indicating that a stronger wind-stress curl may lead to greater OHU.